SYNTHESIS, STRUCTURE AND PROPERTIES OF METAL-ORGANIC COMPOUNDS OF CADMIUM AND VANADIUM

Thesis Submitted for the Degree of

Doctor of Philosophy (Science) 2025

By

PRIYANKA MANNA

Index No: 220/18/Chem./26

Department of Chemistry

Jadavpur University

Kolkata-700032, India

February, 2025

JADAVPUR UNIVERSITY

Department of Chemistry

Kolkata 700032, India

Dr. Partha Mahata

Assistant Professor

Email: parthachem@gmail.com

CERTIFICATE FROM THE SUPERVISOR

This is to certify that the thesis entitled **"Synthesis, Structure and Properties of Metal-Organic Compounds of Cadmium and Vanadium"** submitted by Ms. **Priyanka Manna**, who got her name registered on 1st October, 2018 for the award of Ph.D. (Science) degree of Jadavpur University, is absolutely based upon her own work under the supervision of Dr. Partha Mahata and that neither this thesis nor any part of it has been submitted for either any degree/diploma or any other academic award anywhere before.

Date: 25/02/25

Partha Mahata

(Dr. Partha Mahata)

(Signature of the supervisor date with official seal)

Dr. Partha Mahata
Assistant Professor
Department of Chemistry
Jadavpur University
Kolkata-700 032

Dedicate to

Baba, Maa, Bitu,
and Riddish

ACKNOWLEDGEMENTS

*It is a great bliss and admiration for me that, I am about to submit my Ph.D. thesis entitled "**Synthesis, Structure and Properties of Metal-Organic Compounds of Cadmium and Vanadium**" that includes solely my research activities performed in the Department of Chemistry, Jadavpur University. In this regard, I would like to express my deep sense of thanks and gratitude to all those persons who helped me and contributed to my experience during this time.*

First and foremost, I would like to thank my supervisor, Dr. Partha Mahata, Assistant Professor, Jadavpur University for his constant encouragement, invaluable guidance, suggestions and continuous support. His timely advice and meticulous scrutiny, scholarly advice and scientific approach have helped a lot in every way during my work. Apart from many scientific lessons, he taught me to be focused and be patient in future. Without his resourceful and continuous untiring supervision, this work would not have been possible.

I would like to express my deep sense of gratitude to Dr. Dhritiman Gupta, Department of Physics, School of Advanced Sciences, Vellore Institute of Technology, Vellore for his help on conductivity data collection.

I would like to thank Dr. Deepak Chopra, Department of Chemistry, Indian Institute of Science Education and Bhopal for his help on Single Crystal Data Collection.

I would like to express my gratitude to Prof. Kajal Krishna Rajak, Prof. Chittaranjan Sinha, Prof. Samaresh Bhattattacharya, Prof. Arup Gayen, Prof. Amrita Saha, Prof. Sujoy Kumar Baitalik, Prof. Debajyoti Ghoshal, Prof. Shouvik Chattapadhyay, Prof. Subrata Mukhopadhyay, and Prof. Partha Roy for their kind help and suggestion.

I am also grateful to all the faculty members of Department of Chemistry of Jadavpur University for their kind help.

My heartiest thank goes to my lab mates, especially, Dr. Debal Kanti Singha, Chhatan Das, Sayani Hui, Sourav Sarkar, Pooja Daga, Akash Kumar Chandra, Debamalya Ghosh, Prakash Majee for their invaluable co-operation and suggestions throughout the progress of the work.

I am privileged to thank my parents and my entire family members for their kind understanding, encouragement, and moral supports throughout my life.

Priyanka Manna

Date: Department of Chemistry

Jadavpur University

Kolkata-700032

Contents

Page No.

Preface

The research in the area of metal-organic compounds (MOCs) continues to be interesting due to their structural characteristics, significant porosity and tunable properties. Metal-organic compounds have achieved enormous attention from the scientific community due to their potential applications in different areas such as gas storage, gas separation, catalysis, proton conduction and drug delivery. This kind of materials exhibits interesting optical, electronic and sorption properties.

The newly synthesized metal-organic compounds (MOCs) are thoroughly characterized by several techniques like PXRD, ^{1}H NMR, UV-Vis, FTIR, TGA, gas sorption and Mass analysis. Structure of the metal-organic compounds (MOCs) is checked by single crystal X-ray diffraction techniques. This thesis consists of five chapters based on the synthesis, characterization, study of conductivity and sensing properties of the newly synthesized metal-organic compounds (MOCs).

Chapter 1 presents a brief discussion of the different types of metal organic compounds and summarizing some cadmium and vanadium based literature survey.

Chapter 2 deals the synthesis, structure and effect of hydrogen bonding on the luminescence lifetime and device resistance of two new coordination polymers of formulas $[Cd_2(2,3\text{-pzdc})(tz)_2]$ (**2.1**) and $[Cd_2(2,3\text{-pzdc})(dtz)_2]$ (**2.2**). Lifetime studies from time-resolved spectra show 0.82 and 0.60 ns for compound **2.1** and 2.02 and 1.78 ns for compound **2.2**. The higher lifetimes of the excited states in the case of compound **2.2** establish the role of hydrogen-bond interactions in reducing the nonradiative decay processes. In compound **2.2** device, the overall current magnitude is 10 times higher than that of the compound **2.1** device and series resistance extracted for the compound **2.2** device is ≈ 22 times lower than that of the compound **2.1** device, indicating the higher conductivity of compound **2.2**. This behavior indicates a probable role of hydrogen-bond interactions in the lower resistance and higher conductivity of compound **2.2** compared to compound **2.1**.

Chapter 3 includes the synthesis, structure, dye sorption, and metal ion sensing behavior of new Cd(II) based metal organic framework having formulas $[Cd(PDA)(L)_2]$. The compound **3.1** shows selective and efficient sorption of large anionic dye remazol brilliant blue R (RBBR) in aqueous medium, whereas compound **3.1** exhibits low sorption

towards orange G (OG), methyl orange (MO), methylene blue (MB) and rhodamine B (RhB). The compound **3.1** also exhibits photoluminescence based sensing behaviors towards Fe^{3+}, Cr^{3+} and Al^{3+} ions in aqueous medium based on luminescence quenching effect due to formation of charge transfer species through the molecular level interactions between metal ions (Fe^{3+}/Cr^{3+}/Al^{3+}) and compound **3.1.**

Chapter 4 present the synthesis of new Cd(II)-based 2D compound [Cd(BTCH)(L)] (BTCH = di-anionic 1,3,5-benzene tricarboxylic acid and L = 2,4,5-tri-4-pyridyl-1H-imidazole). The compound **4.1** has been characterized by powder X-ray diffraction, Fourier transform infrared (FTIR) spectroscopy and thermogravimetric analysis (TGA). Aqueous dispersion of compound **4.1** showed emission at 400 nm upon excitation at 300 nm. The compound **4.1** showed photoluminescence-based sensing behaviors towards Fe^{3+}, Al^{3+} and Cr^{3+} ions in aqueous medium based on luminescence quenching. The limit of detection for Fe^{3+}, Al^{3+}, Cr^{3+} ions are 0.568 μM, 1.721 μM and 0.840 μM respectively. Compound **4.1** also showed significant quenching effect in the presence of 2,4,6-trinitrophenol (TNP) with detection limit of 0.302 μM. Compound **4.1** showed luminescence quenching effect due to possibility of formation of molecular level interaction between compound **4.1** and the metal ions (Fe^{3+}, Cr^{3+} and Al^{3+}). The compound **4.1** shows luminescence quenching effect due to the second absorption band TNP and DNP is well overlapped with the emission spectra of **4.1**. So, in the case of TNP and DNP, energy transfers from the excited state of the ligands of compound **4.1**.

Chapter 5 present the synthesized of two new dioxidovanadium compounds using either $V^{IV}OSO_4$. $5H_2O$ or $[V^{IV}O(acac)_2]$ or $NH_4V^{V}O_3$ as the starting material and hydrazone ligands having formula $[V^{V}O_2(L)]$ (L = hydrazone ligand). Both the compound were synthesized in three different methods (acidic, neutral and basic medium). In compound **5.1**, the presence of free hydroxyl groups stabilized the molecular species through intra-molecular O–H…N type hydrogen bond interactions The compound **5.1** showed highly selective luminescence turn on behaviour along with 33 nm blue shift in presence of Al^{3+} ions in aqueous medium. In compound **5.2**, the free amino groups involve in both the intra-molecular N–H…N type and inter-molecular N – H…O type hydrogen bond interactions. Whereas the compound **5.2** showed luminescence quenching behaviour in the presence of Fe^{3+}, Al^{3+} and Cr^{3+} ions. The luminescence response mechanism of both the compounds in presence of metal ions has been correlated with the molecular level interactions.

List of Abbreviations and symbols

a : Crystallographic distance along 'x' axis of a unit cell (in angstrom)

b : Crystallographic distance along 'y' axis of unit cell (in angstrom)

c : Crystallographic distance along 'z' axis of unit cell (in angstrom)

α : Crystallographic angle in a unit cell between b and c (in degree)

β : Crystallographic angle in a unit cell between c and a (in degree)

γ : Crystallographic angle in a unit cell between a and b (in degree)

ρ : Density (in g cm^{-3})

Mo-Kα : Molybdenum Kα radiation

F(000) :Crystallographic (000) plane

Å : Angstrom

τ : Fluorescence Lifetime

π : Pi

σ : Sigma

DFT : Density functional theory

Ksv : Stern-Volmer constant

I : Fluorescence intensity

ex : Excitation

em : Emission

UV : Ultraviolet

Vis : Visible

Λ : Wavelength

% T : Percentage of transmittance

h : Hour(s)

KBr : Potassium bromide

$CHCl_3$: Chloroform

CAN : Acetonitrile

MeOH : Methanol

DCM : Dichloromethane

DMF/dmf : N,N-Dimethylformamide

DMSO/dmso : Dimethyl sulfoxide

DMSO-d_6 : Deuterated dimethyl sulfoxide

mL : Milliliter

μM : Micromolar

nM : Nanomolar

eV : Electron-volt

ESI MS : Electron Spray Ionization Mass spectrometry

FTIR : Furrier Transform Infrared Spectroscopy

NMR : Nuclear Magnetic Resonance

PXRD/XRPD : Powder X-ray Diffraction/X-ray Powder Diffraction

CT : Charge Transfer

PET : Photo-Induced Electron Transfer

PCT : Photo-Induced Charge Transfer

ICT : Internal Charge Transfer

ET : Energy Transfer

FRET : Fluorescence Resonance Energy Transfer

ESIPT : Excited-State Intramolecular Proton Transfer

HOMO : Highest Occupied Molecular Orbital

LUMO : Lowest Unoccupied Molecular Orbital

LOD : Limit of Detection

BTC : 1,3,5-benzenetricarboxylic acid

Pmtz : 5-(pyrimidyl)-tetrazolato

Py : pyridine

JUC-63 : $Cd_2(ABTC)(DMF)_3 \cdot (DMF)_2$

H_4ABTC : 3,3′,5,5′-azobenzenetetracarboxylic acid

CTC : cis,cis-1,3,5-cyclohexanetricarboxylate

DFDA : 9,9-dipropylfluorene-2,7-dicarboxylate anion

LCU-103 : $[Zn_{1.5}(dttz)(Hdpa)]_n$

H_3dttz : 4,5-di(1H-tetrazol-5-yl)-2H-1,2,3-triazole

Hdpa : 4,4′-dipyridylamine

H_2oba :4,4′-oxybis(benzoicacid)

bpy : 4,4′-bipyridine

NH_2-BDC : amino-1,4-benzenedicarboxylic acid

4-bpdb : 1,4-bis(4-pyridyl)-2,3-diaza-2,3-butadiene

2,6-NDC : 2,6-Naphthalenedicarboxylic acid

H_4BTDI : 5,5′-(benzothiadiazole-4,7-diyl)diisophthalic acid

H_2DBA : 2′-amino-1,1′:4,1″-terphenyl-4,4″-dicarboxylic acid

BIBT : 4,7-bi(1*H*-imidazol-1-yl)benzo-[2,1,3]thiadiazole

DMA : N,N- Dimethylacetamide

$PATP^{2-}$: 2-((pyridin-2-ylmethyl)amino)terephthalate

NZF : Nitrofurazone

NFT : nitrofurantoin

H_4BCP : 5-(2,6-bis(4-carboxyphenyl) pyridin-4-yl) isophthalic acid

H_3TCPB :1,3,5-tris(4-carbonylphenyloxy)benzene

H_3ITTC : 4,4′,4″-(1*H*-imidazole-2,4,5-triyl) tribenzoic acid

BS : benzenesulfonate

Tib : 1,3,5-tris(1-imidazolyl)benzene

H_3Pycia : 5-(1Hpyrazole-4-carboxamido)isophthalic acid

H_2PBA : 4-(1Hpyrazol-4-yl)benzoic acid

H_4PTCA : pyrene-1,3,6,8-tetracarboxylic acid

H_4dobdc : 2,5-dihydroxyterephthalic acid

BDC : 1,4-benzenedicarboxylate

4-bpd : 1,4-bis(4-pyridyl)-2,3-diaza-1,3-butadiene

H_2nip : 5-nitroisophthalic acid

pdiq : 6-(pyridin-4-yl)-5,6-dihydrobenzo[4,5]imidazo[1,2-*c*]quinazoline]

4-TP : 4-tetrazole pyridine

H_4BPTC : 3,3′,5,5′-biphenyltetracarboxylic acid

BTB : 1,3,5-tris(4-carboxyphenyl) benzene

IsoNDI : *N*,*N*′-di(4-pyridylacylamino)-1,4,5,8-naphthalene diimide

H_3NTB : 4,4′,4″-nitrilotribenzoic acid

H_3cia : 2-(4-carboxylphenoxy)terephthalic acid

DIN : 1,4-di(imidazol-1-yl)naphthalene

H_2TPA : terephthalic acid

Bib : 1,4-bis(2-methyl-imidazol-1-yl)butane

H_4bptc : 3,3′,5,5′-biphenyltetracarboxylic acid

$BPDC^{2-}$: biphenyl-4,4′-dicarboxylate

PIP : piperazine

H_2-CEP : 2-carboxyethylphosphonic acid

H_5hedp : etidronic acid

Chapter 1

General Introduction

ABSTRACT

Here, we have discussed different types of metal organic compounds. We have explained the sensing behaviour, sorption behaviour, electronic devices of metal organic compounds. We have also summarised some cadmium and vanadium based literature survey.

1.1 INTRODUCTION

Alfred Werner explained the octahedral structure of transition metal complexes in 1893. The mystifying aspect surrounding transition-metal compounds were the source of modern coordination chemistry. Coordination chemistry was tremendously growth from the past 119 years and increases the various synthesis method, various types of structure, and reactivity of transition metal complexes. In 1913, Alfred Werner received the Nobel Prize for his proposed transition-metal compounds and transformation of transition-metal compounds to extended inorganic polymers. In past few decades, coordination chemistry has two new branches such as supramolecular coordination complexes and metal−organic compounds.[1.1,1.2] Supramolecular coordination complexes are distinct systems, in SCCs particular metals and ligands undergo self-assembly to form finite supramolecular complexes.[1.3] Metal-organic compounds (MOCs) are very much intrigued due to exceptional porosity and comparable surface area leading to various potential applications, including catalysis,[1.4-1.9] drug delivery,[1.10-1.13] energy storage devices.[1.14-1.16] and, gas adsorption and separation,[1.17-1.26] magnetism [1.27-1.31] and sensing (Fig. 1.1.1).[1.32-1.35]

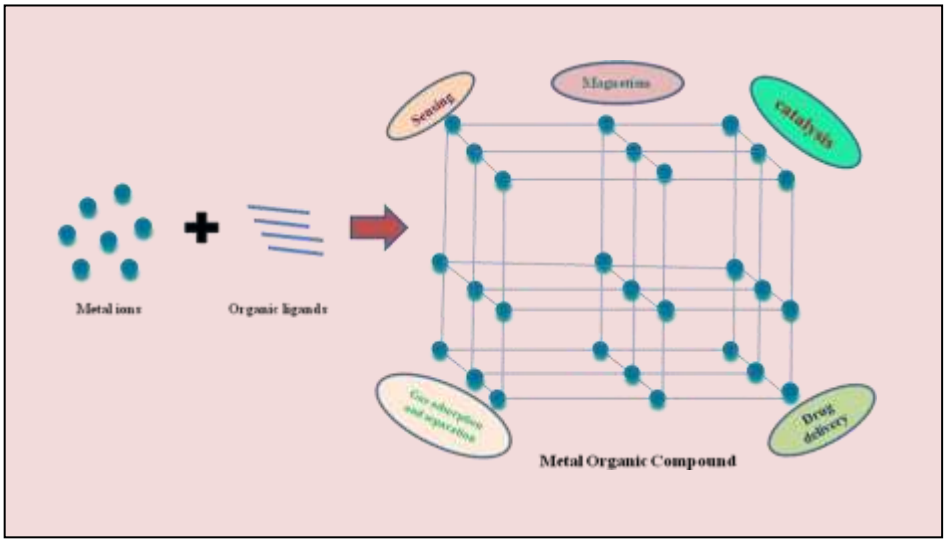

Fig. 1.1.1 General scheme of synthesis of metal-organic compounds and potential applications in different fields.

The extended crystalline structures of MOCs are formed by connecting with metal cations (“nodes”) and polytopic organic ions or molecules (“linker”). In many cases polydentate organic linkers have two types of sites - one is nitrogen and another is oxygen. Nitrogen sites are mainly preferred to bind with transition metals whereas oxygen sites favour to binds with transitions as well as heavy metals likes lanthanides and actinides metals resulting the

proliferation of new structures with infinite number of probable combinations.[1.36,1.37] Michael O'Keeffe, Richard Robson designed the robust network structures using secondary building units (SBUs) and metal centres.[1.38-1.41] First time, Omar M. Yaghi reported metal-organic frameworks with extended network of Cu(4,4'-bpy)$_{1.5}$·NO$_3$(H$_2$O)$_{1.25}$ using Cu(NO$_3$)$_2$·2.5H$_2$O, 4,4'- bpy and 1,3,5- triazine reagents.[1.42] The term "MOF" become more familiar when Yaghi and coworkers constructed the stable and porous metal organic framework (MOF-5).[1.43] The various types of structural connectivity and properties of metal organic compounds were elaborately discuss in the reviews written by Yaghi and O'Keeffe, Schröder and others.[1.44,1.45]

1.2 STRUCTURE OF VARIOUS METAL-ORGANIC COMPOUNDS

The metal organic compounds were formed when metal ions combined with polydentate organic ligands. These polydentate organic ligands act as bridging linkers between two metal nodes. The structures of metal organic compounds (MOCs) were determined by X-ray diffraction techniques. Metal organic compound may be one, two dimensional or three dimensional extended network structures.

Fang *et al*. reported the compound **1.2.1** (see Table 1.1), where the distorted BTC ligands were interconnected between the square and tetrahedral SBUs and formed 3D chiral extended network. The dimensions of elliptical type channel was calculated using two opposite atoms and the values was 9.6 × 11.9 Å^2 viewed along the [100] directions (see Fig. 1.2.1).[1.46]

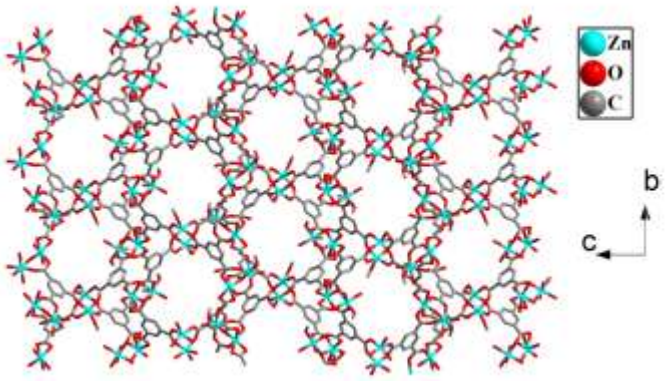

Fig. 1.2.1 The figure shows the view along the [100] direction of the compound **1.2.1** presenting the elliptical channels with about 9.6 × 11.9 Å^2.[1.46]

Dieguez *et al*. reported the compound **1.2.2** (see Table 1.1), where La ions were joined *via* bis-chelating pmtz ligands and formed zigzag shackles along a axis direction, the planes between two neighbouring pmtz ligands were formed dihedral angle is about 79.95° (see Fig. 1.2.2). [1.47]

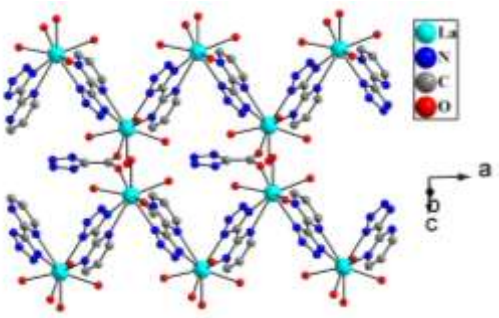

Fig. 1.2.2 The figure shows the zigzag chains of the compound **1.2.2** along a axis.[1.47]

The compound **1.2.3** (see Table 1.1) was constructed by xia *et al*, where the CuCN show a one dimensional double-stranded ribbon structure, and the dimers of copper act as linkers (see Fig. 1.2.3).[1.48]

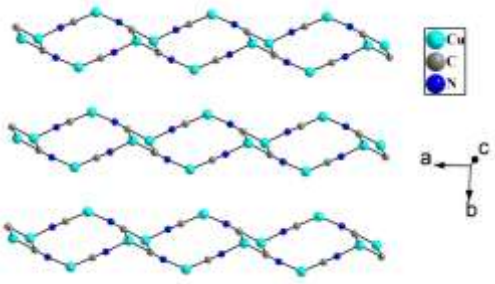

Fig. 1.2.3 One dimensional double-stranded ribbon structures of the compound **1.2.3**.[1.48]

Xiong *et al*. reported the compound **1.2.4** (see Table 1.1), where each secondary building units (SBU) is regarded as a 4-connected node and the L_2 ligands behave as linear linkers. The two dimensional 4-connected uninodal net of $[Cd(L)(Py)_2]_n$ is shown in see Fig.1.2.4.[1.49]

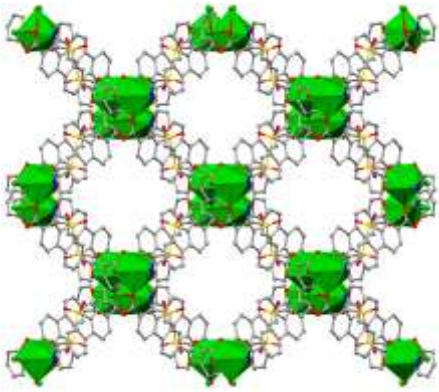

Fig. 1.2.4 The figure shows the ABAB type two dimensional 4-connected network structure of the compound **1.2.4** along the a-axis.[1.49]

Xue et.al reported the compound **1.2.5** (see Table 1.1), named as JUC-63. JUC-63 have exceptional potential application (see Fig.1.2.5).[1.50]

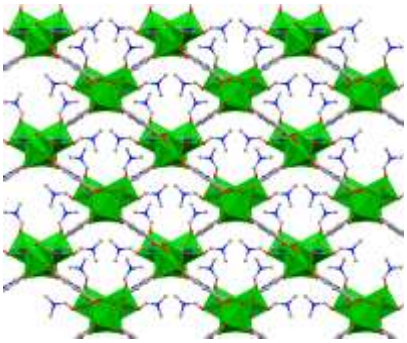

Fig. 1.2.5 A view of 3D framework with rectangular channels contained coordinated DMF molecules of the compound **1.2.5**.[1.50]

Xue et.al reported the compound **1.2.6** (see Table 1.1), where Cd_2 centers have the octahedral geometries and connected the two neighbouring networks to generate a neutral alternating two-fold (6,3) net $[Cd_3(CTC)_2]$ (see Fig.1.2.6).[1.51]

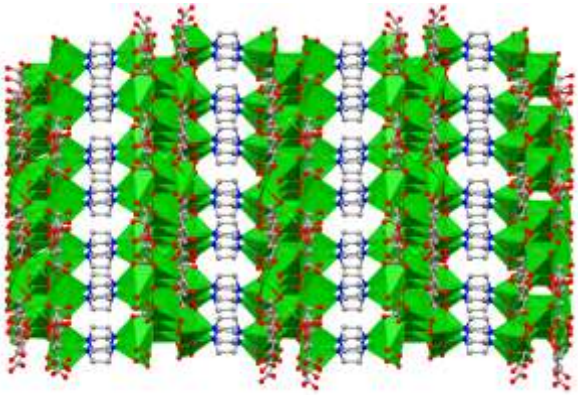

Fig. 1.2.6 Three dimensional view of two-fold alternate (6,3) layer is created from Cd2 centers linking between two neighbouring (6,3) net of the compound **1.2.6**.[1.51]

The compound **1.2.7** was constructed by Qiu *et al*. (see Fig. 1.2.7, Table 1.1), which exhibited excellent luminescence properties.[1.52]

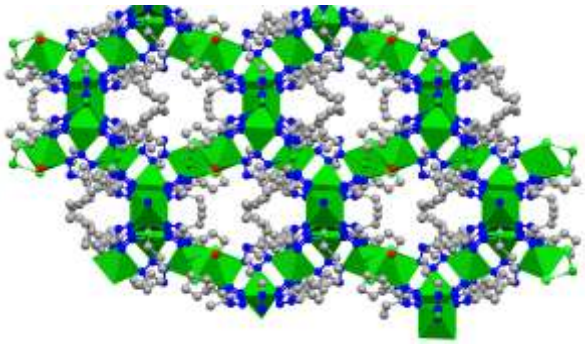

Fig. 1.2.7 Three dimensional supramolecular assembly of the 12-membered ring of the compound **1.2.7** with the nanosized cadmium wheel.[1.52]

Guo *et al*. reported the compound **1.2.8** (see Table 1.1), where the neighbouring chains were joined *via* the $DFDA^{2-}$ ligands and the μ_5 mode formed a three dimensional network with one dimensional rhombic channels along the b axis. Zn-Zn shortest interchain distance is 11.086 Å (see Fig.1.2.8).[1.53]

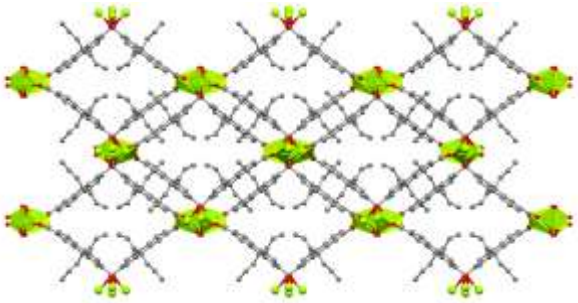

Fig. 1.2.8 Outlook of the 3D framework in the compound **1.2.8**, highlighting the rhombic channels along the b-axis and all alkyls groups are omitted to highlight the channels.[1.53]

Zhang *et al*. reported the structure of compound **1.2.9** (see Fig.1.2.9, Table 1.1), which had various potential application.[1.54]

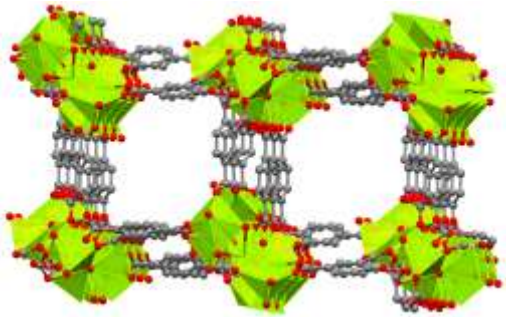

Fig. 1.2.9 Image of the one dimensional channel of the compound **1.2.9** showing two immobilized open Zn^{2+} sites on the pore surfaces of the structure.[1.54]

Yang *et al*. constructed the compound **1.2.10** (see Table 1.1), where the helical shackles were stationed in the alternative right- and left- handed helical alignments were connected *via* ap carboxylate groups in dimonodentate way to spread in the ac planes (see Fig.1.2.10).[1.55]

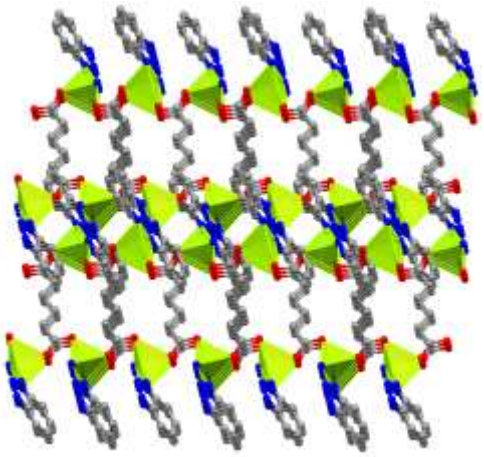

Fig. 1.2.10 Alternative right- and left-handed helical shackles are connected via ap ligands to spread into three dimensional net of the compound **1.2.10**.[1.55]

Motivated by these stratagems, many researchers are focused to the synthesis and characterization of new metal organic compounds using different polydentate ligands mainly nitrogen containing heterocyclic compounds and carboxylates group containing organic moiety to check their various potential applications.[1.56-1.62]

Table 1.1: List of some selected metal organic compounds with molecular formulas.

Code number of the compounds	Molecular formula	Ref.
Compound **1.2.1**	$Zn_3(BTC)_2(DMF)_3(H_2O)'(DMF)(H_2O)$	1.46
Compound **1.2.2**	$La(Pmtz)(TzC)(H_2O)_3](H_2O)$	1.47
Compound **1.2.3**	$[Cu_2(CN)_2(bpze)]\}_n$	1.48
Compound **1.2.4**	$[Cd(L)(Py)_2]_n$	1.49
Compound **1.2.5**	$Cd_2(ABTC)(DMF)_3\cdot(DMF)_2$	1.50
Compound **1.2.6**	$Cd_3(CTC)_2(TED)(H_2O)_2\cdot(H_3O)_2Cl_2$	1.51
Compound **1.2.7**	$\{[Cd_7Cl_2(5BT)_{12}(H_2O)_2$	1.52
Compound **1.2.8**	[Zn(DFDA)]	1.53
Compound **1.2.9**	$[Zn_4(OH)_2(1,2,4\text{-}BTC)_2]$	1.54
Compound **1.2.10**	$[Zn(BTA)(ap)_{0.5}]_n$	1.55

1.3 GENERAL SYNTHESIS METHODS OF METAL ORGANIC COMPOUNDS

1.3.1 Hydrothermal Method. In hydrothermal synthesis the substances are formed through chemical reactions. The chemical reaction occurs in a container with constant temperature and pressure. Hydrothermal method has numerous of advantages such as (a) mild operational conditions, (b) single-step synthetic process, (c) well dispersion in reaction medium. The solvothermal synthesis method is similar to hydrothermal synthesis method, usually MeOH, EtOH, DMF, ethylene glycol and diethylene glycol etc solvants are used in solvothermal method and in hydrothermal method water is used as a solvent. Both hydrothermal and solvothermal method Teflon bomb autoclave is used. The development of pressure in an autoclave is depends upon the filling of volume.[1.63, 1.64] The outlook of the autoclave and the different parts of the autoclave are shown in Fig.1.3.1.

(a) (b)

Fig. 1.3 1 (a) Outlook of the Teflon bomb autoclave, (b) Different portions of the autoclave.

1.3.2 Slow Layer Diffusion Method. The slow layer diffusion method is another technique to synthesis of metal-organic compounds. In this technique two layers of different density is formed. First the solution of metal salt is taken in a vessel, and then the solution of organic compound added to the vessel slowly. At the interface, after the gradual diffusion of the solvent into the separate layer and start to grow of crystal slowly. This technique is usually carried out at room temperature. This technique is more preferable to formation of crystal with pure phase. The schematic presentation of slow layer diffusion method is shown in Fig. 1.3.2.

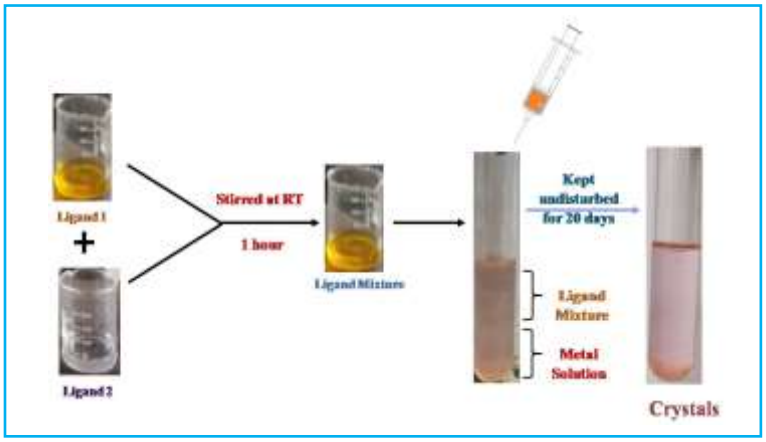

Fig. 1.3.2 Schematic presentation of slow layer diffusion method.

1.4 CHARACTERIZATION TECHNIQUES OF METAL ORGANIC COMPOUNDS

1.4.1 Single Crystal X-ray Diffraction (SCXRD). The crystal data of all the compounds including in this thesis were collected using Bruker D8 Quest machine (see Fig. 1.4.1). During the data collection, Mo Kα (λ=0.71073Å) radiation is used and generator has operated using 50 kV and 1 mA current. The final data sets were reduced by an APEX3 program, while a SAINTPLUS [1.65] program was utilized for the integration of diffraction profiles. The absorption correction (multi-scan) was carried out by a SADABS program.[1.66] We initially solved the structure by SIR 92 [1.67], and the full matrix least-square method (SHELXL-2016)[1.68] was used further, which is present in the WinGx suit of programs (Version 1.63.04a).[1.69,1.70]

Fig.1.4.1 Microfocus Single Crystal X-Ray Diffraction Instrument (BRUKER D8 QUEST).

1.4.2 Powder X-ray Diffraction (PXRD). The powder X-ray diffraction patterns of all the compounds were collected using Bruker D8 Advance X-ray diffractometer with Cu Kα radiation (λ= 1.5418 Å) and generator has operated using 40 kV and 40 mA current (see Fig. 1.4.2). In all the cases, powder XRD patterns show that the new products are formed in pure phase.

Fig.1.4.2 Powder X-ray Diffraction Instrument (BRUKER D8 ADVANCE).

1.4.3 FT-IR Spectroscopy (IR). The FTIR Spectrum of all the compounds was recorded using KBr pellets (Nicolet Magna IR 750 series-II) in the frequency range of 400 to 4000 cm^{-1}. Compounds containing several functional groups were confirmed by infrared spectroscopy.

1.4.4 Thermogravimetric Analysis (TGA). Thermogravimetric analysis (TGA) is an important technique to check the stability of the compounds. Thermo gravimetric analysis (TGA) of all the compounds in this thesis were

checked under nitrogen atmosphere (flow rate = 20 ml min^{-1}) by PerkinElmer Diamond instrument (STA 6000) in the temperature range of 30–800 °C (heating rate = 20 °C min^{-1}).

1.4.5 Gas sorption Technique. Gas sorption isotherms of all the compounds included in this thesis were measured with an Autosorb iQ (Quantachrome Inc., USA). The image of the gas sorption instrument is shown in Fig. 1.4.5.

Fig.1.4.5 Image of Quantachrome Autosorb iQ (Gas adsorbent instrument).

1.4.6 UV-Visible Spectroscopy (UV-Vis). UV-Visible spectroscopy gives the information about the presence of different electronic transitions within the compounds. UV-Vis spectra of all the compounds in this thesis were measured using Shimadzu UV-1900i UV-Vis spectrophotometer and Shimadzu UV 3101PC spectrophotometer (see Fig. 1.4.6).

Fig.1.4.6 Image of UV-Vis spectrophotometer.

1.4.7 Photoluminescence Spectroscopy. In the thesis, photoluminescence studies were checked at room temperature in aqueous media using Horiba FluoroMax4-spectrofluorometer (see Fig. 1.4.7) and Hitachi F-7100 luminescence spectrofluorometer. The solid state photoluminescence spectrums were checked by PerkinElmer spectrofluorimeter model LS55.

Fig.1.4.7 Image of spectrofluorometer.

1.4.8 TCSPC measurement. Time-correlated single photon counting measurements presented in this thesis were measured at room temperature using HORIBA Jobin-Yvon instrument in the nanosecond time domain (see Fig. 1.4.8). The luminescence lifetime decays were collected on a Hamamatsu MCP photomultiplier (R3809) and IBH DAS6 software are used to deconvoluted and for fitting.

Fig.1.4.7 Image of time-correlated single photon counting instrument.

1.5 SENSING BEHAVIOUR OF METAL ORGANIC COMPOUNDS

Metal–organic compounds (MOCs) are the subclass of porous coordination polymers. In recent decades, analytical science has attracted towards MOC-based luminescent sensing platforms. Until now, various types of MOCs have been discover to detect guest targets, likes small organic molecules, ions, gases, antibiotics, organic dyes and biomolecules. MOCs can be behaved as luminescent sensors due to comparable structure, large pore size, and different functional sites. Ligands containing aromatic π-bonds play a crucial role to show the photoluminescence property of metal-organic compounds.[1.71]

Metal ions are very essential to everyday life because of their different biological activity and the exposure and growth of toxic metal ions may cause chronic or sensitive poisoning effect. Similarly the organic dyes show poisoning effect in environment. So, the detection of various metal ions and organic dyes are urgent to monitoring the environmental pollution.[1.72]

Mohan *et al.*[1.73] reported three Ag containing MOFs, such as **MOF 1.5.1, MOF 1.5.2, MOF 1.5.3** (see Table 1.2), these were synthesized by using hydrothermal process. The Ag containing MOFs was exhibited good emission spectra at 365 nm (λ_{ex} = 280 nm) and showed selective sensor towards Fe^{3+} in the presence of other ionic species.

The calculated LOD values of **MOF 1.5.1, MOF 1.5.2, MOF 1.5.3** in case of Fe^{3+} ions were 11.46 × 10^{-6} M, 15.83 × 10^{-6} M, and 15.44 × 10^{-6} M respectively.

Li *et al.*[1.74] reported novel **MOF 1.5.4** (named as **LCU-103**) and it was a good sensing material. **MOF 1.5.4** (see Table 1.2) sense Fe^{3+} and Cu^{2+} in very trace amounts through a luminescent quenching mechanism with low limits of detection (LODs). The LODs values for Fe^{3+} and Cu^{2+} were 1.45 and 1.66 μM, respectively.

Moradi *et al.*[1.75] reported luminescent metal–organic framework, such as **MOF 1.5.5** (see Table 1.2) via solvothermal method. The synthesized three-dimensional microporous **MOF 1.5.5** was detected Fe^{3+} in methanol solution very selectively. The 3D **MOF 1.5.5** was detected Fe^{3+} ions through luminescence quenching mechanism and the limit of detection value was 0.3 μM (17 ppb).

Farahani *et al.*[1.76] constructed **MOF 1.5.6** (see Table 1.2) using NH_2-BDC and 4-bpdb reagents, which was named as TMU-17-NH_2. The fluorescent Zn-based amine/azine-functionalized MOF was synthesized using solvothermal method and the MOF detected Fe^{3+} in DMF solution very selectively. Less than one min Fe^{3+} ion detected by **MOF 1.5.6** and detection limit was 0.7 μM (40 ppb). The luminescence intensity of the synthesized compound was completely quenched in the presence of Fe^{3+} solution, the concentration of Fe^{3+} solution was 10^{-3} M prepared using DMF.

Mukherjee *et al.*[1.77] constructed a highly porous **MOF 1.5.7** (see Table 1.2). The 3D Zn-based **MOF 1.5.7** was synthesized through exploiting the mixed ligand synthesis concept. **MOF 1.5.7** showed two strong emission band one at around 448 nm (λ_{ex} = 390 nm) and another one was at 434 nm (λ_{ex} = 321 nm) respectively. Such types of emission bands are due to the presence of ligand π*−π and/or π*−n transitions. **MOF 1.5.7** showed luminescence enhancement effect in the presence of Cr^{3+} ions and the detection limits (LOD) for Cr^{3+} was found to be 0.025 ppm (0.49 μM).

Li et al.[1.78] reported a new three-dimensional **MOF 1.5.8** (see Table 1.2), named as **JXUST-25**. **MOF 1.5.8** was prepared using Eu^{3+}, 5,5'-(benzothiadiazole-4,7-diyl)diisophthalic acid and benzothiadiazole reagents *via* solvothermal method. The **MOF 1.5.8** containing Eu^{3+} and organic fluorescent ligand were responsible to perform luminescence enhancement effect with blue-shift emission in the case of Cr^{3+}, Al^{3+} and Ga^{3+}. The LOD values of Cr^{3+}, Al^{3+} and Ga^{3+} ions were 0.073, 0.006 and 0.030 ppm, respectively.

Shi *et al.*[1.79] constructed a 2D **MOF 1.5.9** (see Table 1.2) named as Tb-DBA prepared using Tb^{3+} and 2′-amino-1, 1′:4,1′′-terphenyl-4,4′′-dicarboxylic acid reagents through solvothermal method. **MOF 1.5.9** quickly detected the trivalent Fe^{3+}, Cr^{3+} and Al^{3+} ions. The LOD was as low as the nanomolar level. Selectively **MOF 1.5.9** exhibited fluorescence enhancement effect in the presence of trivalent Fe^{3+}, Cr^{3+} and Al^{3+} ions.

A new benzothiadiazole-based **MOF 1.5.10** (see Table 1.2) was solvothermally synthesized by Yao et al.[1.80] **MOF 1.5.10** was prepared using 4,7-bi(1H-imidazol-1-yl) benzo-[2,1,3]thiadiazole and 4,4′-oxybisbenzoate reagents. **MOF 1.5.10** (named as **JXUST-3)** showed simultaneously detection of trivalent metal ions likes Fe^{3+}, Cr^{3+} and Al^{3+} through luminescence enhancement effect, and the LOD values were 0.056 μM, 0.049 μM and 0.055 μM respectively.

A new Co-based **MOF 1.5.11** (see Table 1.2) was solvothermally prepared by Tian *et al.*[1.81] Co-based **MOF 1.5.11** was named as JXUST and it behaved as a multifunctional fluorescence sensor towards three trivalent metal ions (Al^{3+}, Cr^{3+}, and Fe^{3+}) through luminescence enhancement effect with good reusability and The LOD values of Fe^{3+}, Cr^{3+}, and Al^{3+} were 0.10, 0.10, and 0.13 μM, respectively.

Evangelou et al.[1.82] reported a new robust **MOF 1.5.12** (see Table 1.2), named as **Al-MOF-1**. **MOF 1.5.12** can selectively detected the trace amounts of Cr(VI) in real water samples. Cr(VI) being successfully detected through **MOF 1.5.12** at concentrations below the acceptable limits (< 50 ppb).

Hou et al.[1.83] reported two new anionic In based MOFs such as **MOF 1.5.13** (**V101)** and **MOF 1.5.14 (V102).** 2-fold interpenetrated **MOF 1.5.13** were effectively converted to non interpenetrated **MOF 1.5.14** by changing the reaction medium from DMF to DEF. **MOF 1.5.14** (see Table 1.2) can selectively detected traces amount of NZF in water at room temperature, and the detection limit was 0.2 ppm whereas NZF cannot be detected by the presence of **MOF 1.5.13** (see Table 1.2).

Indium−organic framework such as **MOF 1.5.15** (see Table 1.2) was constructed by Zhang et al.[1.84] **MOF 1.5.15** have unique ability towards the detection of NZF with low detection limit.

Zhang *et al.*[1.85] constructed Tb based **MOF 1.5.16** (see Table 1.2) *via* solvothermal methods using tripodal ligand 1,3,5-trisIJ4-carbonylphenyloxy)benzene. **MOF 1.5.16** showed selective sensing properties in the presence of nitrofurantoin (NFT) and nitrofurazone (NZF) in water medium.

Table 1.2: List of some selected metal organic compounds with molecular formula used for sensing studies.

Code number of the compounds	Molecular formula	Ref.
MOF 1.5.1, MOF 1.5.2, MOF 1.5.3	-	1.73
MOF 1.5.4	$[Zn_{1.5}(dttz)(Hdpa)]_n$	1.74
MOF 1.5.5	$[Zn_2(oba)_2(bpy)]$	1.75
MOF 1.5.6	$[Zn(NH_2\text{-}BDC)(4\text{-}bpdb)].2DMF$	1.76
MOF 1.5.7	$[\{Zn_2(2,6\text{-}NDC)_2(L)\}.xG]_n$	1.77
MOF 1.5.8	$\{[(CH_3)_2NH_2][Eu\ (BTDI)]\cdot H_2O\cdot DMF\}_n$	1.78
MOF 1.5.9	Tb-DBA	1.79
MOF 1.5.10	$\{[Zn(BIBT)(oba)]\cdot DMA\}_n$	1.80
MOF 1.5.11	$\{[Co_3(BIBT)_3(BTC)_2(H_2O)_2]\cdot solvents\}_n$	1.81
MOF 1.5.12	$[Al(OH)(PATP)]\cdot solvent$	1.82
MOF 1.5.13 and **MOF 1.5.14**	$\{(Me_2NH_2)[In(BCP)]\cdot 2DMF\}_n$ and $\{(Me_2NH_2)[In(BCP)]\cdot 2.5DEF\}_n$	1.83
MOF 1.5.15	$[Me_2NH_2][In(L)]\cdot 2.5NMF\cdot\ 4H_2O$	1.84
MOF 1.5.16	$Tb(TCPB)(DMF)]\cdot dioxane\cdot 0.5H_2O\}_n$	1.85

1.6 SORPTION BEHAVIOR OF METAL ORGANIC COMPOUNDS

Like zeolites, activated carbon and silica, MOCs possess outstanding adsorption features, due to high crystallinity, large surface area, and easily tunable properties. MOC shows enormous potential for the both adsorption and separation of gas molecule and toxic pollutant like organic dye and various hazardous substances.

Ahmad *et al*[1.86] reported new cobalt **MOF 1.6.1** (see Table 1.3), named as KIUB-MOF-1. This **MOF 1.6.1** have large pore size and can be used for the elimination of cationic and anionic dyes through chemisorption mechanism. Dyes were easily eliminated by **MOF 1.6.1** due to the presence of electrostatic and hydrogen bonding interaction. Adsorption capacity of methyl orange (anionic) was 15,610 mg/g, and for methylene blue and malachite green (cationic) the adsorption capacity were 14,721 mg/g and 5083 mg/g respectively.

Deng *et al*[1.87] reported **MOF 1.6.2** (see Table 1.3) synthesized using heterotopic tripodal nitrogen-containing ligand and named as SCNU-Z2. The anionic **MOF 1.6.2** have effective adsorption capacity towards cationic dyes likes. The sorption capacities of RhB, CV, and MLB were 751.8, 847.4, and 455.6mg/g, respectively.

Gao *et al* [1.88] constructed two mesoporous anionic **MOF 1.6.3** and **MOF 1.6.4** (see Table 1.3). Both **MOF 1.6.3** and **MOF 1.6.4** exhibited absorption and separation of methylene blue (MB) due to the anionic nature of these two MOF having large pore sizes.

Guo *et al* [1.89] hydrothermally prepared **MOF 1.6.5** (see Table 1.3), names as **L-MOF-1** which was stable in both acid and base. N1, N2-bis(pyridin-3-ylmethyl)ethane-1,2-diamine and benzenesulfonate reagents were used to synthesized **MOF 1.6.5**. **MOF 1.6.5** showed high adsorption capacity towards CR in aqueous medium at room temperature. **MOF 1.6.5** exhibited experimental adsorption capacity towards CR was approximately 12 000 mg g^{-1} in 20 min in the pH range of 2.2–4.7.

Li *et al*.[1.90] reported two-dimensional **MOF 1.6.6** (see Table 1.3), named as **BUC-17**. **MOF 1.6.6** was synthesized using hydrothermal process and exhibited superb adsorption capacity towards Congo red (CR), the adsorption capacity CR was approximately 4923.7 mg g^{-1} at room temperature.

Liu *et al* [1.91] reported two Zn based MOF such as **MOF 1.6.7** and **MOF 1.6.8** (see Table 1.3). Both **MOF 1.6.7** and **MOF 1.6.8** were anionic in nature and favourable to sorption towards cationic dye MB^+ and TO^+ based on charge

and size-matching effect. The **MOF 1.6.7** showed adsorption capacity of MB^+ was 29 mg g^{-1} and TO^+ was 13 mg g^{-1}. Similarly, **MOF 1.6.8** showed adsorption capacity of MB^+ was 87 mg g^{-1} and TO^+ was 76 mg g^{-1} respectively.

Huang *et al*.[1.92] reported Mg-based 3D porous **MOF 1.6.9** (see Table 1.3). The 3D **MOF 1.6.9** showed CO_2, O_2, N_2 and H_2 gas-uptake capacities at low temperatures. The 3D **MOF 1.6.9** exhibited selective adsorption capacity towards CO_2 than that of O_2 and N_2 at room temperature.

Rosi *et al*.[1.93] constructed cubic three-dimensional extended porous **MOF 1.6.10** (see Table 1.3). **MOF 1.6.10** adsorbed hydrogen~4.5 weight percent (17.2 hydrogen molecules per formula unit) at 78 K and 1.0 weight percent at room temperature and pressure of 20 bars.

Gong et al [1.94] synthesized highly porous and robust **MOF 1.6.11** (see Table 1.3), named as NU-200. **MOF 1.6.11** exhibited super adsorption capacity in the presence of Xe and the selectivity for a 20/80 v/v mixture of xenon (Xe)/krypton (Kr) at 298 K and 1.0 bar was predicted by high ideal adsorbed solution theory (IAST).

Zhao *et al*.[1.95] reported partially charged Mg-based **MOF 1.6.12** (see Table 1.3), named as FJU-129. **MOF 1.6.12** effectively separate C_2H_2 from CO_2 and quickly adsorb the cationic dye methylene blue (MB). Mg-based MOF exhibited high uptake capacity of C_2H_2 up to 133.8 cm^3 /g at 273 K, 1 bar.

Pan *et al*[1.96] reported robust and porous Ti based **MOF 1.6.13** (see Table 1.3), named as LCU-402 which was synthesized by hydrothermally method. Due to significant stability and permanent porosity **MOF 1.6.13** adsorb CO_2, CH_4, C_2H_2, C_2H_4, and C_2H_6 gas. The adsorption isotherms of CO_2 were recorded at three different temperatures such as 196, 273, and 298 K, respectively. The adsorption isotherms of other gas likes CH_4, C_2H_2, C_2H_4, and C_2H_6 were recorded at 298 K.

Table 1.3: List of some selected metal organic compounds with their molecular formula used for sorption studies.

Code number of the compounds	Molecular formula	Ref.
MOF 1.6.1	-	1.86
MOF 1.6.2	-	1.87
MOF 1.6.3 and **MOF 1.6.4**	$[Zn_3(ITTC)_3](Me_2\ NH_2)_3 \cdot 3DMF \cdot H_2O$ and $[Cd_2(ITTC)_3](Me_2NH_2)5 \cdot 2DMF$	1.88
MOF 1.6.5	$[Cd(H_2L)(BS)_2]_n \cdot 2nH_2O$	1.89
MOF 1.6.6	$[Co_3(tib)_2(H_2O)_{12}](SO_4)_3$	1.90
MOF 1.6.7 and **MOF 1.6.8**	$\{(NH_2Me_2)[Zn(Pycia)]\}_n$ and $\{(NH_2Me_2)[Zn_2(Pycia)(PBA)]\}_n$	1.91
MOF 1.6.9	$[Mg_{16}(PTCA)_8(\mu_2\text{-}H_2O)_8(H_2O)_{16}(dioxane)_8](H_2O)_{13}(DMF)_{26.}$	1.92
MOF 1.6.10	$Zn_4O(BDC)_3$	1.93
MOF 1.6.11	-	1.94
MOF 1.6.12	$[(Me_2NH_2)Mg_{1.5}(4Me\text{-}BDTA) \cdot 6.5DMF \cdot 13.5H_2O]$	1.95
MOF 1.6.13	$Ti_2Ca_2(\mu_3\text{-}O)_2(\mu_2\text{-}\ H_2O)_2(H_2O)_4$	1.96

1.7 ELECTRONIC DEVICES BESED ON METAL ORGANIC COMPOUNDS

Cd(II) based 2D **MOF 1.7.1** (see Table 1.4) was reported by Halder et al.[1.97] **MOF 1.7.1** has interesting conduction properties and the I–V characteristics was measured in both light and dark condition with ITO/ **MOF 1.7.1** /Al configuration showed a highly non-linear rectifying behavior, which signifies its Schottky diode character. In dark situation the conductivity of the configuration was 2.90×10^{-4} S m^{-1} and in the presence of photoirradiation conditions the conductivity of the configuration was 7.16×10^{-4} S m^{-1}.

Two-dimensional Cd based **MOF 1.7.2** (see Table 1.4) was constructed by Bairy *et al.*[1.98] **MOF 1.7.2** showed the electrical conductivity with the metal−semiconductor (MS) junction on an electronic device. The substantial enhancement of electrical conductivity in the presence of light was confirmed by I−V correlation (Λ values in dark condition was 1.12×10^{-3} S m^{-1}, and in the presence of light was 6.33×10^{-3} S m^{-1}).

Lee *et al.*[1.99] reported cobalt based **MOF 1.7.3** (see Table 1.4). **MOF 1.7.3** film exhibited superior pseudo capacitor behaviour and the specific capacitance value was 206.76 F g^{-1}.

Sanda *et al.*[1.100] reported flexible **MOF 1.7.4** and **MOF 1.7.5** (see Table 1.4)**.** Both the MOF showed proton conductivity properties. The conductivity values **MOF 1.7.4** and **MOF 1.7.5** were 2.55×10^{-7} and 4.39×10^{-4} Scm^{-1} at 80°C.

Sadakiyo *et al.*[1.101] constructed oxalate-bridged containing **MOF 1.7.6** (see Table 1.4). In various humidity conditions these synthesized MOFs performed super proton conductivity behaviour due to their hydrophilicity nature. The most hydrophilic sample such as Me-Fe Cr performed high proton conductivity properties was approximately 10^{-4} Scm^{-1}.

Bao *et al.*[1.102] reported 2D 3d−4f phosphonate **MOF 1.7.7** (see Table 1.4). This **MOF 1.7.7** can undergo a phase transition above 45°C and 93% relative humidity, with formation of new compound such as $[H_3O][CoLa(notp)\text{-}(H_2O)_4]ClO_4\cdot3H_2O$(named as CoLa-III). The proton conductivity behaviour

confirmed the release of proton from intralayer phosphonate group into the interlayer space and the proton conductivity value of CoLa-III was 4.24×10^{-5} Scm^{-1}at 25°C.

Table 1.4: List of some selected metal organic compounds with molecular formula used for electronic devices based studies.

Code number of the compounds	Molecular formula	Ref.
MOF 1.7.1	$[Cd(4\text{-}bpd)(SCN)_2]_n$	1.97
MOF 1.7.2	$\{[Cd_2(5\text{-}nip)_2(pdiq)_2(H_2O)_2(CH_3OH)]\cdot H_2O\}_n$	1.98
MOF 1.7.3	-	1.99
MOF 1.7.4 and **MOF 1.7.5**	$\{[Zn(C_{10}H_2O_8)_{0.5}(C_{10}S_2N_2H_8)]\cdot 5H_2O]\}_n$ and $\{[Zn\text{-}(C_{10}H_2O_8)_{0.5}(C_{10}S_2N_2H_8)]\cdot 2H_2O]\}_n$	1.100
MOF 1.7.6	$\{NR_3(CH_2COOH)\}[MCr(ox)_3]\cdot nH_2O$	1.101
MOF 1.7.7	$[Co^{III}La^{III}(notpH)(H_2O)_6]ClO_4\cdot 5H_2O$(CoL a-II)	1.102

1.8 ADVANTAGES OF FLUORESCENCE TECHNIQUE

Detection of biologically essential and non-essential elements using different techniques like atomic absorption spectrometry (AAS), raman spectroscopy (RS), inductively coupled plasma optical emission spectroscopy (ICP-OES), capillary electrophoresis (CE), mass spectrometry (MS), ion mobility spectrometry (IMS), inductively coupled plasma mass spectroscopy (ICPMS), liquid chromatography-tandem mass spectrometry (LC-MS), inductively coupled plasma atomic emission spectroscopy (ICP-AES), flame atomic absorption spectrometry (FAAS), thin chitosan films, and voltammetry etc.[1.103-1.112] But these techniques are onerous, time-consuming and expensive. UV-visible and fluorescence spectroscopic methods are the easiest methods to distinguish environmentally pollutant analytes due to high sensitivity, fast responsive, low-cost, and easy signal detection.

1.9 CLASSIFICATION OF FLUORESCENT SENSORS

Fluorescent sensors can give information about the target analytes (molecules, ions, and bio-molecules) by the means of fluorescence emission process. According to their photoluminescence response, fluorescence emission is classified into four different ways such as (i) photoluminescence enhancement effect (ii) photoluminescence quenching effect (iii) ratiometric and (iv) chemodosimeters.

Photoluminescence enhancement effect: Luminescence enhancement effect means (turn-ON) the increase of the luminescence intensity of the compound in the presence of light due to the various types of interaction (such as H-bonding, π-π, interaction, electrostatic interaction, charge transfer etc) between the MOF (receptor) and analytes. Donation of electron from analytes to receptor (synthesized compounds) increases the electron density in receptor and exhibits enhancement effect.

Photoluminescence quenching effect: Luminescence quenching effect means (turn-OFF) the decrease of the luminescence intensity after the addition of the analytes in MOF (synthesized compounds). In this case analytes have electron withdrawing nature to accept the electron density from the synthesized compounds and decrease the levels of electron density in synthesized compounds resulting luminescence quenching effect.

Ratiometric: Ratiometric is another types of fluorescence method in which intensities of two or more excitation wavelengths or emission maximum spectrum are measured to detect changes to local environment.

Chemodosimeters: Fluorescent chemodosimeters are molecular systems that use in abiotic receptors to achieve the analytes detection with irreversible transduction of photoluminescence signal.

1.10 SENSING MECHANISMS OF FLUOROPHORE

Fluorophore shows different types of signal, depending upon the nature of the compound and the analytes. But in this chapter we are focused on luminescence quenching and luminescence turn on effect. There are many reasons to luminescence quenching and turn on effects, such as Intramolecular charge transfer (ICT), metal–ligand charge transfer (MLCT), förster resonance energy transfer (FRET), photoinduced electron transfer (PET), and excited-state proton transfer (ESPT).[1.113]

1.10.1 Intramolecular charge transfer (ICT)

Intramolecular charge transfer (ICT) process means an electron transfer process. In ICT show that the luminescence intensity changed with shifting of wavelength in both the excitation and emission spectra. The investigating compound has ICT process when the compound contains both an electron-withdrawing group and an electron-donating group; these groups are positioned at opposite sides of compound to generate a dipole in the compound. This process is more sensitive to charge species the dipole of the compound is connected with the dipoles of the solvent to stabilise the investigating compound. However, in ICT process compound shows a broad and long wavelength with shifted spectrum.

1.10.2 Metal–ligand charge transfer (MLCT)

In MLCT electron transfer from electron rich centers to electron deficient centers. Metal should have low oxidation state and containing available number of electron to donate the electron towards the ligand containing low-lying empty orbitals. The MLCT transitions are common for complex compounds having π-acceptor ligands like CO, NO etc. These ligands are accepting the electron from metal full d orbital to empty orbital of the ligands via synergic effect. Upon the absorption of light, metal d electrons are excited to the ligand π^* orbitals resulting, the intense bands with change the oxidation state of the metal.

1.10.3 Förster resonance energy transfer (FRET).

In förster resonance energy transfer (FRET) energy transfer from the excited donor molecule to an acceptor molecule without the appearance of a photon resulting, the luminescence intensity of the donor molecule is quenched. The decrease of luminescence intensity of the donor molecule due to the presence of resonance energy transfer between the donor and acceptor through dipole–dipole interactions. The good overlap between the emission spectrum of the donor and absorption spectrum of the acceptor depend upon the relative orientation of the transition dipole of the donor and acceptor, and the distance of separation between the donor and acceptor, resulting better energy transfer.

1.10.4 Photoinduced electron transfer (PET).

Photoinduced electron transfer (PET) is an excited state phenomenon, when an electron transfers from one excited molecule to other molecules. The electron donor and acceptor distance and oxidation–reduction potentials values of

the compounds are the main criteria for PET. The solvent molecules can involve in the photoinduced electron transfer process. PET can happen between the excited molecules and redox-active molecule present in the same compound. Electron transfer process is reversible, but in reversible path the energy release through non-radiative way. If the donor molecule contains HOMO level in high energy and the acceptor molecule has LUMO level in lower energy then electron will transfer from the HOMO level to the LUMO level, as a result, fluorescence intensity of the compound can be completely quenched.

1.10.5 Excited-state proton transfer (ESPT).

There are some class of molecules those are behaves as weak acids or even bases in ground state, but they are behaves as strong acids in excited state, identified as 'photoacids'. In the excited state Photoacids, is simply transfer their protons to their solvents. In aqueous solutions the compound shows the dramatic change of luminescence spectra in the presence of pH due to the excited-state proton transfer (ESPT) process. In most cases, compounds show their spectra with different wavelength due to presence of both protonated and deprotonated forms of the photoacid. When the protondonor and proton-acceptor groups present in the same molecules with close proximity then molecules exhibits luminescence spectra *via* ESPT process.

1.11. A BRIEF DISCUSSION OF CADMIUM BASED METAL ORGANIC COMPOUNDS

Wu *et al.*[1.114] reported **Cd-1** (see Table 1.5) which was synthesized by hydrothermal methods using $Cd(ClO_4)_2 \cdot 6H_2O$ and 5,5′- [ethane-1,2-diylbis(oxy)]diisophthalic acid (H_4EDDA), named as **Cd−EDDA**. **Cd-1** behave as mercury (II) sensor in pure water and shows dual-emission, one strong emission at approximately 350 nm and another very weak emission at around 410 nm when excited wavelength at 310 nm. The luminescence intensity at 350 nm significantly decreases, and at the same time the ligand-based emission at 410 nm becomes prominent with the accumulative addition of Hg^{2+} ions. The LOD value of **Cd-1** in the presence of Hg^{2+} was 2 nM.

Pachfule *et al.*[1.115] constructed porous **Cd-2** (see Table 1.5)**,** named as **Cd-4TP-1,** synthesized using solvothermal process. Due to the permanent porosity pachfule *et al* studies H_2 and CO_2 uptake properties. **Cd-2** uptake H_2 at 77 K and 1 atm pressure was 1.17 wt % and similarly, **Cd-2** uptake CO_2 at 273 K and 1 atm pressure was 2.70 mmol/g.

Xu *et al.*[1.116] reported **Cd-3** (named as **CdBPTC**) was synthesized by solvothermal method using $Cd(NO_3)_2 \cdot 4H_2O$ and 3,3′ ,5,5′ -biphenyltetracarboxylic acid (H4BPTC) as a reagent. **Cd-3** (see Table 1.5) showed excellent

fluorescence quenching efficiency (at 427 nm) in the presence of Fe^{3+} was approximately 100% (the concentration of Fe^{3+} was 1.0×10^{-3} mol·L $^{-1}$). The calculated limit of detection value of **Cd-3** in the presence of Fe^{3+} was 9.04 ppm.

Fan *et al.*[1.117] reported **Cd-4** and **Cd-5** (abbreviated as **CUST-532** and **CUST533).** Both **Cd-4** and **Cd-5** (see Table 1.5) were behaved like multifunctional chemical sensors. **Cd-4** showed maximum emission at 439 nm (λ_{ex} = 376 nm) and **Cd-5** showed maximum emission at 439 nm (λ_{ex} = 370 nm). Both **Cd-4** and **Cd-5** exhibited conspicuous quenching effect in the presence of NFT antibiotics. The detection limits (LOD) value of **Cd-4** was 4.40×10^{-7} M and in case of **Cd-5** was 7.80×10^{-7} M for NFT. Both **Cd-4** and **Cd-5** showed the highest decrease of luminescence intensity in the presence of Fe^{3+}. Luminescence quenching efficiency of **Cd-4** was 91.7% and in case of **Cd-5** was 93% for Fe^{3+}. LODs for Fe^{3+} sensing was 1.12×10^{-6} M in the case of **Cd-4** and 2.29×10^{-6} M for **Cd-5**. Similarly, luminescence quenching efficiency **Cd-4** and **Cd-5** were 96.7% and 98% for $Cr_2O_7^{2-}$. Their LOD for sensing $Cr_2O_7^{2-}$ were 1.4×10^{-6} M and 1.2×10^{-6} M for **Cd-4** and **Cd-5**.

Cd-6 (see Table 1.5) synthesized using 2-amino-1,4-benzenedicarboxylate, 4,40 – azopyridine and N,N-dimethylacetamide reagents and **Cd-6** was reported by Debnath *et al*[1.118]. **Cd-6** was synthesized *via* solvothermal method and exhibited turn on sensing behavior in the presence of tri-positive metal ions (Al^{3+}, Fe^{3+}, Cr^{3+}) and showed luminescence quenching effect for nitroaromatics compounds. **Cd-6** exhibited significant luminescence quenching effect (emission maxima at~428 nm) in the presence of 2,4,6-trinitrophenol. **Cd-6** exhibited 80, 16 and 15 fold luminescence enhancement effect in Cr^{3+}, Fe^{3+} and Al^{3+} ions, respectively. LOD values for Cr^{3+}, Fe^{3+}, Al^{3+} ions and TNP were 0.45 µM, 0.88 µM and 0.38 µM and 7.03 µM, respectively.

Zhang *et al.*[1.119] constructed **Cd-7** (see Table 1.5) *via* solvothermal process, named as **ZH-102.** The synthesized **Cd-7** showed multiple chromic properties. **Cd-7** exhibited photochromic properties probably electron transfers from the O atom of carbonyl to the N atom of the NDI moieties. **Cd-7** exhibited the excellent hydrochromism properties, the colour of the crystal remain unchanged at 120 °C, after constantly heating the crystal at 200 °C, the colour of the crystal changes into a coffee colour. **Cd-7** showed vapochromic behavior by showing the prominent eye detectable colour change towards NH_3, BA, PA, TEA, and DMA vapour for 10 seconds.

Wang *et al.*[1.120] synthesized **Cd-8** (see Table 1.5) *via* solvothermal method using N,Ndimethylacetamide, 4,4′,4″-nitrilotribenzoic acid, and (E)-4,4′-(ethene1,2-diyl)bis[(N-pyridin-3-yl)benzamide] reagents. **Cd-8** showed dual

emission peak one at around 465 nm and another at around 503 nm with excited wavelength at 350 nm. The luminescence intensity of **Cd-8** decreases almost 97.2% and 97.4% with increasing concentration of Fe^{3+} and $Cr_2O_7^{2-}$. The LOD values Fe^{3+} and $Cr_2O_7^{2-}$ were 5.1×10^{-5} M and 5.3×10^{-5} M respectively. The quenching effect of **Cd-8** in case of NB was the most prominent. The sensitivity of **Cd-8** towards NB was detected by performing titration experiments in the DMA solution. The fluorescence intensity gradually weakened with increasing the volumes of NB. The LOD value of **Cd-8** in the presence of NB was 4.2×10^{-5} M.

Surib *et al.*[1.121] reported **Cd-9** (see Table 1.5)**,** which was synthesized by using hydrothermal method. So, improve the properties of **Cd-9** *via* intercalating Fe^{3+}, Zn^{2+}, and Ag^{+} into the framework through an ion-exchange method. Fe^{3+} inserted into the **Cd-9** showed strong photo response in visible region, **Cd-9** showed a broader and wider emission at 440 nm upon excitation wavelength at 325 nm, when, Zn^{2+} and Ag^{+} insert in **Cd-9**, **Cd-9** showed strong photo response in ultraviolet light region at 425 nm and 420 nm, respectively. The pure **Cd-9** had energy difference at around 3.6 eV, whereas in the case of Zn– **Cd-9**, Ag– **Cd-9**, and Fe– **Cd-9** the energy difference were 3.4 eV, 3.5 eV, and 2.0 eV, respectively. The energy gap of Fe^{3+} intercalated **Cd-9** was lower than Zn^{2+} and Ag^{+} intercalated **Cd-9**. So, this Fe– **Cd-9** was enabled to easy charge transfer and showed broad spectrum in the visible region.

Xu *et al.*[1.122] reported **Cd-10, Cd-11** and **Cd-12** (see Table 1.5) *via* hydrothermal process. The porous framework of **Cd-10** had larger one dimensional channel than that of **Cd-11** and **Cd-12**. So **Cd-10** showed high N_2 absorption and exhibited linear N_2 isotherm. **Cd-10** adsorbs CO_2 up to 5.9 $cm^3\ g^{-1}$ at 195 K and 1 atm. **Cd-11** and **Cd-12** adsorbs CO_2 6.3 $cm^3\ g^{-1}$ and 17.8 $cm^3\ g^{-1}$ respectively at 195 K and 1 atm. **Cd-10, Cd-11** and **Cd-12** were showed solid state strong photo-luminescent spectra. Only **Cd-10** exhibited selective photo-luminescent quenching behaviour in the presence of NO_2^- anions.

Singha *et al.*[1.123] reported three–dimensional **Cd-11** (see Table 1.5). **Cd-11** detected iodide ion using luminescence-based mechanism. **Cd-11** showed emission maximum at 290 nm when excitation wavelength was 226 nm and the photoluminescence intensity decrease almost 93% of the initial photoluminescence intensity. The LOD value of **Cd-11** in the presence of iodide ion was 0.63 µM (80 ppb).

Zhang *et al.*[1.124] reported luminescent-active microporous **Cd-12** (see Table 1.5). **Cd-12** acts as luminescence sensor towards nitrobenzene, Fe^{3+}, $Cr_2O_7^{2-}$ in aqueous medium *via* luminescence quenching effect. This **Cd-12** quenched the luminescence efficiency around 86.1% after dropwise addition of NB up to 350 µL and LOD values was 5.35 10^{-}

^{5} M. Similarly, after the addition of 300 µL Fe^{3+} the fluorescence intensity quenched approximately 90% and the LOD value for Fe^{3+} was 7.06 10^{-5} M. This MOF also showed quenching effect in the presence $Cr_2O_7^{2-}$ (95%) and for $Cr_2O_7^{2-}$ LOD was as low as 1.82 10^{-5} M. All the cases **Cd-12** showed luminescence intensity at around 398 nm upon excitation wavelength at 320 nm.

Yu *et al*.[1.125] synthesized **Cd-13** (see Table 1.5) using 1,4-di(imidazol-1-yl)naphthalene, and terephthalic acid. **Cd-13** showed luminescence quenching efficiency towards $Cr_2O_7^{2-}$ and I^- were 90% and 94% upon excitation at 230 nm and $Cr_2O_7^{2-}$ exhibited 92% quenching efficiency upon excitation 290 nm. The LOD value in case of $Cr_2O_7^{2-}$ ion were 1.36×10^{-6} (excitation wavelengths at 230) and 8.37×10^{-7} M (excitation wavelengths at 290 nm). LOD for I^- was 1.78×10^{-7} M at 230 nm excitation. At 230 nm and at 290 nm excitation, **Cd-13** performed quenching rates of pesticides were in the order NTP > 2, 4-D > TPM > MMT > IMI > CAR ≈ DIP ≈ PCNB > TPN > GLY and IMI > NTP > MMT respectively.

Wang et al.[1.126] constructed 3D **Cd-14** and **Cd-14** (see Table 1.5)**,** showed emission maxima at around 395 nm (λ_{ex} = 300 nm), the quenching efficiency for TNP in 20 ppm was 44.5% and in 240 ppm was 85%. The photo luminescent intensity of **Cd-14** for Fe^{3+} was highly significant at 6.05×103 M^{-1}. The LOD for TNP and Fe^{3+} were 1.77 ppm and 1.56 ppm.

Chen et al.[1.127] reported **Cd-15** (see Table 1.5) which exhibited discriminating luminescence enhancement effect in case of Al^{3+} and Ca^{2+} in aqueous medium at 376 nm. They have studied the relation between the luminescent intensity of **Cd-15** with time. The time-dependent emission spectra indicate that the luminescence intensities remain unchanged with time.

Table 1.5: List of some selected cadmium based metal organic compounds.

Code number of the compounds	Molecular formula	Ref.
Cd-1	$\{[Cd_{1.5}(C_{18}H_{10}O_{10})]\cdot(H_3O)(H_2O)_3\}_n$	1.114
Cd-2	$[Cd_3(4\text{-}TP)_6]$	1.115
Cd-3	$\{[Me_2NH_2]_2[CdBPTC]\cdot 6H_2O\}_n$	1.116
Cd-4 and **Cd-5**	$[Cd_3\cdot L\cdot(BTB)_2\cdot$ 2DMF] and $[(Cd_3O_2)\cdot L\cdot BTC]$	1.117
Cd-6	$\{[Cd(L_1)(L_2)](DMA)\}_n$	1.118
Cd-7	$[Cd(IsoNDI)(ClO_4)\cdot H_2O]_n$	1.119
Cd-8	$[Cd_3(L)(NTB)_2(DMA)_2]\cdot 2DMA$	1.120
Cd-9	-	1.121
Cd-10, Cd-11 and **Cd-12**	$[Cd_3(\mu_3\text{-}L_1)_2(\mu_2\text{-}L_1)_2(\mu_2\text{-}Cl)_2Cl_4]_n$,$\{[Cd_2(\mu_3\text{-}L_1)_2(\mu_2\text{-}Br)_2Br_2]\cdot 1.05H_2O\}_n$ and $\{[Cd_2(\mu_2\text{-}L_1)_3(L_1)_2(\mu_2\text{-}I)2]\cdot(CdI4)\cdot 1.5H_2O\}_n$	1.122
Cd-11	-	1.123
Cd-12	$[Cd_3\ (cia)_2\ (4,4'\text{-bipy})\ (H_2O)_2]_n$	1.124
Cd-13	$[Cd(DIN)(TPA)(H_2O)]_n$	1.125
Cd-14	$[Cd_2(btc)(bib)(HCOO)(H_2O)\cdot H_2O]_n$	1.126
Cd-15	$[Cd_2(bptc)(HCOO)]\cdot NH_2(CH_3)_2\cdot 3H_2O$	1.127

1.12 A BRIEF DISCUSSION OF VANADIUM BASED COMPOUNDS

Khan et al.[1.128] synthesized new framework such as **V-1** (see Table 1.6) and contains 3D arrays of vanadium oxide nanoclusters $\{V_{18}O_{42}(AO_4)\}$ which was interconnected through {-O−Cd−O-} bridging groups. The synthesized materials showed promising sensing properties towards $\{NO_x\}$ (NO and NO_2) gases with superior sensitivity.

Barthelet et al.[1.129] hydrothermally synthesized the new **V-2** MOF (see Table 1.6) named as MIL-47. Due to permanent porosity **V-2** exhibited gas sorption behaviours in liquid nitrogen. The calculated BET surface area and Langmuir surface area were 930 (30) $m^2\ g^{-1}$ and 1320 (2) $m^2\ g^{-1}$ respectively. **V-2** showed type I isotherm without hysteresis upon desorption. MIL-47 also showed antiferromagnetic behavior below T_N = 95(5) K.

Barthelet et al.[1.130] hydrothermally synthesized two 3D frameworks such as **V-3** (named as MIL-60) and **V-4** (named as MIL-61). **V-3** and **V-4** (see Table 1.6) both have same inorganic building block consisting with the trans chains of $V^{III}O_4(OH)_2$ octahedra and performed different magnetic behaviours. **V-3** exhibited paramagnetic behaviour and **V-4** performed antiferromagnetic behaviour orders below T_N =55(5) K.

Barthelet et al.[1.131] prepared 3D vanadium complex such as **V-5** (see Table 1.6), named as MIL-71 *via* hydrothermal conditions. In **V-5** the octahedra unit such as $V^{III}O_2(OH)_2F_2$ connected by the terephthalate linkers form a layers structure. **V-5** showed antiferromagnetic behaviour with Neel temperatures below 20 K.

Liu et al.[1.132] synthesized **V-6** (see Table 1.6) via solvothermal and microwave methods. At 303 K the new V^{IV}-Based MOF showed adsorption isotherms of type I shape for both CO_2 and CH_4. The uptake capacities of CO_2 and CH_4 per gram were 4.8 mmol at 25 bar and 1.4 mmol at 27 bar, CO_2 and CH_4 isotherms were characteristically different at 265K. At 12.5 bar CO_2 sorption isotherm suddenly increase and reach up to 14 mmol g^{-1} at 28 bar but not for CH_4.

Liu et al.[1.133] synthesized vanadium compound such as **V-7** (see Table 1.6), labeled as **COMOC-3** by hydrothermal methods. **COMOC-3** was performed catalytic properties in cyclohexene through liquid-phase oxidation. The conversion of cyclohexene was 38% after 7 h reaction, and selectivity of cyclohexene oxide was 82%. The TON and TOF values were calculated in 7 h to maintained the catalytic performance. The TON and TOF values for the first run were 39.0 and 5.6 h^{-1}. Similarly TON and TOF values for the second were 30.7 and 4.4 h^{-1}.

Yan et al.[1.134] successfully prepared rod-like vanadium MOF such as **V-8** (see Table 1.6). **V-8** had specific capacitance 572.1 F g^{-1} and current density was 0.5 A g^{-1}. This performance was showed that **V-8** electrode was behaving as good supercapacitors.

Wang et al.[1.135] synthesized a porous V^{IV}– porphyrin-based metal−organic framework such as **V-9** (see Table 1.6). **V-9** was the good platform for inert C(sp3)−H bond heterogenous activation and functionalization under mild conditions. Moreover, the various numbers of catalytically active sites into metal−organic frameworks would apprehend a multiple-site synergistic catalytic process together with metalloporphyrin.

Lv et al.[1.136] reported 3D nickel−vanadium MOF such as **V-10** (see Table 1.6) supported on nickel foam, such as **V-10@NF** was formed *via* ultrasound and solvothermal two-step process. **V-10@NF** showed good OER and HER catalytic activities. The electrochemical test results showed that **V-10@NF** had low over potentials and the values of HER and OER were 89 and 244 mV respectively. The HER and OER values in the corresponding Tafel slopes of **V-10@NF** were 98.3 and 38.1 mV dec^{-1}. The bifunctional electrocatalyst showed the cell voltage was 1.55 V and the current density was 10 mA cm^{-2}, So, Ni2V-MOFs@NF exhibited better catalytic activities than the commercial Pt/C (20%) and RuO_2 catalysts.

Kong et al.[1.137] reported a series of trimetallic V-based MOFs were synthesized through pore-space-partition (PSP) strategy, the trimetallic MOFs are Fe_2 **V-11**, Co_2 **V-12**, Mg_2 **V-13**, Ni_2 **V-14**, and Zn_2 **V-15** (see Table 1.6). Among these V-MOFs **Fe_2V-11** have high chemical and structural stabilities and showed superior electrocatalytic activities of OER and HER. Moreover, the fabricated cell of **Fe_2V-11/NF**|| Pt/C/NF showed the long-term electrochemical stability and water electrolysis showed the voltage was approximately 1.6 V at 10mA cm^{-2}.

Kanoo et al.[1.138] synthesized 3D **V-16** (see Table 1.6) by using hydrothermal process and autogenous pressure. **V-16** showed high thermal stability and exhibits adsorption of gases likes CO_2, N_2 and solvent molecules likes EtOH, MeOH. VMOF exhibited antiferromagnetic behaviours at low temperature through super exchange processes between the V^{4+}centers and PO_3^{2-} moieties.

Han et al.[1.139] prepared **V-17** (see Table 1.6) based on nickel foam (NF) via solvothermal method. **V-17 @NF** showed excellent electrocatalytic properties and performed HER and OER in alkaline medium. The HER and OER values of **V-17 @NF** composite were 147 mV and 246 mV respectively at 10 mA/cm^2.

Rocha et al.[1.140] reported a arrays of three diamensional modular trinodal mixed-MOF **V-18** to **V-24** (see Table 1.6)**.** The SBU was formed at room temperature and the presence of both transition metal (V^{4+}) and a lanthanide ion (Eu^{3+}) and this MOF showed multi-wavelength emission. The colour of the emission was easily changed from white to purplish-blue through changing the excitation maximum.

Wang et al.[1.141] prepared vanadium-based MOF such as **V-25** (see Table 1.6), named as MIL-47 using hydrothermal method. The material had excellent conductive properties and very efficiently **V-25** containing metal centers performed redox kinetics and deliver a remarkable cyclability with a minimum reduction was about 0.03 % for 1000 cycles at 1 C.

Table 1.6: List of some vanadium based compounds.

Code number of the compounds	Molecular formula	Ref.
V-1	$[Cd^{II}_3(H_2O)_{12}V^{IV}_{16}V^{V}_2O_{36}(OH)_6(AO_4)]\cdot 24H_2O$	1.128
V-2	$V^{III}(OH)\{O_2C\text{-}C_6H_4\text{-}CO_2\}\cdot x(HO_2CC_6H_4\text{-}CO_2H)$ (x~0.75)	1.129
V-3 and **V-4**	$(V^{III}(OH))_2\{C_6H_2(CO_2)_4\},4H_2O$ and $V^{III}(OH)\{_2(O_2C)C_6H_2(COOH)_2\},H_2O$	1.130
V-5	$V^{III}_2(OH)_2F_2\{O_2C\text{-}C_6H_4\text{-}CO_2\}\cdot H_2O$	1.131
V-6	$[VO(BPDC)]\ (DMF)_{0.1}(H_2O)_{0.5}$	1.132
V-7	$V^{IV}O(O_2C\text{–}C_{10}H_6\text{–}CO_2)$	1.133
V-8	$(V^{IV}(O)(bdc)$	1.134
V-9	-	1.135
V-10	Ni_2V MOFs	1.136
Fe $_2$ **V-11**, Co $_2$ **V-12**, Mg $_2$ **V-13,** Ni $_2$ **V-14**, and Zn $_2$ **V-15**	Fe $_2$ V-MOF, Co $_2$ V-MOF, Mg $_2$ V-MOF, Ni $_2$V-MOF ,and Zn $_2$V-MOF	1.137
V-16	$\{(H_2PIP)_{0.5}[VO(CEP)]\cdot H_2O\}$	1.138
V-17	-	1.139
V-18 to V-24	$M_4[M_{12}V_{24}O_{24}(OH)_8(H_2hedp)_8(Hhedp)_{16}(H_2O)_{64+n}]\cdot 88+y(H_2O)$, where M^{3+} will be Y^{3+}, Ce^{3+}, Sm^{3+}, Eu^{3+}, Tb^{3+}, Gd^{3+} and Er^{3+}.	1.140
V-25	-	1.141

1.13 REFERENCES

(1.1) T. R. Cook, Y.-R. Zheng, and P. J. Stang, *Chem. Rev*., 2013, **113**, 734−777.

(1.2) K. Bowman-James, *Acc. Chem. Res*., 2005, **38**, 671.

(1.3) R. L. Paul, Z. R. Bell, J. C. Jeffery, J. A. McCleverty, and M. D. Ward, *Proc. Natl. Acad. Sci*., 2002, **99**, 4883-4888.

(1.4) A. Bavykina, N. Kolobov, I.S. Khan, J.A. Bau, A. Ramirez, J. Gascon, *Chem. Rev*., 2020, **120**, 8468–8535.

(1.5) J. G. Sabate, A. Corma, F. Kapteijn, L. I Xamena, *ACS Catal*., 2014, **4**, 361− 378.

(1.6) J. Liu, L. Chen, H. Cui, J. Zhang, L. Zhang, C.-Y. Su, *Chem. Soc. Rev*., 2014, **43**, 6011−6061.

(1.7) T. Zhang, W. Lin, *Chem. Soc*. *Rev*., 2014, **43**, 5982− 5993.

(1.8) M. Yoon, R. Srirambalaji, K. Kim, *Chem. Rev*., 2012, **112**, 1196−1231.

(1.9) J. Y. Lee, O. K. Farha, J. Roberts, K. A. Scheidt, S. T. Nguyen, J. T. Hupp, *Chem. Soc. Rev*., 2009, **38**, 1450−1459.

(1.10) S. Lawson, A. Siemers, J. Kostlenick, Q. Al-Naddaf, K. Newport, A.A. Rownaghi, F. Rezaei, *ACS Appl. Bio Mater*., 2021, **4**, 6874–6880.

(1.11) P. Horcajada, R. Gref, T. Baati, P. K. Allan, G. Maurin, P. Couvreur, G. Férey, R. E. Morris and C. Serre, *Chem. Rev*., 2012, **112**, 1232.

(1.12) J. Della Rocca, D. Liu and W. Lin, *Acc. Chem. Res*., 2011, **44**, 957.

(1.13) M. C. Bernini, D. Fairen-Jimenez, M. Pasinetti, A. J. Ramirez-Pastor and R. Q. Snurr, *J. Mater. Chem. B*, 2014, **2**, 766.

(1.14) G. Ferey, F. Millange, M. Morcrette, C. Serre, M.-L. Doublet, J.-M. Greneche, J.-M. Tarascon, *Angew. Chem., Int. Ed*., 2007, **46**, 3259−3263.

(1.15) M. Yoon, K. Suh, S. Natarajan, K. Kim, *Angew. Chem., Int. Ed*., 2013, **52**, 2688−2700.

(1.16) K. M. Choi, H. M. Jeong, J. H. Park, Y.-B. Zhang, J. K. Kang, O. M. Yaghi, *ACS Nano*., 2014, **8**, 7451−7457.

(1.17) K. Sumida, D. L. Rogow, J. A. Mason, T. M. McDonald, E. D. Bloch, Z. R. Herm, T.-H. Bae, J. R. Long, *Chem. Rev*., 2012, **112**, 724−781.

(1.18) K. V. Kumar, K. Preuss, M.-M. Titirici, F. Rodríguez-Reinoso, *Chem. Rev*., 2017, **117**, 1796–1825.

(1.19) L. Zou, J. Yuan, Y. Yuan, J. Gu, G. Li, L. Zhang, Y. Liu, *CrystEngComm*., 2019, **21**, 3289–3294.

(1.20) M. P. Suh, H. J. Park, T. K. Prasad, D.-W. Lim, *Chem. Rev*., 2012, **112**, 782− 835.

(1.21) H. Wu, Q. Gong, D. H. Olson, J. Li, *Chem. Rev*., 2012, **112**, 836−868.

(1.22) J.-R. Li, J. Sculley, H.-C. Zhou, *Chem. Rev*., 2012, **112**, 869−932.

(1.23) J. B. Decoste, G. W. Peterson, *Chem. Rev*., 2014, **114**, 5695−5727.

(1.24) N. C. Burtch, H. Jasuja, K. S. Walton, *Chem. Rev*., 2014, **114**, 10575−10612.

(1.25) S. Qiu, M. Xue, G. Zhu, *Chem. Soc. Rev*., 2014, **43**, 6116−6140.

(1.26) Y. He, W. Zhou, G. Qian, B. Chen, *Chem. Soc. Rev*., 2014, **43**, 5657−5678.

(1.27) M. Mukoyoshi, M. Maesato, S. Kawaguchi, Y. Kubota, K. Cho, Y. Kitagawa, and H. Kitagawa, *Inorg. Chem*., 2022, **61**, 7226−7230.

(1.28) M. Arjmandi, A. Altaee, A. Arjmandi, M. P. Chenar, M. Peyravi, M. Jahanshahi, *Solid State Sciences*., 2020, **106**, 106292.

(1.29) Y. Hu, Z. Huang, J. Liao, G. Li, *Anal. Chem*., 2013, **85,** 14 6885-6893.

(1.30) Q. Li, S. Jiang, Sh Ji, D. Shi, H. Li, *J. Porous Mater*., 2015, **22,** 1205–1214.

(1.31) G. Chakraborty, I.-H. Park, R. Medishetty, J. J. Vittal, *Chem. Rev*., 2021, **121**, 3751–3891.

(1.32) D. K. Singha, P. Majee , S. K. Mondal, P. Mahata, *Journal of Photochemistry and Photobiology A: Chemistry*., 2018, **356,** 389–396.

(1.33) S. Jensen, K. Tan, W. Lustig, D. Kilin, J. Li, Y. J. Chabal, and T. Thonhauser, *J. Mater. Chem. C*., 2019, **7**, 2625-2632.

(1.34) X.-Y. Guo , Z.-P. Dong , F. Zhao , Z.-L. Liu and Y.-Q. Wang, New J. Chem., 2019, **43**, 2353.

(1.35) Q.-B. Bo, H.-Y. Wang and D.-Q. Wang, *New J. Chem*., 2013, **37**, 380.

(1.36) L. E. Kreno, K. Leong, O. K. Farha, M. Allendorf, R. P. Van Duyne, and J. T. Hupp, *Chem. Rev*., 2012, **112**, 1105–1125.

(1.37) D. J. Tranchemontagne, J. L. Mendoza-Cortes, M. O'Keeffe, O. M. Yaghi, *Chem. Soc. Rev*., 2009, **38**, 1257.

(1.38) O. D.-Friedrichs, M. O'Keeffe and O. M. Yaghi, *Phys. Chem. Chem. Phys*., 2007, **9**, 1035–1043.

(1.39) M. O'Keeffe, M. A. Peskov, S. J. Ramsden and O. M. Yaghi, *Acc. Chem. Res*., 2008, **41**, 1782.

(1.40) B. F. Hoskins and R. Robson, *J. Am. Chem. Soc*., 1990, **112**, 1546.

(1.41) R. Robson, *J. Chem. Soc., Dalton Trans.*, 2000, 3735–3744.

(1.42) O. M. Yaghi and H. Li, *J. Am. Chem. Soc*., 1995, **117**, 10401-10402.

(1.43) H. Li, M. Eddaoudi, M. O'Keeffe and M. Yaghi, *Nature*., 1999, **402**, 276.

(1.44) O. Delgado-Friedrichs, M. O'Keeffe and O. M. Yaghi, Phys. Chem. Chem. Phys., 2007, **9**, 1035.

(1.45) R. J. Hill, D. L. Long, N. R. Champness, P. Hubberstey and M. Schröder, Acc. Chem. Res., 2005, **38**, 337.

(1.46) Q. Fang, G. Zhu, M. Xue, J. Sun, F. Sun, and S. Qiu, *Inorg. Chem.* 2006, **45**, 3582–3587.

(1.47) A. Rodrı´guez-Dieguez, A. Salinas-Castillo, A. Sironi, J. M. Seco and E. Colacio, CrystEngComm, 2010, **12**, 1876–1879.

(1.48) J. Xia, Z.-j. Zhang, W. Shi, J.-f. Wei, and P. Cheng, Crystal Growth & Design, 2010, **10**, 2323-2330.

(1.49) S. Xiong, S. Wang, X. Tang and Z. Wang, CrystEngComm, 2011, **13**, 1646–1653.

(1.50) M. Xue, G. Zhu, Y. Li, X. Zhao, Z. Jin, E. Kang, S. Qiu, Cryst. Growth Des, 2008, **8**, 2478.

(1.51) M. Xue, G. Zhu, Y. Zhang, Q. Fang, I. J. Hewitt, S. Qiu, Cryst. Growth Des. 2008, **8**, 427.

(1.52) Y. Qiu, Y. Li, G. Peng, J. Cai, L. Jin, L. Ma, H. Deng, M. Zeller, S. R. Batten, Cryst. Growth Des. 2010, **10**, 1332.

(1.53) H.-D. Guo, X.-M. Guo, S. R. Batten, J.-F. Song, S.-Y. Song, S. Dang, G.-L. Zheng, J.-K. Tang, and H.-J. Zhang, *Cryst. Growth Des.* 2009, **9**, 1394–1401.

(1.54) Z. Zhang, S. Xiang, X. Rao, Q. Zheng, F. R. Fronczek, G. Qian, B. Chen, Chem. Commun., 2010, **46**, 7205.

(1.55) E.-C. Yang, H.-K. Zhao, B. Ding, X.-G. Wang, X.-J. Zhao, Cryst. Growth Des., 2007, **7**, 2009.

(1.56) G. Férey, *Chem. Soc. Rev*., 2008, **37**, 191.

(1.57) C. N. R. Rao, S. Natarajan and R. Vaidhyanathan, *Angew. Chem. Int. Ed*., 2004, **43**, 1466.

(1.58) D. W. Breck, Zeolite Molecular Sieves, 1974.

(1.59) A. K. Cheetham, C. N. R. Rao and R. K. Feller, *Chem. Commun*., 2006, 4780–4795.

(1.60) D. Maspoch, D. Ruiz-Molina and J. Veciana, *Chem. Soc. Rev*., 2007, **36**, 770.

(1.61) M. J. Rosseinsky, *Microporous Mesoporous Mater*., 2004, **73**, 15.

(1.62) J. L. C. Rowsell and O. M. Yaghi, *Microporous Mesoporous Mater*., 2004, **73**, 3-14.

(1.63) A.D. Li, W.C. Liu, *Composites Science and Engineering*., 2010, 108-158.

(1.64) S. Choudhury, S. Paul, S. Goswami, K. Deb, *Nanotechnology in Biomedicine*., 2022, 21-44.

(1.65) Bruker Apex3 v2017.3-0, Saint V8.38A, SAINT V8.38A; Bruker AXS Inc.: Madison, WI, 2018.

(1.66) L. Krause, R. Herbst-Irmer, G. M. Sheldrick, D. Stalke, J. Appl. Crystallogr., 2015,**48**, 3− 10.

(1.67) A. Altomare, G. Cascarano, C. Giacovazzo, A. Guagliardi, Completion and Refinement of Crystal Structures with SIR92. J. Appl. Crystallogr., 1993, **26,** 343−350.

(1.68) G. M. Sheldrick, Crystal Structure Refinement with SHELXL. Acta Crystallogr., Sect. C: Struct. Chem., 2015, **71,** 3−8.

(1.69) L. J. Farrugia, WinGX suite for Small-Molecule Single-Crystal Crystallography. J. Appl. Crystallogr., 1999, **32**, 837−838.

(1.70) A. L. Spek, Single-Crystal Structure Validation with the Program PLATON. J. Appl. Crystallogr., 2003, **36**, 7−13.

(1.71) Y. Liu, X.-Y. Xie, C. Cheng, Z.-S. Shao and H.-S. Wang, *J. Mater. Chem. C.*, 2019, **7**, 10743—10763.

(1.72) L. Guan, Z. Jiang, Y. Cui, Y. Yang, D. Yang, and G. Qian, *Adv. Optical Mater*., 2021, **9**, 2002180.

(1.73) B. Mohan, S. Ma, S. Kumar, Y. Yang, and P. Ren, *ACS Appl. Mater. Interfaces*., 2023, **15**, 17317−17323.

(1.74) Y.-W. Li, J. Li, X.-Y. Wan, D.-F. Sheng, H. Yan, S.-S. Zhang, H.-Y. Ma, S.-N. Wang, D.-C. Li, Z.-Y. Gao, J.-M. Dou, and D. Sun, *Inorg. Chem.*, 2021, **60**, 671–681.

(1.75) E. Moradi, R. Rahimi, V. Safarifard, *Polyhedron*., 2019, **159**, 251–258.

(1.76) Y. D. Farahani, V. Safarifard, *Journal of Solid State Chemistry*., 2019, **270**, 428–435.

(1.77) D. Mukherjee, A. Pal, S. C. Pal, A. Saha, and M. C. Das, *Inorg. Chem*., 2022, **61**, 16952−16962.

(1.78) Y. Li, D.-G. Cai, Z.-H. Zhu, H. Xu, T.-F. Zheng, J.-L. Chen, S.-J. Liu and H.-R. Wen, *Dalton Trans*., 2023, **52**, 4167–4175.

(1.79) M. Shi, C. Fu, J. Yu, Y. Yang and P. Shi, *New J. Chem*., 2022, **46**, 18911.

(1.80) S.-L. Yao, Y.-C. Xiong, X.-M. Tian, S.-J. Liu, H. Xu, T.-F. Zheng, J.-L. Chen and H.-R. Wen, *CrystEngComm*., 2021, **23**, 1898–1905.

(1.81) X.-M. Tian, S.-L. Yao, C.-Q. Qiu, T.-F. Zheng, Y.-Q. Chen, H. Huang, J.-L. Chen, S.-J. Liu, and H.-R. Wen, *Inorg. Chem.*, 2020, **59**, 2803–2810.

(1.82) D. Evangelou, A. Pournara, C. Tziasiou, E. Andreou, G. S. Armatas, and M. J. Manos, *Inorg. Chem.*, 2022, **61**, 2017−2030.

(1.83) S.-L. Hou, J. Dong, X.-L. Jiang, Z.-H. Jiao, C.-M. Wang, and B. Zhao, *Anal. Chem*., 2018, **90**, 1516−1519.

(1.84) B. Zhang, P.-Y. Guo, L.-N. Ma, B. Liu, L. Hou, and Y.-Y. Wang, *Inorg. Chem*., 2020, **59**, 5231−5239.

(1.85) J. Zhang, L. Gao, Y. Wang, L. Zhai, X. Niu and T. Hu, *CrystEngComm.*, 2019, **21**, 7286.

(1.86) K. Ahmad, H.-U.-R. Shah, S. Parveen, T. Aziz, H. A. Naseem, M. Ashfaq, A. Rauf, *Journal of Molecular Structure.*, 2021, **1242**, 130898.

(1.87) S.-Q. Deng, Y.-L. Miao, Y.-L. Tan, H.-N. Fang, Y.-T. Li, X.-J. Mo, S.-L. Cai, J. Fan, W.-G. Zhang, and S.-R. Zheng, *Inorg. Chem*., 2019, **58**, 13979−13987.

(1.88) Y. Gao, Y. Li, C. Liang, P. Cen, J. Xi, Y. Guo, W. Song and X. Liu, *Dalton Trans*., 2021, **50**, 17603.

(1.89) D.-D. Guo, B. Li, Z.-P. Deng, L.-H. Huo and S. Gao, *Dalton Trans*., 2021, **50**, 7818–7825.

(1.90) J.-J. Li, C.-C. Wang, H.-f. Fu, J.-R. Cui, P. Xu, J. Guoa and J.-R. Li, *Dalton Trans*., 2017, **46**, 10197.

(1.91) X.-T. Liu, S.-S. Chen, S.-M. Li, H.-X. Nie, Y.-Q. Feng, Y.-N. Fan, M.-H. Yu, Z. Chang and X.-H. Bu, *CrystEngComm*., 2020, **22**, 5941.

(1.92) Y.-L. Huang, Y.-N. Gong, L. Jiang and T.-B. Lu, *Chem. Commun*., 2013, **49**, 1753.

(1.93) N. L. Rosi, J. Eckert, M. Eddaoudi, D. T. Vodak, J. Kim, M. O'Keeffe and O. M. Yaghi, Science, 2003, **300**, 1127–1129.

(1.94) W. Gong, Y. Xie, T. D. Pham, S. Shetty, F. A. Son, K. B. Idrees, Z. Chen, H. Xie, Y. Liu, R. Q. Snurr, B. Chen, B. Alameddine, Yong Cui, and O. K. Farha, *J. Am. Chem. Soc*., 2022, **144**, 3737−3745.

(1.95) D. Zhao, Q. Song, Y. Li, L. Li, F. Yuan, Y. Yang, S. Xiang, and Z. Zhang, *ACS Appl. Nano Mater*., 2023, **6**, 9523−9530.

(1.96) X. Pan, X. Si, X. Zhang, Q. Yao, Y. Li, W. Duan, Y. Qiu, J. Su and X. Huang, Dalton Trans., 2023, **52**, 3896.

(1.97) S. Halder, A. Dey, A. Bhattacharjee, J. O.-Castro, A. Frontera, P. P. Ray and P. Roy, *Dalton Trans.*, 2017, **46**, 11239.

(1.98) G. Bairy, A. Dey, B. Dutta, P. P. Ray, and C. Sinha, *Cryst. Growth Des*., 2022, **22**, 3138−3147.

(1.99) D. Y. Lee, S. J. Yoon, N. K. Shrestha, S.-H. Lee, H. Ahn, S.-H. Han, *Microporous and Mesoporous Materials*., 2012, **153**, 163–165.

(1.100) S. Sanda, S. Biswas, and S. Konar, *Inorg. Chem*., 2015, **54**, 1218−1222.

(1.101) M. Sadakiyo, H. Ōkawa, A. Shigematsu, M. Ohba, T. Yamada and H. Kitagawa, *J.Am.Chem.Soc*., 2012, **134**, 5472−5475.

(1.102) S.-S. Bao, K. Otsubo, J. M. Taylor, Z. Jiang, L.-M. Zheng, and H. Kitagawa, *J.Am.Chem.Soc*., 2014, **136**, 9292−9295.

(1.103) J. Posta, H. Berndt, S.-K. Luo and G. Schaldach, *Anal. Chem*., 1993, **65**, 2590–2595.

(1.104) J. Moros and J. J. Laserna, *Analytical Chemistry*, 2011, **83**, 6275-6285.

(1.105) D. Moreno-González, F. J. Lara, N. Jurgovská, L. Gámiz-Gracia and A. M. García-Campaña, *Analytica Chimica Acta*, 2015, **891**, 321-328.

(1.106) M. Tabrizchi and V. Ilbeigi, *Journal of Hazardous Materials*, 2010, **176**, 692-696.

(1.107) G. Cerchiaro, T. M. Manieri and F. R. Bertuchi, *Metallomics*, 2013, **5**, 1336–1345.

(1.108) C. Blasco, A. D. Corcia and Y. Picó, *Food Chemistry*, 2009, **116**, 1005-1012.

(1.109) T. Shamspur, I. Sheikhshoaie and M. H. Mashhadizadeh, *J. Anal. At. Spectrom*.,2005,**20**, 476–478.

(1.110) C. M. G. Berg, *Anal. Chem*., 2006, **78**, 156–163.

(1.111) H. A. McIlwee, C. L. Schauer, V. G. Praig, R. Boukherroub , S. Szunerits, *Analyst*, 2008, **133**, 673–677.

(1.112) K. Pomazal, C. Prohaska, I. Steffan, G. Reich and J. F. K. Huber, *Analyst*, 1999, **124**, 657–663.

(1.113) P. Mahata, S. K. Mondal, D. K. Singha and P. Majee, Dalton Trans., 2017, **46**, 301.

(1.114) P. Wu, Y. Liu, Y. Liu, J. Wang, Y. Li, W. Liu, and J. Wang, *Inorg. Chem*., 2015, **54**, 11046−11048.

(1.115) P. Pachfule and R. Banerjee, *Cryst. Growth Des*. 2011, **11**, 5176–5181.

(1.116) L.-L. Xu, Q.-F. Zhang, D. Wang, G.-W. Wu and H. Cai, *Molecules*., 2021, **26**, 6847.

(1.117) M. Fan, B. Sun, X. Li, Q. Pan, J. Sun, P. Ma, and Z. Su, *Inorg. Chem*., 2021, **60**, 9148−9156.

(1.118) R. Debnath, R. Bhowmick, P. Ghosh, S. Biswas and S. Koner, *New J. Chem*., 2022, **46**, 8523.

(1.119) G. Zhang, C. Fu, H. Zhang and H. Zhang, *CrystEngComm*., 2021, **23**, 4513.

(1.120) X. Wang, Y. Liu, H. Lin, N. Xu, G. Liu, X. Wang, Z. Chang and J. Li, *CrystEngComm*., 2020, **22**, 6626.

(1.121) N. A. Surib, L. C. Sim, K. H. Leong, A. Kuila, P. Saravanan, K. M. Lo, S. Ibrahim, D. Bahnemann and M. Jang, *RSC Adv*., 2017, **7**, 51272.

(1.122) Y. Y. Xu, X. X. Wu, Y. Y. Wang, X. M. Su, S. X. Liu, Z. Z. Zhu, B. Ding, Y. Wang, J. Z. Huo and G. X. Du, *RSC Adv*., 2014, **4**, 25172.

(1.123) D. K. Singha, P. Majee , S. K. Mondal, P. Mahata, *Journal of Photochemistry and Photobiology A: Chemistry*., 2018, **356**,389–396.

(1.124) Y.-N. Zhang, J.-L. Chen, C.-Y. Su, W.-H. Huang, *Journal of Solid State Chemistry*., 2021, **302,** 122407.

(1.125) B.-Y. Yu, Z.-P. Wang, H.-Y. Ding, F.-F. Miao, A.-Z. Yang, W.-T. Zhao, Y. Jia, H.-Q. Zhao, *Journal of Molecular Structure.*, 2023, **1291**,135891.

(1.126) J. Wang, J. Wu, L. Lu, H. Xu, M. Trivedi, A. Kumar, J. Liu and M. Zheng, *Front. Chem*., 2019, **7**, 244.

(1.127) W. Chen, Y. Lin, X. Zhang, N. Xu, P. Cheng, *Inorganic Chemistry Communications*., 2017, **79**, 29–32.

(1.128) M. I. Khan, N. R. Putrevu, S. Ayesh, E. H. Yohannes, B. Cage, and R. J. Doedens, *Cryst. Growth Des*., 2013, **13**, 4667−4672.

(1.129) K. Barthelet, J. Marrot, D. Riou, and G. Fe´rey, Angew. *Chem. Int. Ed*., 2002, **41**, No. 2.

(1.130) . Barthelet, D. Riou, M. Nogues, and G. Fe´rey, *Inorg. Chem*., 2003, **42**, 1739−1743.

(1.131) K. Barthelet, K. Adil, F. Millange, C. Serre, D. Riou and G. Fe´rey, *J. Mater. Chem*., 2003, **13**, 2208–2212.

(1.132) Y.-Y. Liu, S. Couck, M. Vandichel, M. Grzywa, K. Leus, S. Biswas, D. Volkmer, J. Gascon, F. Kapteijn, J. F. M. Denayer, M. Waroquier, V. V. Speybroeck, and P. V. D. Voort, *Inorg. Chem*., 2013, **52**, 113−120.

(1.133) Y. Y. Liu, K. Leus, M. Grzywa, D. Weinberger, K. Strubbe, H. Vrielinck, R. Van Deun, D. Volkmer, V. Van Speybroeck and P. Van der Voort, *Eur. J. Inorg. Chem*., 2012, 2819.

(1.134) Y. Yan, Y. Luo, J. Ma, B. Li, H. Xue, and H. Pang, *Small*., 2018, 1801815.

(1.135) Y. Wang, L. Zhao, G. Ji, C. He, S. Liu, and C. Duan, *ACSAppl.Mater. Interfaces*., 2022, **14**, 2794−2804.

(1.136) J. Lv, P. Liu, F. Yang, L. Xing, D. Wang, X. Chen, H. Gao, X. Huang, Y. Lu, and G. Wang, *ACSAppl.Mater. Interfaces*., 2020, **12**, 48495−48510.

(1.137) Y. Kong, D. Xiong, C. Lu, J. Wang, T. Liu, S. Ying, X. Ma, and F.-Y. Yi, *ACS Appl. Mater. Interfaces*., 2022, **14**, 37804−37813.

(1.138) P. Kanoo, A. C. Ghosh, and T. K. Maji, *Inorg. Chem*., 2011, **50**, 5145–5152.

(1.139) L. Han, J. Xu, Y. Huang, W. Dong, X. Jia, *Chinese Chemical Letters*., 2021, **32**, 2263-2268.

(1.140) J. Rocha, F. A. A. Paz, F.-N. Shi, R. A. S. Ferreira, T. Trindade, and L. D. Carlos, *Eur. J. Inorg. Chem*., 2009, 4931–4945.

(1.141) Y. Wang, S. Cao, J. Zhao, X. Zhang, X. Du, J. Li, F. Wu, *Journal of Alloys and Compounds*., 2023, **960**, 170922.

Chapter 2

Effect of Hydrogen Bonding on the Luminescence Lifetime and Device Resistance: A Case Study Based on Two New Related Cd-Based Coordination Polymers

ABSTRACT

Two new coordination polymers of formulas $[Cd_2(2,3\text{-pzdc})(tz)_2]$ (**2.1**) and $[Cd_2(2,3\text{-pzdc})(dtz)_2]$ (**2.2**) {2,3- pzdc = 2,3-pyrazine dicarboxylate, tz = 1,2,4-triazolate, dtz = 3,5- diamino-1,2,4-triazolate)} were synthesized via hydrothermal techniques. Both the compounds were characterized by single crystal X-ray analysis, PXRD, FTIR, and TGA. Single crystal X-ray analysis shows that both the structures are three dimensional in nature and connectivity-wise they are similar to each other. In compound **2.2**, the presence of N−H···O hydrogen bond interactions further stabilized the structure. Aqueous dispersion of both the compounds showed a strong dual emission-one at around 353 nm and another at 369 nm upon excitation at 280 nm. Lifetime studies from time-resolved spectra show 0.82 and 0.60 ns for compound **2.1** and 2.02 and 1.78 ns for compound **2.2**. The higher lifetimes of the excited states in the case of compound **2.2** establish the role of hydrogen-bond interactions in reducing the nonradiative decay processes. To explore the junction properties at the Al/material interface of these Schottky barrier diodes, the dark J−V characteristics of both of the devices (ITO/PEDOT/compound **2.1**/Al and ITO/PEDOT/compound **2.2**/Al) were analyzed using the well-known Shockley diode equation. In both the devices (with compound **2.1** and compound **2.2**), asymmetric behavior is observed under forward and reverse bias, indicating rectification. However, in the compound **2.2** device, the overall current magnitude is 10 times higher than that of the compound **2.1** device. The series resistance extracted for the compound **2.2** device is ≈ 22 times lower than that of the compound **2.1** device, indicating the higher conductivity of compound **2.2**. This behavior indicates a probable role of hydrogen-bond interactions in the lower resistance and higher conductivity of compound **2.2** compared to compound **2.1**.

2.1 INTRODUCTION

Coordination polymers (CPs) are a unique class of solid crystalline materials with diverse structural features assembled by the connectivity of metal ions or metal clusters and organic ligands.[2.1] Though the covalent, coordinate, and ionic bonds are the key to form the overall structure, the stability of these structures also depends on the hydrogen bonds, π-π interactions, and other noncovalent weaker interactions.[2.2.−2.8] Over the last two decades, the research on CPs has caught attention due to their structural features and a wide range of potential applications such as gas storage, gas separation, magnetism, catalysis, drug delivery, proton conduction, and sensing.[2.8−2.36] CPs are valuable to conventional porous materials such as zeolites and carbon-based materials due to their systematic structural tuneability through the different combinations of metal ions and organic ligands.[2.37,2.38] Recently, the luminescence property of CPs has become an interesting field of research as the luminescence properties of CPs are very sensitive and depend on their structural characteristics, the coordination environment of the metal ions, the nature of the pore surface, and the presence of guest molecules.[2.39] Among the various 3d metal-based CPs, Zn- and Cd-based CPs show high intense intraligand luminescence due to the absence of d−d transitions for their d^{10} electronic configuration.[2.40] The organic part of CPs after promotion to its excited state returns to the ground state via both radiative and nonradiative pathways. When the radiative pathway is predominant, the molecule exhibits luminescence. It is important to consider that increase of the structural stability and rigidification of the feeble parts of the compounds through restriction of the rotation, hydrogen bonds, and other noncovalent interactions would marginalize the nonradiative pathway and lead to the subsequent increase of luminescence lifetime.[2.41] All of the processes that may occur between the absorption and emission of light are illustrated by the Jablonski diagram.[2.41] Upon the excitation of light, a luminophore is usually promoted to its higher electronic energy states, i.e., S_2, S_3 etc., or a higher vibrational level of S_1. Then, it rapidly loses some of its excess energy to the surroundings as heat and returns to the ground vibrational level of the first excited state (S_1), which is termed as internal conversion (IC). A similar kind of energy loss may also lead to the transfer of a singlet excited state to the triplet excited state; this radiation-less transition is called intersystem crossing (ISC). Then, the molecule from the lowest vibrational level of the S_1 or T_1 state returns to its ground state (S_0) by either nonradiative or radiative ways. Nonradiative transitions from S_1 or T_1 to S_0 are termed as IC and ISC, respectively. The radiative transition results in luminescence emission and is further distinguished by the terms fluorescence ($S_1 \rightarrow S_0$) and phosphorescence ($T_1 \rightarrow S_0$), respectively. 2,3-Pyrazinedicarboxylic acid (2,3-H_2pzdc) and its deprotonated anions perform as multifunctional ligands through six potential coordination sites using the oxygen atoms of the carboxylic groups and the nitrogen atoms of the pyrazine ring.[2.42] 2,3-H_2pzdc shows several interesting features: (a) it can be partly or completely deprotonated and forms

H_2pzdc, Hpzdc$^-$, and pzdc^{2-} to maintain the pH balance, which allows H_2pzdc to display various acid-dependent coordination modes; (b) the deviation of carboxyl groups from the plane of the pyrazine ring and the steric effect between the two adjacent carboxylates enable pzdc to link metal ions in different directions with the construction of helical structures; and (c) the flexible, multidentate coordination sites create the highest probability of the formation of a higher-dimensional structure. Since the lanthanide(III) ions show a high affinity for ligands with oxygen donors and the transition-metal ions present a strong tendency to coordinate to nitrogen donors, a ligand with nitrogen and oxygen as donor atoms, like pzdc, is an admirable candidate to get stable molecule-based architectures with both types of metal ions.[2.43] Some lanthanide(III) and transition-metal ion complexes of 2,3-pzdc in the presence of other auxiliary ligands are summarized in Table 2.1.[2.44–2.63] From the crystal engineering and structural predictability points of view, five-membered heterocycle ligands such as imidazole, pyrazole, triazole, tetrazole etc. and their derivatives have wide use as bridging ligands in neutral or anionic forms. One of such ligands, 1,2,4-triazole, can bridge two metal centers in a neutral form, or can bridge three metal centers in a trazolate form, and exhibits an extensive ability to bridge metal ions to afford polynuclear compounds with extraordinary structural diversity and facile accessibility of the new materials.[2.64–2.75] In the present work, we used 1,2,4-triazole and 3,5-diamino 1,2,4-triazole as secondary ligands. We synthesized two new three-dimensional coordination polymers, [Cd_2(2,3-pzdc)-$(tz)_2$], **2.1**, and [Cd_2(2,3-pzdc)$(dtz)_2$], **2.2**. The structures of compounds **2.1** and **2.2** were elucidated using high-resolution X-ray diffraction (SCXRD). Both the compounds have related three-dimensional structures, except for the presence of N−H···O hydrogen-bond interactions only in compound **2.2**. The additional presence of hydrogen-bond interactions plays a key role in enhancing the luminescence lifetime in compound **2.2** compared to compound **2.1**, as well as in the lower resistance and higherconductivity of compound **2.2** during their assessment for Schottky diode behaviors.

Table 2.1: A summary of 2,3-pzdc containing coordination polymers in the presence of different auxiliary ligands.

Compounds	**Dimensionality**	**Importance**	**Reference**
$[Mn(Pzdc)_2 \cdot 2H_2O]$ $[MnPzdc \cdot (H_2O)_2 \cdot 2H_2O]_n$	0 D and 1D	Magnetic properties	44
$[Cu_2Mg(pzdc)_2(H_2O)_5 \cdot 2H_2O]_n$	2D	Photoluminescence and catalytic properties	45
$Pb_2Cl_2(Hpzdc)_2(H_2O)_2$ $Pb(pzdc)(H_2O)$ $Pb_3(pzdc)_3(H_2O)$	1D, 2D and 3D	Structural transformations and cation exchange	46
$(NH_4)_2[RE_2(pzdc)_4(H_2O)_2]$ (RE = Y(1), Sm(2))	3D	Solid state photoluminescence	47
$\{[Ln_2Cd(2,3pzdc)_4(H_2O)_6] \cdot 2H_2O\}_n$ [Ln = La (1), Pr (2), Nd (3)] and $\{[Ln_2(2,3\text{-}pzdc)_3(H_2O)_5] \cdot 3H_2O\}_n$ [Ln = Eu (4), Tb (5), Dy (6), Ho (7), Er (8)]	3D	Photoluminescence and magnetic properties	48
$[Zn(pzdc) \cdot 3H_2O] \cdot H_2O$ (1), $[Zn_2(pzdc)_2 \cdot 4H_2O] \cdot 2.5H_2O$ (2), and $[Zn(pzdc)(phen) \cdot 4H_2O]_n$ (3)	1D	Solid state photoluminescence	49
$[Ag_4(pzdc)_2] \cdot H_2O$ (1), and $[Gd_2Ag_6(pzdc)_6(H_2O)_9] \cdot 8H_2O$ (2) and $[LnAg(pzdc)_2(H_2O)_2] \cdot 2H_2O$ [Ln = Tb (3), Dy (4), Ho (5), Er (6)]	3D and 2D	Magnetic Properties	50
$[Ln_2(2,3\text{-}pzdc)_2(ox)(H_2O)_2]_n$ [Ln(III) = Ce, Nd, Sm, Eu, Gd, Tb, or Er].	2D	Photoluminescence	51
$\{[Cu_2(\mu\text{-}Cl)_2(\mu_3\text{-}Hpzdc)(Cl)(H_2O)_2] \cdot 1.5H_2O\}_n$ (1) and $\{[Cd(\mu\text{-}Cl)(\mu\text{-}Hpzdc)] \cdot H_2O\}_n$ (2)	3D and 2D	Solid state photoluminescence; H_2 and CH_4 adsorption	52
$Cu_2(pzdc)_2(bix)$	3D	CO_2 adsorption	53
$[Co(\mu\text{-}pzdc)(H_2O)\ (2\text{-}meim)_2]_n$ (1), $[Cu(pzdc)(2\text{-}meim)_3].DMF$ (2), $\{[Cu(\mu_3\text{-}pzdc)\ (2\text{-}meim)_2Cu(\mu\text{-}pzdc)(2\text{-}meim)].CH_3OH.2H_2O\}_n$ (3), $[Zn(\mu\text{-}pzdc)(H_2O)_3]_n$ (4), $\{[Zn(\mu\text{-}pzdc)(NH_3)_2(H_2O)].H_2O\}_n$ (5), $\{[Cd(\mu\text{-}pzdc)\ (im)_3].0.13H_2O\}_n$ (6), $\{[Cd(\mu\text{-}pzdc)(N\text{-}mim)_3].3H_2O\}_n$ (7) and $[Cd(\mu\text{-}pzdc)(2\text{-}meim)_3]_n$ (8).	1D and 0 D	Hydrogen gas adsorption, photoluminescence and antimicrobial activities	54
$Cu_2(pzdc)_2(bpp)$	3D	N_2 and CO_2 adsorption	55
Cu(pzdc)(pia)	3D	Effect of lithium incorporation into the framework to enhance	56

		CO_2 adsorption	
$Tb_2(2,3\text{-pzdc})_2(ox)(H_2O)_2]_n$	3D	Sensing of cytidine triphosphate	57
$\{[Cu_2(pyzdc)].0.83H_2O\}_n$	3D	Single-crystal-to-single-crystal structural transformation and small molecules adsorption	58
$Cu_2(pzdc)_2(bpy)$	3D	Hysteretic adsorption–desorption process of CO_2	59
$\{Cu_2(pzdc)_2(bpy)\}$	3D	Thermally induced changes in CPs using DSC, XRD and NMR	60
$[Cu_2(pzdc)_2(pyrazine)]_n$	3D	Ethylene/Ethane separation	61
$\{[Cu_2(pzdc)_2(bpy)],G\}$	3D	Adsorption of nitrogen, benzene, and water	62
$[Cd(pzdc)(phen)] \cdot H_2O$ (**1**), $Cd_2(pzdc)_2(4,4'\text{-bpy})(H_2O)_2$ (**2**) and $[Cu_4(pzdc)_4(phen)_2(H_2O)_4] \cdot 10H_2O$ (**3**)	1D and 2D	Solid state photoluminescence	63

2.2 EXPERIMENTAL SECTION

2.2.1 Materials. The required chemicals for the synthesis of compound **2.1** and **2.2**, $Cd(OAc)_2 \cdot 2H_2O$ (Sigma-Aldrich, 98%), 2,5-pyrazinedicarboxylic acid (Aldrich, 98%), 3,5-Diamino-1,2,4-triazole (Aldrich, 97%), 1,2,4-triazole (Aldrich, 97%) and NaOH (Merck, 97%) were used as received without further purification. The water used was double distilled.

2.2.2 Synthesis of compound 2.1. Compound **2.1** was prepared by employing hydrothermal method. $Cd(OAc)_2 \cdot 2H_2O$ (0.06799 g, 0.25 mM), 2,3-pyrazinedicarboxylic acid (0.04332 g, 0.25 mM) were dispersed in 5 mL water. 1,2,4-triazole (0.0176 g, 0.25mM) and NaOH (0.02 g, 0.5 mM) were added with continuous stirring, and the mixture was homogenized at room temperature for 30 min. The final reaction mixture was sealed in a 23 mL polytetrafluoroethylene-lined stainless-steel autoclave and heated at 180°C for 72 h. The initial pH value of the reaction mixture was 6, and no appreciable change in pH was noted after the reaction. The final product containing

large quantities of octahedral-shaped crystals, was filtered, washed with deionized water under vacuum, and dried at ambient conditions (see Fig. 2.1).

Fig. 2.1 Image of single crystal of $[Cd_2(2,3\text{-pzdc})(tz)_2]$, **2.1.**

2.2.3 Synthesis of compound 2.2. Compound **2.2** was prepared by employing a similar experimental condition. For this purpose, $Cd(OAc)_2{\cdot}2H_2O$ (0.06799 g, 0.25 mM), 2,3-pyrazinedicarboxylic acid (0.02166 g, 0.125 mM) were dispersed in 3 mL water and 3,5-Diamino-1,2,4-triazole (0.02527 g, 0.25mM) and NaOH (0.01 g, 0.25 mM) were added with continuous stirring, and the mixture was homogenized at room temperature for 30 min. The final reaction mixture was sealed in a 6 mL polytetrafluoroethylene-lined stainless-steel autoclave and heated at 180 °C for 96 h. The initial pH value of the reaction mixture was 6, and no appreciable change in pH was noted after the reaction. The final product, containing large quantities of orange-coloured block-shaped crystals, was filtered, washed with deionized water under vacuum, and dried at ambient conditions (see Fig. 2.2).

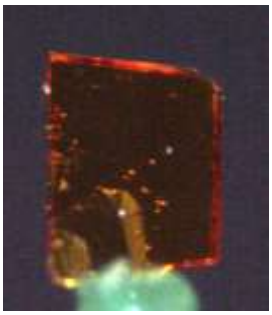

Fig. 2.2 Image of single crystal of $[Cd_2(2,3\text{-pzdc})(dtz)_2]$, **2.2.**

2.2.4 Instrumentations. Powder X-ray diffraction (XRD) patterns were recorded on well- grinded samples in the 2θ range 5-50º using Bruker D8 Advance X-ray diffractometer with Cu Kα radiation (λ= 1.5418 Å) operating at 40 kV and 40 mA. The FTIR Spectrum (400-4000 cm^{-1}) of the both compounds were noted using KBr pellets (Nicolet Magna IR 750 series-II). Thermogravimetric analysis (TGA) of the both compounds were carried out under

nitrogen atmosphere (flow rate = 20 ml min^{-1}) using a PerkinElmer Diamond instrument (STA 6000) in the temperature range of 40–850 °C (heating rate = 20 °C min^{-1}).

2.2.5 Single-Crystal Structure determination of compound 2.1 and 2.2. Suitable single crystals of [Cd_2(2,3-pzdc)$(tz)_2$], **2.1** and [Cd_2(2,3- pzdc)$(3,5\text{-dtz})_2$**], 2.2,** were carefully selected under a polarising microscope and glued carefully to a thin glass fiber. The single crystal data were collected using Bruker D8 Quest machine. The X-ray generator was operated at 50 kV and 1 mA using Mo Kα (λ=0.71073Å) radiation. Data were collected with ω scan width of 0.5º. A total of 408 frames were collected in three different setting of φ (0, 90, 180º) keeping sample-to-detector distance fixed at 6.03 cm and the detector position (2θ) fixed at -25º. The final data sets were reduced by an APEX3 program, while a SAINTPLUS[2.76] program was utilized for the integration of diffraction profiles. The absorption correction (multi-scan) was carried out by a SADABS program.[2.77] We initially solved the structure by SIR 92,[2.78] and the full matrix least-square method (SHELXL-2016[2.79]) was used further, which is present in the WinGx suit of programs (Version 1.63.04a).[2.80,2.81] We successfully located all the non-hydrogen atoms from Fourier maps and refined them with anisotropic displacement parameters at the final cycles. Finally, we fixed all the hydrogen atoms at calculated positions and included them in the refinement process using riding model associated with isotropic thermal parameters. Details of the structure solution and final refinement is given in the Table 2.2.

Table 2.2: Crystal Data and Structure Refinement Parameters of compound **2.1** and **2.2**.

Parameters	Compound **2.1**	Compound **2.2**
Empirical formula	$C_5H_3CdN_4O_2$	$C_{10}H_{10}Cd_2N_{12}O_4$
Formula weight	263.51	587.10
Crystal system	Tetragonal	Tetragonal
Space group	$P4_32_12$	$P4_1$
a(Å)	7.8420(5)	7.6531(5)
b(Å)	7.8420(5)	7.6531(5)
c(Å)	25.1314(18)	26.0055(18)
α(deg)	90	90
β (deg)	90	90
γ (deg)	90	90
Volume($Å^3$)	1545.5(2)	1523.1(2)
Z	8	4
Calculated density, ρ_{calc}(g cm^{-3})	2.265	2.560
Absorption coefficient, μ (mm^{-1})	2.786	2.848
Temperature (K)	273(2)	273(2)
Wavelength(Mo Kα) (Å)	0.71073	0.71073
θ range (deg)	2.721 to 27.112	2.661 to 27.103
Final R indices [I>2sigma(I)]	R_1 = 0.0334, wR_2 = 0.0857	R_1 = 0.0316, wR_2 = 0.0892
R indices (all data)	R_1 = 0.0340, wR_2 = 0.0859	R_1 = 0.0326, wR_2 = 0.0986

$R_1=\Sigma||F_0|-|F_c||/\Sigma|F_0|$; $wR_2= \{\Sigma [w(F_0^2-F_c^2)^2]/\Sigma [w(F_0^2)^2]\}^{1/2}$,$w=1/[\sigma^2(F_0)^2+ (aP)^2+ bP]$;

$P= [max. (F_0,0)^2 +2(F_c)^2]/3$ where a = 0.0375, b = 5.1344 for **2.1** and a = 0.0436, b = 3.5377 for **2.2** .

2.2.6 Photoluminescence measurements. Photoluminescence (PL) spectra of compound **2.1** and **2.2** were recorded at room temperature in aqueous media using a Horiba FluoroMax4 spectrofluorometer. The dispersions of compound **2.1** was prepared by using 2.6 mg of compound **2.1** in 2.6 mL distilled water and performing ultrasonic agitation for 10 minutes. The dispersions of compound **2.2** was prepared by using 3 mg of compound **2.2** in 3 mL distilled water and performing ultrasonic agitation for 10 minutes and staying this both dispersed solution of compound **2.1** and **2.2** for one day, then performed photoluminescence studies. The solution of 2,3- pyrazine dicarboxylic acid was prepared by dissolving 4.4 mg of 2,3-$pzdcH_2$ in 4.4 mL distilled water. The solution of 1,2,4-

triazole and 3,5-diamino 1,2,4- triazole were prepared by using 4.1 mg of 1,2,4- triazole and 5.7 mg of 3,5- diamino 1,2,4- triazole in 4.1 mL and 5.7 mL of distilled water, then performed photoluminescence studies. Each photoluminescence titrations were carried out using 400 µL of the above stock solution with 2 mL distilled water taken in a quartz cuvette. UV-Vis spectra of compound **2.1** and compound **2.2** were checked using UV-Vis-spectrofluorometer SHIMADZU (UV-1900i). Time-correlated single photon counting (TCSPC) measurements were carried out at room temperature in water using HORIBA Jobin-Yvon instrument in the nanosecond time domain. For TCSPC measurement, the excitation wavelength was selected at 280 nm and emission decays curve monitored at 353 nm and 369 nm in the both compound. The photoluminescence lifetime decays were collected on a Hamamatsu MCP photomultiplier (R3809). All the decays were deconvoluted and fitted with exponential function using IBH DAS6 software.

2.2.7 Device Fabrication using compound 2.1 and 2.2. Initially, Indium Tin Oxide (ITO) coated glass substrates were cleaned with soap solution followed by rinsing in deionized water in ultrasonicator bath for 15 to 20 minutes. ITO substrates were subsequently sonicated in acetone and isopropanol for 10 minutes each and dried by flushing with air. Finally, substrates were treated in UV-Ozone chamber (Holmarc, HO-TH-UVT) for 30 minutes to make the ITO surface hydrophilic and remove any organic impurities. DMSO was used as a solvent for these materials and the mixture was sonicated for long time to form a stable dispersion (≈ 60 mg/mL). PEDOT: PSS was spin coated on ITO at 2000 rpm for 60sec and was annealed at 100 °C to evaporate the remaining water. Prepared solution was then spun at 600 rpm for 60 sec followed by 2000 rpm for 60sec and annealed for few seconds in air on a hot plate to evaporate the solvent. The spin coating routine was repeated few times to make a thick uniform film (≈ 1 µm) free of any pinhole. Schottky diode device configuration, ITO/PEDOT/**2.1**/Al and ITO/PEDOT/ **2.2** /Al, were completed by slow evaporation of Al (0.2Å/s) through shadow mask under high vacuum (≈10^{-5} mbar) condition.

2.2.8 Device Measurement. Current voltage was performed in air ambient using a source meter unit (Ossila) under dark condition in the voltage range +10V to -10 V.

2.3 RESULTS AND DISCUSSION

2.3.1 Structure of compound 2.1. The asymmetric unit of compound **2.1** consists of one crystallographically independent Cd^{2+} ion, half pyrazine-2,3-dicarboxylate (2,3-pzdc) and one 1,2,4-triazolate (tz) (Fig. 2.3). The Cd^{2+} ion is coordinated by two oxygen atoms of carboxylates of 2,3-pzdc, three nitrogen atoms of tz ligands and one nitrogen atom of pyrazine ring (2,3-pzdc) and has a distorted octahedral geometry (see Fig. 2.4a). Each pyrazine-2,3-dicarboxylate connects four Cd^{2+} ions through the two carboxylates groups and two nitrogen atoms of the

pyrazine ring (see Fig. 2.4b). The Cd−O bonds have an average distance of 2.41 Å and the Cd–N bonds have an average distance of 2.31 Å. The O/N-Cd-O/N bond angles are in the range of 68.2(2) - 176.3(3)°. The selected bond distances and angles for compound **2.1** are listed in table 3 and 4.

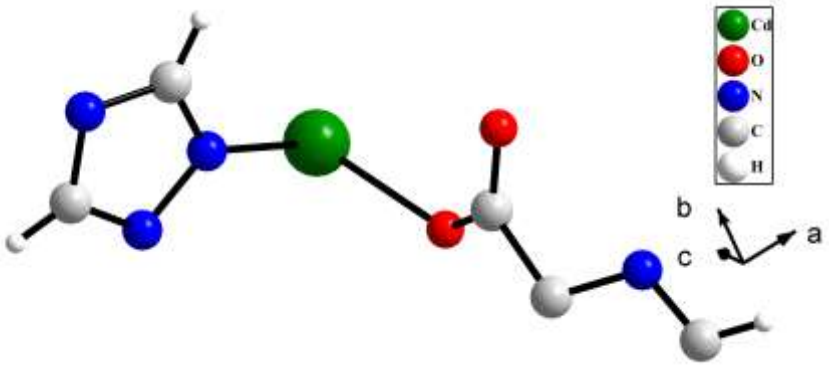

Fig. 2.3 The asymmetric unit of $[Cd_2(2,3\text{-pzdc})(tz)_2]$, **2.1**.

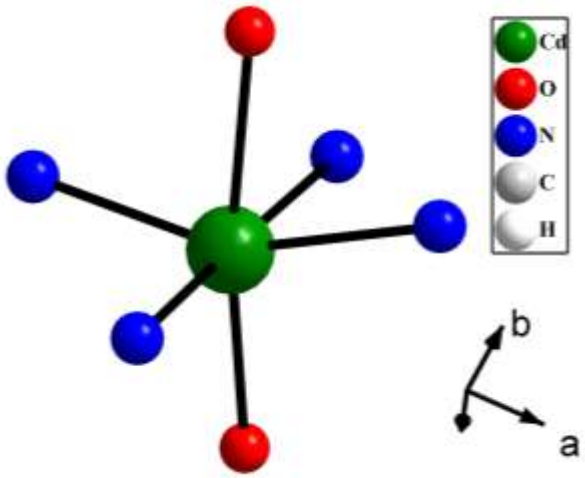

(a)

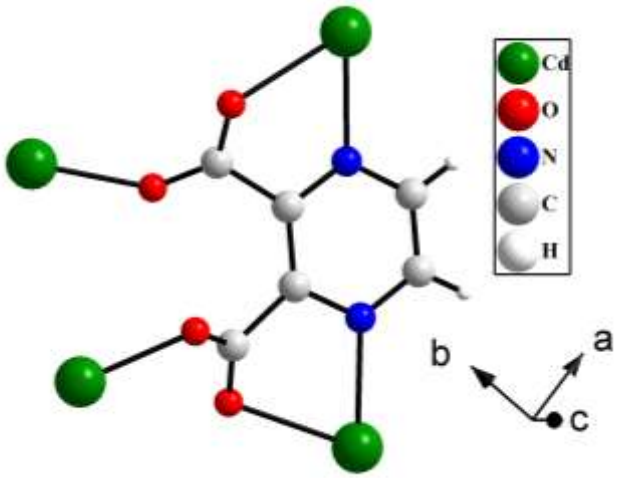

(b)

Fig. 2.4 (a) Coordination geometry around Cd^{2+} ion in $[Cd_2(2,3\text{-pzdc})(tz)_2]$, **2.1**. (b) Binding modes of 2,3-pzdc ligand in **2.1**.

Table 2.3: Selected bond distances (Å) observed in compound **2.1**.

Compound **2.1**			
Bond	Distance	Bond	Distance
Cd(1)-O(1)	2.309(6)	Cd(1)-N(2)	2.272(6)
Cd(1)-O(2)#3	2.503(6)	Cd(1)-N(3)#1	2.283(7)
Cd(1)-N(1)#3	2.364(6)	Cd(1)-N(4)#2	2.304(7)

Symmetry transformations used to generate equivalent atoms:

For **2.1**: #1 -y+1,-x+1,-z+1/2; #2 -y+3/2,x+1/2,z-1/4; #3 -y+1,-x+2,-z+1/2.

Table 2.4: Selected bond angles observed in compound **2.1**.

Compound **2.1**			
Angle	Amplitude (º)	Angle	Amplitude (º)
N(2)-Cd(1)-N(3)#1	94.6(2)	N(4)#2-Cd(1)-N(1)#3	84.4(3)
N(2)-Cd(1)-N(4)#2	176.3(3)	O(1)-Cd(1)-N(1)#3	105.0(2)
N(3)#1-Cd(1)-N(4)#2	88.4(3)	N(2)-Cd(1)-O(2)#3	88.8(3)
N(2)-Cd(1)-O(1)	96.1(3)	N(3)#1-Cd(1)-O(2)#3	88.2(3)
N(3)#1-Cd(1)-O(1)	97.9(3)	N(4)#2-Cd(1)-O(2)#3	89.2(3)
N(4)#2-Cd(1)-O(1)	85.5(2)	O(1)-Cd(1)-O(2)#3	171.8(2)
N(2)-Cd(1)-N(1)#3	92.0(2)	N(1)#3-Cd(1)-O(2)#3	68.2(2)
N(3)#1-Cd(1)-N(1)#3	155.3(3)		

Symmetry transformations used to generate equivalent atoms:

For **2.1**: #1 -y+1,-x+1,-z+1/2; #2 -y+3/2,x+1/2,z-1/4; #3 -y+1,-x+2,-z+1/2.

In this structure, Cd^{2+} ions are connected by 2,3-pzdc ligands to generate a two-dimensional structure (Fig. 2.5a). Based on the connectivity between these two, the structure can be reduced to 4,4'-topology where 2,3-pzdc acts as a four connected node (Fig. 2.5b). The two-dimensional structures are connected by tz ligands to form overall three-dimensional structure (Fig. 2.6).

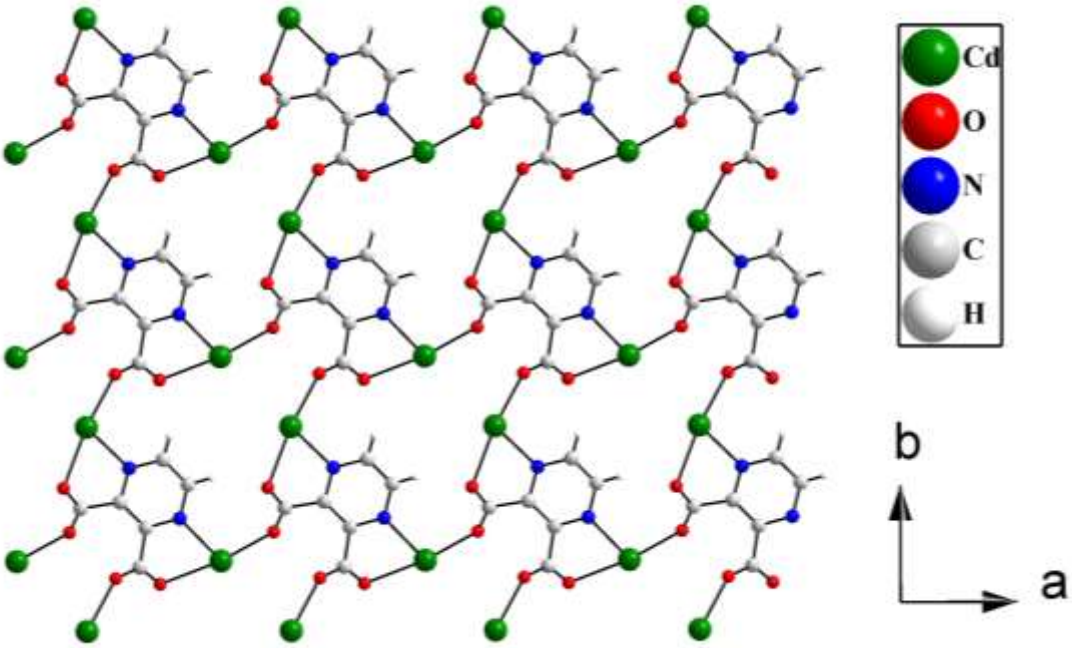

(a)

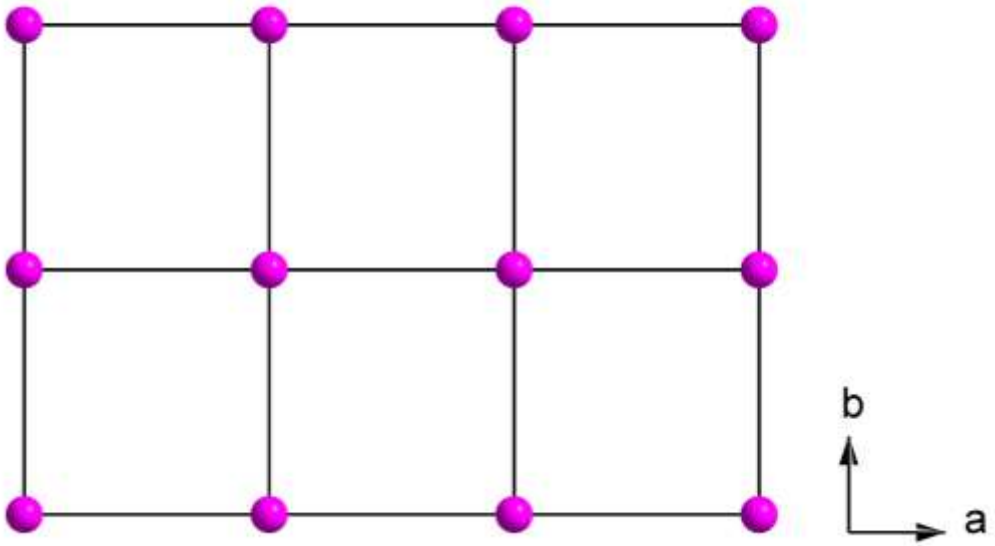

(b)

Fig. 2.5 (a) The two-dimensional connectivity between Cd^{2+} ions and 2,3-pzdc ligands in $[Cd_2(2,3\text{-pzdc})(tz)_2]$, **2.1**, in the *ab* plane. (b) Formation of 4,4-' network topology based on 4-connected 2,3-pydz nodes (shown as purple spheres)

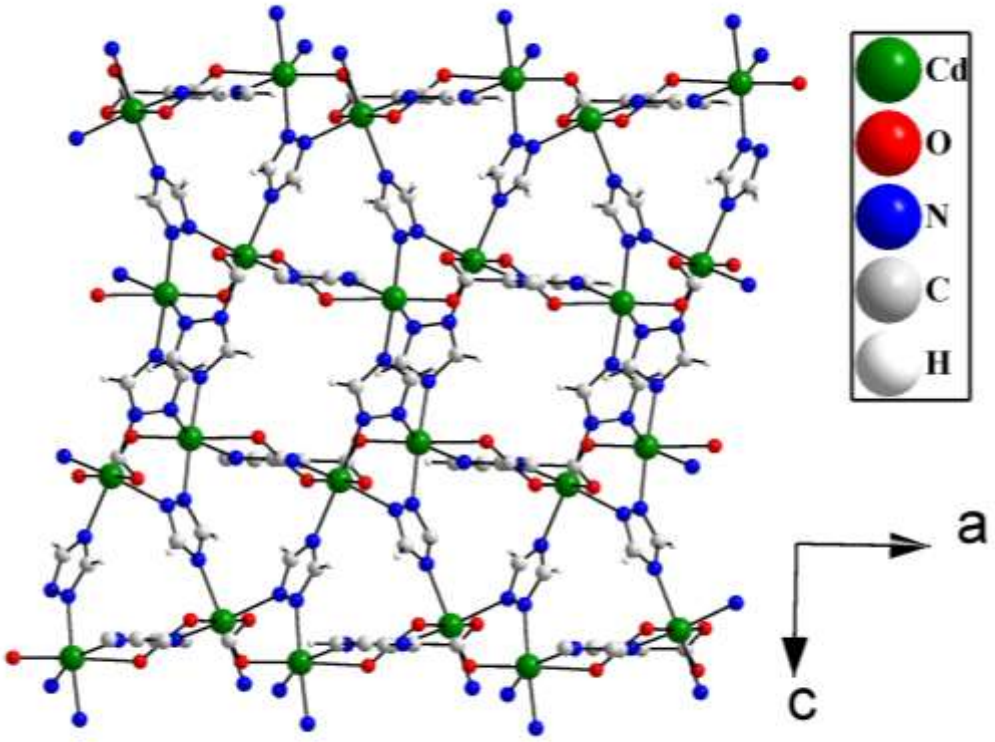

Fig. 2.6 Figure shows three-dimensional structure in $[Cd_2(2,3\text{-pzdc})(tz)_2]$, **2.1**, where the layers are connected by tz ligands to form pillared layer structure.

2.3.2 Structure of compound 2.2. The asymmetric unit of compound **2.2** consists of two crystallographically independent Cd^{2+} ions, one pyrazine-2,3-dicarboxylate (2,3-pzdc) and two 3,5-diamino-1,2,4-triazolates (dtz) (Fig. 2.7). Both the Cd^{2+} ions are coordinated by two oxygen atoms of carboxylates of 2,3-pzdc, three nitrogen atoms of tz ligands and one nitrogen atom of pyrazine ring (2,3-pzdc) and has a distorted octahedral geometry (see Fig. 2.8a). Each pyrazine-2,3-dicarboxylate connects four Cd^{2+} ions through the two carboxylates groups and two nitrogen atoms of the pyrazine ring (see Fig. 2.8b). The Cd−O bonds have an average distance of 2.44 Å and the Cd–N bonds have an average distance of 2.33 Å. The O/N-Cd-O/N bond angles are in the range of 66.9(3)- 172.7(3)°. The selected bond distances and angles for compound **2.2** are listed in table 5 and 6.

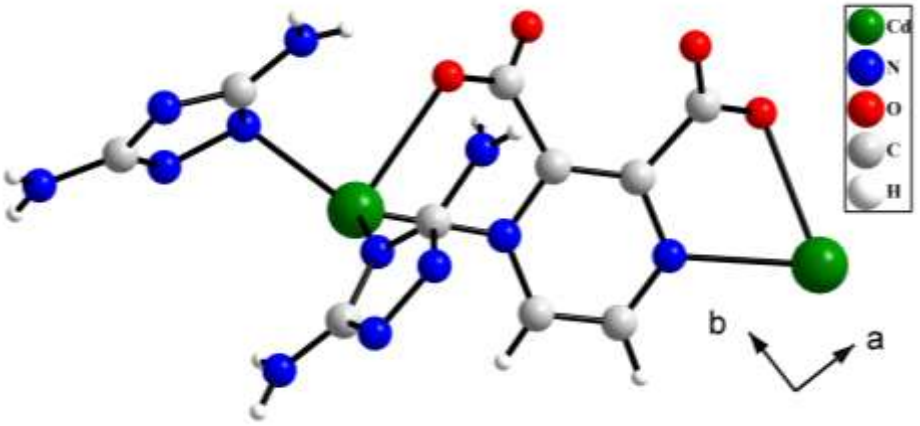

Fig. 2.7 The asymmetric unit of $[Cd_2(2,3\text{-pzdc})(dtz)_2]$, **2.2**.

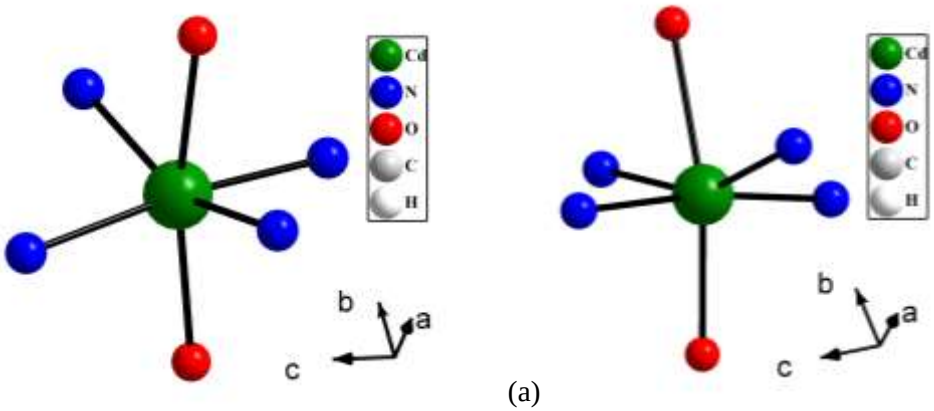

(a)

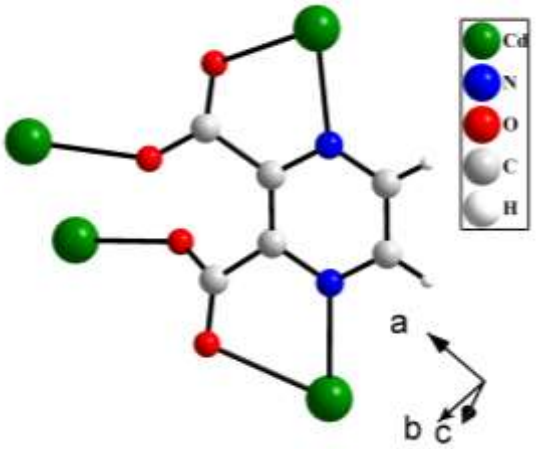

(b)

Fig. 2.8 (a) Coordination geometry around Cd^{2+} ions [Cd(1) in left and Cd(2) in right] in $[Cd_2(2,3\text{-pzdc})(dtz)_2]$, **2.2**. (b) Binding modes of 2,3-pzdc ligand in **2.2**.

Table 2.5: Selected bond distances (Å) observed in compound **2.2**.

Compound **2.2**			
Bond	Distance	Bond	Distance
Cd(1)−O(1)	2.552(8)	Cd(2)−O(2)#5	2.324(8)
Cd(1)−O(3)#2	2.322(8)	Cd(2)−O(4)	2.559(8)
Cd(1) −N(1)	2.401(10)	Cd(2)−N(2)	2.402(10)
Cd(1)−N(5)	2.336(9)	Cd(2)−N(7)#3	2.281(9)
Cd(1)−N(6)#1	2.295(9)	Cd(2)−N(9)#4	2.297(8)
Cd(1)−N(8)	2.274(9)	Cd(2)−N(10)#6	2.350(9)

Symmetry transformations used to generate equivalent atoms:

For **2.2**: #1 y,-x+1,z-1/4; #2 x-1,y,z; #3 y+1,-x,z-1/4; #4 x+1,y-1,z; #5 x,y-1,z; #6 y,-x,z-1/4

Table 2.6: Selected bond angles observed in compound **2.2**.

Compound **2.2**			
Angle	Amplitude (º)	Angle	Amplitude (º)
N(8)-Cd(1)-N(6)#1	90.9(3)	N(7)#3-Cd(2)-N(9)#4	90.9(3)
N(8)-Cd(1)-O(3)#2	110.9(3)	N(7)#3-Cd(2)-O(2)#5	111.2(3)
N(6)#1-Cd(1)-O(3)#2	86.1(3)	N(9)#4-Cd(2)-O(2)#5	86.6(3)
N(8)-Cd(1)-N(5)	91.2(3)	N(7)#3-Cd(2)-N(10)#6	91.1(3)
N(6)#1-Cd(1)-N(5)	172.7(3)	N(9)#4-Cd(2)-N(10)#6	172.6(3)
O(3)#2-Cd(1)-N(5)	86.6(3)	O(2)#5-Cd(2)-N(10)#6	86.0(3)
N(8)-Cd(1)-N(1)	153.3(3)	N(7)#3-Cd(2)-N(2)	153.2(3)
N(6)#1-Cd(1)-N(1)	90.8(3)	N(9)#4-Cd(2)-N(2)	90.8(3)
O(3)#2-Cd(1)-N(1)	95.9(3)	O(2)#5-Cd(2)-N(2)	95.5(3)
N(5)-Cd(1)-N(1)	90.5(3)	N(10)#6-Cd(2)-N(2)	90.6(3)
N(8)-Cd(1)-O(1)	86.4(3)	N(7)#3-Cd(2)-O(4)	86.0(3)
N(6)#1-Cd(1)-O(1)	93.3(3)	N(9)#4-Cd(2)-O(4)	93.9(3)
O(3)#2-Cd(1)-O(1)	162.8(3)	O(2)#5-Cd(2)-O(4)	162.7(3)
N(5)-Cd(1)-O(1)	93.8(3)	N(10)#6-Cd(2)-O(4)	93.4(3)
N(1)-Cd(1)-O(1)	66.9(3)	N(2)-Cd(2)-O(4)	67.2(3)

Symmetry transformations used to generate equivalent atoms:

For **2.2**: #1 y,-x+1,z-1/4; #2 x-1,y,z; #3 y+1,-x,z-1/4; #4 x+1,y-1,z; #5 x,y-1,z; #6 y,-x,z-1/4

In this structure, Cd^{2+} ions are by 2,3-pzdc to generate a two-dimensional structure similar to **2.1** (see Fig. 2.9a). Based on the connectivity between these two, the structure can also be reduced to 4,4'-topology where 2,3-pzdc acts as a four connected node (see Fig. 2.9b). The two-dimensional structures are connected by dtz ligands to form overall three-dimensional structure (Fig. 2.10).

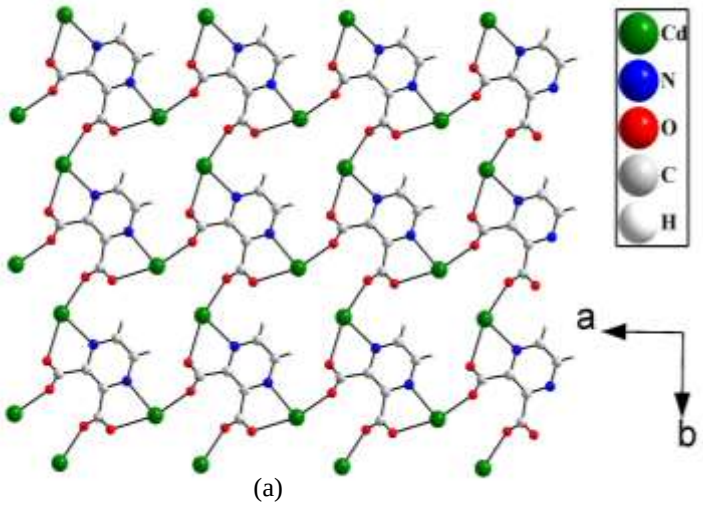

(a)

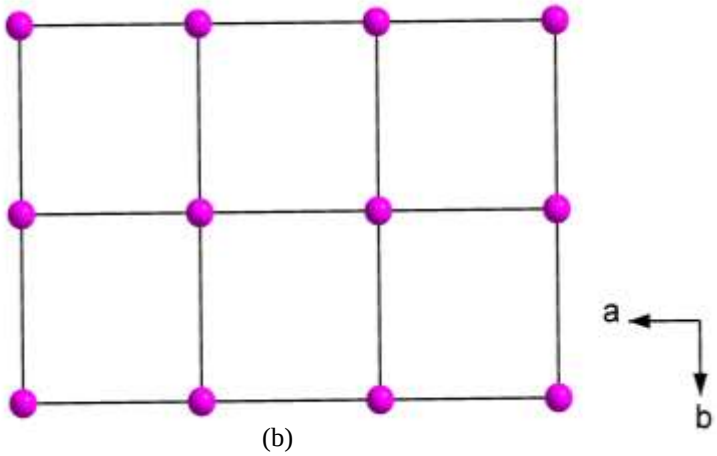

(b)

Fig. 2.9 (a) The two-dimensional connectivity between Cd^{2+} ions and 2,3-pzdc ligands in $[Cd_2(2,3\text{-pzdc})(dtz)_2]$, **2.2**, in the *ab* plane. (b) Formation of 4,4-' network topology based on 4-connected 2,3-pydz nodes (shown as purple spheres)

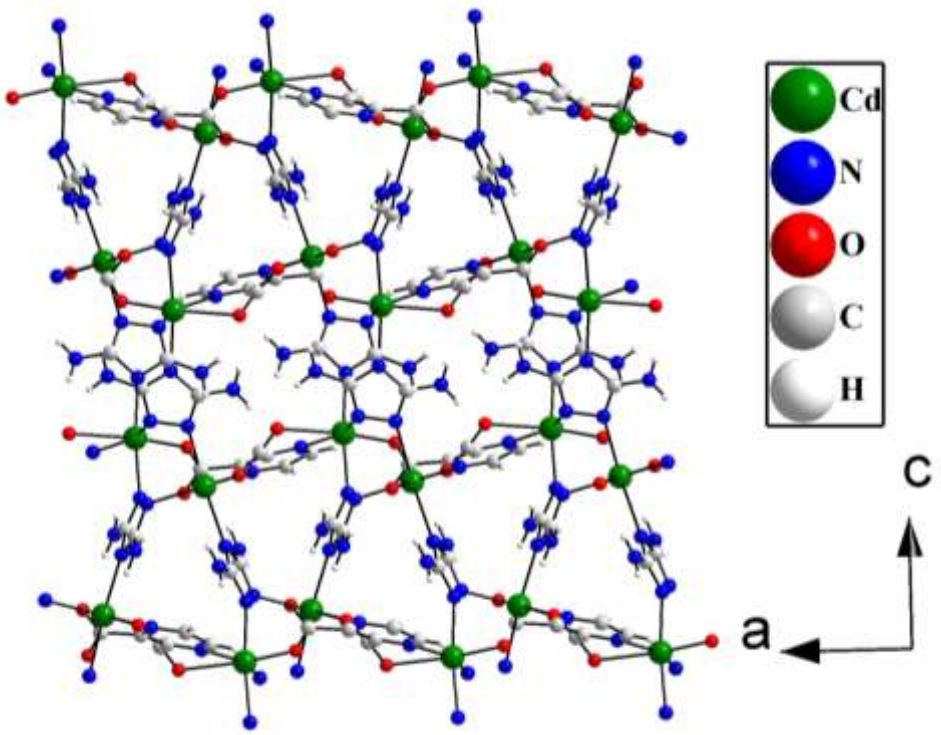

Fig. 2.10 Figure shows three-dimensional structure in $[Cd_2(2,3\text{-pzdc})(dtz)_2]$, **2.2**, where the layers are connected by dtz ligands to form pillared layers structure.

Additionally, the presence of N-H….O hydrogen bond interactions originated from amino groups of dtz ligand and carboxylate oxygens of the 2,3-pzdc ligand stabilized the structure further (Fig. 2.11). A complete list of these interactions is given in table 7.

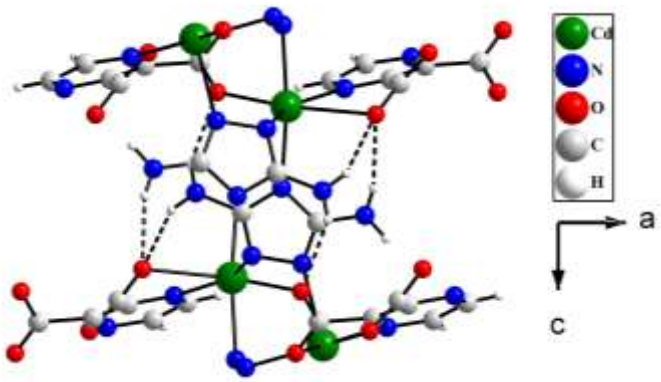

Fig. 2.11 Figure shows the connectivity between two layers through the dtz ligands in $[Cd_2(2,3\text{-pzdc})(dtz)_2]$, **2.2**. Dotted lines represent hydrogen-bond interactions.

Table 2.7: Selected hydrogen-bond interaction in $[Cd_2(2,3\text{-pzdc})(dtz)_2]$, **2.2**.

D – H….A[a]	D – H (Å)	H….A (Å)	D….A (Å)	D – H ….A (°)
N(3) --H(3A) ..O(4)#1	0.86	2.37	3.1374	149
N(3) --H(3B) ..O(3)#2	0.86	2.11	2.8003	137
N(4) --H(4B) ..O(1)	0.86	2.19	3.0271	166
N(11) --H(11A) ..O(1)	0.86	2.38	3.1498	149
N(11) --H(11B) ..O(2)#3	0.86	2.12	2.8009	136
N(12) --H(12B) ..O(4)#4	0.86	2.16	3.0002	165

[a] #1 -y,1+x,1/4+z; #2 x,1+y,z; #3 1-y,x,1/4+z; #4 1-y,1+x,1/4+z

2.3.3 Structural Comparison. If we consider between the double asymmetric unit of compound **2.1** (z = 8) and single asymmetric unit of compound **2.2** (z = 4), then we can say that only difference is the presence of the two amino group of dtz ligands in compound **2.2**. From the table **2.2**, it important to note that both the compound crystallised in same crystal system *i.e.* tetragonal. Compound **2.1** is longer around 0.19 Å along *a* and *b* axis whereas compound **2.2** is longer around 0.87 Å along *c* axis. In overall, the presence of amino groups and the originated hydrogen bond interactions probably is the factor for the reduced volume of compound **2.2** than compound **2.1** (1545.5 $Å^3$ for **2.1** and 1523.1 $Å^3$ for **2.2**).

2.3.4 Initial Characterizations. Powder X-ray diffraction (XRD) patterns were recorded on well-grinded compounds (**2.1** and **2.2**) in the 2θ range of 5−50° (see Fig. 2.12 and Fig. 2.13). The experimental XRD patterns indicated that the new products are in excellent harmony with the simulated XRD patterns generated from single-crystal X-ray diffraction data. The FTIR spectrum of both the compounds was recorded in the spectral range 4000−500 cm−1 (see Fig. 2.14). Thermogravimetric analysis (TGA) of both the compounds was carried out in nitrogen atmosphere from 30 to 700 °C with a heating rate of 20 °C min−1 (see Fig. 2.15). Compound **2.1** shows a mass loss in three steps (at 104, 419, and 468 °C), whereas compound **2.2** shows the mass loss in two steps (at 450 and 534 °C; see Fig. 2.15). The final decomposition temperature of compound **2.2** is higher than that of compound **2.1**. This indicates a higher thermal stability of compound **2.2**.

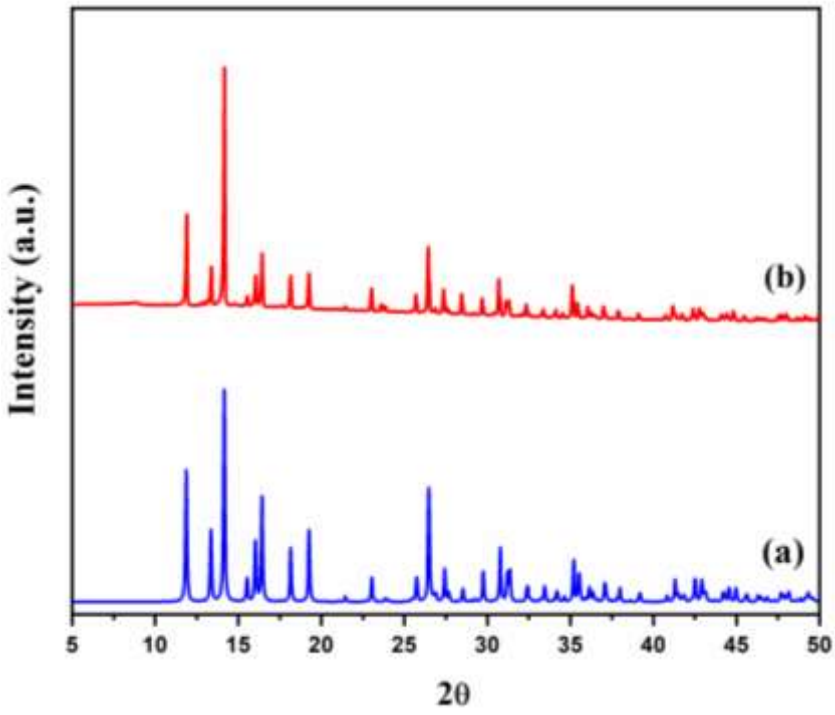

Fig. 2.12 Powder XRD (CuKα) patterns of $[Cd_2(2,3\text{-pzdc})(tz)_2]$, **2.1**: (a) simulated from single crystal X-ray data, (b) experimental.

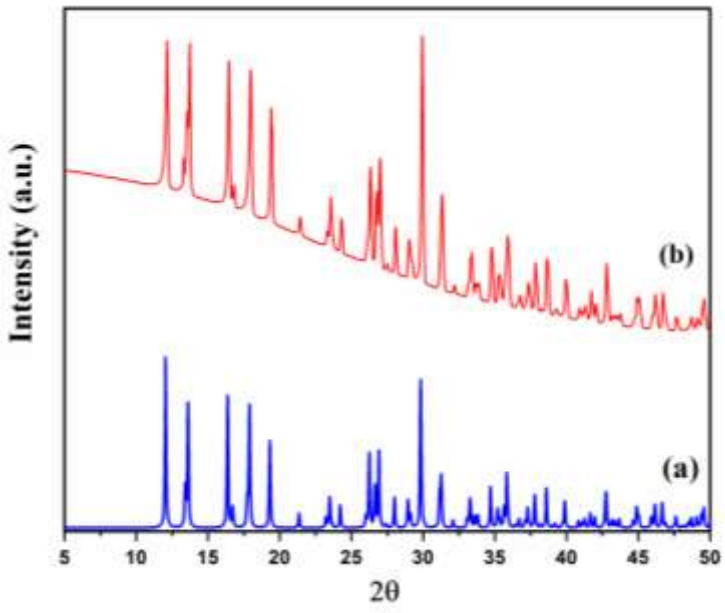

Fig. 2.13 Powder XRD (CuKα) patterns of $[Cd_2(2,3\text{-pzdc})(dtz)_2]$, **2.2**: (a) simulated from single crystal X-ray data, (b) experimental.

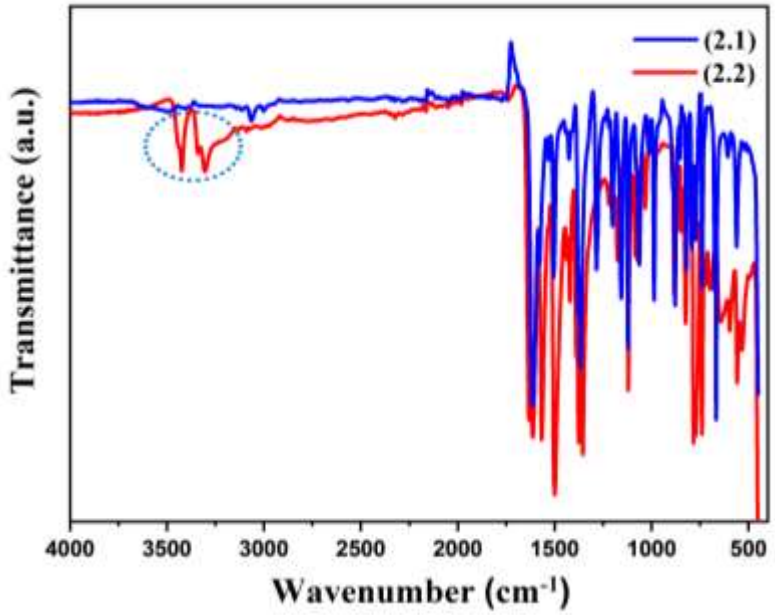

Fig. 2.14 IR spectrum of [Cd_2(2,3-pzdc)$(tz)_2$], **2.1,** and [Cd_2(2,3-pzdc)$(dtz)_2$], **2.2**. The encircled areas denote the presence of free amine groups in compound **2.2**.

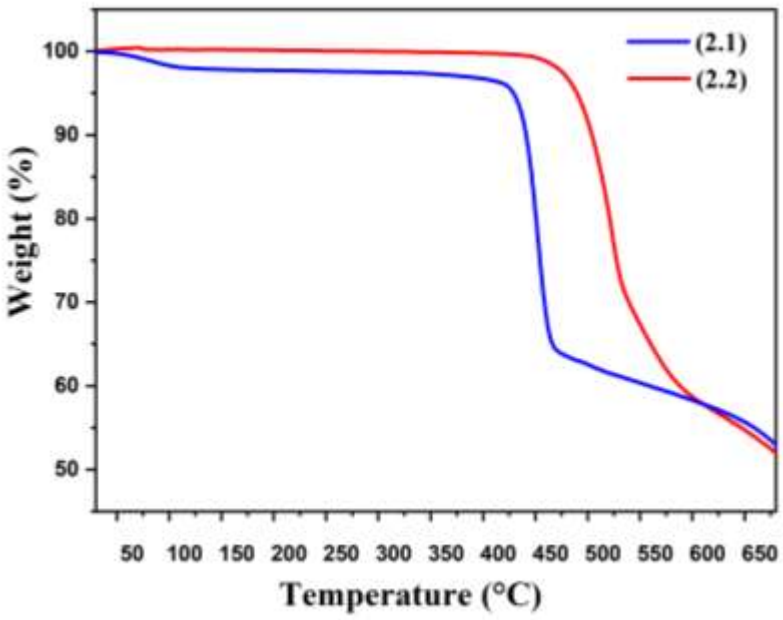

Fig. 2.15 Thermogravimetric analysis (TGA) of [Cd_2(2,3-pzdc)$(tz)_2$], **2.1,** and [Cd_2(2,3-pzdc)$(dtz)_2$], **2.2** in nitrogen atmosphere.

2.3.5 Photoluminescence behaviour of compound 2.1 and 2.2. The absorption spectra of both the compounds were measured by using their aqueous dispersion (see Fig. 2.16). The photoluminescence properties were investigated by using their aqueous dispersion upon excitation at 280 nm. Both the compounds show strong duel emission, one emission around 353 nm another one is 369 nm (see Fig. 2.17 and Fig. 2.18). It is common that coordination polymers with d^{10} metal ions such as Cd^{2+} and π-conjugated aromatic organic ligands show excellent photoluminescence property. The emission behaviours of all the ligands are weak and broad in nature. Both emission peaks of the two compounds can be assigned as intra-ligand luminescence. Lifetime measurement of the excited states corresponds to the two emissions (353 nm and 369 nm) show lifetime in the range of nanosecond (see Fig. 2.19). The detailed of the lifetime measurement are shown in table 8.

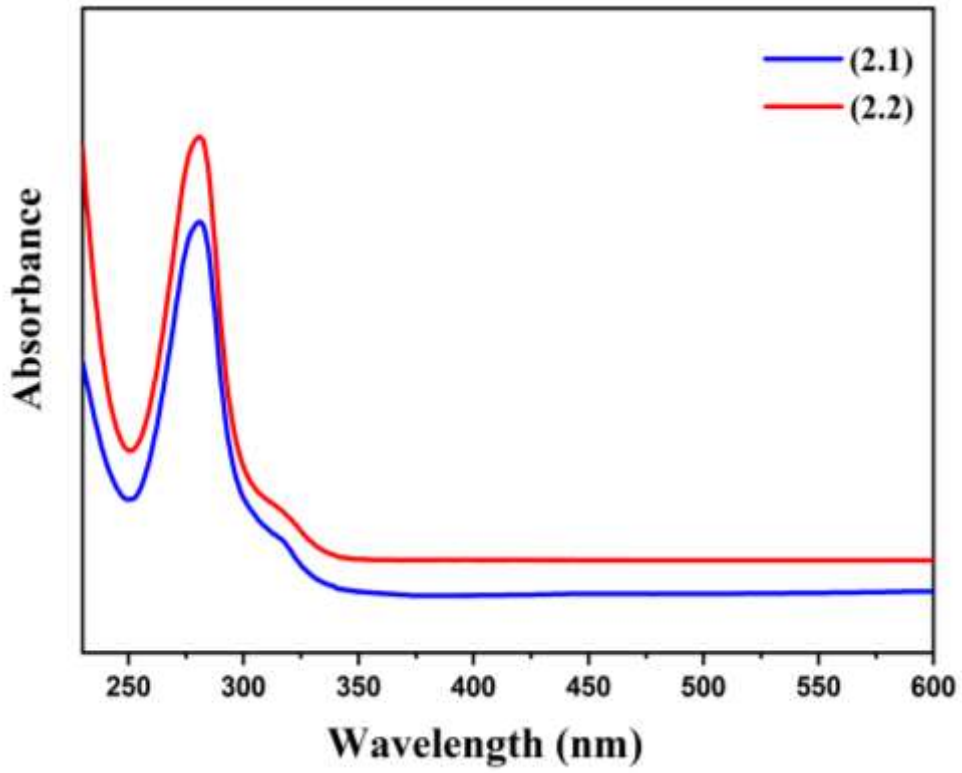

Fig. 2.16 Absorption spectra of $[Cd_2(2,3\text{-pzdc})(tz)_2]$, **2.1,** and $[Cd_2(2,3\text{-pzdc})(dtz)_2]$, **2.2**.

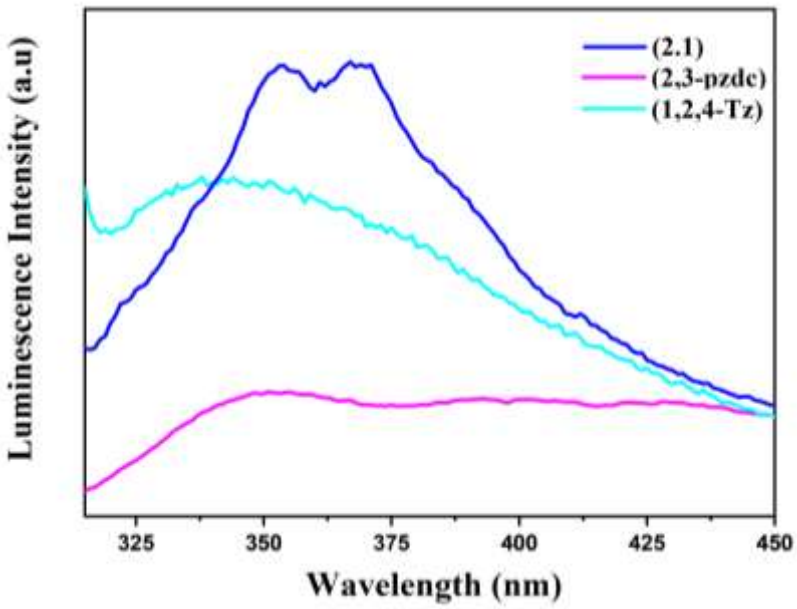

Fig. 2.17 Figure shows luminescence spectra of aqueous dispersion of $[Cd_2(2,3\text{-pzdc})(tz)_2]$, **2.1**, 2,3-pyrazine dicarboxylic acid (2,3-pzdc) and 1,2,4 triazole (1,2,4-tz) upon excitation at 280 nm.

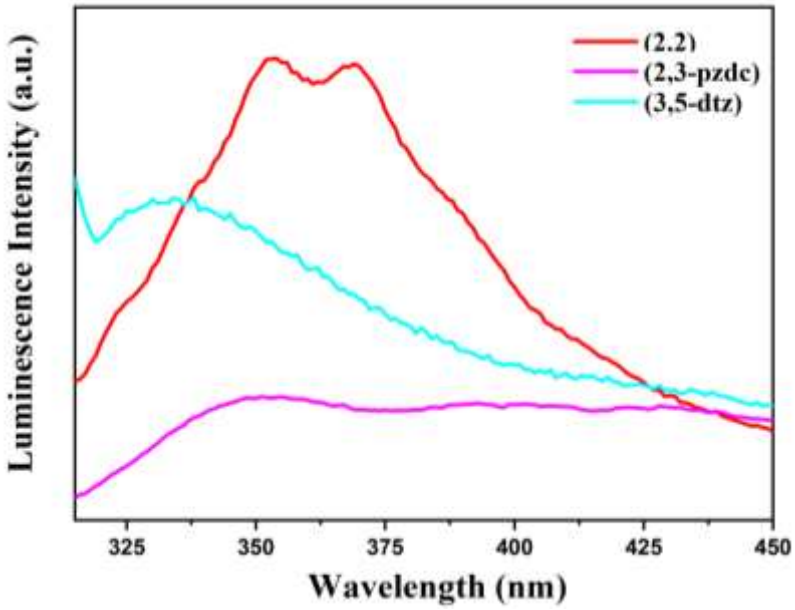

Fig. 2.18 Figure shows luminescence spectra of an aqueous dispersion of $[Cd_2(2,3\text{-pzdc})(3,5\text{-dtz})_2]$, **2.2,** 2,3-pyrazine dicarboxylic acid (2,3-pzdc) and 3,5-diamino 1,2,4-triazole (3,5-dtz) upon excitation at 280 nm.

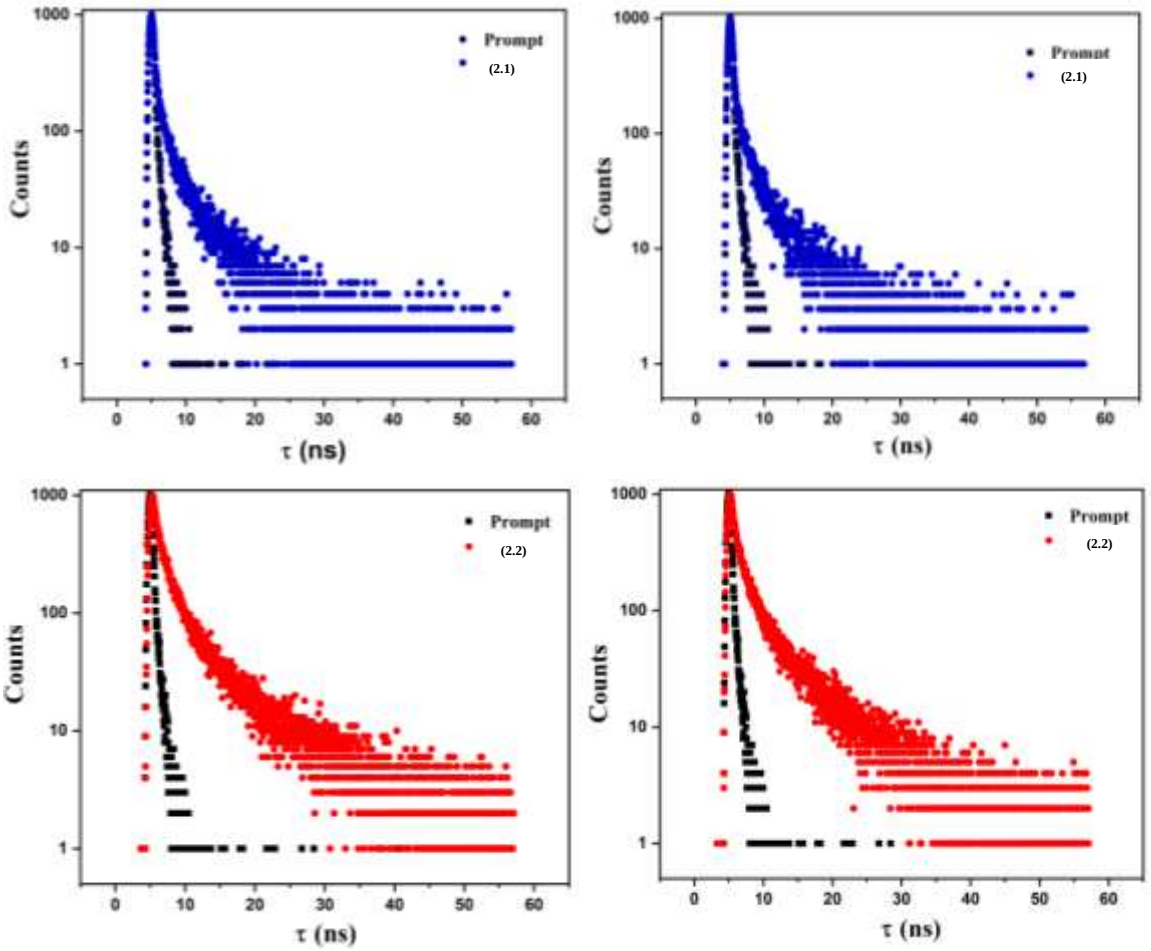

Fig. 2.19 Top Panel: Time resolved spectra of **2.1** at λ_{ex} = 280 nm and λ_{em} = 353 nm (left), λ_{em} = 369 nm (right).

Down panel: Time resolved spectra of **2.2** at λ_{ex} = 280 nm and λ_{em} = 353 nm (left), λ_{em} = 369 nm (right).

Table 2.8: Luminescence lifetime data of compound **2.1** and **2.2** from time resolved spectra.

Compound	**λ_{ex} (nm)**	**λ_{em} (nm)**	**Lifetime (ns)**
2.1	280	353	0.81
		369	0.60
2.2	280	353	2.02
		369	1.78

The luminescence life times of both the emissions of compound **2.2** are much higher than the compound **2.1** (Table 8). This result suggests that hydrogen bond interaction has an important role in the lifetime of the excited states. In compound **2.2**, the presence of N-H….O hydrogen bond interactions increased the stability and rigidity of the framework of the coordination polymers. The increased rigidity of the ligands reduces the nonradiative decay generated through the vibration of the framework and increases the lifetime of the excited states in compound **2.2**. Enhancement of the luminescence lifetime through hydrogen-bond interactions has been reported earlier in metal-organic complexes, and it has been established based on the completion between radiative and nonradiative transitions.[2.82]

2.3.6 Schottky Diode Behaviors. To assess the junction properties at the Al/material interface of these Schottky barrier diodes, the dark *J-V* characteristics of all the devices ITO/PEDOT/compound **2.1**/Al and ITO/PEDOT/ compound **2.2**/Al were analysed and using well known Shockley-diode equation:

$$J = J_0\left[\exp\left(\frac{qV_D}{\eta kT}\right) - 1\right] \qquad (1)$$

where J is the forward current, J_0 is the reverse saturation current. By treating the charge carrier injection under thermionic emission theory, J_0 is expresses as, $J_0 = A^*T^2\exp\left(-\frac{e\varphi_B}{kT}\right)$. Here, A^* is the effective Richardson constant and the value was considered as 120 $\mathrm{A/cm^2K^2}$ (for all the devices)[2.83], φ_B is the Schottky barrier height at Al/material interface and η is the diode ideality factor. For large forward bias voltages ($V_D > 3kT/q$) and assuming a series resistance R_s, eq 1 can be written as,

$$I = I_0\exp\left(\frac{q}{\eta kT}(V - IR_s)\right) \qquad (2)$$

where $I = J \times A$ and $I_0 = J_0 \times A$ ($A = 0.2\ \mathrm{cm^2}$ is the area of the device) and IR_s is the voltage drop across the series resistance of the device. Differentiation of eq 2 leads to,

$$\frac{dV}{d(\ln\frac{I}{I_0})} = \frac{\eta kT}{q} + IR_s \qquad (3)$$

Linear part of the $dV/d\left(\ln\frac{I}{I_0}\right)$ versus I plot (Fig. 2.20b and Fig. 2.21b) yield R_s as the slope and $\eta kT/q$ as y-axis intercept. To evaluate the Schottky-barrier height φ_B at the Al/material interface a function $H(I)$ is defined as $H(I) = V - \frac{\eta kT}{q}\ln\left(\frac{I}{AA^*T^2}\right)$. On substituting the expression for J_0 and $H(I)$, eq 1 takes a simpler form: $H(I) = IR_s + n\varphi_B$. Using the value of idelaity factor (η) already extracted, a plot of $H(I)$ vs I yield a straight line

with y-intercept yielding the value of φ_B (Fig. 2.20c and Fig. 2.21c). Further R_s can be extracted and compared with the previously obtained value for consistency.[2.83] The parameters extracted from these graphs have been summarized in Table 9.

The current vs voltage plot (Fig. 2.20a and Fig. 2.21a) shows a nonlinear behavior of the current as the bias voltage is increased. In both the devices (with compounds **2.1** and **2.2**), asymmetric behavior is observed under forward and reverse bias, indicating rectification. The rectification ratio (i.e., the ratio between forward current and reverse current at the same voltage level) in these devices is in the range≈2−4. However, in the compound **2.2** device, the overall current magnitude is 10 times higher compared to the compound **2.1** device. The series resistance extracted for the compound **2.2** device is≈22 times lower as compared to the compound **2.1** device, indicating a higher conductivity of compound **2.2**. It is important to note that the lower resistance and higher conductivity of compound **2.2** indicate the possible role of hydrogen-bond interactions. The effect of hydrogen-bond interactions for higher electrical conductivities has been well established in hydrogen-bonded solids where lowering of the energy barrier produced though extended hydrogen bonding was shown.[2.84]

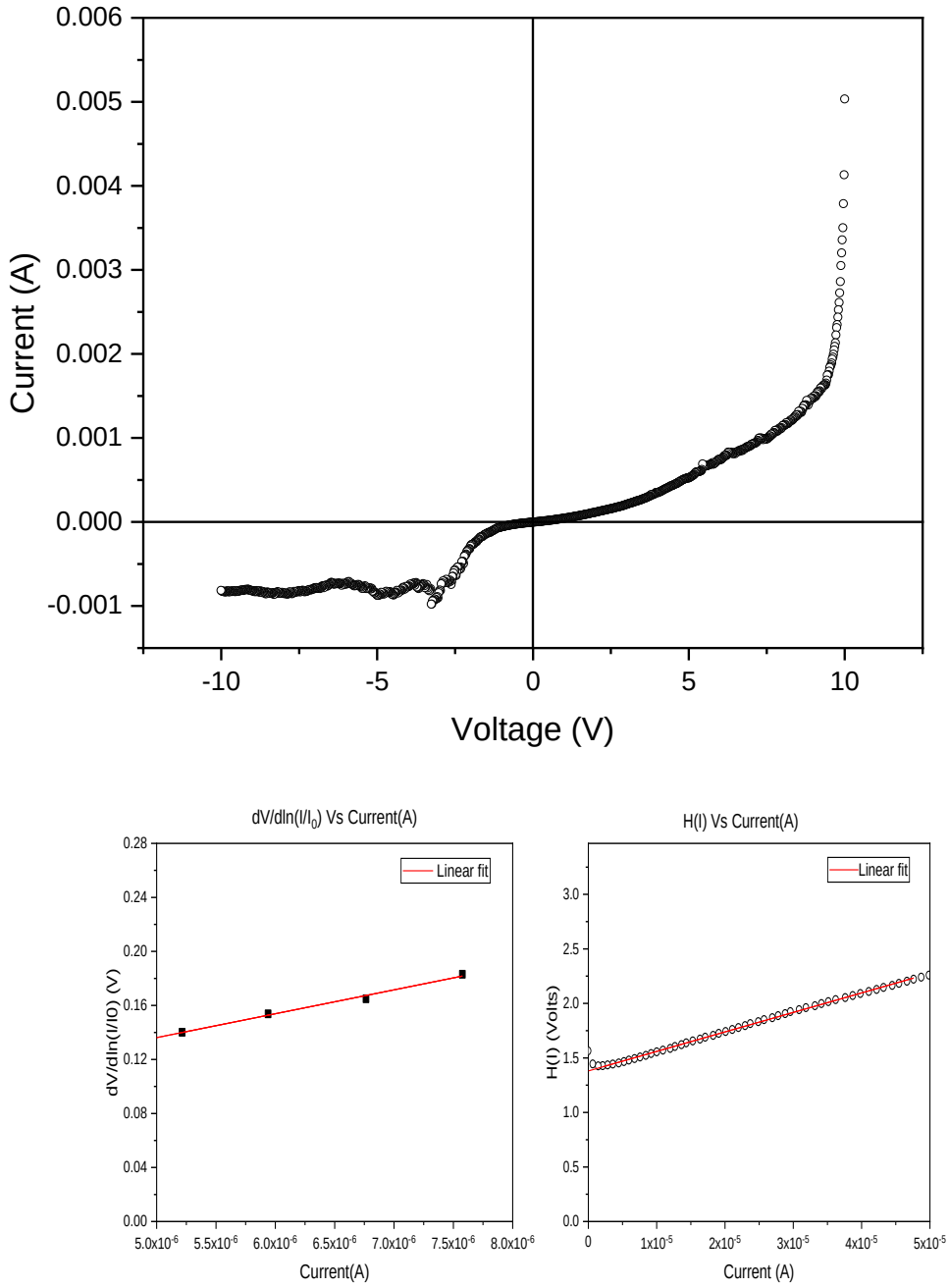

Fig. 2.20 (a) I-V characteristics under dark condition for the device ITO/PEDOT/**2.1**/Al (b) Plot of $dV/d\left(\ln\frac{I}{I_0}\right)$ versus I in dark condition (C) H(I) vs. I for the device in dark condition.

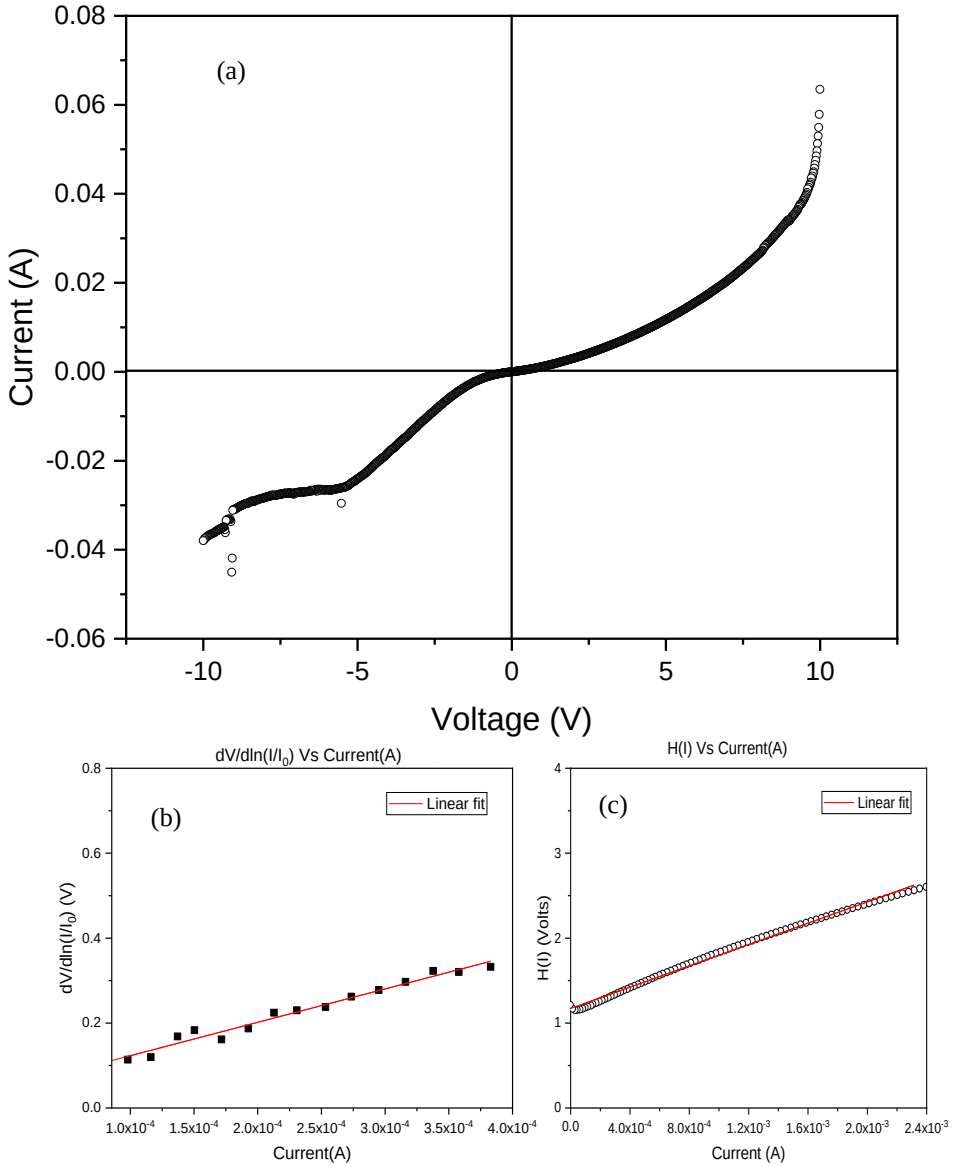

Fig. 2.21 (a) I-V characteristics under dark condition for the device ITO/PEDOT/**2.2**/Al (b)Plot of $dV/d\left(\ln\frac{I}{I_0}\right)$ versus I in dark condition (C) H(I) vs. I for the device in dark condition.

Table 2.9: Schottky diode Parameters of compound **2.1** and **2.2**.

Device Structure	Series resistance R_s (Ω)		Ideality factor (n)	Barrier height φ_B (eV)
	From $dV/d\left(\ln\frac{I}{I_0}\right)$ vs I	From $H(I)$ vs I		
ITO/PEDOT/compound **2.1**/Al	17689.49 ± 1179.20	17886.58 ± 76.62	1.84	0.745
ITO/PEDOT/compound **2.2**/Al	786.22 ± 36.43	627.29 ± 5.12	1.7	0.689

2.4 CONCLUSIONS

We have successfully synthesized two new three-dimensional Cd-based coordination polymers. The compounds were characterized by single-crystal X-ray and powder X-ray diffraction, Fourier transform infrared (FTIR) spectra and thermogravimetric analysis (TGA). The structural similarity between the two structures enables us to extract the role of the N−H···O hydrogen-bond interactions present in compound **2.2**. Time-resolved luminescence studies show a higher lifetime of the excited states of compound **2.2** (0.81 and 0.60 ns forcompound **2.1** and 2.02 and 1.78 ns for compound **2.2**). The correlation between the life time and the hydrogen-bond interactions suggests that the nonradiative decay paths are less favorable in compound **2.2** than in compound **2.1**. The junction properties at the Al/material interface of these Schottky barrier diodes and the dark J−V characteristics of both of the devices. (ITO/PEDOT/compound **2.1**/Al and ITO/PEDOT/compound **2.2**/Al) were analyzed using the well-known Shockley diode equation. In both the devices (with compounds **2.1** and **2.2**),an asymmetric behavior is observed under forward and reverse bias, indicating rectification. However, in the compound **2.2** device, the overall current magnitude is 10 times higher than that of the compound **2.1** device. The series resistance extracted for the compound **2.2** device is ≈22 times lower than that of the compound **2.1** device, indicating a higher conductivity of compound **2.2**. This behavior also indicates a probable role of hydrogen-bond interactions in the lower resistance and higher conductivity of compound **2.2** than compound **2.1**.

2.5 REFERENCES

(2.1) S. Natarajan, P. Mahata, *Chem. Soc. Rev*., 2009, **38**, 2304−2318.

(2.2) M.-L. Hu, S. A. A. Razavi, M. Piroozzadeh, A. Morsali, *Inorg. Chem. Front*., 2020, **7**, 1598−1632.

(2.3) O. M. Yaghi, H. Li, *J. Am. Chem. Soc*., 1995, **117**, 10401−10402.

(2.4) O. M. Yaghi, G. Li, H. Li, *Nature*., 1995, **378**, 703− 487 706.

(2.5) J. He, J. Yu, Y. Zhang, Q. Pan, R. Xu, *Inorg. Chem*., 2005, **44**, 9279−9282.

(2.6) H. Yin, S.-X. *Polyhedron.*, 2007, **26**, 3103−3111.

(2.7) Y. -H. Zhao, Z.-M. Su, Y.-M. Fu, K.-Z. Shao, P. Li, Y. Wang, X.-R. Hao, D.-X. Zhu, S.-D. Liu, *Polyhedron.*, 2008, **27**, 583−592.

(2.8) C. D. Ene, F. Tuna, O. Fabelo, C. Ruiz-Perez, A. M. Madalan, H. W. Roesky, M. Andruh, *Polyhedron.*, 2008, **27**, 574−582.

(2.9) P. Horcajada, C. Serre, M. Vallet-Regí, M. Sebban, F. Taulelle, G. Ferey, *Angew. Chem*., 2006, **118**, 6120−6124.

(2.10) S. Kitagawa, R. Matsuda, *Coord. Chem. Rev*., 2007, **251**, 2490− 2509.

(2.11) S. Kitagawa, S.-i. Noro, T. Nakamura, Chem. Commun., 2006, 701− 707.

(2.12) S. Kitagawa, K. Uemura, *Chem. Soc. Rev*., 2005, **34**, 109−119.

(2.13) Z. Wang, S. M. Cohen, *J. Am. Chem. Soc*., 2007, **129**, 12368−12369.

(2.14) M. Eddaoudi, J. Kim, N. Rosi, D. Vodak, J. Wachter, M. O'Keeffe, O. M. Yaghi, *Science*., 2002, **295**, 469−472.

(2.15) N. L. Rosi, J. Eckert, M. Eddaoudi, D. T. Vodak, J. Kim, M. O'Keeffe, O. M. Yaghi, *Science.*, 2003, **300**, 1127−1129.

(2.16) C. L. Cahill, D. T. D. Lill, M. Frisch, *CrystEngComm.*, 2007, **9**, 15−26.

(2.17) M. D. Allendorf, C. A. Bauer, R. K. Bhakta, R. J. T. Houk, *Chem. Soc. Rev*., 2009, **38**, 1330−1352.

(2.18) R. J. Hill, D.-L. Long, P. Hubberstey, M. Schroder, N. R. Champness, *J. Solid State Chem*., 2005, **178**, 2414−2419.

(2.19) K. E. Knope, H. Kimura, Y. Yasaka, M. Nakahara, M. B. Andrews, C. L. Cahill, *Inorg. Chem*., 2012, **51**, 3883−3890.

(2.20) X. Zhao, B. Xiao, A. J. Fletcher, K. M. Thomas, D. Bradshaw, M. J. Rosseinsky, *Science.*, 2004, **306**, 1012− 1015.

(2.21) K. H. Cho, D. D. Borges, U.-H. Lee, J. S. Lee, J. W. Yoon, S. J. Cho, J. Park, W. Lombardo, D. Moon, A. Sapienza, G. Maurin, J.-S. Chang, *Nat Commun*., 2020, **11**, No. 5112.

(2.22) H. Li, M. Eddaoudi, M. O'Keeffe, O. M. Yaghi, *Nature.*, 1999, **402**, 276−279.

(2.23) M. Mon, R. Bruno, S. Sanz-Navarro, C. Negro, J. Ferrando-Soria, L. Bartella, L. D. Donna, M. Prejano, T. Marino, A. Leyva-` Pérez, D. Armentano, E. Pardo, *Nat Commun*., 2020, **11**, No. 3080.

(2.24) S. M. Moosavi, A. Nandy, K. M. Jablonka, D. Ongari, J. P. Janet, P. G. Boyd, Y. Lee, B. Smit, H. J. Kulik, *Nat Commun*., 2020, 11, No. 4068.

(2.25) P. Horcajada, T. Chalati, C. Serre, B. Gillet, C. Sebrie, T. Baati, J. F. Eubank, D. Heurtaux, P. Clayette, C. Kreuz, J.-S. Chang, Y. K. Hwang, V. Marsaud, P.-N. Bories, L. Cynober, S. Gil, G. Férey, P. Couvreur, R. Gref, *Nat. Mater*., 2010, **9**, 172−178.

(2.26) V. R. Cherkasov, E. N. Mochalova, A. V. Babenyshev, J. M. Rozenberg, I. L. Sokolov, M. P. Nikitin, *Acta Biomater*., 2020, **103**, 223−236.

(2.27) H. Dong, G.-X. Yang, X. Zhang, X.-B. Meng, J.-L. Sheng, X.-J. Sun, Y.-J. Feng, F.-M. Zhang, *Chem. - Eur. J.* 2018, **24**, 17148−17154.

(2.28) Z. Meng, H. Huang, D. Huang, F. Zhang, P. Mi, *J. Colloid Interface Sci*., 2021, **581**, 31−43.

(2.29) M. Mohammad, M. Lisiecki, K Liang,. A. Razmjou, V. Chen, *Appl. Mater. Today*., 2020, **21**, No. 100884.

(2.30) X. Zhao, X. Bu, T. Wu, S.-T. Zheng, L. Wang, P. Feng, *Nat. Commun*., 2013, **4**, No. 2344.

(2.31) A. V. Desai, B. Manna, A. Karmakar, A. Sahu, D. S. K. A. Ghosh, *Angew. Chem*., Int. Ed. 2016, **55**, 7811−7815.

(2.32) T. Li, L. Liu, Z. Zhang, Z. Han, *Sep. Purif. Technol.*, 2020, **237**, No. 116360.

(2.33) Y. Yuan, F. Sun, L. Li, P. Cui, G. Zhu, *Nat. Commun*., 2014, **5**, No. 4260.

(2.34) Z. Huang, M. Zhao, C. Wang, S. Wang, L. Dai, L. Zhang, L. Xu, *Chem. Eng. J.*, 2020, **384**, No. 123343.

(2.35) F. Yang, G. Xu, Y. Dou, B. Wang, H. Zhang, H. Wu, W. Zhou,; J.-R. Li, B. Chen, *Nat. Energy*., 2017, **2**, 877−883.

(2.36) L. E. Kreno, K. Leong, O. K. Farha, M. Allendorf, R. P. V. Duyne, and J. T. Hupp, *Chem. Rev*., 2012, **112**, 1105−1125.

(2.37) G. Férey, *Dalton Trans*., 2009, 4400−4415.

(2.38) G. Férey, *Chem. Soc. Rev*., 2008, **37**, 191−214.

(2.39) Y. Cui, Y. Yue, G. Qian, B. Chen, *Chem. Rev*., 2012, **112**, 1126−1162.

(2.40) D. K. Singha, P. Majee, S. Mandal, S. K. Mondal, P. Mahata, *Inorg. Chem*., 2018, **57**, 12155−12165.

(2.41) P. Mahata, S. K. Mondal, D. K. Singha, P. Majee, *Dalton Trans*., 2017, **46**, 301−328.

(2.42) L.-R. Yang, S. Song, W. Zhang, H.-M. Zhang, Z.-W. Bu, T.-G. Ren, Synth. Met. 2011, **161**, 647−654.

(2.43) M. V. Marinho, D. O. Reis, W. X. C. Oliveira, L. F. Marques, H. O. Stumpf, M. Deniz, J. Pasan, C. Ruiz-Perez, J. Cano, F. Lloret, M. Julve, *Inorg. Chem*., 2017, **56**, 2108−2123.

(2.44) J.-Z. Zou, Z. Xu, W. Chen, K. M. Lo, X.-Z. You, *Polyhedron*., 1999, **18**, 1507−1512.

(2.45) X. Zheng, Y. Chen, J. Ran, L. Li, *Sci. Rep*., 2020, **10**, No. 6273.

(2.46) F. Y. Wardana, S.-W. Ng, A. C. Wibowo, *Cryst. Growth Des*., 2015, **15**, 5930−5938.

(2.47) K. Yang, J.-H. Luo, Z.-H. Liu, *Inorg. Chim. Acta*., 2012, **391**, 206−209.

(2.48) J.-W. Zhang, Y. Man, Y.-N. Ren, W.-H. Liu, B.-Q. Liu, Y.-P. Dong, *Inorg. Chim. Acta*., 2019, **488**, 41−48.

(2.49) X.-M. Lin, L. Chen, H.-C. Fang, Z.-Y. Zhou, X.-X. Zhou, J.-Q. Chen, A.-W. Xu, Y.-P. Cai, *Inorg. Chim. Acta*., 2009, **362**, 2619−2626.

(2.50) F. Zhang, X. Zou, P. Yan, J. Sun, G. Hou, G. Li, Cryst. Growth Des., 2015, **15**, 1249−1258.

(2.51) P. C. R. Soares-Santos, L. Cunha-Silva, F. A. A. Paz, R. A. S. Ferreira, J. Rocha, L. D. Carlos, H. I. S. Nogueira, *Inorg. Chem*., 2010, **49**, 3428−3440.

(2.52) G. Günay, O. Z. Yesilel, M. S. Soylu, S. Keskin, H. Dal, Synth. Met. 2011, **161**, 2471−2480.

(2.53) R. R. Arrieta-Pérez, J. N. Primera-Pedrozo, J. Exley, and A. J. Hernandez-Maldonado, Cryst. Growth Des. 2018, **18**, 1676−1685.

(2.54) G. Günay, O. Z. Yesilel, C. Darcan, S. Keskin, O. Büyükgüngör, Inorg. Chim. Acta., 2013, **399**, 19−35.

(2.55) A. J. Hernández-Maldonado, R. R. Arrieta-Perez, J. N. Primera Pedrozo, J. Exley, *Cryst. Growth Des*., 2015, **15**, 4123−4131.

(2.56) K. Riascos-Rodríguez, S. Marks, P. G. Evans, S. P. Hernández-Rivera, J. L. Ruiz-Caballero, D. Piñero, A. J. Hernández-Maldonado, *Cryst. Growth Des*., 2020, **20**, 3898−3912.

(2.57) X. J. Zhao, R. X. He, Y. F. Li, *Analyst*., 2012, **137**, 5190−5192.

(2.58) S. Mohapatra, H. Sato, R. Matsuda, S. Kitagawa, T. K. Maji, *CrystEngComm*., 2012, **14**, 4153−4156.

(2.59) K. Riascos-Rodríguez, A. J. Schroeder, M. R. Arend, P. G. Evans, A. J. Hernández-Maldonado, *Dalton Trans.*, 2014, **43**, 10877−10884.

(2.60) O. J. García-Ricard, R. Fu, A. J. Hernandez-Maldonado, *J. Phys. Chem. C*., 2011, **115**, 3595−3601.

(2.61) K. Kishida, Y. Watanabe, S. Horike, Y. Watanabe, Y. Okumura, Y. Hijikata, S. Sakaki, S. Kitagawa, *Eur. J. Inorg. Chem*., 2014, **2014**, 2747−2752.

(2.62) R. Matsuda, R. Kitaura, S. Kitagawa, Y. Kubota, T. C. Kobayashi, S. Horike, M. Takata, *J. Am. Chem. Soc*., 2004, **126**, 14063−14070.

(2.63) H. Yin, S.-X. Liu, Polyhedron., 2007, **26**, 3103−3111.

(2.64) R.-B. Zhang, Z.-J. Li, Y.-Y. Qin, J.-K. Cheng, J. Zhang, Y.-G. Yao, *Inorg. Chem*., 2008, **47**, 4861−4876.

(2.65) S. Ferrer, F. Lloret, I. Bertomeu, G. Alzuet, J. Borrás, S. García-Granda, M. Liu-González, J. G. Haasnoot, *Inorg. Chem*., 2002, **41**, 5821−5830.

(2.66) M. H. Klingele, S. Brooker, *Coord. Chem. Rev*., 2003, **241**, 119−132.

(2.67) J.-P. Zhang, Y.-B. Zhang, J.-B. Lin, X.-M. Chen, *Chem. Rev*., 2012, **112**, 1001−1033.

(2.68) J.-P. Zhang, Y.-Y. Lin, X.-C. Huang, X.-M. Chen, *J. Am. Chem. Soc*., 2005, **127**, 5495−5506.

(2.69) J.-P. Zhang, Y.-Y. Lin, W.-X. Zhang, X.-M. Chen, *J. Am. Chem. Soc*., 2005, **127**, 14162−14163.

(2.70) J.-P. Zhang, S.-L. Zheng, X.-C. Huang, X.-M. Chen, *Angew. Chem., Int. Ed*. 2004, **43**, 206−209.

(2.71) W. Ouellette, J. R. Gala′n-Mascaro′s, K. R. Dunbar, J. Zubieta, *Inorg. Chem*., 2006, **45**, 1909−1911.

(2.72) W. Ouellette, B. S. Hudson, J. Zubieta, *Inorg. Chem*., 2007, **46**, 4887−4904.

(2.73) W. Ouellette, A. V. Prosvirin, V. Chieffo, K. R. Dunbar, B. Hudson, J. Zubieta, *Inorg. Chem*., 2006, **45**, 9346−9366.

(2.74) M. Singh, S. Senthilkumar, S. Rajput, S. Neogi, *Inorg. Chem*., 2020, **59**, 3012− 3025.

(2.75) H.-P. Li, S.-N. Li, H.-M. Sun, M.-C. Hu, Y.-C. Jiang, Q.-G. Zhai, *Cryst. Growth Des*., 2018, **18**, 3229−3235.

(2.76) Bruker Apex3 v2017.3-0, Saint V8.38A, SAINT V8.38A; Bruker AXS Inc.: Madison, WI, 2018.

(2.77) L. Krause, R. Herbst-Irmer, G. M. Sheldrick, D. Stalke, *J. Appl. Crystallogr*., 2015, **48**, 3− 10.

(2.78) A. Altomare, G. Cascarano, C. Giacovazzo, A. Guagliardi, *J. Appl. Crystallogr*., 1993, **26**, 343−350.

(2.79) G. M. Sheldrick, Crystal Structure Refinement with SHELXL. Acta Crystallogr., Sect. C: Struct. Chem. 2015, 71, 3−8.

(2.80) L. J. Farrugia, WinGX suite for Small-Molecule Single-Crystal Crystallography. J. Appl. Crystallogr. 1999, **32**, 837−838.

(2.81) A. L. Spek, Single-Crystal Structure Validation with the Program PLATON. J. Appl. Crystallogr. 2003, **36**, 7−13.

(2.82) G.-J. Zhao, B. H. Northrop, K.-L. Han, P. J. Stang, *J. Phys. Chem. A*., 2010, **114**, 9007−9013.

(2.83) S. M. Sze, K. K. Ng, Physics of Semiconductor Devices, 3rd ed.; John Wiley & Sons, Inc: Hoboken, New Jersey, 2007.

(2.84) C. C. Gravatt, P. M. Gross, *J. Chem. Phys*., 1967, **46**, 413− 419.

Chapter 3

Selective dye sorption and metal ion sensing behaviours of a new Cd-based MOF

ABSTRACT

A Cd(II)-based metal–organic framework (MOF) [Cd(PDA)(L)$_2$] (PDA = 1,4-phenylenediacetate and L = 2,4,5-tri-4-pyridyl-1H-imidazole), **3.1**, has been synthesized by solvothermal method and characterized by single-crystal X-ray diffraction techniques, powder X-ray diffraction, Fourier Transform Infrared (FTIR) and thermogravimetric analysis (TGA). The single crystal X-ray studies show that connectivity among Cd^{2+} ions, PDA and 2,4,5-tri-4-pyridyl-1H-imidazole ligands form two-dimensional structure. The two dimensional structures are arranged in AAA….fashion to form a three dimensional packing arrangement. The compound **3.1** shows selective and efficient sorption of large anionic dye remazol brilliant blue R (RBBR) in aqueous medium, whereas compound **3.1** exhibits low sorption towards orange G (OG), methyl orange (MO), methylene blue (MB) and rhodamine B (RhB). The compound **3.1** also exhibits photoluminescence based sensing behaviors towards Fe^{3+}, Cr^{3+} and Al^{3+} ions in aqueous medium based on luminescence quenching effect. However, photoluminescence studies in the presence of other common metal ions such as Cd^{2+}, Cu^{2+}, Mg^{2+}, Ca^{2+}, Co^{2+}, K^{+}, Mn^{2+}, Pb^{2+}, Zn^{2+}, Na^{+} in aqueous medium show negligible turn on effect. The limit of detection for $Fe^{3+,}$ Cr^{3+}, Al^{3+} ions were 75, 257 and 107 ppb, respectively. Compound **3.1** also showed comparable gas sorption capacity towards CO_2 (64.5 cm^3/g), N_2 (72.25 cm^3/g) and H_2 (45.30 cm^3/g) at 1 bar.

3.1 INTRODUCTION

In recent years, pollution-free water has become a research hotspot in chemistry and materials science.[3.1–3.3] Water pollution originating from toxic and poorly degradable industrial by products including a variety of organic and inorganic com pounds such as organic dyes, phenols, pesticides, fertilizers, hydrocarbons, detergents, oils, greases and pharmaceuticals has become a critical environmental problem due to its potential negative effects on human and animal health.[3.4–3.7] Because of their extraordinary electronic and optical properties, organic dyes with intriguing chromophores have been widely used in textile, paper, leather, printing, plastic, cosmetic, and pharmaceutical industries.[3.8,3.9] Dye ingredients are one of the common water pollutants.[3.10] However, most organic dyes are toxic, mutagenic, carcinogenic or teratogenic agents resulting in a serious threat to human health, aquatic organisms and the food web.[3.11–3.13] Neutral, positively and negatively charged dyes are mostly immune towards light and oxidation because of their steady complex as well as aromatic structures. Hence, the degradation of dyes is too difficult owing to their unimaginable water solubility, thereby resulting in a serious pollution. Con sequently, it is a great imperative to eradicate these dyes before release into the environment using profitable strategies.[3.14–3.19] Many methods such as chemical, biological and physical degradation, photocatalytic degradation, and membrane filtration technologies have been developed to eliminate dye con tamination from waste water. Among these techniques, sorption of dyes via porous materials including zeolites, metal oxides, and activated carbon and porous polymers like MOFs has been regarded as one of the most favourable techniques because of its low cost, high efficiency and eco-friendly nature, which can avoid secondary pollution.[3.20–3.23] Metal–organic frameworks (MOFs) with tremendous poros ity and a large surface area are receiving great attention towards adsorbents for hazardous molecules, e.g. gas molecules and organic molecules.[3.24,3.25] MOFs with an adjustable pore structure, admirable thermal and chemical stability, and coordinatively unsaturated metal sites are immensely promising elements in dye sorption and separation, sensing, gas storage, drug delivery, magnetism and catalysis.[3.26–3.32] Generally, MOFs are designed by polydentate organo-linkers with transition metal containing nodes connected by chemical bonds. A ligand moiety with integrated functional groups and the structural aesthetics of MOFs can induce feasible supramolecular inter actions between the dynamic sorption sites of the MOFs and dye molecules via hydrogen bonding and electrostatic π....π stacking interactions. The active sites of MOFs and the aromatic probes of organic dyes also play a crucial role in effective sorption. With growing diversity, designable channels, and functional tenability, MOF-based materials show significant dye sorption properties.[3.33–3.37] Like organic dyes, metal ions manifest severe contamination in the environment.[3.38] Iron deficiency or overloading results in various functional disorders such as sleep loss, skin diseases, decreased immunity, anaemia, endotoxemia, hepatic cirrhosis, and

Huntington's and Alzheimer's diseases.[3.39–3.49] Correspond ingly, carbohydrate, fat, and nucleic acid metabolism proceeds through chromium ions, and cardiovascular diseases and dia betes mellitus are a result of the inadequacy of chromium ions.[3.50–3.55] Aluminium is a non-essential trace element for the human body. It is involved in manufacturing of several products. Absorption of the toxic aluminium impacts human health and promotes dementia, osteoporosis, and Parkinson's disease.[3.56–3.59] Hence, it is exceedingly needed to develop sensitive detectors to detect these metal ions in aqueous solution. With evolving technology, many methods have been technologically advanced to monitor and detect such heavy metal ions, e.g. atomic absorp tion spectrometry (AAS), inductively coupled plasma optical emis sion spectroscopy (ICP-OES), liquid chromatography (LC), ion mobility spectrometry (IMS), etc. But these detection procedures are arduous, time-consuming and most of the methods are expensive. Therefore, highly sensitive, low-cost, fast responding and simple techniques are required. Now, the rational design and development of fluorescent chemical sensors has become one of the most unique areas to detect these metal ions.[3.60–3.63] On the other hand, the increase of the CO_2 level in the atmosphere has adverse effects on our environment. Thus, maintaining the CO_2 level in the atmosphere is an exigent task. Metal–organic frameworks provide an effective and encouraging approach to CO_2 adsorption due to their regular networks or cages and high surface area.[3.64–3.67] Motivated by these stratagems, we have synthesized a two dimensional Cd(II) based porous MOF by a solvothermal method using 1,4-phenylenediacetic acid and the 2,4,5-tri-4- pyridyl-1H-imidazole ligand. The crystal structure of compound **3.1** was elucidated using high resolution X-ray diffraction (XRD). Compound 1 showed effective sorption of remazol brilliant blue R (RBBR) through electrostatic and π....π stacking interactions. Compound **3.1** also exhibited photoluminescence-based sensing behaviors towards Fe^{3+}, Cr^{3+} and Al^{3+} ions in aqueous medium based on the luminescence quenching effect with limits of detection of 75, 257 and 107 ppb, respectively.

3.2 EXPERIMENTAL SECTION

3.2.1 Materials. The required chemicals for the synthesis of compound **3.1**, namely, $Cd(OAc)_2{\cdot}2H_2O$ (Sigma-Aldrich, 98%), 1,4-phenylenediacetic acid (TCI, 98%), 4-pyridinecarboxaldehyde (Aldrich, 97%), ammonium acetate (Merck, 97%), NaOH (Merck, 97%), DMF (Merck, 99%), and ethanol (Sigma-Aldrich, 99%), were used as received without further purification. The chemicals used for the dye sorption and metal ion sensing experiments were remazol brilliant blue R (Sigma-Aldrich), orange G (Sigma-Aldrich), methyl orange (Sigma-Aldrich), methylene blue (Sigma-Aldrich), rhodamine B (Sigma-Aldrich), ferric(III) sulphate hydrate (Loba-Chemie, 99%), chromium(III) nitrate nonahydrate (Sigma-Aldrich, 99%), aluminium(III) nitrate nonahydrate (Merck, 95%), cadmium(II) chloride monohydrate (Merck, 98%), copper(II) chloride dihydrate (Merck, 99%), magnesium(II)

chloride hexahydrate (Merck, 98%), calcium(II) chloride dihydrate (Merck, 98%), cobalt(II) chloride hexahydrate (Merck, 98%), potassium(I) chloride (Merck, 99%), manganese(II) chloride tetrahydrate (Merck, 99%), lead(II) nitrate (Merck, 99%), zinc(II) sulfate heptahydrate (Merck, 99%), and sodium(I) chloride (Merck, 99%). The water used was double distilled.

3.2.2 Synthesis of compound 3.1. Initially 2,4,5-tri-4-pyridyl-1H-imidazole monohydrate was synthesized using 4-pyridinecarboxaldehyde and ammonium acetate, NaOH, and ethanol based on a reported procedure.[3.68] Compound **3.1** was prepared by employing a solvothermal method. $Cd(OAc)_2 \cdot 2H_2O$ (0.01695 g, 0.0625 mM), 1,4-phenylenediacetic acid (0.01235 g, 0.0625 mM), and 2,4,5-tri 4-pyridyl-1H-imidazole monohydrate (0.0208 g, 0.0625 mM) were dispersed in 3 mL DMF with continuous stirring, and the mixture was homogenized at room temperature for 30 minutes. The final reaction mixture was sealed in a 23 mL polytetrafluoroethylene-lined stainless-steel autoclave and heated at 140°C for 48 h. The initial pH value of the reaction mixture was 6 and no appreciable change in pH was noted after the reaction. The final product containing large quantities of block-shaped yellow colour crystals was filtered, washed with DMF under vacuum, and dried under ambient conditions.

3.2.3 Instrumentations. Powder X-ray diffraction (XRD) pattern was recorded on well ground sample in the 2θ range 5-50º using Bruker D8 Advance X-ray diffractometer with Cu Kα radiation (λ = 1.5418 Å) operating at 40 kV and 40 mA. The FTIR Spectrum (400-4000 cm^{-1}) of the compound **3.1** was noted using Nicolet Magna IR 750 series-II. Thermogravimetric analysis (TGA) of the compound **3.1** was carried out under nitrogen atmosphere (flow rate = 20 ml min^{-1}) using PerkinElmer Diamond instrument (STA 6000) in the temperature range of 30–800 °C (heating rate = 20 °C min^{-1}). Gas sorption isotherms for N_2 (77 K), H_2 (77 K), CO_2 (195 K) in the pressures range 0–1 bar were measured with an Autosorb iQ (Quantachrome Inc., USA). UV-Vis spectra of compound **3.1** and details sorption study of organic dyes were checked using Shimadzu UV-1900i UV-Vis spectrophotometer. Emission spectrum of compound **3.1** and details luminescence titration in presence of metal ions were recorded at room temperature in aqueous media (at 300 nm excitation wavelength) using Horiba FluoroMax4-spectrofluorometer. Time-correlated single photon counting (TCSPC) measurements were carried out at room temperature in water using HORIBA Jobin-Yvon instrument in the nanosecond time domain. The luminescence lifetime decays were collected on Hamamatsu MCP photomultiplier (R3809). All the decays were deconvoluted and fitted with exponential function using IBH DAS6 software.

3.2.4 Single-crystal structure determination of compound 3.1. Single-crystal X-ray data for the crystal of compound **3.1** were collected at 100 K on a Bruker APEX II diffractometer equipped with a graphite monochromator and a Mo Ka radiation source (l = 0.71073 Å). Unit cell measurement, data collection, integration,

scaling, and absorption corrections for the crystal were done using Bruker Apex II software.[3.69] Data reduction was done using Bruker SAINT suite.[3.70] The crystal structure was solved by direct methods and refined by the full matrix least squares method using SHELXL 2018[3.71] present in the Olex2 interface.[3.72] Absorption correction was applied using the numerical absorption correction method implemented in SADABS.[3.73] All non hydrogen atoms were refined anisotropically and all hydrogen atoms were positioned geometrically and refined using a riding model with Uiso(H) = 1.2Ueq. The two pyridine rings connected to imidazole are disordered in nearly a 1:1 ratio. Therefore, the disordered rings have been treated by fixing an occupancy of 0.5 to each disordered part. As a satisfactory disorder model for the solvent was not found for electron density corresponding to disordered solvent molecules in the voids, the Olex2 Solvent Mask routine (similar to PLATON/SQUEEZE) was used to mask out the disordered electron density. Geometrical calculations were done using PARST[3.74] and PLATON.[3.75] Details of the structure solution and final refinement are given in Table 3.1.

Table 3.1: Crystal Data and Structure Refinement Parameters of $[Cd(PDA)(L)_2]$ (PDA = 1,4-phenylenediacetate acid and L = 2,4,5-tri-4-pyridyl-1H-imidazole), **3.1**.

Empirical formula	$C_{14}H_{10.50}Cd_{0.50}N_{2.50}O_2$
Formula weight	301.95
Crystal system	Orthorhombic
Space group	*Cmca*
a(Å)	15.0905(10)
b(Å)	18.1837(9)
c(Å)	28.8807(13)
α(deg)	90
β (deg)	90
γ (deg)	90
Volume($Å^3$)	7924.9(7)
Z	16
Calculated density, ρ_{calc}(mg /m^3)	1.012
Absorption coefficient, μ (mm^{-1})	0.580
Temperature	100(2) K
Wavelength (Mo Kα) (Å)	0.71073
θ range (deg)	1.890 to 28.422
Final R indices [I>2sigma(I)]	R_1 = 0.0961, wR_2 = 0.2133
R indices (all data)	R_1 = 0.1195, wR_2 = 0.2235

$R_1=\Sigma||F_0|-|F_c||/\Sigma|F_0|$; $wR_2=\{\Sigma[w(F_0^2-F_c^2)^2]/\Sigma[w(F_0^2)^2]\}^{1/2}$, $w=1/[\sigma^2(F_0)^2+(aP)^2+bP]$;

$P=[\max.(F_0,0)^2+2(F_c)^2]/3$ where a = 0.0548, b = 139.0607 for **3.1**.

3.2.5 Dye sorption studies. Dye sorption experiments were carried out with different types of dyes such as remazol brilliant blue R (RBBR), orange G (OG), methylene blue (MB), methyl orange (MO), and rhodamine B (RhB). For the sorption studies of these dyes, five different solutions were prepared by mixing 50 mg compound **3.1** with 50 mL aqueous solutions of the dye (RBBR/OG/MO/MB/RhB) with a molar concentration of 5×10^{-5} M through proper shaking in separate volumetric flasks at room temperature. The sorption behaviour of compound **3.1** was

monitored by UV-Vis spectroscopy. For that, 2 mL mixture solutions were collected from the stock solution at different time intervals. Subsequently, the samples were centrifuged and used for the absorbance measurements. Furthermore, a similar experiment was conducted by using five different molar concentrations of RBBR: 5×10^{-5} M, 10×10^{-5} M, 15×10^{-5} M, 20×10^{-5} M, and 25×10^{-5} M to determine the sorption kinetics of RBBR dye.

3.2.6 Optical Studies. Fluorescence spectrum of compound **3.1** was recorded at room temperature in aqueous medium using Horiba FluoroMax4-spectrofluorometer. The dispersion of compound **3.1** was prepared by using 3.5 mg of compound **3.1** in 3.5 mL distilled water and ultra-sonicated for 3 minutes. 50 µL of the stock solution was taken in 2 ml of water into a quartz cuvette and used for absorption and fluorescence studies. 5mM aqueous solution of various metal ions (Fe^{3+}, Cr^{3+}, Al^{3+}, Cd^{2+}, Cu^{2+}, Mg^{2+}, Ca^{2+}, Co^{2+}, K^{+}, Mn^{2+}, Pb^{2+}, Zn^{2+} and Na^{+}) was prepared for sensing studies. Time-correlated single photon counting (TCSPC) measurements of compound **3.1** was carried out at room temperature using the excitation wavelength at 300 nm and emission decays curve monitored at 398 nm.

3.3 RESULTS AND DISCUSSION

3.3.1 Initial characterization. The powder X-ray diffraction (XRD) pattern was recorded on a well-ground sample of compound **3.1** in the 2θ range of 5−50° (see Fig. 3.1). The merged PXRD patterns indicated that the experimental PXRD pattern of the new product is in excellent agreement with the simulated XRD pattern generated from single-crystal X-ray diffraction data. The FTIR spectrum of compound **3.1** was recorded in the spectral range of 4000–400 cm^{-1} (see Fig. 3.2). The IR spectrum shows a sharp peak at 3387 cm^{-1} which indicates the presence of water molecules in compound **3.1**. Thermogravimetric analysis (TGA) of compound **3.1** was carried out in a nitrogen atmosphere from 30°C to 800°C at a heating rate of 20°C min^{-1} (see Fig. 3.3). The TGA curve of compound **3.1** shows the stepwise loss of solvent molecules from compound **3.1**, but we are unable to detect these solvent molecules by the single-crystal structure of **3.1**. The calculated values from the molecular formula determined from SCXRD indicate a weight loss of 78.75% due to the decomposition of the compound to CdO. However, the experimental value of weight loss is 81.3%. This difference indicates the presence of solvent molecules in compound **3.1**.

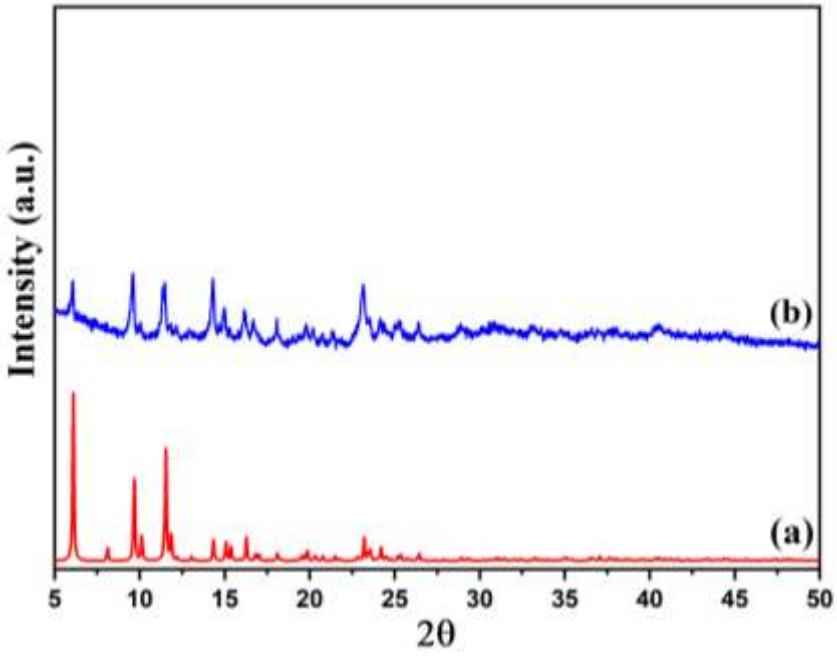

Fig. 3.1 Powder XRD (CuKα) patterns of [Cd(PDA)$(L)_2$], **3.1**: (a) simulated from single crystal X-ray data, (b) experimental.

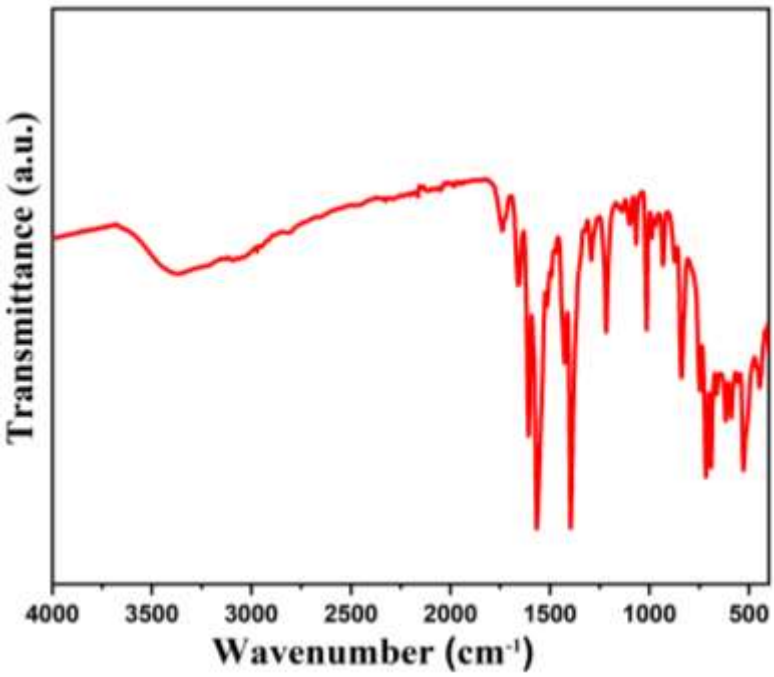

Fig. 3.2 IR spectrum of [Cd(PDA)$(L)_2$], **3.1**.

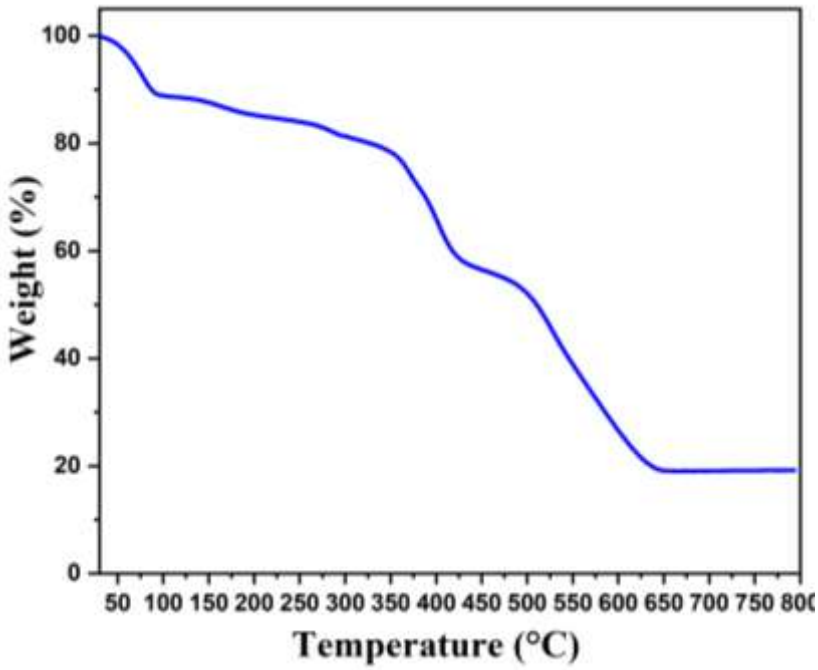

Fig. 3.3 Thermogravimetric analysis (TGA) of $[Cd(PDA)(L)_2]$, **3.1**, in nitrogen atmosphere.

3.3.2 Structural Description. The asymmetric unit of compound **3.1** consists of half crystallographically independent Cd^{2+} ion, half 1,4-phenylenediacetate (PDA) and one 2,4,5-tri-4-pyridyl-1H-imidazole ligand (Fig. 3.4a). Here, Cd^{2+} ions are coordinated with four carboxylate oxygen atoms of 1,4-phenylenediacetates (PDA) and three nitrogen atoms of 2,4,5-tri-4-pyridyl-1H-imidazole ligands occupying distorted pentagonal bipyramidal geometry (Fig.3.4b). The Cd-O bonds have average bond distance of 2.4 Å and the Cd-N bonds have average bond distance of 2.35 Å. The O/N-Cd-O/N bond angles are in the range of 53.85 (17) - 176.1 (2)°. The selected bond distance and bond angels are listed in Table 3.2 and Table 3.3 respectively.

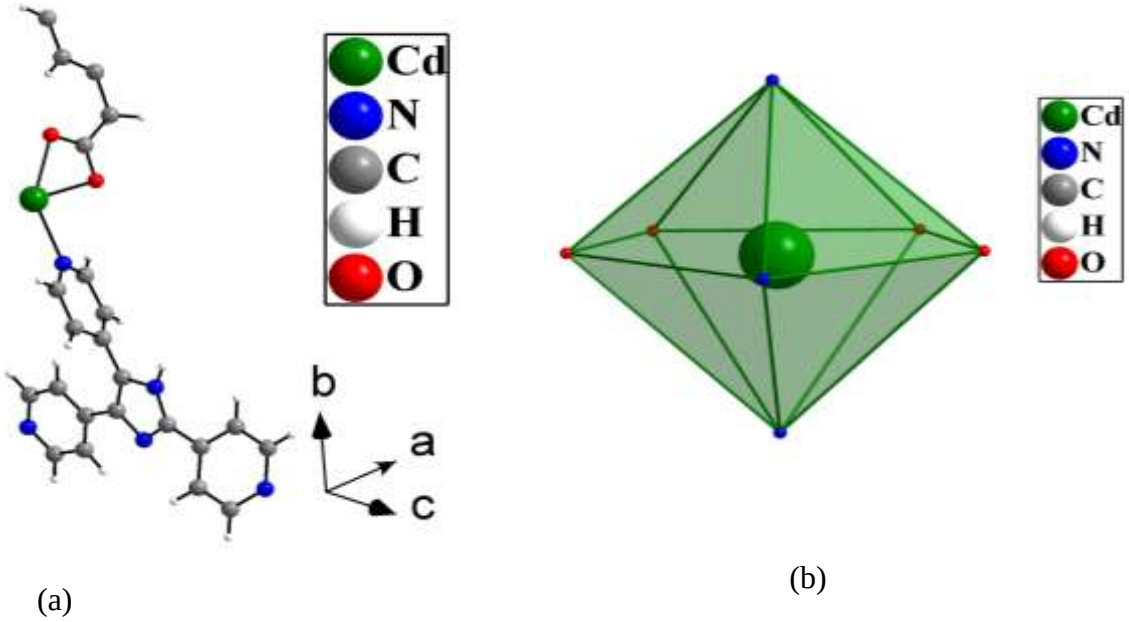

(a) (b)

Fig. 3.4 (a) Figure shows the asymmetric unit of $[Cd(PDA)(L)_2]$ (PDA = 1,4-phenylenediacetate and L = 2,4,5-tri-4-pyridyl-1H-imidazole), **3.1**. (b) The distorted pentagonal bipyramidal geometry around Cd^{2+} ions.

Table 3.2: Selected bond distances (Å) observed in [Cd(PDA)(L)$_2$] (PDA = 1,4-phenylenediacetate and L = 2,4,5-tri-4-pyridyl-1H-imidazole), **3.1**.

Bond	Distances, Å	Bond	Distances, Å
Cd(1)−O(1)	2.342(5)	Cd(1)−N(1)	2.350(4)
Cd(1)−O(1)#1	2.342(5)	Cd(1) −N(2)	2.352(7)
Cd(1) −O(2)	2.462(7)	Cd(1)−N(3)#2	2.348(7)
Cd(1)−O(2) #1	2.462(7)		

Symmetry transformations used to generate equivalent atoms: #1 -x+1, y, z; #2 -x+1, -y+1, -z+1

Table 3.3: Selected Bond Angles (deg) observed in [Cd(PDA)(L)$_2$], **3.1**.

Angle	Amplitude (º)
O (1) −Cd(1)−O(1) # 1	83.9 (3)
O (1) −Cd(1)−N(3) # 2	91.35 (17)
O (1) # 1 −Cd(1)−N(3) # 2	91.36 (17)
O (1) −Cd(1)−N(1)	91.57 (16)
O (1) # 1−Cd(1)−N(1)	91.57 (16)
N (3) # 2−Cd(1)−N(1)	176.1 (2)
O (1) −Cd(1)−N(2)	137.93 (13)
O (1) # 1−Cd(1)−N(2)	137.93 (13)
N (3) # 2−Cd(1)−N(2)	91.3 (3)
N (1) −Cd(1)−N(2)	84.7 (2)
O (1) −Cd(1)−O(2)	53.85 (17)
O (1) # 1−Cd(1)−O(2)	137.72 (18)
N (3) # 2−Cd(1)−O(2)	91.91 (13)
N (1) −Cd(1)−O(2)	87.70 (13)
N (2) −Cd(1)−O(2)	84.10 (11)
O (1) −Cd(1)−O(2) # 1	137.72 (17)
O (1) # 1 −Cd(1)−O(2) # 1	53.85 (17)
N (3) # 2 −Cd(1)−O(2) # 1	91.91 (13)
N (1) −Cd(1)−O(2)	87.70 (13)
N (2) −Cd(1)−O(2)	84.10 (11)
O (1) −Cd(1)−O(2) # 1	137.72 (17)
O (1) # 1 −Cd(1)−O(2) # 1	53.85 (17)
N (3) # 2 −Cd(1)−O(2) # 1	91.91 (13)
N (1) −Cd(1)−O(2) # 1	87.70 (13)
N (2) −Cd(1)−O(2) # 1	84.10 (12)
O (2) −Cd(1)−O(2) # 1	167.7 (2)

Symmetry transformations used to generate equivalent atoms:

For **3.1**: #1 -x+1, y, z; #2 -x+1, -y+1, -z+1.

In this structure, two Cd^{2+} ions are connected through two PDA ligands to form a dimeric unit where both the carboxylate groups of PDA ligands are bidentate in nature (Fig. 3.5a). On the otherhand, each 2,4,5-tri-4-pyridyl-1H-imidazole ligand connects three Cd^{2+} ions (Fig. 3.5b). The connectivity among Cd^{2+} ions, PDA and 2,4,5-tri-4-pyridyl-1H-imidazole ligands form an overall two-dimensional structure (Fig. 3.6a). The two dimensional structures are arranged in AAA….fashion to form a three dimensional packing arrangement (Fig. 3.6b)

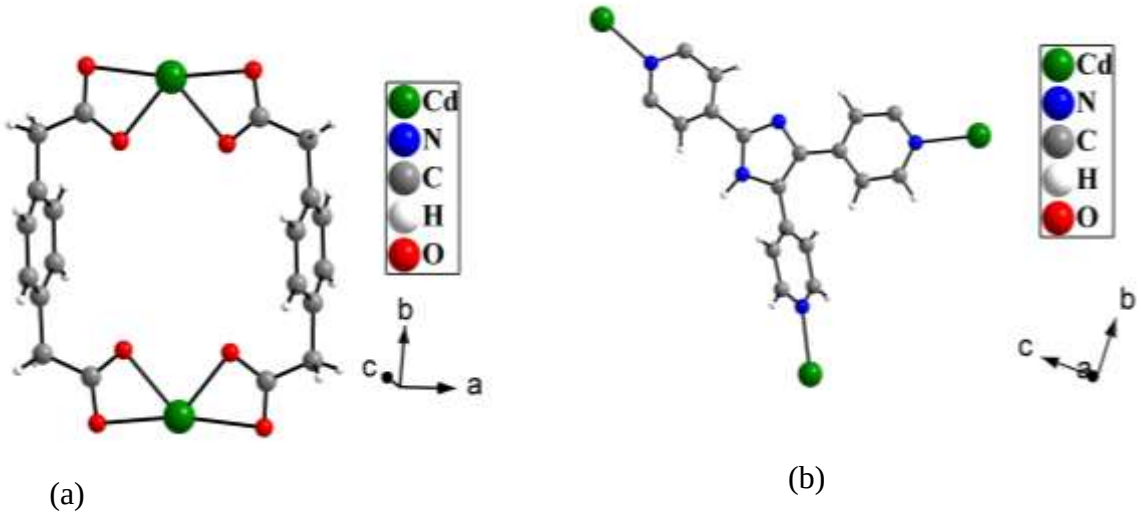

(a) (b)

Fig. 3.5 (a) Figure shows the connectivity between two Cd^{2+} ions through PDA ligands in $[Cd(PDA)(L)_2]$ (PDA = 1,4-phenylenediacetate and L = 2,4,5-tri-4-pyridyl-1H-imidazole), **3.1**. (b) coordination mode of 2,4,5-tri-4-pyridyl-1H-imidazole ligand.

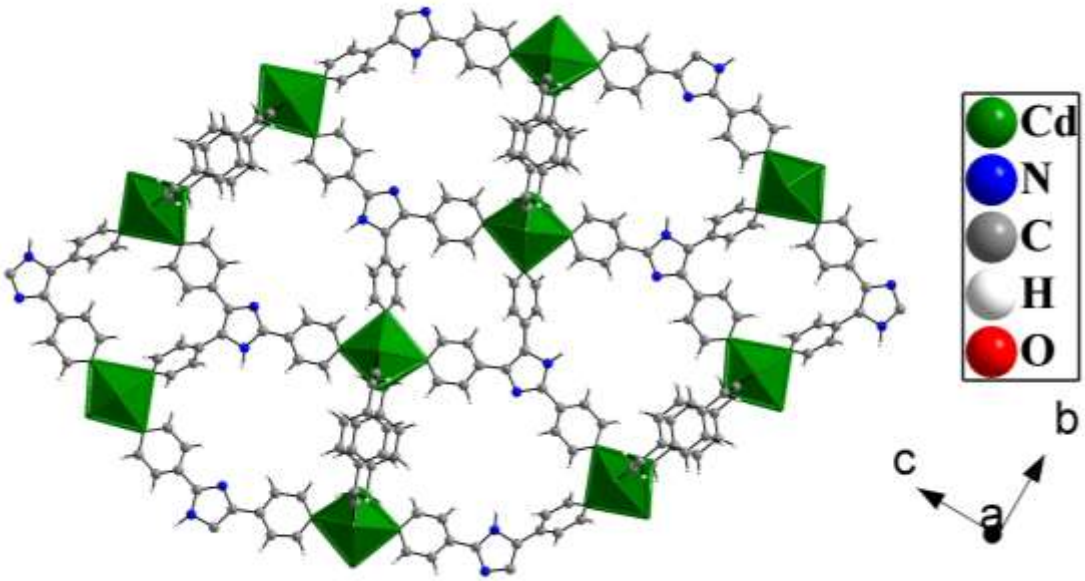

(a)

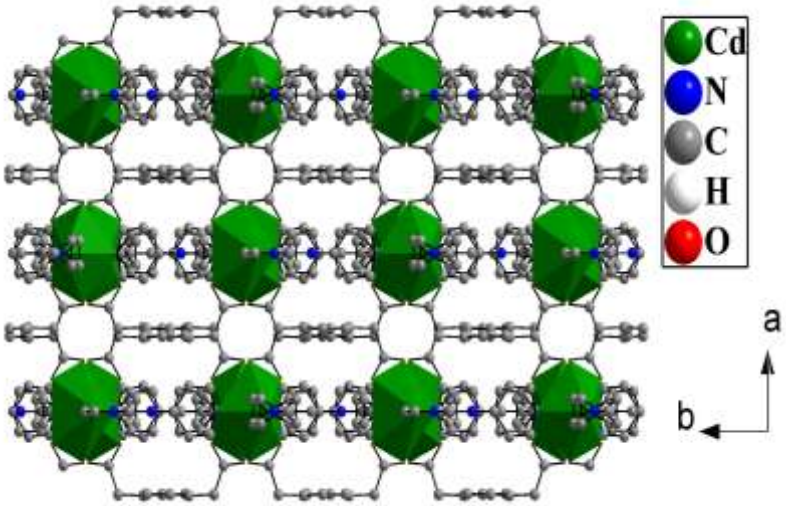

(b)

Fig. 3.6 (a) Figure shows the two-dimensional connectivity among Cd^{2+} ions, PDA and 2,4,5-tri-4-pyridyl-1H-imidazole ligands in $[Cd(PDA)(L)_2]$ (PDA = 1,4-phenylenediacetate and L = 2,4,5-tri-4-pyridyl-1H-imidazole), **3.1**. (b) The three dimensional packing arrangement of the two dimensional structures.

In the two-dimensional structure, PDA acts as simple connector (connects two Cd^{2+} ions). Whereas L ligand acts as 3-connected node and the Cd^{2+} ion acts four connected node (see Fig. 3.7). If you consider the overall connectivity, then the two-dimensional structure reduced to a binodal structure with Schläfli symbol $(4^1.5^3.7^2)(4^1.5^2)_2$.

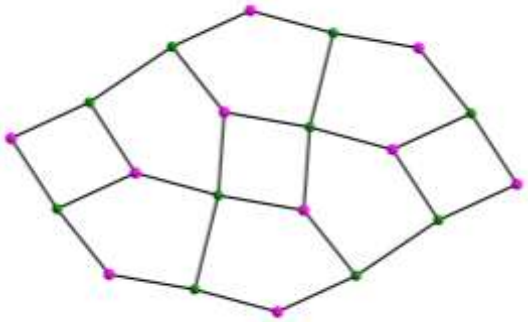

Fig. 3.7 Figure shows the network structure based on 3-connected L ligands and four connected Cd^{2+} ions of $[Cd(PDA)(L)_2]$, **3.1**.

3.3.3 Dye sorption studies. RBBR, OG and MO were chosen as the anionic dyes and MB and RhB were selected as the cationic dyes for the dye sorption experiment. Compound **3.1** showed 43% sorption of RBBR dye in 5 minutes and 95% sorption in 5 hrs (Fig. 3.8). Sorption of OG, MO (smaller anionic dye) and MB, RhB (larger cationic dye) are relatively small with 41%, 27%, 34%, 5%, respectively, in 5 hrs (see Fig. 3.9- Fig. 3.12). Visual photographs of the time dependent sorption studies in all the five systems are shown in Fig. 3.13-Fig. 3.17.

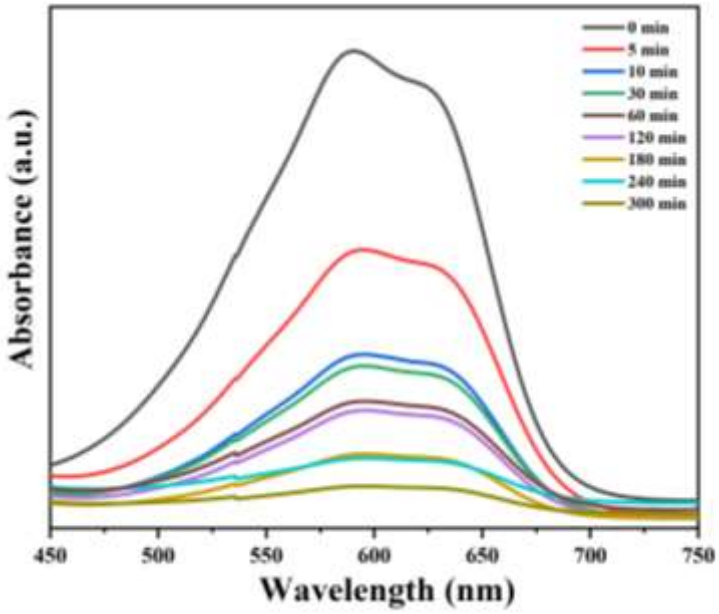

Fig. 3.8 UV-Vis absorption spectra of Remazol Brilliant Blue R (RBBR) during the time dependent sorption study using compound **3.1**.

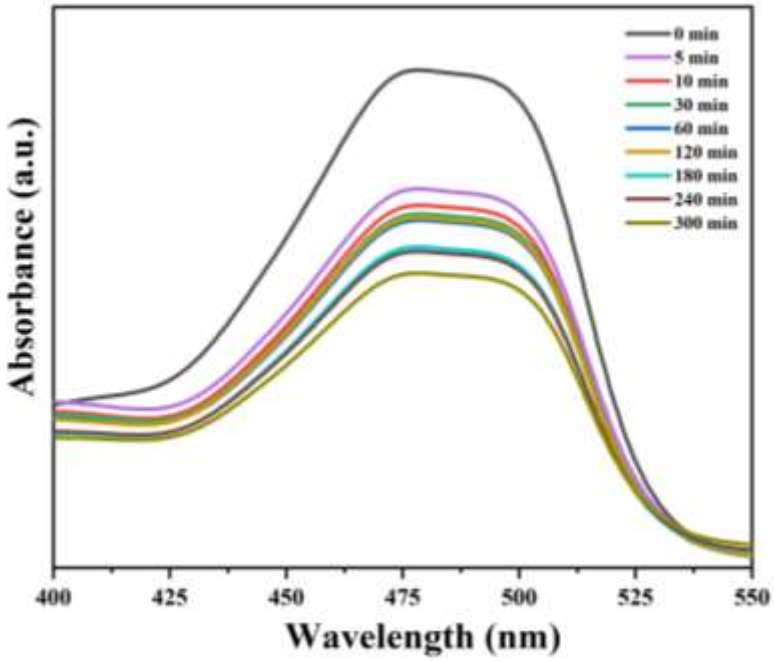

Fig. 3.9 UV-Vis absorption spectra of Orange G (OG) during the time dependent sorption study using compound **3.1**.

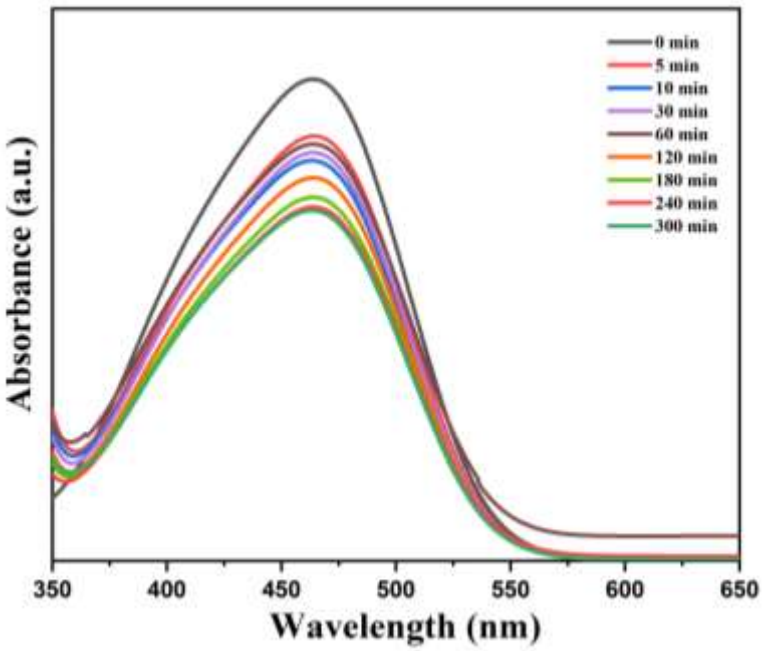

Fig. 3.10 UV-Vis absorption spectra of Methyl Orange (MO) during the time dependent sorption study using compound **3.1**.

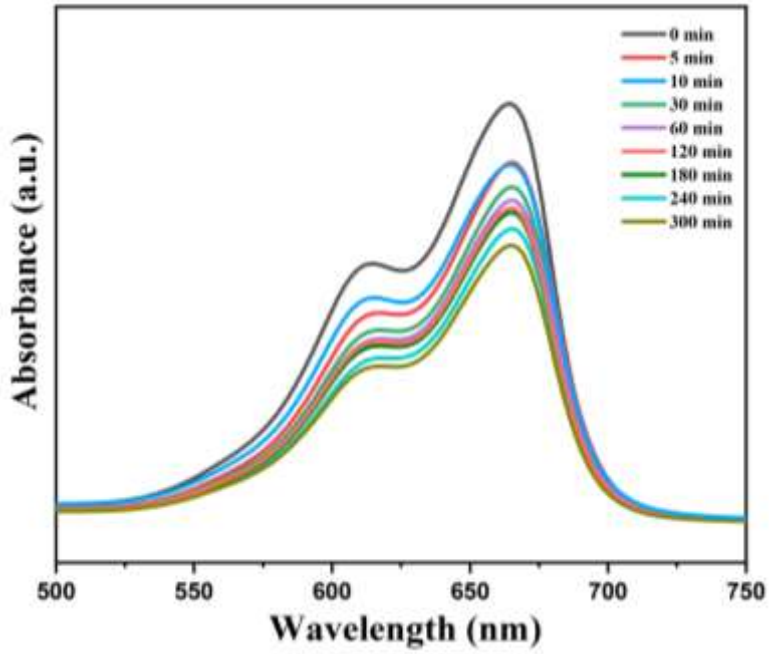

Fig. 3.11 UV-Vis absorption spectra of Methylene Blue (MB) during the time dependent sorption study using compound **3.1**.

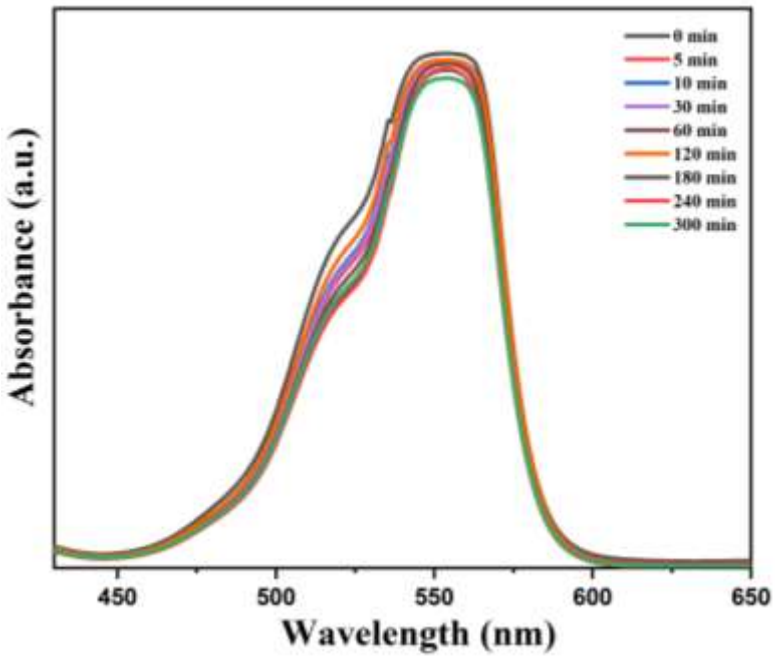

Fig. 3.12 UV-Vis absorption spectra of Rhodamine B (RhB) during the time dependent sorption study using compound **3.1**.

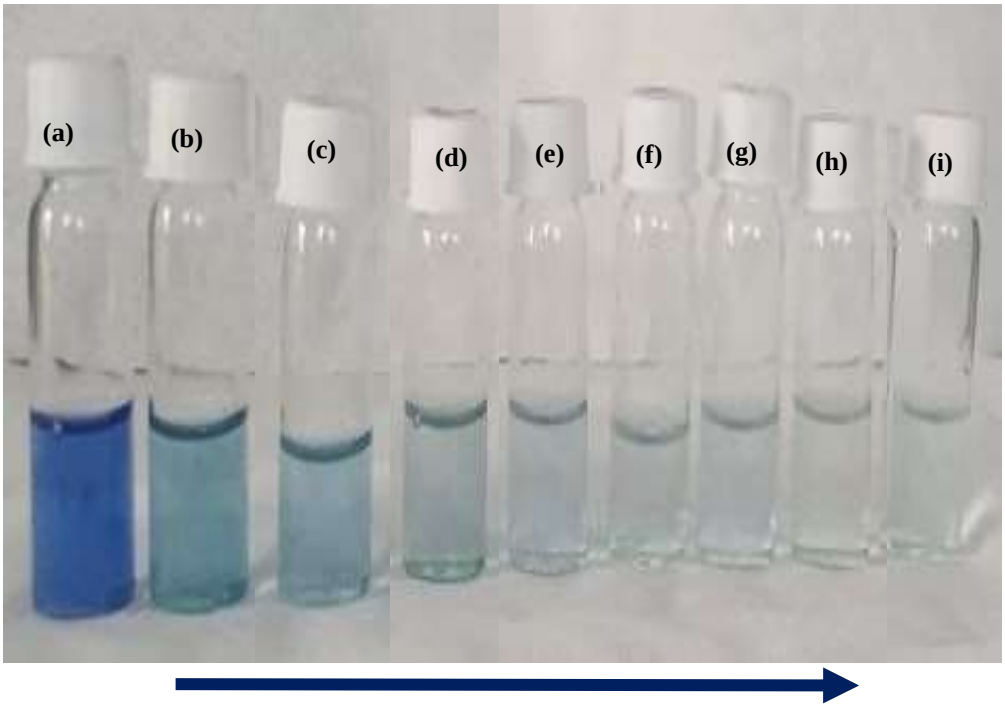

Fig. 3.13 Figure shows the photographs of colour intensity changes of the RBBR during the sorption study: (a) initial solution, (b) after 5 min, (c) after 10 min, (d) after 30 min, (e) after 60 min, (f) after 120 min, (h) after 180 min, (h) after 240 min, (i) after 300 min.

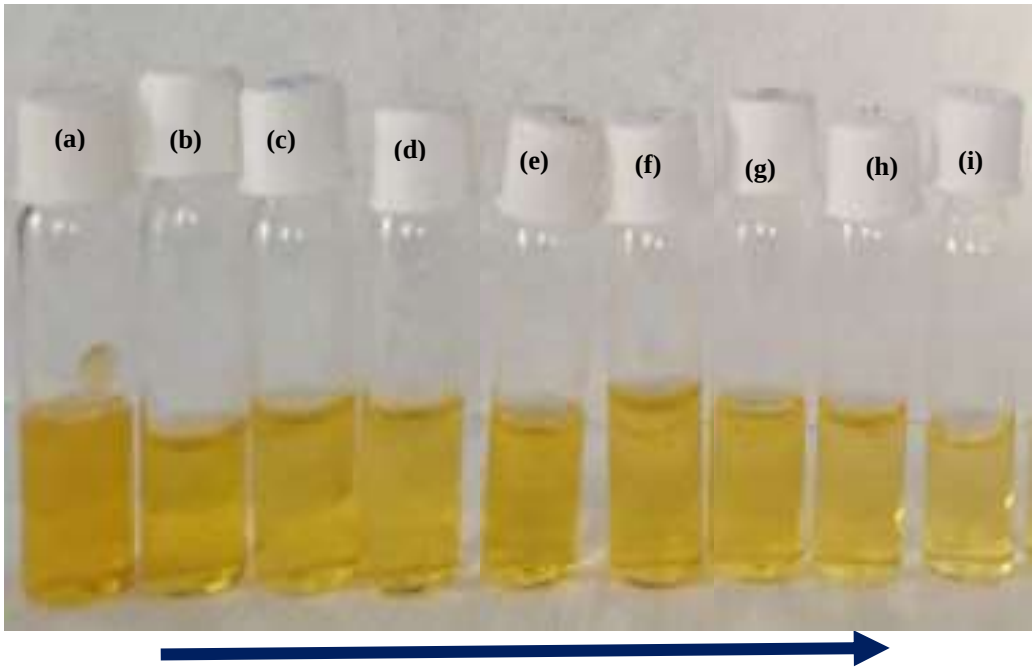

Fig. 3.14 Figure shows the photographs of colour intensity changes of the OG during the sorption study: (a) initial solution, (b) after 5 min, (c) after 10 min, (d) after 30 min, (e) after 60 min, (f) after 120 min, (h) after 180 min, (h) after 240 min, (i) after 300 min.

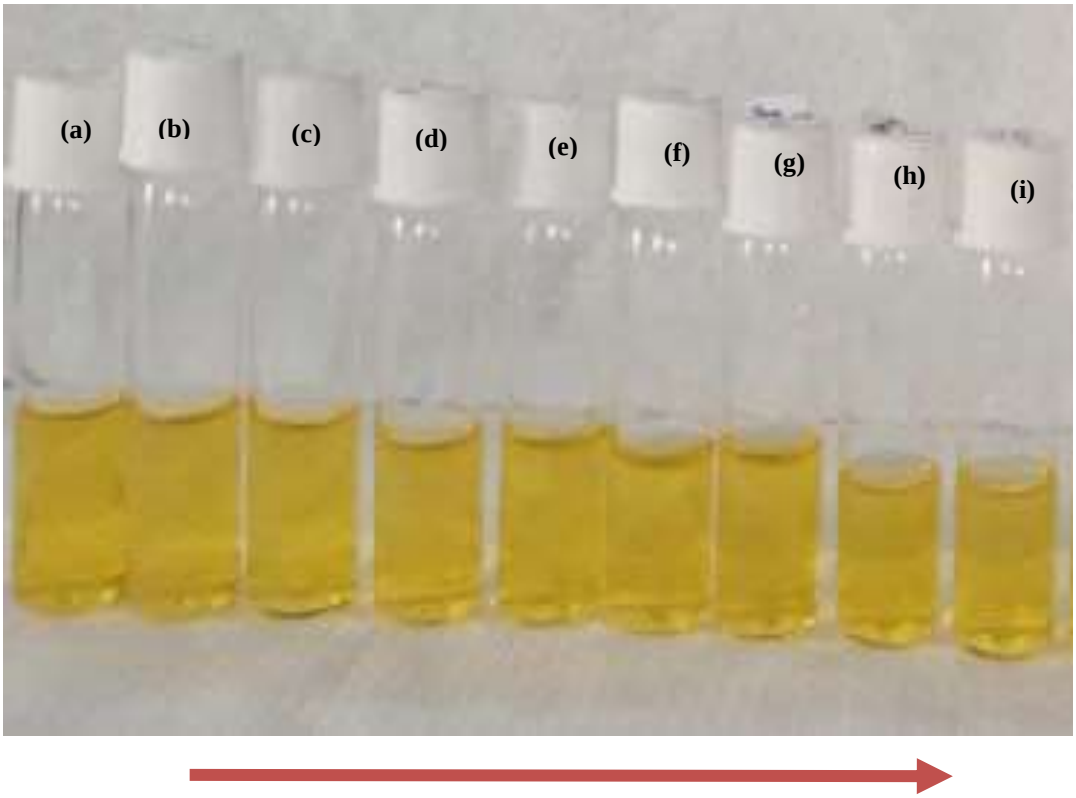

Fig. 3.15 Figure shows the photographs of colour intensity changes of the MO during the sorption study: (a) initial solution, (b) after 5 min, (c) after 10 min, (d) after 30 min, (e) after 60 min, (f) after 120 min, (h) after 180 min, (h) after 240 min, (i) after 300 min.

Fig. 3.16 Figure shows the photographs of colour intensity changes of the MB during the sorption study: (a) initial solution, (b) after 5 min, (c) after 10 min, (d) after 30 min, (e) after 60 min, (f) after 120 min, (h) after 180 min, (h) after 240 min, (i) after 300 min.

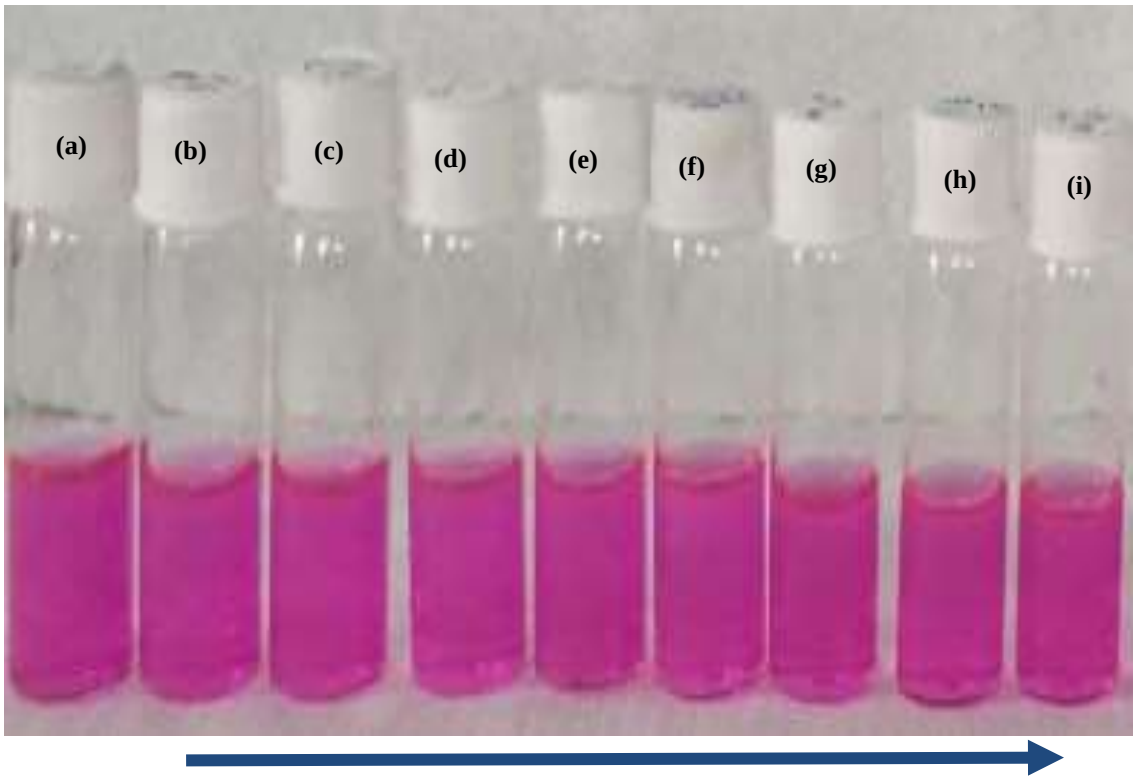

Fig. 3.17 Figure shows the photographs of colour intensity changes of the RhB during the sorption study: (a) initial solution, (b) after 5 min, (c) after 10 min, (d) after 30 min, (e) after 60 min, (f) after 120 min, (h) after 180 min, (h) after 240 min, (i) after 300 min.

This result shows the higher sorption behaviour of **3.1** towards larger anionic dye RBBR. This is probably due to the electrostatic and π···π interactions between the electron deficient organic ligands and larger anionic dyes. For the case of MB and RhB due to their cationic nature, the electrostatic repulsions prevent efficient sorption. In spite of anionic nature, the sorption of OG and MO is also negligible. This is probably due to less efficient electrostatic interactions owing to their smaller size.

The RBBR sorption capacity of compound **3.1** was investigated by measuring the absorption spectra using five different concentrations of RBBR. It was observed that compound **3.1** sorbed 30.83 mg g^{-1} of RBBR from 5×10^{-5} M (31.32 mg L^{-1}) RBBR solution and 150.78 mg g^{-1} of RBBR from 25×10^{-5} M (156.62 mg L^{-1}) RBBR solution within 5 hrs (Fig. 3.18). The dye desorption property of RBBR@**3.1** was checked by dissolving RBBR@**3.1** in water for 48 hrs to confirm whether the RBBR sorbed only at the surface of **3.1**. There is no trace of RBBR dye from RBBR@**3.1** were observed in water suggesting the strong molecular level interactions.

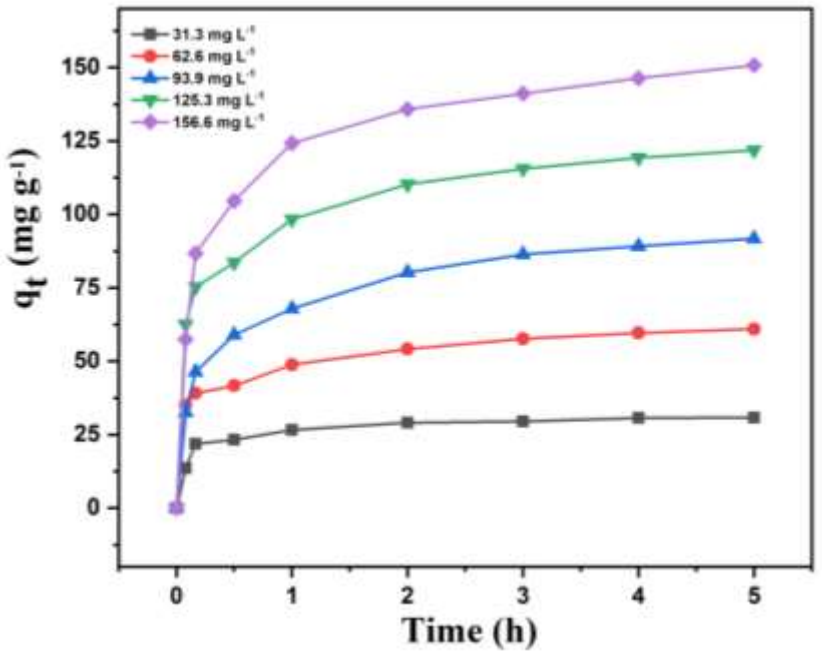

Fig. 3.18 Time-dependent sorption studies with five different concentrations of RBBR dye using compound **3.1** (where q_t represent sorption capacity at time t).

Furthermore, the kinetic model was explored to explain the RBBR sorption behaviour towards **3.1**. It was found that pseudo-second-order kinetics model was fitted with high coefficient R^2 (0.998) as shown in Table 3.4. The following equation describes the pseudo-second-order kinetics model.[3.76]

$$t/q_t = 1/K_2 q^2_e + t/q_e$$

here q_t refers to the sorption capacity at time t(h), K_2 is the rate constant of second-order sorption (h g mg^{-1}) and q_e gives the sorption capacity at equilibrium. From the plot of t/q_t versus t, in the case of RBBR dye towards **3.1**, shown in Fig. 3.19, straight lines could be fitted, from which values of q_e and K_2 can be determined from the slope and intercept, respectively.

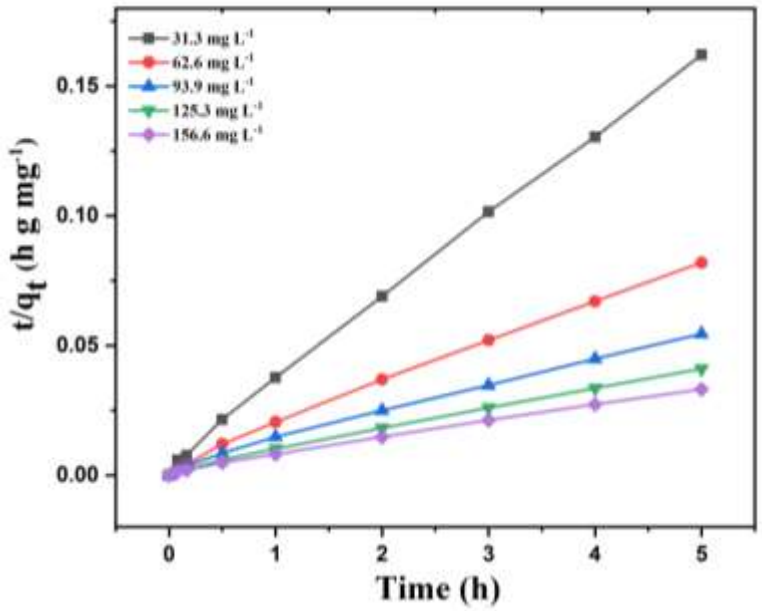

Fig. 3.19 Simulation of a pseudo-second-order kinetic model for the sorption study of RBBR dye using compound **3.1**.

Table 3.4: Pseudo-second-order kinetic parameters for RBBR dye sorption into $[Cd(PDA)(L)_2]$, **3.1**.

Adsorbent	q_e(mg g^{-1})	K_2 (h g mg^{-1})	R^2
Cd-MOF	31.23	0.292	0.998
	61.50	0.112	0.996
	93.63	0.051	0.995
	123.15	0.056	0.997
	152.20	0.042	0.997

The Langmuir isotherm was also employed to understand the mechanism of the sorption. The following equation describes the Langmuir model.[3.1,3.77]

$$c_e/ q_e = c_e/ q_m + 1 /q_m K_L$$

here c_e is the equilibrium concentration of the sorbed dye (mg L^{-1}), K_L gives the Langmuir sorption constant (L mg^{-1}) and q_m is the maximum sorption capacity of the adsorbent (mg g^{-1}). The plot of c_e/q_e versus c_e of RBBR@**3.1** leads to a straight line (in Fig. 3.20), these slope and intercept produced the values of K_L and q_m, respectively, as shown in Table 3.5. The high correlation coefficient R^2 value (1.00) for RBBR clearly suggested that the sorption of RBBR dye is well fitted with the Langmuir model.

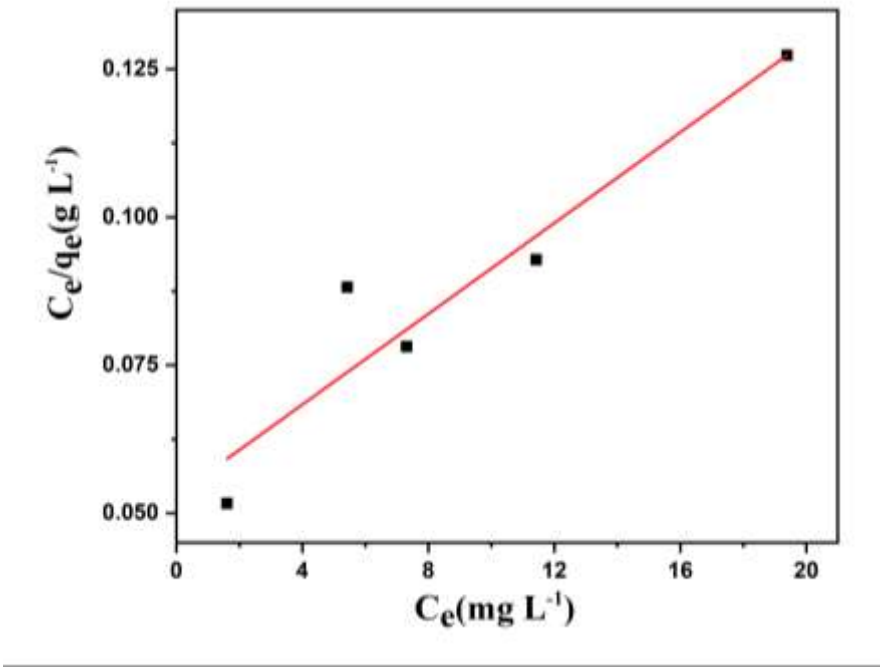

Fig. 3.20 Langmuir model for RBBR dye sorbed into compound **3.1**.

Table 3.5: Parameters of Langmuir model for RBBR dye sorption into [Cd(PDA)$(L)_2$], **3.1.**

Adsorbent	Dye	K_L (L mg^{-1})	Q_m (mg g^{-1})	R^2
Cd-MOF	RBBR	0.071	263.15	1

Finally, the crystallinity and stability of compound **3.1** was rechecked by PXRD after the RBBR dye sorption process, as shown in Fig. 3.21. The PXRD pattern of different composite (RBBR@**3.1** after the dye consuming process is smoothly matches with the experimental one for the fresh compound, which indicates that the MOF retains its crystallinity to a good extent. A summary of RBBR dye sorption behaviours using various materials are shown in table 3.6.

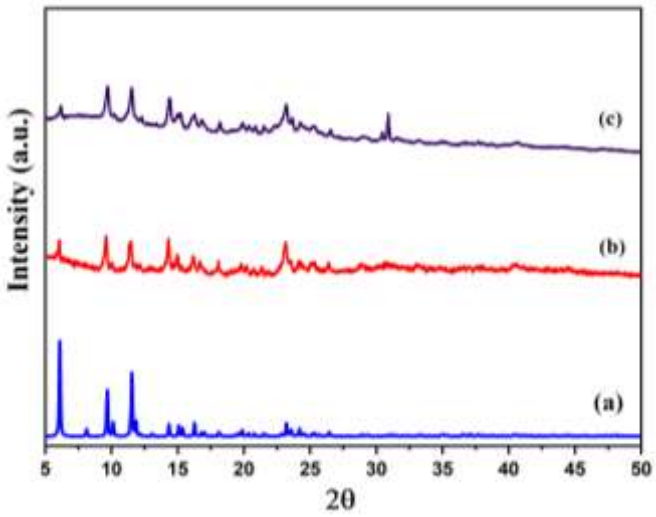

Fig. 3.21 Powder XRD (CuKα) patterns of $[Cd(PDA)(L)_2]$, **3.1**: (a) simulated from single crystal X-ray data, (b) experimental. (c) RBBR@ **3.1** after 300 min.

Table 3.6: A Summary of RBBR dye sorption using various materials.

Materials	Efficiency (%)	Time	Ref.
NMIL88(Fe)-Lac and HS NMIL88(Fe)-Lac	90.8 and 92.0	3 h and 2 h	79
ZIF-8 and ZIF-67	98 and 95	2 h	80
TiO_2-ZrO_2- Laccase and TiO_2-ZrO_2-SiO_2- Laccase	90 and 76	24 h	81
Magnetic copper alginate beads	75.8	4 h	82
CS-SA/ALG/MTN	54.3	½ h	83
Immobilized laccase	64	48 h	84
PU microspheres	64.1	6 h	85
Trametes maxima IIPLC-32	92.3	—	86
Amberlyst A21	89.23	2½ h	87
Thuja orientalis (ACTOL)	82	5 h	88
$[Cd(PDA)(L)_2]$	95	5 h	This work

3.3.4 Metal ion detection. Compound **3.1** shows luminescence behaviour in aqueous medium at room temperature. The absorption spectrum of compound **3.1** is shown in Fig. 3.22. The aqueous dispersion of compound **3.1** exhibited blue emission centered at 398 nm upon excitation at 300 nm due to intraligand $\pi^* \rightarrow \pi$ and $\pi^* \rightarrow$ n transitions. The luminescence spectrum in the solid state shows emission at 488 nm upon excitation at 300 nm and this emission is red-shifted with respect to the ligand based emissions (see Fig. 3.23, Fig. 3.24). To explain the sensitivity of **3.1** towards a trace amount of metal ions, luminescence-based titration was carried out with the gradual addition of various metal ions into a quartz cuvette containing 2 mL distilled water and 50 mL water dispersion of **3.1**. For the addition of Fe^{3+} ions, it showed a gradual decrease of luminescence intensity as well as shift of the emission maximum from 398 nm to 445 nm (Fig. 3.25). For the addition of Cr^{3+} ions, the emission maximum shifted from 398 nm to 439 nm along with a decrease in emission intensity (Fig. 3.26). In the case of Al^{3+} ions, a decrease of luminescence intensity was observed with a negligible shift of the emission maximum (Fig. 3.27). Similar luminescence-based experiments were also carried out with other metal ions such as Cd^{2+}, Cu^{2+}, Mg^{2+}, Ca^{2+}, Co^{2+}, K^+, Mn^{2+}, Pb^{2+}, Zn^{2+}, and Na^+ (see Fig. 3.28–3.32). The changes of luminescence intensity based on the emission at 398 nm in the case of all metal ions after the addition metal ions upto 48.30 µM shown in Fig. 3.33, as bar diagram with respect of $[I_0\text{-}I/I_0]$ *versus* analytes (I = luminescence intensity after the addition of metal ions at 48.30 µM, I_0 = luminescence intensity before the addition of metal ions). These results indicate that compound **3.1** shows significantly different luminescence behaviour towards these metal ions. The incremental addition of Fe^{3+} shows almost 88.60% of luminescence quenching, which comparatively higher than that of Cr^{3+} (69.58%) and Al^{3+} (59.01%). The incremental addition of other metal ions (upto 48.30 µM) in aqueous dispersion of compound **3.1** shows the low to moderate increasing order of luminescence intensity.

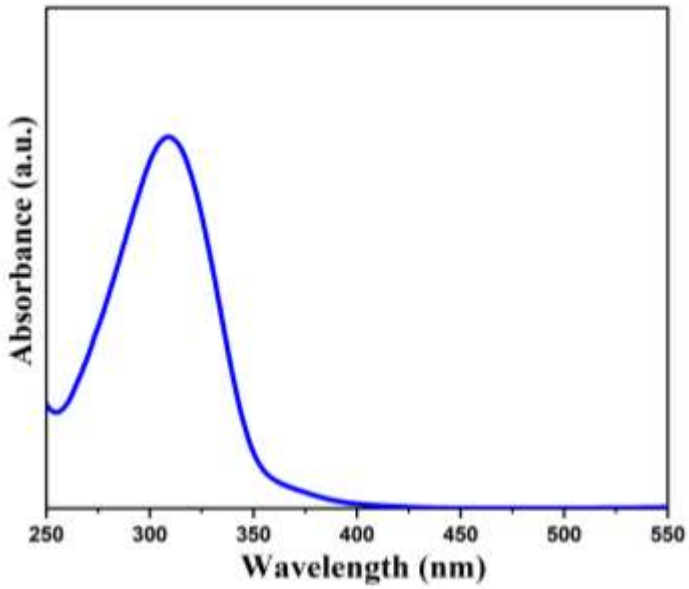

Fig. 3.22 Absorption spectrum of [Cd(PDA)$(L)_2$], **3.1**.

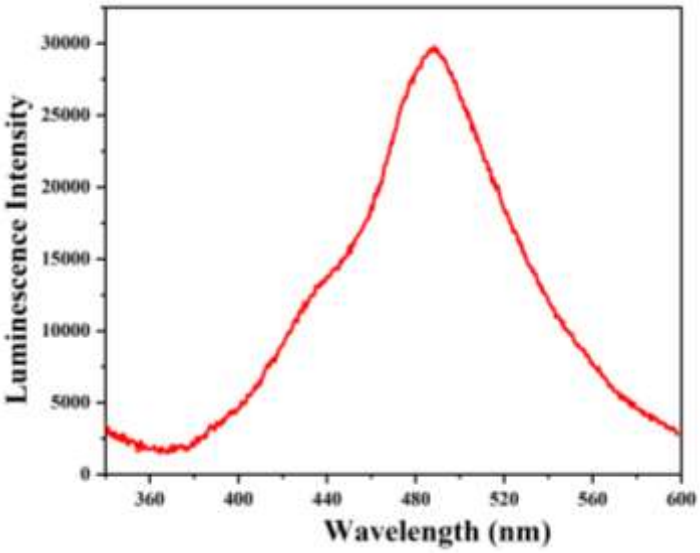

Fig. 3.23 Emission spectra of **3.1** in solid state (λ_{ex} = 300 nm).

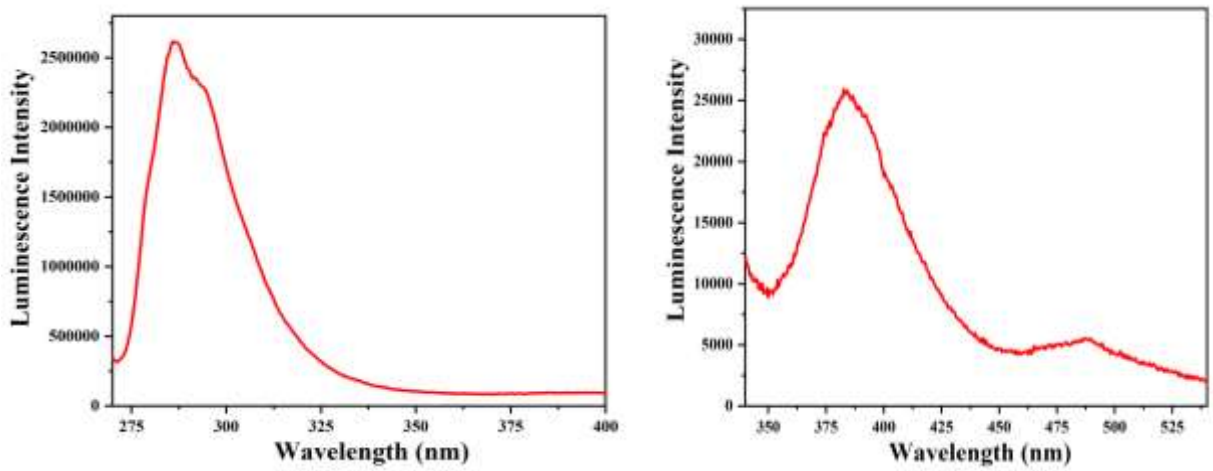

Fig. 3.24 (a) Emission spectra of 1,4-phenylenediacetic acid in solid state (λ_{ex} = 263 nm). (b) Emission spectra of 2,4,5-tri-4-pyridyl-1H-imidazole in solid state (λ_{ex} = 300 nm).

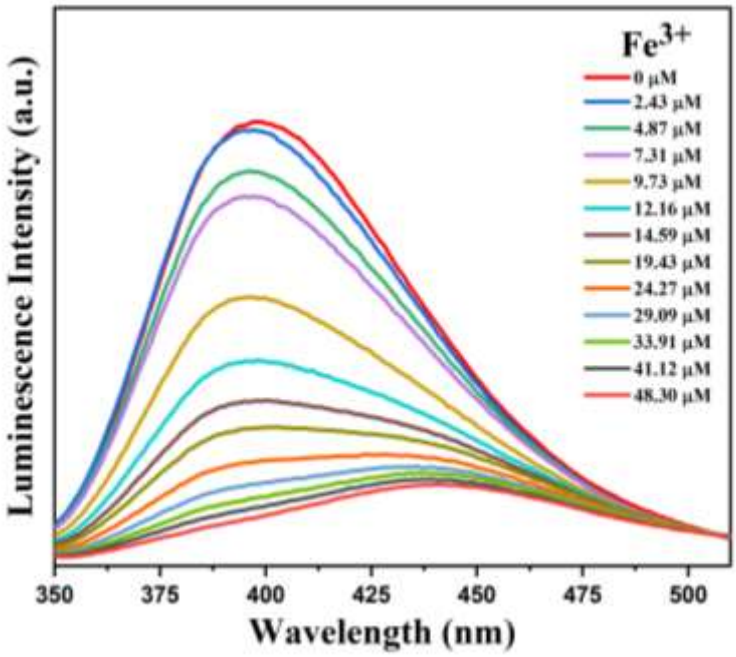

Fig. 3.25 Emission spectra of **3.1** dispersed in water upon incremental addition of water solution of Fe^{3+} ion (λ_{ex} = 300 nm). Final concentration of Fe^{3+} in the medium is indicated in the legend.

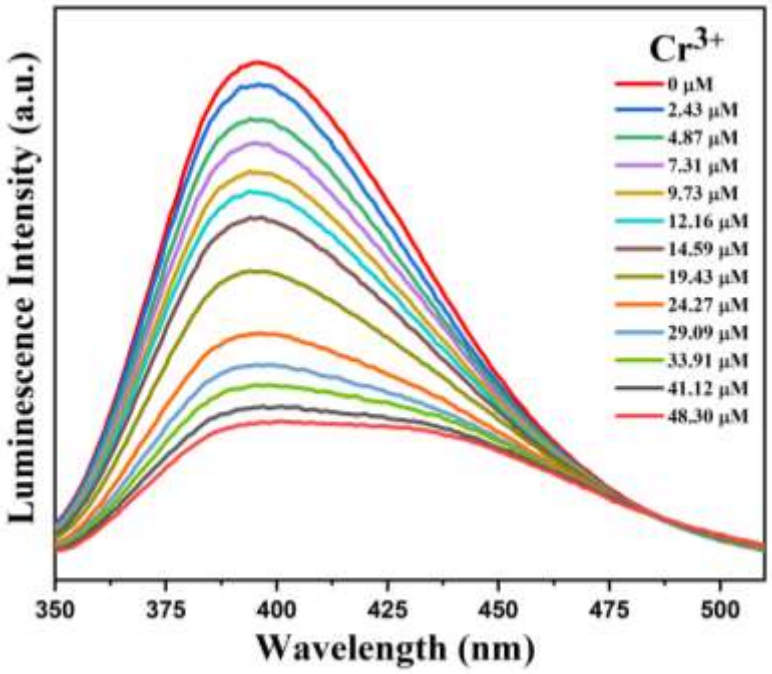

Fig. 3.26 Emission spectra of **3.1** dispersed in water upon incremental addition of water solution of Cr^{3+} ion (λ_{ex} = 300 nm). Final concentration of Cr^{3+}in the medium is indicated in the legend.

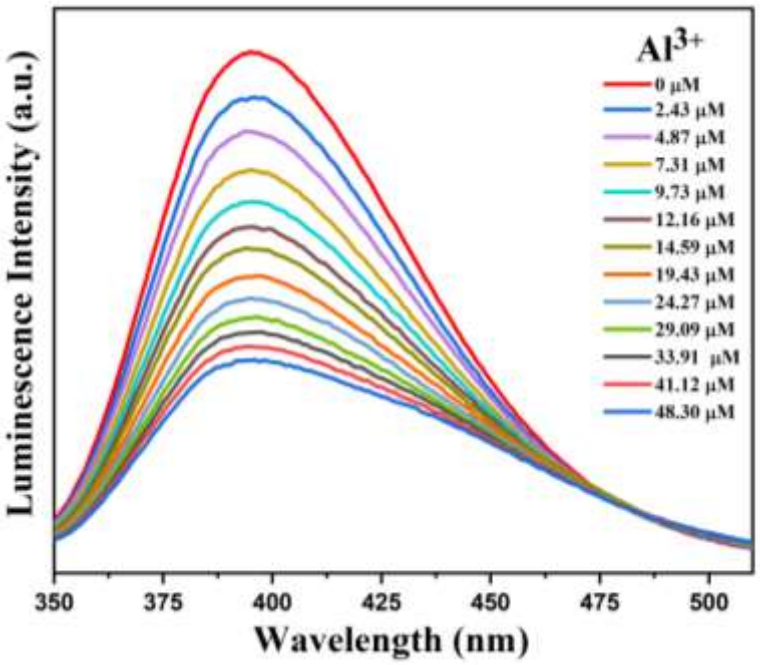

Fig. 3.27 Emission spectra of **3.1** dispersed in water upon incremental addition of water solution of Al^{3+} ion (λ_{ex} = 300 nm). Final concentration of Al^{3+} in the medium is indicated in the legend.

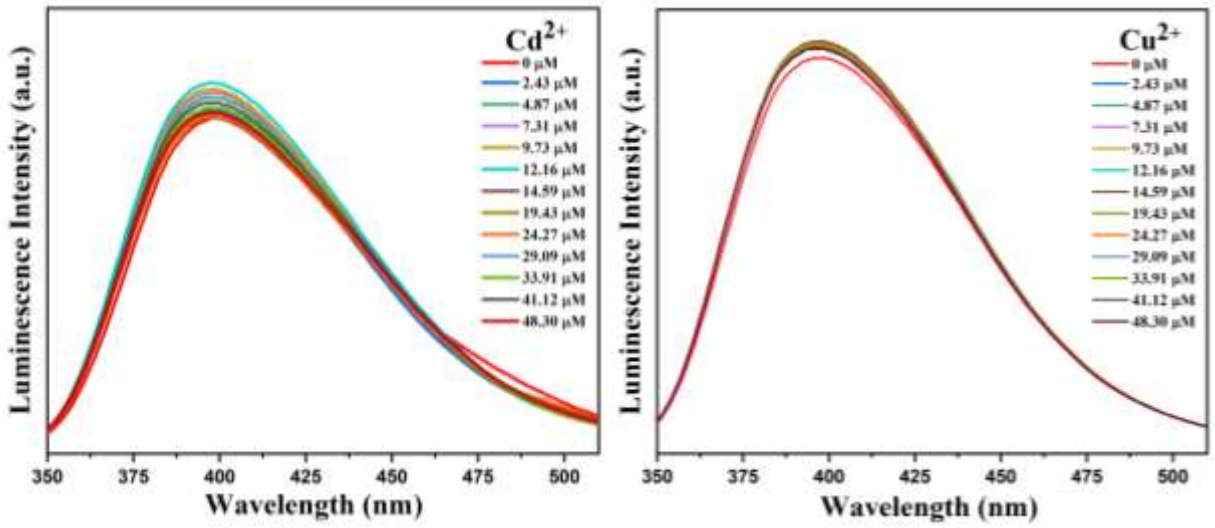

Fig. 3.28 (a) Emission spectra of **3.1** dispersed in water upon incremental addition of water solution of Cd^{2+} ions (λ_{ex} = 300 nm). Final concentration of Cd^{2+} ions in the medium is indicated in the legend. (b) Emission spectra of **3.1** dispersed in water upon incremental addition of water solution of Cu^{2+} ions (λ_{ex} = 300 nm). Final concentration of Cu^{2+} ions in the medium is indicated in the legend.

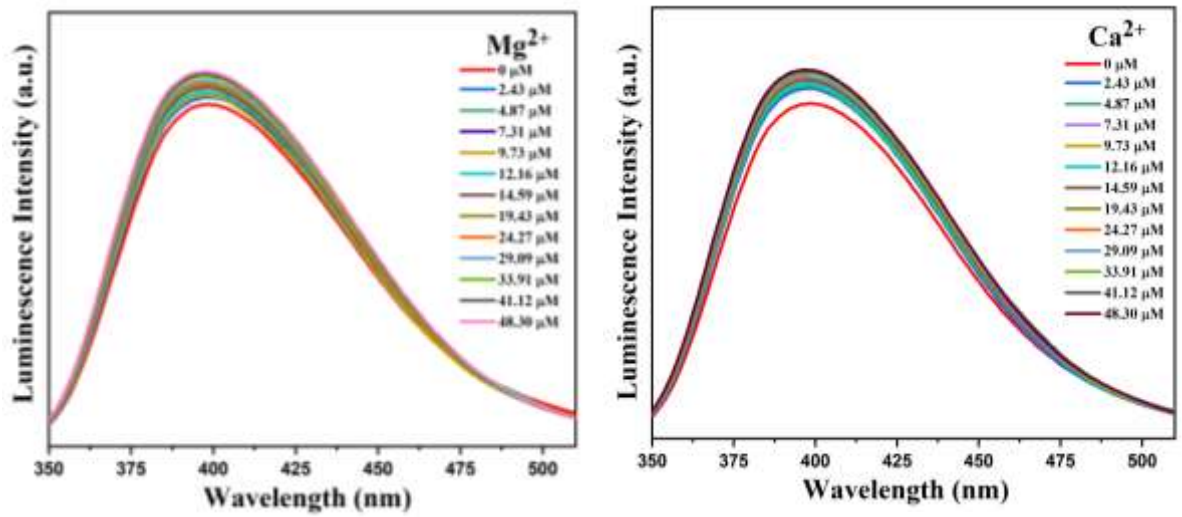

Fig. 3.29 Emission spectra of **3.1** dispersed in water upon incremental addition of water solution of Mg^{2+} ions (λ_{ex} = 300 nm). Final concentration of Mg^{2+} ions in the medium is indicated in the legend. (b) Emission spectra of **3.1** dispersed in water upon incremental addition of water solution of Ca^{2+} ions (λ_{ex} = 300 nm). Final concentration of Ca^{2+} ions in the medium is indicated in the legend.

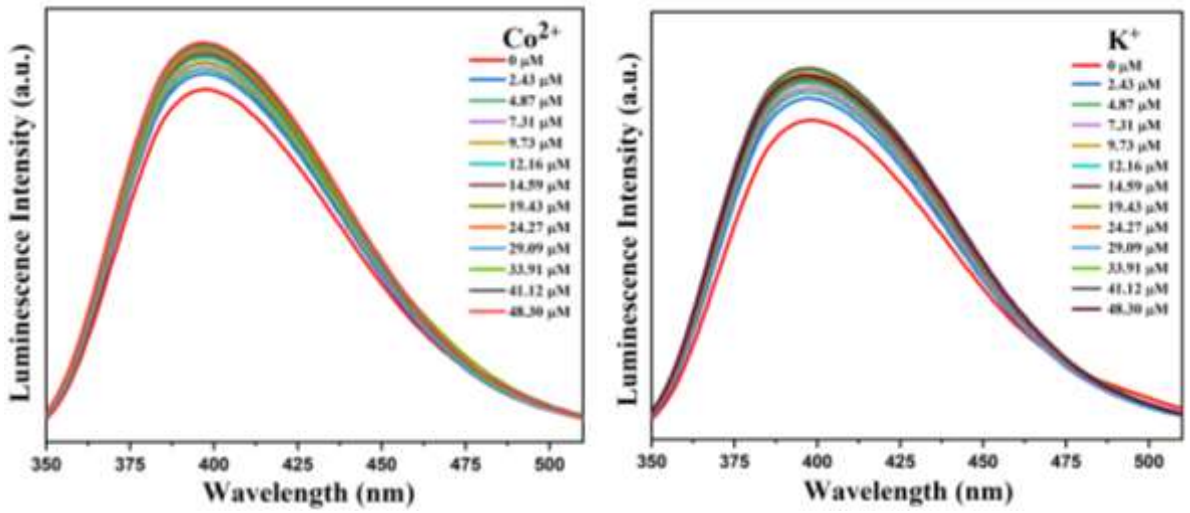

Fig. 3.30 Emission spectra of **3.1** dispersed in water upon incremental addition of water solution of Co^{2+} ions (λ_{ex} = 300 nm). Final concentration of Co^{2+} ions in the medium is indicated in the legend. (b) Emission spectra of **3.1** dispersed in water upon incremental addition of water solution of K^{+} ions (λ_{ex} = 300 nm). Final concentration of K^{+} ions in the medium is indicated in the legend.

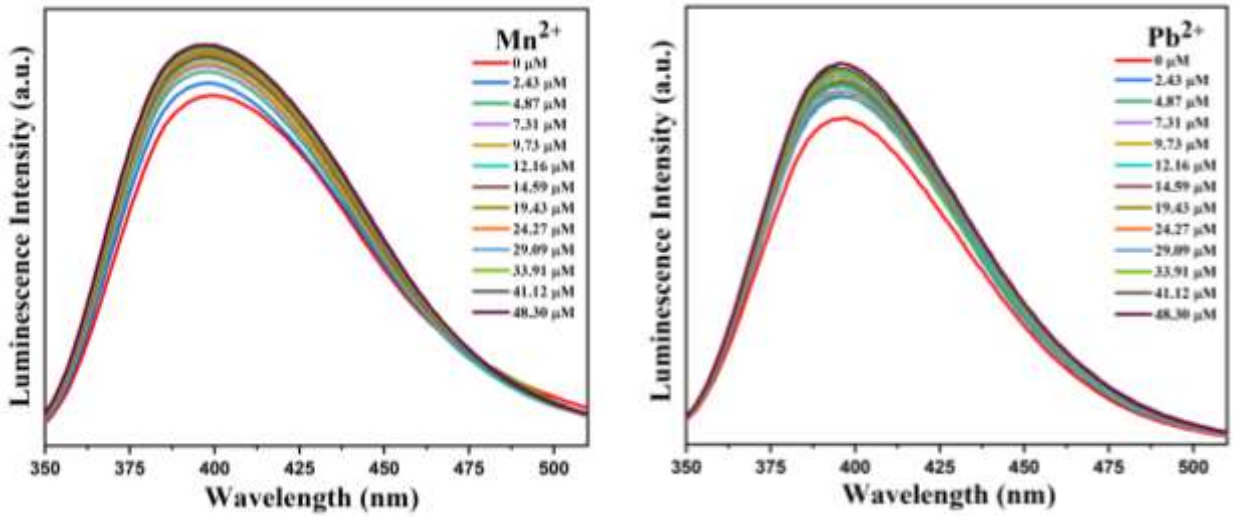

Fig. 3.31 (a) Emission spectra of **3.1** dispersed in water upon incremental addition of water solution of Mn^{2+} ions (λ_{ex} = 300 nm). Final concentration of Mn^{2+} ions in the medium is indicated in the legend. (b) Emission spectra of **3.1** dispersed in water upon incremental addition of water solution of Pb^{2+} ions (λ_{ex} = 300 nm). Final concentration of Pb^{2+} ions in the medium is indicated in the legend.

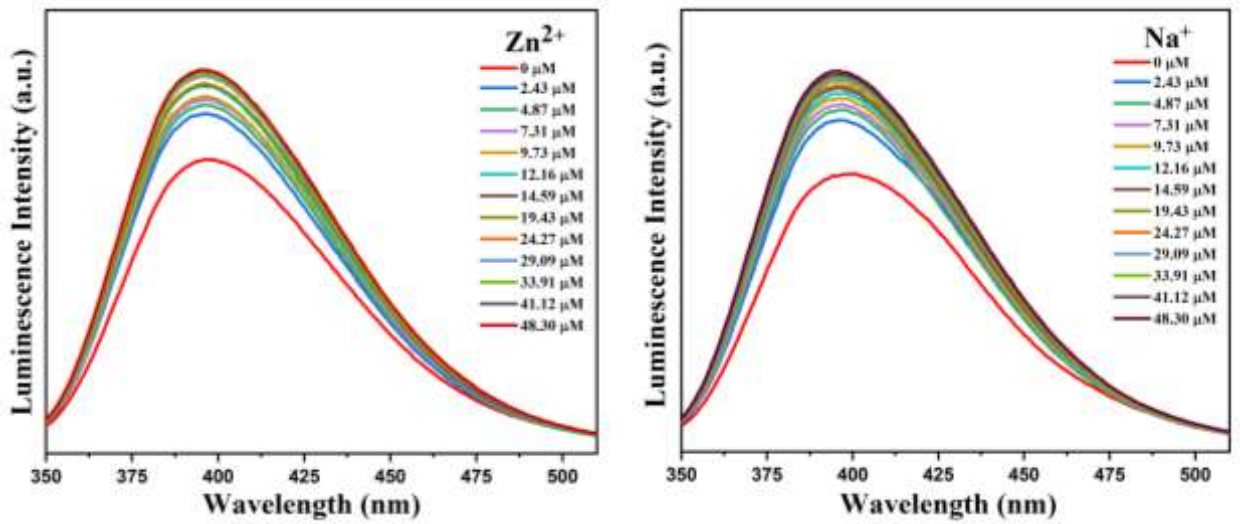

Fig. 3.32 (a) Emission spectra of **3.1** dispersed in water upon incremental addition of water solution of Zn^{2+} ions (λ_{ex} = 300 nm). Final concentration of Zn^{2+} ions in the medium is indicated in the legend. (b) Emission spectra of **3.1** dispersed in water upon incremental addition of water solution of Na^{+} ions (λ_{ex} = 300 nm). Final concentration of Na^{+} ions in the medium is indicated in the legend.

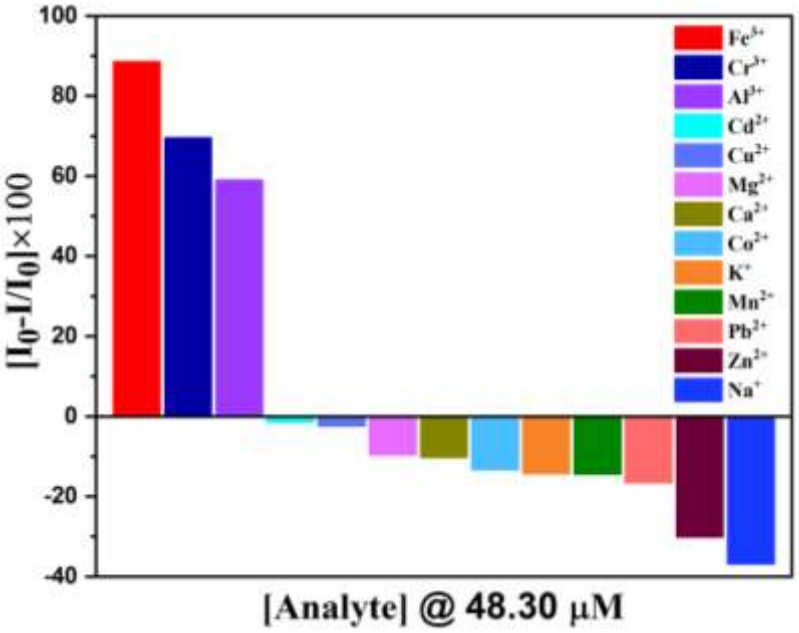

Fig. 3.33 Percentage of luminescence quenching and turn on of compound **3.1** (at 300 nm excitation) in presence of different metal ions with 48.30 μM concentration.

The limit of detections for the luminescence quenching responses in the presence of Fe^{3+}, Cr^{3+}, Al^{3+} ions have been calculated and the values are 75, 257 and 107 ppb for Fe^{3+}, Cr^{3+}, Al^{3+} ions, respectively (see Fig. 3.34-Fig. 3.36). The observed detection limit is comparable to the higher limit of U.S. Environmental Protection Agency (according to EPA the maximum Contaminant Levels of iron, chromium and aluminium are 300 ppb, 100 ppb, 200 ppb respectively).[3.78] We have also checked the selectivity of the compound **3.1** by observing the luminescence quenching effect of Fe^{3+} and Cr^{3+} in the presence of Cd^{2+}, Cu^{2+}, Mg^{2+}, Ca^{2+}, Co^{2+}, K^{+}, Mn^{2+}, Pb^{2+}, Zn^{2+} and Na^{+} ions. The photoluminescence spectrum of compound **3.1** in aqueous medium was recorded using specifically designed experimental protocol, and to this experimental strategies 2.43 μM of 5mM aqueous solution of metal ions was added in **3.1** with sequentially followed by the addition of 5mM aqueous solution of Fe^{3+} and Cr^{3+} ion solution continuously upto 48.30 μM and monitoring the corresponding emissions spectrums (see Fig. 3.37 and Fig. 3.38). Initially addition of various ions shows small luminescence turn on effect. However, the addition of aqueous solution of Fe^{3+} and Cr^{3+} ions give significant luminescence quenching, and the quenching efficiency of Fe^{3+} and Cr^{3+} remaining unaffected, even though further addition sequences. The sensitivity of the metal ions is also explained by using Stern-Volmer plots. The equation of Stern-Volmer (SV) is $(I_0/I) = K_{SV}[A]+1$, where I and I_0 are the luminescence intensities of the probe, after and before addition of the analytes, [A] is the molar concentration

and K_{SV} is the luminescence quenching constant respectively. As shown in Fig.3.39, the linear increase in $[I_0/I]$ of all metal ions, at concentration region up to 48.30 µM. With increasing concentration, the linear variation of SV plot generally increases due to static quenching. We have fitted the experimental data (up to 48.30 µM) in the S-V equation to get the value of quenching constants (K_{SV}), and the obtained K_{SV} values are 23.29×10^4 M^{-1}, 5.06×10^4 M^{-1}, 3.09×10^4 M^{-1} for Fe^{3+}, Cr^{3+}, Al^{3+} ions, respectively (Fig. 3.40).

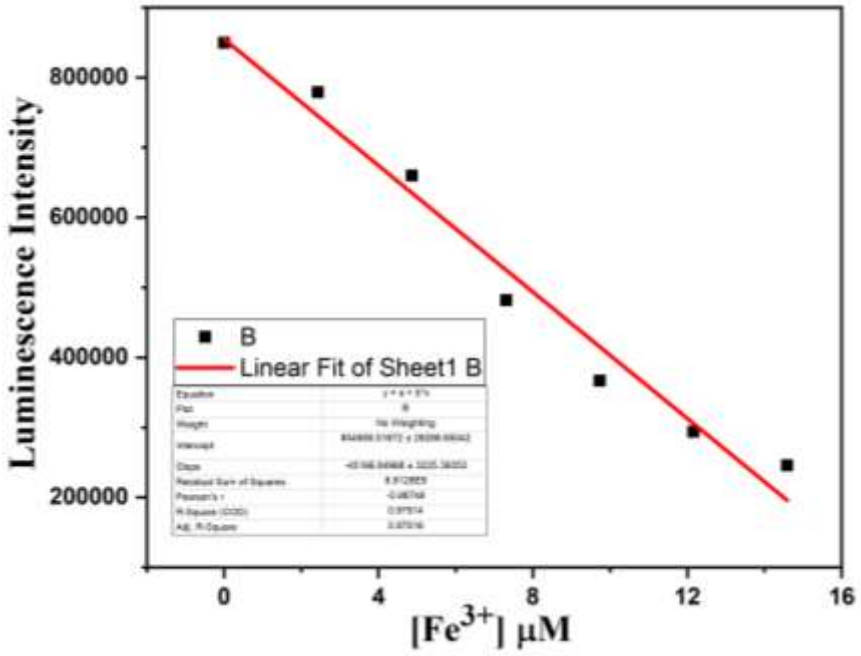

Fig. 3.34 The plot of the changes of luminescence intensity of compound **3.1** (λ_{em} = 398 nm) vs concentration of Fe^{3+} solution (upto 14.59 µM) indicating the detection limit, which calculated using the equation, LOD = 3σ/m, where σ = standard deviation of blank determination and m = slope of the linear curve.

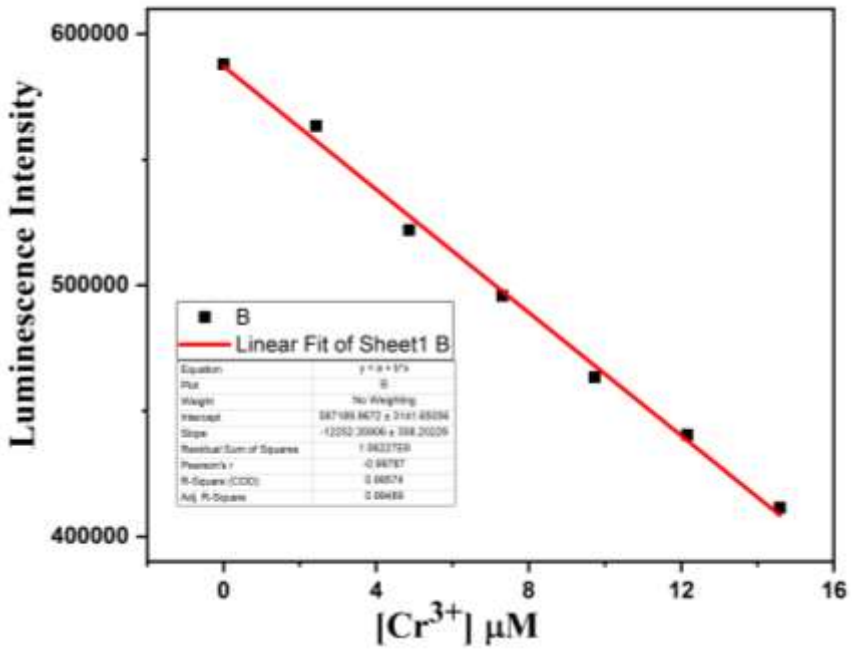

Fig. 3.35 The plot of the changes of luminescence intensity of compound **3.1** (λ_{em} = 398 nm) vs concentration of Cr^{3+} solution (upto 14.59 µM) indicating the detection limit, which calculated using the equation, LOD = 3σ/m, where σ = standard deviation of blank determination and m = slope of the linear curve.

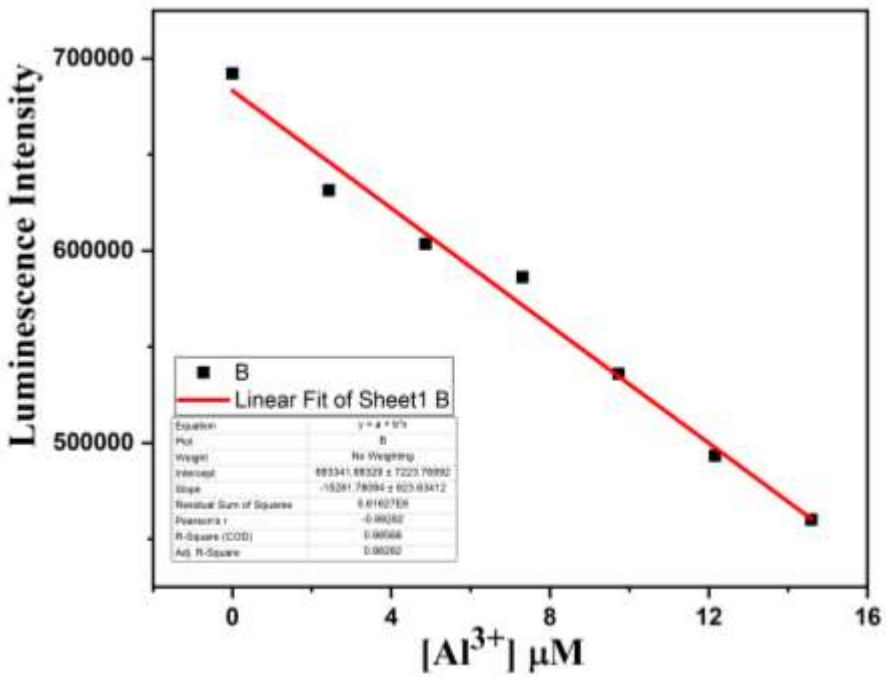

Fig. 3.36 The plot of the changes of luminescence intensity of compound **3.1** (λ_{em} = 398 nm) vs concentration of Al^{3+} solution (upto 14.59 µM) indicating the detection limit, which calculated using the equation, LOD = 3σ/m, where σ = standard deviation of blank determination and m = slope of the linear curve.

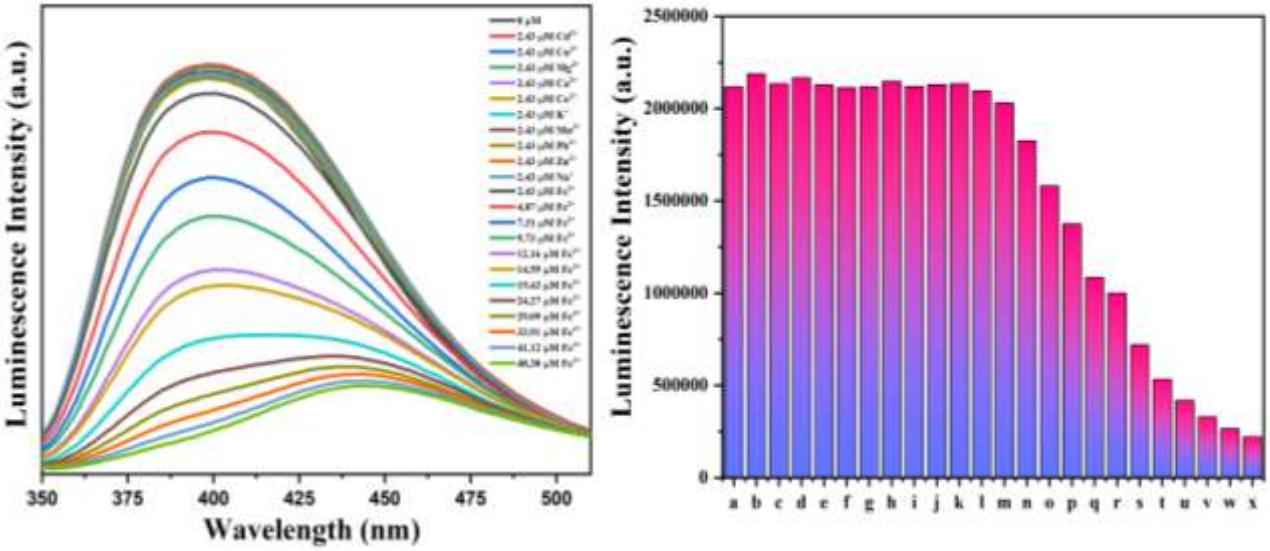

Fig. 3.37 (a) Emission spectra of **3.1** dispersed in water upon incremental addition of Fe^{3+}solution in the presence of 2.43 μM concentration of various metal ions (λ_{ex} = 300 nm). (b) Bar diagram presenting the luminescence intensity (observed at 398 nm) after the consecutive addition of the analytes. The composition and concentration of the system were as follows: (a) **3.1** in aqueous dispersion, (b) a + 2.43 μM Cd^{2+}, (c) b + 2.43 μM Cu^{2+}, (d) c + 2.43 μM Mg^{2+}, (e) d + 2.43 μM Ca^{2+}, (f) e + 2.43 μM Co^{2+}, (g) f + 2.43 μM K^{+}, (h) g + 2.43 μM Mn^{2+}, (i) h + 2.43 μM Pb^{2+}, (j) i + 2.43 μM Zn^{2+}, (k) j + 2.43 μM Na^{+}, (l) k + 2.43 μM Fe^{3+}, (m) l + 2.43 μM Fe^{3+}, (n) m + 2.43 μM Fe^{3+}, (o) n + 2.43 μM Fe^{3+}, (p) o + 2.43 μM Fe^{3+}, (q) p + 2.43 μM Fe^{3+}, (r) q + 4.87 μM Fe^{3+}, (s) r + 4.87 μM Fe^{3+}, (t) s + 4.87 μM Fe^{3+}, (u) q + 4.87 μM Fe^{3+}, (v) r + 4.87 μM Fe^{3+}, (w) s + 7.31 μM Fe^{3+}, and (x) s + 7.31 μM Fe^{3+}.

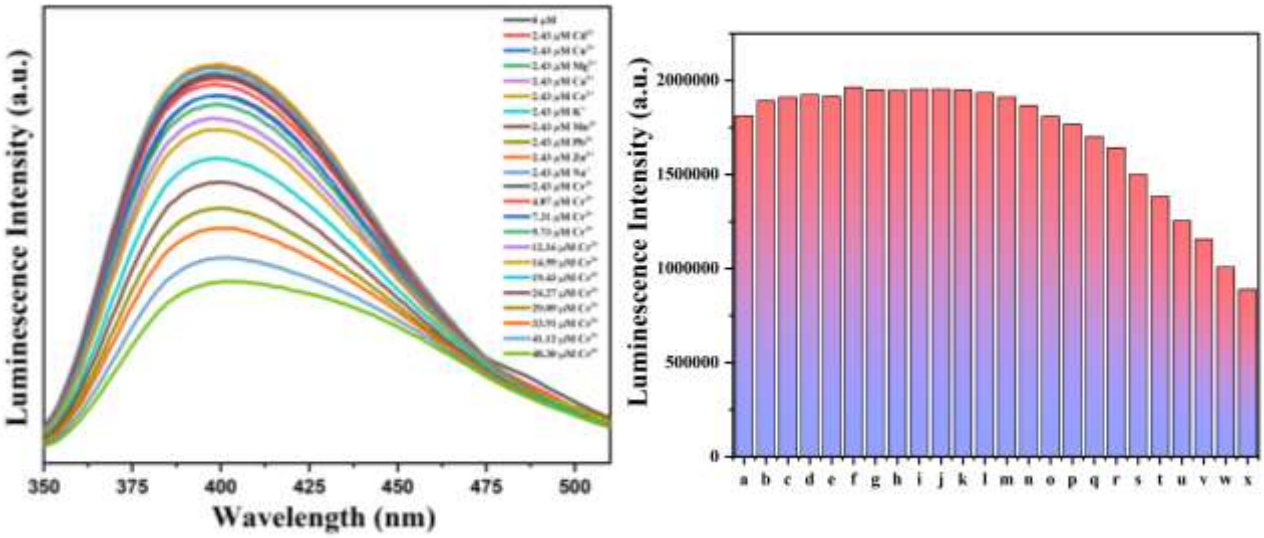

Fig. 3.38 (a) Emission spectra of **3.1** dispersed in water upon incremental addition of Cr^{3+}solution in the presence of 2.43 µM concentration of various metal ions (λ_{ex} = 300 nm). (b) Bar diagram presenting the luminescence intensity (observed at 398 nm) after the consecutive addition of the analytes. The composition and concentration of the system were as follows: (a) **3.1** in aqueous dispersion, (b) a + 2.43 µM Cd^{2+}, (c) b + 2.43 µM Cu^{2+}, (d) c + 2.43 µM Mg^{2+}, (e) d + 2.43 µM Ca^{2+}, (f) e + 2.43 µM Co^{2+}, (g) f + 2.43 µM K^{+}, (h) g + 2.43 µM Mn^{2+}, (i) h + 2.43 µM Pb^{2+}, (j) i + 2.43 µM Zn^{2+}, (k) j + 2.43 µM Na^{+}, (l) k + 2.43 µM Cr^{3+}, (m) l + 2.43 µM Cr^{3+}, (n) m + 2.43 µM Cr^{3+}, (o) n + 2.43 µM Cr^{3+}, (p) o + 2.43 µM Cr^{3+}, (q) p + 2.43 µM Cr^{3+}, (r) q + 4.87 µM Cr^{3+}, (s) r + 4.87 µM Cr^{3+}, (t) s + 4.87 µM Cr^{3+}, (u) q + 4.87 µM Cr^{3+}, (v) r + 4.87 µM Cr^{3+}, (w) s + 7.31 µM Cr^{3+}, and (x) s + 7.31 µM Cr^{3+}.

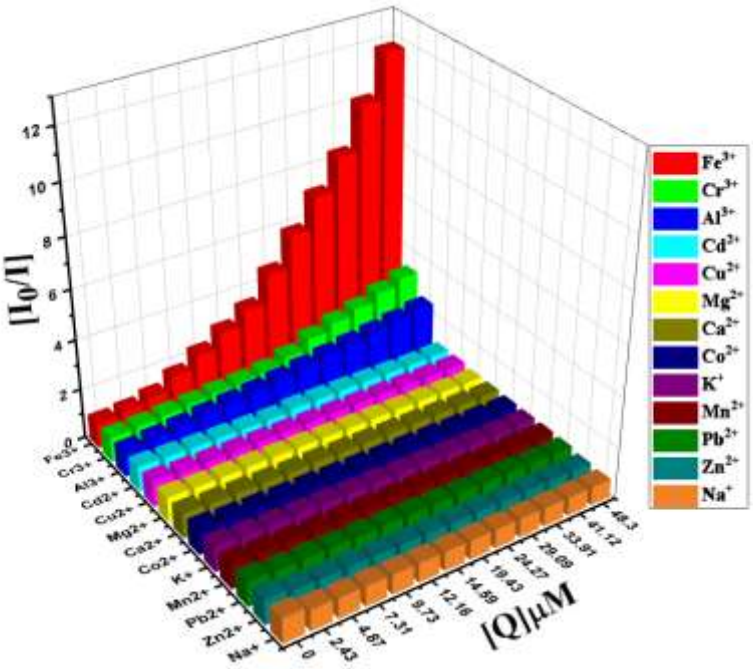

Fig. 3.39 Stern-Volmer plots of various metal ions in higher concentration range (upto 48.30 μM) for compound **3.1**.

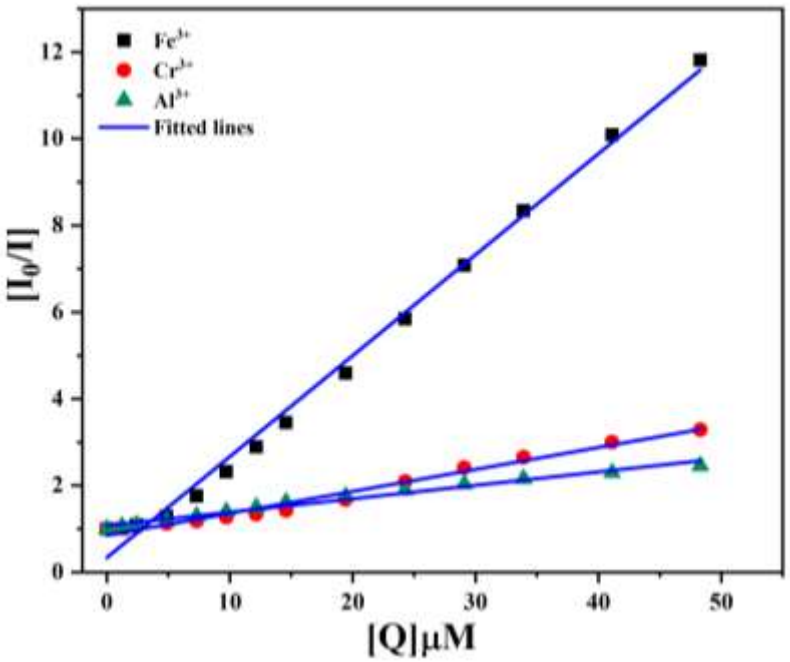

Fig. 3.40 The plot of I_0 /I of compound **3.1** (at 300 nm excitation wavelength) vs concentration of various metal ions upto 48.30 μM. I_0 and I are luminescence intensity in absence and presence of various metal ions, respectively.

The time-correlated single photon counting (TCSPC) of the compound **3.1** with the incremental addition of Fe^{3+}, Cr^{3+}, Al^{3+} metal ions were also checked (see Fig. 3.41-3.43 and Table 3.7). In all the three cases, the luminescence life time have been increased with the addition metal ions. This indicate the formation of charge transfer species through the molecular level interactions between metal ions ($Fe^{3+}/Cr^{3+/}Al^{3+}$) and compound **3.1**. The molecular level interactions through the formation of charge transfer species increased the structural rigidity. With the enhanced structural rigidity, the non-radiative decay pathways minimised. As a result the incremental values of luminescence life time have been observed with the addition of $Fe^{3+}/Cr^{3+}/Al^{3+}$ ions. In this respect titrations using absorption spectroscopy with the incremental addition of Fe^{3+}, Cr^{3+}, Al^{3+}, Cd^{2+}, Cu^{2+}, Mg^{2+}, Ca^{2+}, Co^{2+}, K^{+}, Mn^{2+}, Pb^{2+}, Zn^{2+}, and Na^{+} ions in aqueous dispersion of compound **3.1** is highly informative. For Fe^{3+}, Cr^{3+} and Al^{3+} ions, a new charge transfer bands have been observed at~375 nm and its intensity increased with the increasing concentration of metal ions. The presence of the charge transfer bands proved the static quenching baviour in presence of Fe^{3+}, Cr^{3+} and Al^{3+} ions. The quenching constant values for the three ions are in the order of Fe^{3+}> Cr^{3+}> Al^{3+}. This is according to the ease of formation of charge transfer species and their stability order. Absorption spectra of similar titrations remain unchanged in case of Cd^{2+}, Cu^{2+}, Mg^{2+}, Ca^{2+}, Co^{2+}, K^{+}, Mn^{2+}, Pb^{2+}, Zn^{2+} and Na^{+} ions (see Fig. 3.44-3.50). This studies indicate the sensing of the three metal ions are selective with respect to other common metal ions. Summary of sensing of Fe^{3+}, Cr^{3+} and Al^{3+} ions using MOF materials are shown in Table 3.8, Table 3.9 and Table 3.10.

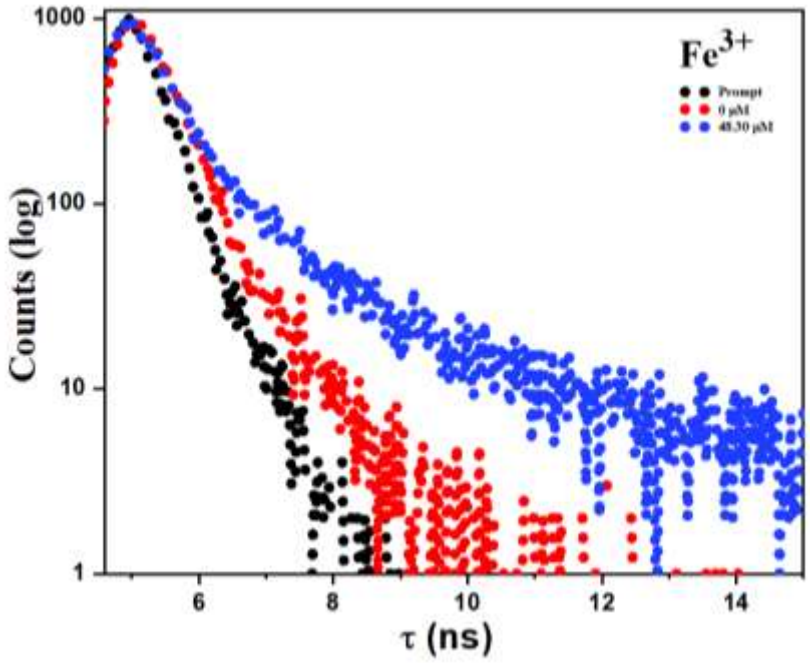

Fig. 3.41 Luminescence lifetime decay profile of compound **3.1** before and after the addition of the Fe^{3+} ions. The final concentration of Fe^{3+} ions in the medium is indicated in the legend. The instrument response function (prompt) is also shown. Here, λ_{ex} = 300 nm and λ_{em} = 398 nm were set during the experiment.

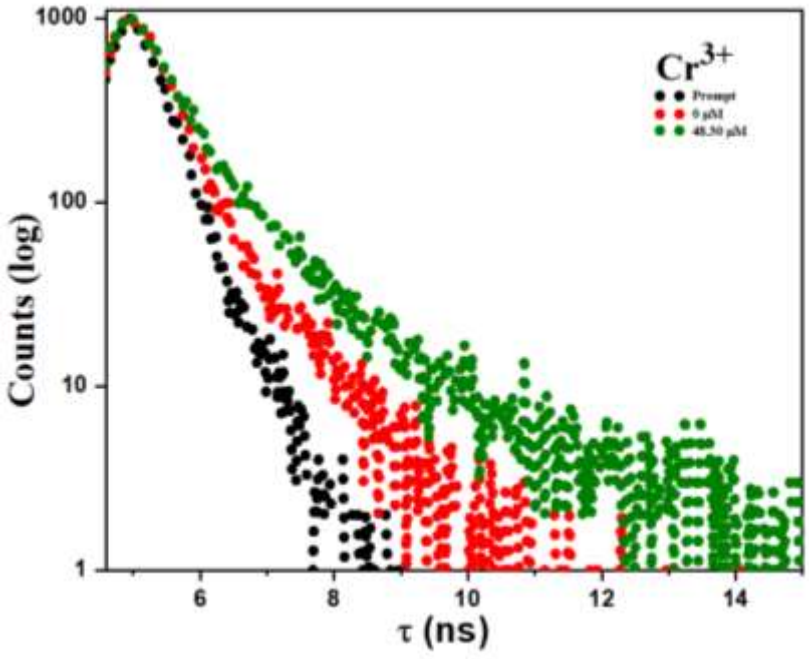

Fig. 3.42 Luminescence lifetime decay profile of compound **3.1** before and after the addition of the Cr^{3+} ions. The final concentration of Cr^{3+} ions in the medium is indicated in the legend. The instrument response function (prompt) is also shown. Here, λ_{ex} = 300 nm and λ_{em} = 398 nm were set during the experiment.

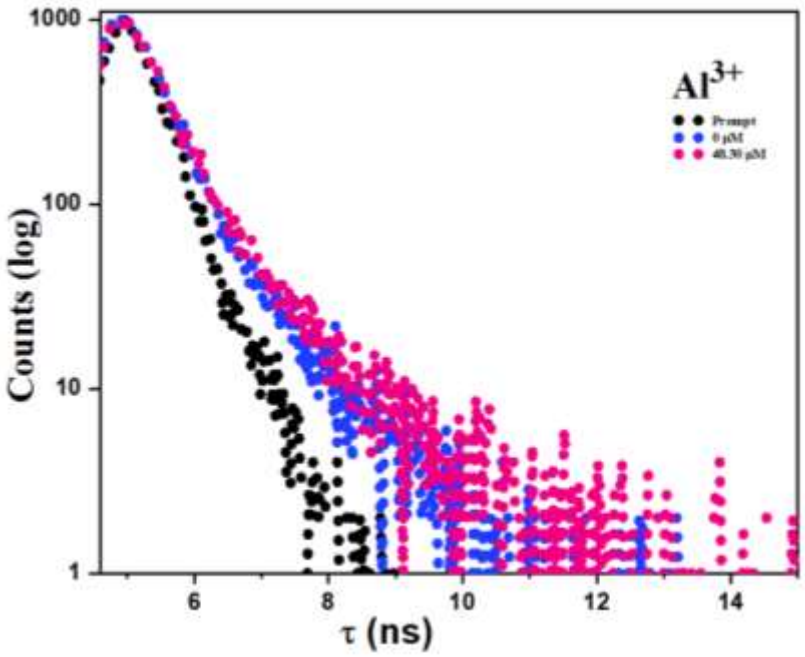

Fig. 3.43 Luminescence lifetime decay profile of compound **3.1** before and after the addition of the Al^{3+} ions. The final concentration of Al^{3+} ions in the medium is indicated in the legend. The instrument response function (prompt) is also shown. Here, λ_{ex} = 300 nm and λ_{em} = 398 nm were set during the experiment.

Table 3.7: Details about the time-resolved luminescence decays of compound **3.1** (λ_{ex} = 300 nm and λ_{em} = 398 nm) in presence of Fe^{3+}, Cr^{3+}, Al^{3+} solution.

Metal ions	Concentration (μM)	Lifetime (ns)			
		T_1	T_2	$T_{av} = (T_1+T_2)/2$	τ(ns)
Fe^{3+}	0	0.2030	0	0.101	0.203
	48.30	0.1479	1.2854	0.716	0.344
Cr^{3+}	0	0.2321	0	0.116	0.232
	48.30	0.1590	1.3480	0.753	0.490
Al^{3+}	0	0.2415	0	0.120	0.241
	48.30	0.1322	1.0551	0.593	0.301

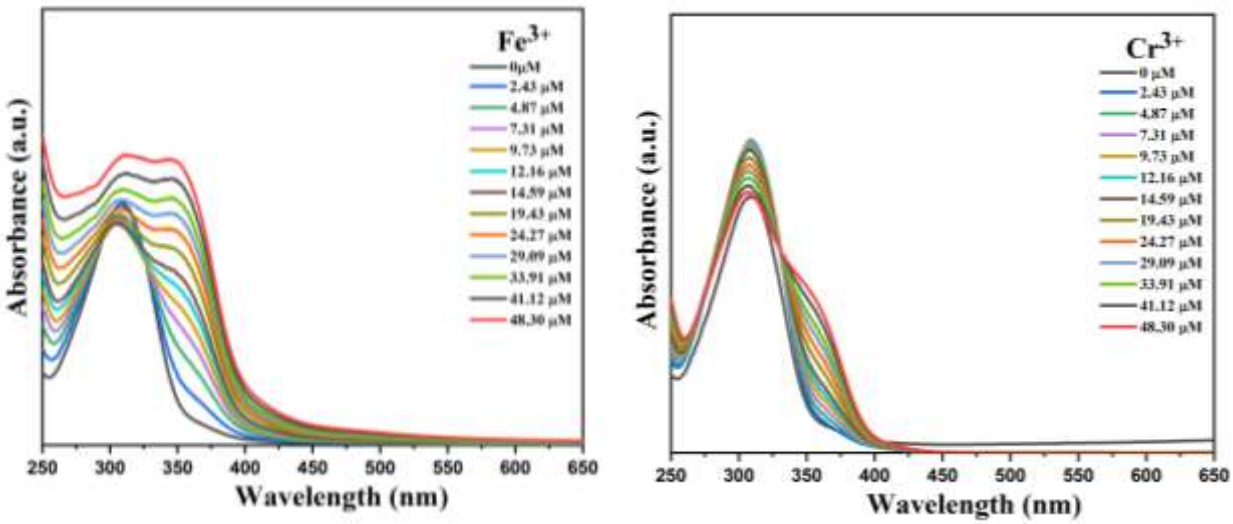

Fig. 3.44 (a) Absorption spectra of **3.1** dispersed in water upon incremental addition of water solution of Fe^{3+} ions. Final concentration of Fe^{3+} ions in the medium is indicated in the legend. (b) Absorption spectra of **3.1** dispersed in water upon incremental addition of water solution of Cr^{3+} ions. Final concentration of Cr^{3+} ions in the medium is indicated in the legend.

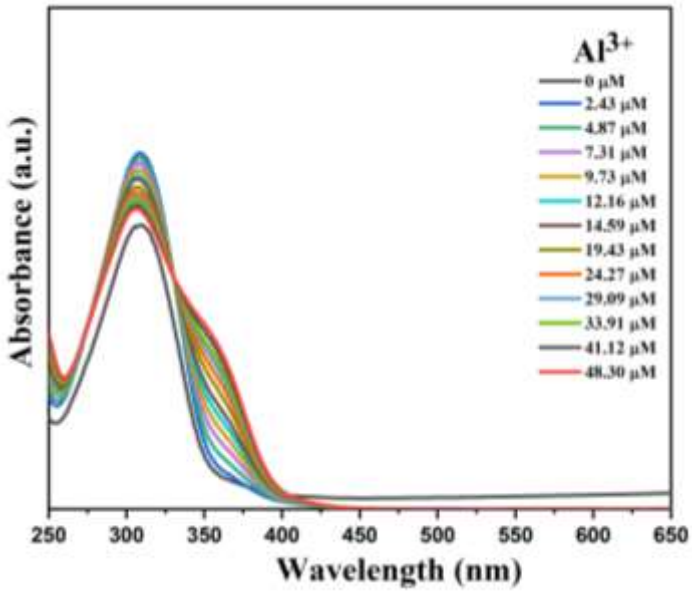

Fig. 3.45 Absorption spectra of **3.1** dispersed in water upon incremental addition of water solution of Al^{3+} ions. Final concentration of Al^{3+} ions in the medium is indicated in the legend.

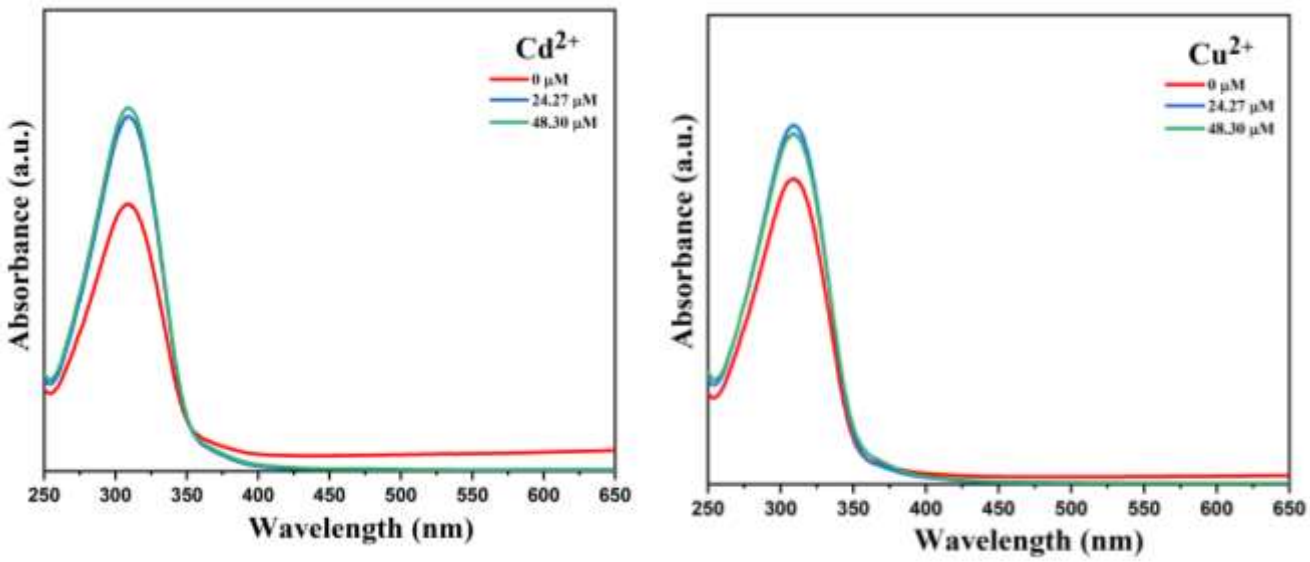

Fig. 3.46 (a) Absorption spectra of **3.1** dispersed in water upon incremental addition of water solution of Cd^{2+} ions. Final concentration of Cd^{2+} ions in the medium is indicated in the legend. (b) Absorption spectra of **3.1** dispersed in water upon incremental addition of water solution of Cu^{2+} ions. Final concentration of Cu^{2+} ions in the medium is indicated in the legend.

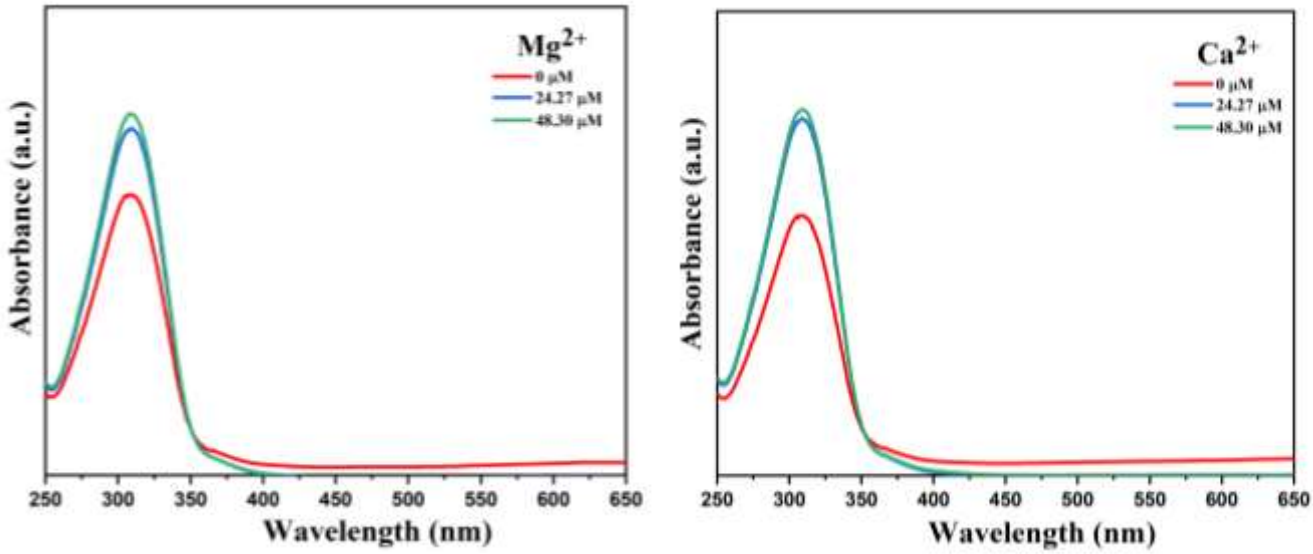

Fig. 3.47 (a) Absorption spectra of **3.1** dispersed in water upon incremental addition of water solution of Mg^{2+} ions. Final concentration of Mg^{2+} ions in the medium is indicated in the legend. (b) Absorption spectra of **3.1** dispersed in water upon incremental addition of water solution of Ca^{2+} ions. Final concentration of Ca^{2+} ions in the medium is indicated in the legend.

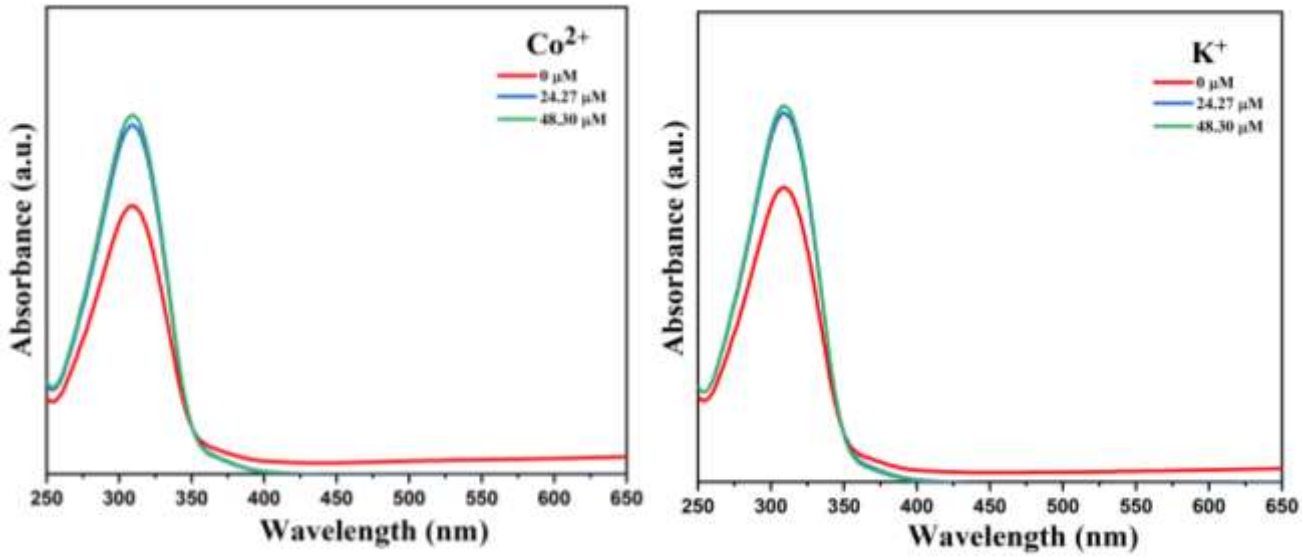

Fig. 3.48 (a) Absorption spectra of **3.1** dispersed in water upon incremental addition of water solution of Co^{2+} ions. Final concentration of Co^{2+} ions in the medium is indicated in the legend. (b) Absorption spectra of **3.1** dispersed in water upon incremental addition of water solution of K^{+} ions. Final concentration of K^{+} ions in the medium is indicated in the legend.

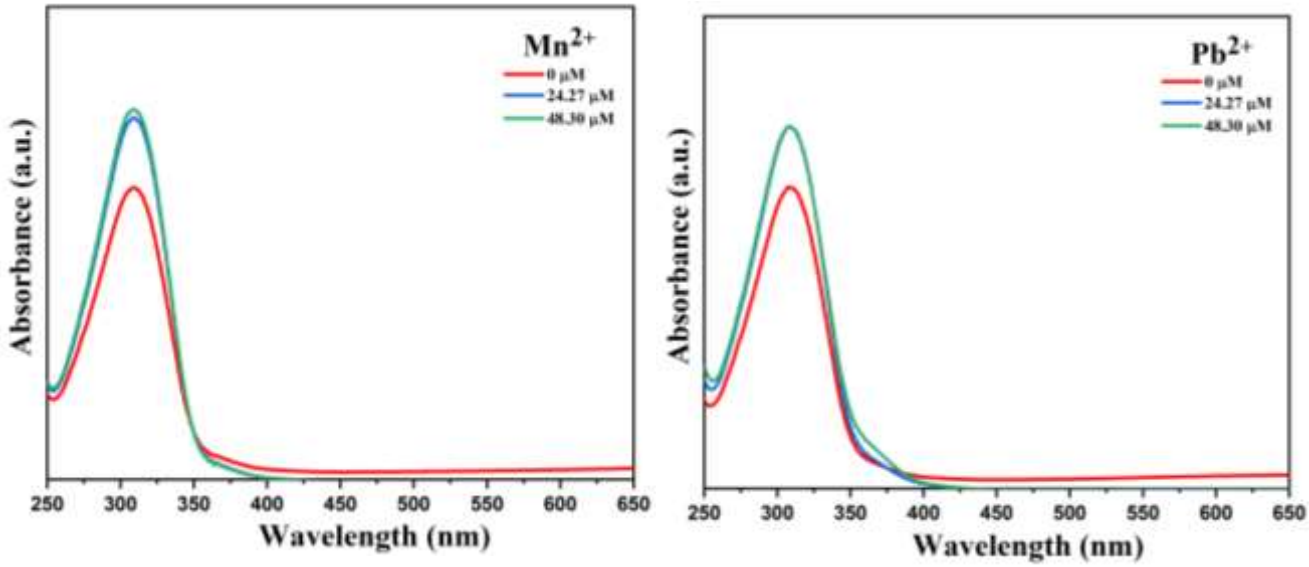

Fig. 3.49 (a) Absorption spectra of **3.1** dispersed in water upon incremental addition of water solution of Mn^{2+} ions. Final concentration of Mn^{2+} ions in the medium is indicated in the legend. (b) Absorption spectra of **3.1** dispersed in water upon incremental addition of water solution of Pb^{2+} ions. Final concentration of Pb^{2+} ions in the medium is indicated in the legend.

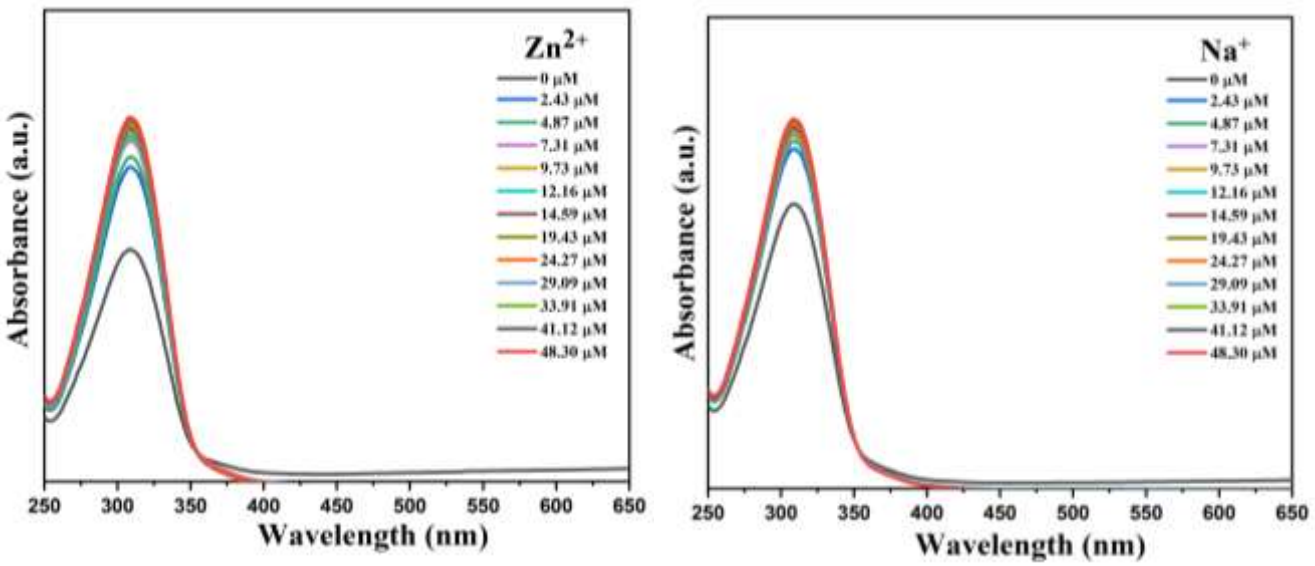

Fig. 3.50 (a) Absorption spectra of **1** dispersed in water upon incremental addition of water solution of Zn^{2+} ions. Final concentration of Zn^{2+} ions in the medium is indicated in the legend. (b) Absorption spectra of **1** dispersed in water upon incremental addition of water solution of Na^{+} ions. Final concentration of Na^{+} ions in the medium is indicated in the legend.

Table 3.8: A summary of luminescence-based sensing of Fe^{3+} ion using MOFs.

MOF	Medium	LOD (μM)	K_{sv} (M^{-1})	Ref.
$\{[Cd_2(SA)_2(L)_2]\cdot H_2O\}_n$	DMF	2.4	2.1×10^4	89
$[Cd_2(OBA)_2(BPTP)(H_2O)]$	DMF	0.36	—	90
$[Zn(5\text{-}AIP)(Ald\text{-}4)]\cdot H_2O$	H_2O	0.30	9.00×10^4	91.
$[Zn(L)(bpdc)]\cdot 1.6H_2O$	DMF	5.62	1.73×10^4	92
$[Cd(H_2BDDA)]_n$	H_2O	—	8.79×10^4	93
$[Cd(PAM)(4\text{-}bpdb)_{1.5}]\cdot DMF$	H_2O	0.3	3.5×10^4	94
$[Cu(tpp)\cdot H_2O]_{2n}$	H_2O	10	4.6×10^4	95
$\{[Cd_3(L^{2-})_3(H_2O)]\cdot(DMF)\cdot(H_2O)\}_n$	DMF	—	2.07×10^4	96
$[Zn_2(oba)_2(bpy)]$	MeOH	0.3	5.8×10^4	97
Ag-MOFs(1−3)	H_2O	11.46, 15.83, 15.44	(0.936, 1.033, and 0.888) $\times 10^4$	98
JXUST-18	EtOH	0.196	—	99
$[Cd(PDA)(L)_2]$	H_2O	1.34	23.29×10^4	This work

Table 3.9: A summary of luminescence-based sensing of Cr^{3+} ions using MOFs.

MOF	Medium	LOD (μM)	K_{sv} (M^{-1})	Ref.
$[Zn\ (tbda)]_n$	H_2O	180	2.68×10^3	100
$[Eu_2(tpbpc)_4 \cdot CO_3 \cdot 4H_2O] \cdot DMF \cdot solvent$	H_2O	68.8	5.14×10^2	101
$\{[Zn(H_2dhbdc)(bpycz)] \cdot 0.5H_2O\}_n$	H_2O	8.22	4.85×10^3	102
$[Zn(Br\text{-}1,4\text{-}bdc)\ (bpycz)]_n$	H_2O	4.73	4.04×10^3	102
$\{[Zn(tta)_{0.5}(m\text{-}bimb)] \cdot H_2O\}_n$	DMF	—	0.65	103
$[Zn_2(TPOM)(NH_2\text{–}BDC)_2] \cdot 4H_2O$	DMF	4.9	—	52
$[Zn(L)(H_2O)] \cdot H_2O$	H_2O	2.44	2.03×10^4	104
[Zn(5-AIP)(Ald-4)]·H2O	H_2O	0.46	2.30×10^4	91
$\{[Zn(BIBT)(oba)] \cdot DMA\}_n$	EtOH	0.049	—	105
$[Me_2NH_2]_4[Zn_6(qptc)_3(trz)_4] \cdot 6H_2O$	H_2O	1	4.39×10^4	106
$Zn_3(bpdc)_2(pdc)(DMF) \cdot 6DMF$	DMF	25.1	3870	107
$[Cd(PDA)(L)_2]$	H_2O	4.95	5.06×10^4	This work

Table 3.10: A summary of luminescence-based sensing of Al^{3+} ions using MOFs.

MOF	Medium	LOD (μM)	Ksv (M^{-1})	Ref.
{[Zn_2(O-BTC)(4,4′-BPY)$_{0.5}$(H_2O)$_3$]·(H_2O)$_{1.5}$·(DMA)$_{0.5}$}$_n$	EtOH	3.70	—	59
[Zn(DMA)(TBA)]	H_2O	1.97	1.33×10^4	108
[Co_2(dmimpym)(nda)$_2$]$_n$	DMF	0.7	—	109
{[Cd(CDC)(L)]}$_n$	DMF	61	2.6×10^3	89
[Cd(L)(phen)$_2$]·5H_2O	DMF	0.113	2.49×10^4	110
HPU-24@Ru	H_2O	11.63	—	111
{[Co(L)(bibp)]}$_n$	H_2O	1.52	1.97×10^4	112
[Zn(5-AIP)(Ald-4)]·H_2O	H_2O	0.35	2.80×10^4	91
[Cd(PAM)(4-bpdb)$_{1.5}$]·DMF	H_2O	0.56	2.3×10^4	113
{[Cd_2(SA)$_2$(L)$_2$]·H_2O}$_n$	DMF	93	5.4×10^3	89
[Co(OBA)(DATZ)$_{0.5}$(H_2O)]	H_2O	2.5	—	114
[Cd(PDA)(L)$_2$]	H_2O	3.96	3.09×10^4	This work

3.3.5 Gas Sorption Studies. CO_2, N_2, H_2 gas adsorption studies were performed by using compound **3.1** to check the porosity of **3.1**. The adsorption isotherm of compound **3.1** indicates the type I for CO_2. For N_2 and H_2 only surface adsorption has been observed. The compound **3.1** adsorbed CO_2 gas up to 64.5 cm^3/g at 195 K. **3.1** also exhibits N_2 adsorption up to 72.25 cm^3/g and the uptake value for H_2 sorption is 45.30 cm^3/g at 77 K, respectively. Carbon dioxide, nitrogen and hydrogen adsorption isotherms of compound **3.1** are shown in Fig 3.51-Fig. 3.53. The BET surface area of compound **3.1** is 11.635 m^2 /g. A summary of CO_2 adsorption using various MOF materials are shown in Table 3.11.

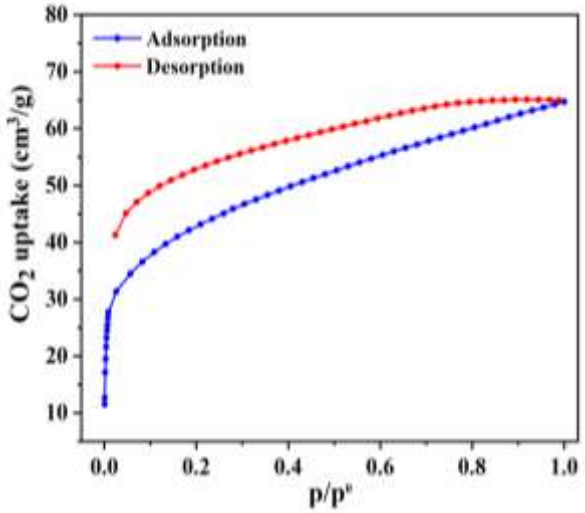

Fig. 3.51 CO_2 gas sorption isotherm of **3.1** at 195 K.

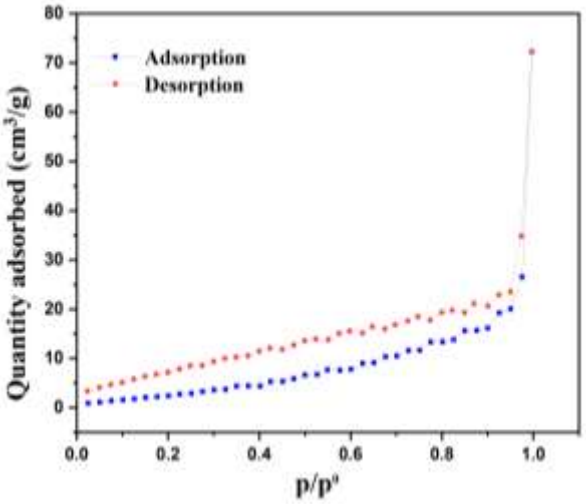

Fig. 3.52 N_2 gas sorption isotherm of **3.1** at 77 K.

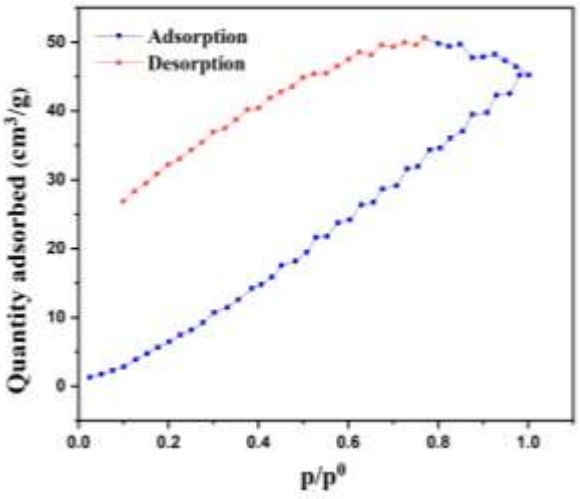

Fig. 3.53 H_2 gas sorption isotherm of **3.1** at 77 K.

Table 3.11: A summary of CO_2 gas adsorption using MOFs.

MOFs	Surface area from N_2 adsorption [$m^2\ g^{-1}$]	CO_2 uptake cm^3/g at 195 K	Ref.
$\{[Cd_2(sdb)_2(4\text{-bpmh})_2(H_2O)]\}_n \cdot 2n(H_2O)$	—	39.19	115
$\{[Cd_2(sdb)_2(3\text{-bpmh})_2]\}_n \cdot 3n(H_2O) \cdot n(C_6H_5NO)$	—	60.9	115
$[Mg_{16}(PTCA)_8(\mu_2\text{-}H_2O)_8(H_2O)_{16}(dioxane)_8].(H_2O)_{13}.(DMF)_{26}$	438.1	160.5	116
$\{[Zn(H_2dhbdc)(bpycz)] \cdot 0.5H_2O\}_n$	291.4	101.1	102
$[Zn(Br\text{-}1,4\text{-}bdc)(bpycz)]_n$	288.5	98.6	102
Cu-MOF	945	201.6	117
$[Cu_3(3,3'\text{-}dmglut)_3(bte)] \cdot 6(H_2O)\}_n$ and $[Cu(3,3'\text{-}dmglut)(btp)_{0.5}] \cdot 2(H_2O)\}_n$	—	21 and 26.2	118
Cu–MOP	270.9	96.5	119
ZnDatzBdc	303	92.5	120
$[Cd(PDA)(L)_2]$	11.635	64.5	This work

3.4 CONCLUSION

In summary, a new two dimensional Cd-based metal organic framework was successfully prepared by using 1,4-phenylenediacetic acid and 2,4,5-tri-4-pyridyl-1H-imidazole as organic ligands under solvothermal conditions for potential application. The synthesized compound has been characterized by single-crystal X-ray diffraction techniques, powder X-ray diffraction, Fourier Transform Infrared (FTIR) and thermogravimetric analysis (TGA). The single crystal X-ray studies showed that connectivity among Cd^{2+} ions, PDA and 2,4,5-tri-4-pyridyl-1H-imidazole ligands form two-dimensional structure. The two dimensional structures are arranged in AAA….fashion to form a three dimensional packing arrangement. The compound showed selective and efficient sorption of large anionic dye remazol brilliant blue R (RBBR) in aqueous medium following strong electrostatic and π···π interactions. The compound also exhibited photoluminescence based sensing behaviors towards Fe^{3+}, Cr^{3+} and Al^{3+} ions in aqueous medium based on luminescence quenching effect. The limit of detection for $Fe^{3+,}$ Cr^{3+}, Al^{3+} metal ions were 75, 257 and 107 ppb, respectively. It also showed gas adsorption capacity towards CO_2 (64.5 cm^3/g), N_2 (72.25 cm^3/g) and H_2 (45.30 cm^3/g) at 1 bar. These results indicate that the synthesized compound could be multifunctional with respect to dye sorption, metal ions sensing and gas adsorption.

3.5 REFERENCES

(3.1) H. Kaur, R. Kumar, A. Kumar, V. Krishnan and R. R. Koner, *Dalton Trans*., 2019, **48**, 915–927.

(3.2) R. Rajak, M. Saraf, A. Mohammad and S. M. Mobin, *J. Mater. Chem. A*., 2017, **5**, 17998–18011.

(3.3) W. Fan, X. Wang, B. Xu, Y. Wang, D. Liu, M. Zhang, Y. Shang, F. Dai, L. Zhang and D. Sun, *J. Mater. Chem. A*., 2018, **6**, 24486–24495.

(3.4) D.-D. Guo, B. Li, Z.-P. Deng, L.-H. Huo and S. Gao, *Dalton Trans*., 2021, **50**, 7818–7825.

(3.5) E. M. Dias and C. Petit, *J. Mater. Chem. A*., 2015, **3**, 22484– 22506.

(3.6) C.-C. Wang, J.-R. Li, X.-L. Lv, Y.-Q. Zhang and G. Guo, *Energy Environ. Sci.*, 2014, **7**, 2831–2867.

(3.7) X. Gao, G. Sun, F. Ge, and H. Zheng, *Inorg. Chem.*, 2019, **58**, 8396−8407.

(3.8) X. Shi, Y. Zu, S. Jiang, and F. Sun, *Inorg. Chem*., 2021, **60**, 1571−1578.

(3.9) H. Li, X. Cao, C. Zhang, Q. Yu, Z. Zhao, X. Niu, X. Sun, Y. Liu, L. Ma and Z. Li, *RSC Adv.*, 2017, **7**, 16273–16281.

(3.10) B. Parmar, K. K. Bisht, G. Rajput and E. Suresh, *Dalton Trans.*, 2021, **50**, 3083–3108.

(3.11) S. Wei, X. Hu, H. Liu, Q. Wang and C. He, *J. Hazard. Materials*., 2015, **294**, 168−176.

(3.12) N. S. Bobbitt, M. L. Mendonca, A. J. Howarth, T. Islamoglu, J. T. Hupp, O. K. Farha and R. Q. Snurr, *Chem. Soc. Rev.*, 2017, **46**, 3357–3385.

(3.13) R. Zhao, Y. Wang, X. Li, B. Sun and C. Wang, *ACS Appl. Mater. Interfaces.*, 2015, **7**, 26649–26657.

(3.14) Y. Han, S. Sheng, F. Yang, Y. Xie, M. Zhao and J.-R. Li, *J. Mater. Chem. A.*, 2015, **3**, 12804–12809.

(3.15) Y. Shen, C.-C. Fan, Y.-Z. Wei, J. Du, H.-B. Zhu and Y. Zhao, *Dalton Trans.*, 2016, **45**, 10909–10915.

(3.16) D.-M. Chen, W. Shi and P. Cheng, *Chem. Commun.*, 2015, **51**, 370–372.

(3.17) Z. Aksu, *Process Biochem*., 2005, **40**, 997−1026.

(3.18) A. Mohammad, K. Kapoor and S. M. Mobin, *ChemistrySelect*., 2016, **1**, 3483–3490.

(3.19) Y. Song, R.-Q. Fan, K. Xing, X. Du, T. Su, P. Wang and Y.-L. Yang, *Cryst. Growth Des.*, 2017, **17**, 2549–2559.

(3.20) U. I. Gaya and A. H. Abdullah, *J. Photochem. Photobiol C.*, 2008, **9**, 1–12.

(3.21) S. Smeets, D. Xie, L. B. McCusker, C. Baerlocher, S. I. Zones, J. A. Thompson, H. S. Lacheen and H.-M. Huang, *Chem. Mater.*, 2014, **26**, 3909−3913.

(3.22) P. Tian, X.-Y. Han, G.-L. Ning, H.-X. Fang, J.-W. Ye, W.-T. Gong and Y. Lin, *ACS Appl. Mater. Interfaces*., 2013, **5**, 12411−12418.

(3.23) L. Zhang, J.-S. Sun, F. Sun, P. Chen, J. Liu and G. Zhu, *Chem. Eur*. J., 2019, **25**, 3903−3908.

(3.24) M. Naqi Ahamad, M. Shahnawaz Khan, M. Shahid and M. Ahmad, *Dalton Trans.*, 2020, **49**, 14690–14705.

(3.25) Y. Gao, Y. Li, C. Liang, P. Cen, J. Xi, Y. Guo, W. Song and X. Liu, *Dalton Trans.*, 2021, **50**, 17603–17610.

(3.26) Y. Wen, Q. Liu, S. Su, Y. Yang, X. Li, Q.-L. Zhu and X. Wu, *Nanoscale.*, 2020, **12**, 12767–12772.

(3.27) Q. Meng, X. Xin, L. Zhang, F. Dai, R. Wang and D. Sun, *J. Mater. Chem. A.*, 2015, **3**, 24016–24021.

(3.28) A. Dhakshinamoorthy, A. M. Asiri and H. Garcia, *Adv. Mater.*, 2019, **31**, 1900617.

(3.29) J. R. Long and O. M. Yaghi, *Chem. Soc. Rev.*, 2009, **38**, 1213–1314.

(3.30) M. Dinca, A. Dailly, Y. Liu, C. M. Brown, D. A. Neumann and J. R. Long, *J. Am. Chem. Soc.*, 2006, **128**, 16876– 16883.

(3.31) G.-H. Yu, C.-L. Yang, H.-L. Zhao, A.-X. Yu, G. Zhang, D.-Y. Du, and Z.-M. Su, *Inorg. Chem*., 2022, **61**, 5318−5325.

(3.32) Z.-G. Liang, G.-M. Li, X.-Y. Ren, J.-H. Li, J. Pan, and S.-D. Han, *Inorg. Chem*., 2023, **62**, 8663−8669.

(3.33) A. Phan, C. J. Doonan, F. J. Uribe-Romo, C. B. Knobler, M. O′ keeffe and O. M. Yaghi, *Acc. Chem. Res.*, 2010, **43**, 58–67.

(3.34) H.-C. Zhou, J. R. Long, and O. M. Yaghi, *Chem. Rev*., 2012, **112**, 673−674.

(3.35) J. Y. Lee, O. K. Farha, J. Roberts, K. A. Scheidt, S. B. T. Nguyen and J. T. Hupp, *Chem. Soc. Rev*., 2009, **38**, 1450−1459.

(3.36) M. Z. Wu, J. Y. Shi, P. Y. Chen, L. Tian, and J. Chen, *Inorg. Chem*., 2019, **58**, 3130−3136.

(3.37) Y.-K. Deng, H.-F. Su, J.-H. Xu, W.-G. Wang, M. Kurmoo, S.-C. Lin, Y.-Z. Tan, J. Jia, D. Sun and L.-S. Zheng, *J. Am. Chem. Soc.*, 2016, **138**, 1328−1334.

(3.38) M.-L. Chen, Z.-L. Qi, W.-T. Jin, Z. Xu, Y.-H. Cheng and Z.-H. Zhou, *CrystEngComm*., 2021, **23**, 7442–7449.

(3.39) X.-M. Tian, S.-L. Yao, C.-Q. Qiu, T.-F. Zheng, Y.-Q. Chen, H. Huang, J.-L. Chen, S.-J. Liu**,** and H.-R. Wen, *Inorg. Chem*., 2020, **59**, 2803−2810.

(3.40) M. Zheng, H. Tan, Z. Xie, L. Zhang, X. Jing and Z. Sun, *ACS Appl. Mater. Interfaces.*, 2013, **5**, 1078−1083.

(3.41) W.-Q. Tong, W.-N. Liu, J.-G. Cheng, P.-F. Zhang, G.-P. Li, L. Hou and Y.-Y. Wang, *Dalton Trans*., 2018, **47**, 9466–9473.

(3.42) N. C. Andrews, *N. Engl. J. Med*., 1999, **341**, 1986.

(3.43) Q. Zhao, F. Li and C. Huang, *Chem. Soc. Rev*., 2010, **39**, 3007 -3030.

(3.44) S. K. Sahoo, D. Sharma, R. K. Bera, G. Crisponi and J. F. Callan, *Chem. Soc. Rev*., 2012, **41**, 7195 -7227.

(3.45) K. P. Carter, A. M. Young and A. E. Palmer, *Chem. Rev*., 2014, **114**, 4564 –4601.

(3.46) H. Zhang, R. Fan, W. Chen, J. Fan, Y. Dong, Y. Song, X. Du, P. Wang, and Y. Yang, *Cryst. Growth Des*., 2016, **16**, 5429−5440.

(3.47) S. Chen, Z. Shi, L. Qin, H. Jia, and H. Zheng, *Cryst. Growth Des*., 2017, **17**, 67−72.

(3.48) M. Fan, B. Sun, X. Li**,** Q. Pan**,** J. Sun, P. Ma, and Z. Su, *Inorg. Chem.*, 2021, **60**, 9148–9156.

(3.49) X.-P. Zhang, L. Fu, O. A. Blatova, G.-H. Cui, *Journal of Solid State Chemistry.*, 2023, **324**, 124124.

(3.50) T.-Y. Gu, M. Dai, D. J. Young, Z.-G. Ren, and J.-P. Lang, *Inorg. Chem*., 2017, **56**, 4668−4678.

(3.51) R. Lv, J. Wang, Y. Zhang, H. Li, L. Yang, S. Liao, W. Gu and X. Liu, *J. Mater. Chem. A*., 2016, **4**, 15494−15500.

(3.52) Y. Yu, Y. Wang, H. Yan, J. Lu, H. Liu, Y. Li**,** S. Wang**,** D. Li, J. Dou, L. Yang, and Z. Zhou, *Inorg. Chem.*, 2020, **59**, 3828–3837.

(3.53) D. A. Brown, W. K. Glass, M. R. Jan and R. M. W. Mulders, *Environ. Technol. Lett*., 1986, **7**, 283−288.

(3.54) M. Bellouard, M. Gasser, S. Lenglet, F. Gilardi, N. Bararpour, M. Augsburger, A. Thomas and J.-C. Alvarez**,** *Chem. Res. Toxicol.*, 2022, **35**, 807–816.

(3.55) C. Fu, X. Sun, G. Zhang, P. Shi**,** and P. Cui, *Inorg. Chem.*, 2021, **60**, 1116–1123.

(3.56) Y.-P. Li, X.-H. Zhu, S.-N. Li, Y.-C. Jiang, M.-C. Hu, and Q.-G. Zhai, *ACS Appl. Mater. Interfaces*., 2019, **11**, 11338−11348.

(3.57) W.-X. Li, J.-H. Gu, H.-X. Li, M. Dai, D. J. Young, H.-Y. Li, and J.-P. Lang, *Inorg. Chem*., 2018, **57**, 13453−13460.

(3.58) X. Zheng, Y. Zhao, P. Jia, Q. Wang, Y. Liu, T. Bu, M. Zhang, F. Bai, and L. Wang, *Inorg. Chem*., 2020, **59**, 18205−18213.

(3.59) M.-H. Yu, T.-L. Hu and X.-H. Bu, *Inorg. Chem. Front*., 2017, **4**, 256–260.

(3.60) J. Posta, H. Berndt, S.-K. Luo and G. Schaldach, *Anal. Chem*., 1993, **65**, 2590−2595.

(3.61) T. Wu, C. Liu, K. J. Tan, P. P. Hu and C. Z. Huang, Anal. Bioanal. Chem., 2010, **397**, 1273–1279.

(3.62) S. Liu, F. Lu and J.-J. Zhu, Chem. Commun., 2011, **47**, 2661– 2663.

(3.63) S.-H. Park, N. Kwon, J.-H. Lee, J. Yoon and I. Shin, *Chem. Soc. Rev*., 2020, **49**, 143−179.

(3.64) Y. Jiang, L. Sun, J. Du, Y. Liu, H. Shi, Z. Liang, and J. Li, *Cryst. Growth Des*., 2017, **17**, 2090−2096.

(3.65) J. Lü, C. Perez-Krap, M. Suyetin, N. H. Alsmail, Y. Yan, S. Yang, W. Lewis, E. Bichoutskaia, C. C. Tang, A. J. Blake, R. Cao and M. Schröder, *J. Am. Chem. Soc*., 2014, **136**, 12828−12831.

(3.66) D. T. Phan, M. Maeder, R. C. Burns and G. Puxty, *Environ. Sci. Technol*., 2014, **48**, 4623−4629.

(3.67) D. Qian, C. Lei, E.-M. Wang, W.-C. Li and A.-H. Lu, *ChemSusChem*., 2014, **7**, 291−298.

(3.68) Q. Huang, *Acta Cryst*., 2009. **E65**, o2329.

(3.69) V. U. M. Apex2, M86-E01078, Bruker Analytical X-ray Systems Madison, WI, 2006.

(3.70) S. S. Siemens, Siemens Analytical X-ray Instruments Inc. Madison, MI, 1995.

(3.71) G. M. Sheldrick, *Acta Crystallogr C Struct Chem*., **2015,** 71, 3-8.

(3.72) O. V. Dolomanov, L. J. Bourhis, R. J. Gildea; J. A. K. Howard; H. Puschmann, *J. Appl. Crystallogr*., 2009, **42**, 2, 339-341.

(3.73) SADABS, Bruker AXS Inc., Madison, WI, 2014.

(3.74) M. J. Nardelli, *Appl. Crystallogr*., 1995**, 28**, 659.

(3.75) A. L. Spek, *Acta Crystallogr*., 2009**, D65**, 148.

(3.76) Y. S. Ho, G. McKay, *Process Biohem*., 1999, **34**, 451−465.

(3.77) W.-J. Ji, R.-Q. Hao, W.-W. Pei, L. Feng and Q.-G. Zhai, *Dalton Trans*., 2018, **47**, 700−707.

(3.78) A. M. Dietrich and G. A. Burlingame, *Environ. Sci. Technol*., 2015, **49**, 708−720.

(3.79) Y. Zhang, P. Hu, Y. Muhammad, Y. Tang, S. Shao, Z. Gao, J. Wang, R. Wang, Y. Hu, L. Kuang, Z. Zhao, Z. Zhao, *Chemical Engineering Journal*., 2021, **405**, 127003.

(3.80) L. E. Mphuthi, E. Erasmus, and E. H. G. Langner, *ACS Omega.*, 2021, **6**, 31632−31645.

(3.81) K. Antecka, J. Zdarta, K. Siwinska-Stefa ´ nska, ´ G. Sztuk, E. Jankowska, P. Oleskowicz-Popiel, T. Jesionowski, *Catalysts*., 2018, **8**, 402.

(3.82) T.T. Le, K. Murugesan, C.-S. Lee, C.H. Vu, Y.-S. Chang, J.-R. Jeon, *Bioresour. Technol.*, 2016, **216**, 203–210.

(3.83) A. H. Jawad, A. S. Abdulhameed, S. N. Surip, Z. A. ALOthman, *Journal of Polymers and the Environment* 2023, **31**, 3768–3782.

(3.84) P. M. dos Santos, J. R. Baruque, R. K. de Souza Lira, S. G. F. Leite, R. P. do Nascimento, C. P. Borges, R. Wojcieszak, and I. Itabaiana, Jr. *Int. J. Mol. Sci.* 2022, 23, 9363.

(3.85) X. Jiang, Y. Yu, X. Li, X. Z. Kong, *Chemical Engineering Journal*, 2017, **328**, 1043-1050.

(3.86) S. Naseem, R. S. Rawal, D. Pandey S. K. Suman, *Environmental Science and Pollution Research*, 2023, **30**, 84898–84917.

(3.87) G. Ozturk, H. Silah, *Environmental Processes*.,2020 **7**, 479–492.

(3.88) M. C. Arya, P. S. Bafila, D. Mishra, K. Negi, R. Kumar, A. Bughani, *SN Applied Sciences*., 2020 **2**, 265.

(3.89) S. Chand, M. Mondal, S. C. Pal, A. Pal, S. Maji, D. Mandal and M. C. Das, *New J. Chem*., 2018, **42**, 12865– 12871.

(3.90) L.-J. Han, W. Yan, S.-G. Chen, Z.-Z. Shi and H.-G. Zheng, *Inorg. Chem*., 2017, **56**, 2936–2940.

(3.91) P. Daga, P. Manna, P. Majee, D. K. Singha, S. Hui, A. K. Ghosh, P. Mahata and S. K. Mondal, *Dalton Trans*., 2021, **50**, 7388.

(3.92) Z.-Q. Liu, Y. Zhao, X.-D. Zhang, Y.-S. Kang, Q.-Y. Lu, M. Azam, S. I. Al-Resayes and W.-Y. Sun, *Dalton Trans*., 2017, **46**, 13943–13951.

(3.93) T. Shu, N. Wang, Y. Li, D. Fu, H. Fan, M. Luo and S. Yue, *ChemistrySelect*., 2017, **2**, 12046–12050.

(3.94) R. Lv, Z. Chen, X. Fu, B. Yang, H. Li, J. Su, W. Gu and X. Liu, *J. Solid State Chem*., 2018, **259**, 67–72.

(3.95) Y. Song, R. Fan, X. Du, K. Xing, Y. Dong, P. Wang and Y. Yang, *RSC Adv*., 2016, **6**, 110182–110189.

(3.96) L.-S. Li, X. Wang, Y.-Y. Jia, S.-X. Xu, M.-H. Yu and Y.-H. Zhang, *Eur. J. Inorg. Chem*., 2018, 1068–1072.

(3.97) E. Moradi, R. Rahimi, V. Safarifard, *Polyhedron*., 2019, **159**, 251–258.

(3.98) B. Mohan, S. Ma, S. Kumar, Y. Yang, and P. Ren, *ACS Appl. Mater. Interfaces*., 2023, **15**, 17317−17323.

(3.99) D.-G. Cai, C.-Q. Qiu, Z.-H. Zhu, T.-F. Zheng, W.-J. Wei, J.-L. Chen, S.-J. Liu, and H.-R. Wen, *Inorg. Chem*., 2022, **61**, 14770−14777.

(3.100) X. Liang, Y. Jia, Z. Zhan and M. Hu, *Appl. Organomet. Chem*., 2019, **33**, e4988.

(3.101) J. Liu, G. Ji, J. Xiao and Z. Liu, *Inorg. Chem.*, 2017, **56**, 4197–4205.

(3.102) C.-H. Yeh, M.-J. Tsai, P.-C. Lee, and J.-Y. Wu, *Inorg. Chem.*, 2023, https://doi.org/10.1021/acs.inorgchem.3c01800.

(3.103) X.-T. Zhang, H.-T. Chen, B. Li, G.-Z. Liu and X.-Z. Liu, *Dalton Trans*., 2018, **47**, 1202–1213.

(3.104) X.-Y. Guo, F. Zhao, J.-J. Liu, Z.-L. Liu and Y.-Q. Wang, *J. Mater. Chem. A*., 2017, **5**, 20035–20043.

(3.105) S.-L. Yao, Y.-C. Xiong, X.-M. Tian, S.-J. Liu, H. Xu, T.-F. Zheng, J.-L. Chen and H.-R. Wen, *CrystEngComm*., 2021, **23**, 1898–1905.

(3.106) X.-X. Jia, R.-X. Yao, F.-Q. Zhang and X.-M. Zhang, *Inorg. Chem*., 2017, **56**, 2690–2696.

(3.107) X. Meng, M.-J. Wei, H.-N. Wang, H.-Y. Zang and Z.-Y. Zhou, *Dalton Trans*., 2018, **47**, 1383–1387.

(3.108) X. Zhang, X. Luo, N. Zhang, J. Wu and Y.-Q. Huang, *Inorg. Chem. Front*., 2017, **4**, 1888–1894.

(3.109) W.-M. Chen, X.-L. Meng, G.-L. Zhuang, Z. Wang, M. Kurmoo, Q.-Q. Zhao, X.-P. Wang, B. Shan, C.-H. Tung and D. Sun, *J. Mater. Chem. A*., 2017, **5**, 13079–13085.

(3.110) S.-S. Chen, Z.-Y. Zhang, R.-B. Liao, Y. Zhao, C. Wang, R. Qiao, and Z.-D. Liu, *Inorg.Chem.*, 2021, **60**, 4945–4956.

(3.111) H. Li, Y. Wang, F. Jiang, M. Li, Z. Xu, *Dalton Trans*., 2023, **52**, 3846–3854.

(3.112) R. Luo, C. Xu, G. Chen, C.-Z. Xie, P. Chen, N. Jiang, D.-M. Zhang, Y. Fan, and F. Shao, *Cryst. Growth Des.*, 2023, **23**, 4, 2395–2405.

(3.113) R. Lv, Z. Chen, X. Fu, B. Yang, H. Li, J. Su, W. Gu and X. Liu, *J. Solid State Chem*., 2018, **259**, 67–72.

(3.114) D. K. Singha and P. Mahata, *Inorg. Chem*., 2015, **54**, 6373– 6379.

(3.115) S. Parshamoni, J. Telangae and S. Konar, *Dalton Trans*., 2015, **44**, 20926–20935.

(3.116) Y.-L. Huang, Y.-N. Gong, L. Jiang and T.-B. Lu, *Chem. Commun.*, 2013, **49**, 1753–1755.

(3.117) S. Nandi, R. Maity, D. Chakraborty, H. Ballav, and R. Vaidhyanathan, *Inorg. Chem.*, 2018, **57**, 5267−5272.

(3.118) G. Pahari, S. Ghosh, A. Halder, D. Ghoshal, *Cryst.GrowthDes.*, 2021, **21**, 2633−2642.

(3.119) L.-H. Liu, L. Liu, H.-R. Chi, C.-N. Li and Z.-B. Han, *Chem. Commun.*, 2022, **58**, 6417.

(3.120) J. Peng, Z. Liu, Y. Wu, S. Xian, Z. Li, *ACS Appl. Mater. Interfaces.*, 2022, **14**, 21089−21097.

Chapter 4

A Two-Dimensional Mixed Ligands based Coordination Polymer of Cadmium: Synthesis, Single Crystal Structure and Luminescence Quenching based Sensing Behaviours towards $Fe^{3+,}$ Cr^{3+}, Al^{3+} ions and TNP in Aqueous Phase

A Two-Dimensional Mixed Ligands based Coordination Polymer of Cadmium: Synthesis, Single Crystal Structure and Luminescence Quenching based Sensing Behaviours towards $Fe^{3+,}$ Cr^{3+}, Al^{3+} ions and TNP in Aqueous Phase

ABSTRACT

A new Cd(II)-based compound [Cd(BTCH)(L)] (BTCH = di-anionic 1,3,5-benzene tricarboxylic acid and L = 2,4,5-tri-4-pyridyl-1H-imidazole), **4.1**, has been synthesized by hydrothermal method. The structure determined by single-crystal X-ray diffraction revealed two dimensional extended assemblies based on connectivity of Cd^{2+} ions with two ligands. The presence of one free carboxylic acid groups of each BTCH ligand and one non-bonded pyridine ring of each L ligand makes the two-dimensional layer structure stabilized through the hydrogen bond interactions. The compound has been characterized by powder X-ray diffraction, Fourier transform infrared (FTIR) spectroscopy and thermogravimetric analysis (TGA). Aqueous dispersion of compound **4.1** showed emission at 400 nm upon excitation at 300 nm. The compound **4.1** also exhibited photoluminescence-based sensing behaviors towards Fe^{3+}, Al^{3+} and Cr^{3+} ions in aqueous medium based on luminescence quenching effect. However, photoluminescence studies in presence of other common metal ions showed either negligible quenching effect or moderate to low turn on effect for Ni^{2+}, K^{+}, Zn^{2+}, Cd^{2+} Cu^{2+}, Ca^{2+}, Mn^{2+}, Na^{+}, Co^{2+}, Fe^{2+}, Pb^{2+}, Mg^{2+} in aqueous. The limit of detection for Fe^{3+}, Al^{3+}, Cr^{3+} ions are 0.568 μM, 1.721 μM and 0.840 μM respectively. Compound **4.1** also showed significant quenching effect in the presence of 2,4,6-trinitrophenol (TNP) with detection limit of 0.302 μM.

A Two-Dimensional Mixed Ligands based Coordination Polymer of Cadmium: Synthesis, Single Crystal Structure and Luminescence Quenching based Sensing Behaviours towards $Fe^{3+,}$ Cr^{3+}, Al^{3+} ions and TNP in Aqueous Phase

4.1 INTRODUCTION

Over the past few decades a hot research topic for the scientists is coordination polymers (CPs) because of their significant porosity, unusual flexibility, physical and chemical properties.[4.1-4.6] The variable pore structure, excellent stability of CPs made them promising materials for sensing, gas storage, proton conductivity, catalysis, magnetism, drug delivery, and many others.[4.7-4.18] The porous CPs were generated using organic linkers with metal ions or clusters. Diversity of structure of CPs is mostly dependent on various factors such as metal to ligand ratio, counter-ions, coordination modes of the metal ions, solvents, and synthesis procedures. Various synthesis processes have been developed for the formation of CPs such as diffusion, hydro-, solvo- and ionothermal process etc. Amongst these processes, hydro-/solvothermal process is the most popular method for crystallization.[4.19-4.23] The fascinating architectures of CPs are receiving great attention for many types of pollutants, such as nitro aromatic compounds, metal ions. CPs containing conjugated organic ligands and electron rich metal centers are responsible to exhibit photoluminescence property. Due to the presence of various types of interactions, such as hydrogen bonds and electrostatic π-π interactions, vander Waals forces, covalent and non-covalent interactions between the poisonous compounds like nitro aromatic compounds and metal ions with CP, the luminescence intensity can be significantly altered by changing the emission intensities. Nitro aromatic compounds, mainly TNP, and metal ions (trivalent metal ions such as Fe^{3+}, Cr^{3+} and Al^{3+}) create a noticeable risk to human health and social security as they can contaminate groundwater, air, and soil. The trivalent metal ions such as Fe^{3+}, Cr^{3+}, and Al^{3+} are the fundamental elements that are dispersed in biological systems and the environment.[4.3, 4.24-4.34] Iron take part in hemoglobin formation, and transport the oxygen from the lung to tissues. Iron excess and shortage can lead to various pathogenic effects such as anemia, sleep loss, skin diseases, hepatic cirrhosis and Parkinson's disease.[4.35-4.46] The non-essential trace element for the human body and the third most abundant element in the environment is aluminium, and the random use of aluminium foil and utensils in daily life can directly affect the human health. Absorption of the toxic aluminium can damage the bone system and promote osteoporosis, dementia, and consuming the excess Al^{3+} is the main cause of Alzheimer's disease.[4.47-4.52] The essential micronutrient chromium is used to maintain various metabolism processes in the human body. The excessive intake of Cr^{3+} in the body is poisonous, resulting in the formation of malignant cells, and the deficiency of Cr^{3+} may cause cardiovascular diseases and diabetes mellitus. Carbohydrate, fat, and nucleic acid metabolism proceeds through chromium ions.[4.53-

[4.60] Like metal ions, nitro aromatic compounds create hazardous effects on the environment because of their explosive strength and numerous uses in the fireworks, dye, leather, textile, and pharmaceutical industries. Among the various nitro aromatic compounds, TNP is the most dangerous due to easily contamination in water and soil.[4.61-4.64] So, concerning the serious issues it is very important to develop a new technique to detect these harmful compounds for homeland security. For identification of these pollutants in the earth curst, different types of analytical methods has been used such as atomic absorption spectrophotometry (AAS), gas chromatography, inductively coupled plasma mass spectrometry (ICP-MS), mass spectrometry, Raman spectroscopy, ion mobility spectrometry (IMS), potentiometry, etc. But these methods are very much time-consuming, costly and require proper operational skills to operate these sophisticated instruments. CPs with luminescence properties are a good class of sensing probe to detect these pollutants due to their fast response time, high selectivity, sensitivity, low cost, and simplicity.[4.65-4.70] In conformity with the aforementioned points, we have synthesized a highly stable two dimensional Cd(II)-based CP of formula [Cd(BTCH)(L)], **4.1,** by hydrothermal method using trimesic acid and the 2,4,5-tri-4 pyridyl-1H-imidazole ligand. The crystal structure of compound **4.1** was elucidated using high resolution X-ray diffraction (XRD). Compound **4.1** showed effective luminescent sensor behavior towards trivalent Fe^{3+}, Al^{3+}, and Cr^{3+} ions in an aqueous medium based on the luminescence quenching effect with detection limits of 0.568 μM, 1.721 μM and 0.840 μM, respectively. Compound **4.1** also acted as a good sensor for TNP in an aqueous medium based on the luminescence quenching effect with a detection limit of 0.302 μM. Overall, compound **4.1** behaved as functional probe with high selectivity and sensitivity.

4.2. EXPERIMENTAL SECTION

4.2.1. Materials. The required chemicals for the synthesis of 2,4,5-tri-4 pyridyl-1H-imidazole ligand was 4-pyridinecarboxaldehyde (Aldrich, 97%), ammonium acetate (Merck, 97%), ethanol (Sigma-Aldrich, 99%) and water. The required chemicals for the synthesis of compound **4.1**, $Cd(OAc)_2 \cdot 2H_2O$ (Sigma-Aldrich, 98%), trimesic acid (Sigma-Aldrich, 95%), 2,4,5-tri-4 pyridyl-1H-imidazole ligand, NaOH (Merck, 97%), and water were used as received without further purification. The chemicals used for detection experiments were ferric(III) sulphate hydrate (Loba-chemie, 99%), chromium(III) nitrate nonahydrate (Sigma-Aldrich, 99%), aluminium(III) nitrate nonahydrate (Merck, 95%), nickel chloride hexahydrate (Loba-chemie, 97%), potassium(I) chloride (Merck, 99%),

copper(II) chloride dihydrate (Merck, 99%), calcium(II) chloride dihydrate (Merck, 98%), manganese(II) chloride tetrahydrate (Merck, 99%), sodium(I) chloride (Merck, 99%), cobalt(II) chloride hexahydrate (Merck, 98%), iron(II) chloride tetrahydrate (Sigma-Aldrich, 99%), lead (II) nitrate (Merck, 99%), magnesium(II) chloride hexahydrate (Merck, 98%), cadmium(II) chloride monohydrate (Merck, 98%), zinc(II) sulfate heptahydrate (Merck, 99%), 2,4,6-trinitrophenol (TNP) (Aldrich, 98%), 2,4-dinitrophenol (DNP) (Aldrich, 98%), 1,2-dinitrobenzene (1,2-DNB) (Aldrich, 99%), 4-nitrotoluene (NT) (Aldrich, 99%), benzene (B) (Merck, 99%), 1,3-dinitrobenzene (1,3-DNB) (Aldrich, 97%), phenol (PhOH) (Merck, 99%), 1,4-dinitrobenzene (1,4-DNB) (Aldrich, 98%), 1,3,5-trihydroxybenzene (THB) (Aldrich, 97%), 2,4-dinitrotoluene (DNT) (Aldrich, 97%), and toluene (T) (Merck, 99.5%). The water used was double distilled.

4.2.2. Synthesis of compound 4.1. Initially 2,4,5-tri-4-pyridyl-1H-imidazole monohydrate was synthesized using 4-pyridinecarboxaldehyde and ammonium acetate, NaOH, and ethanol based on reported procedure.[4.71] Compound **4.1** was synthesized by employing hydrothermal method. $Cd(OAc)_2 \cdot 2H_2O$ (0.0679 g, 0.25 mM), trimesic acid (0.0536 g, 0.25 mM), and 2,4,5-tri-4-pyridyl-1H-imidazole monohydrate (0.0835 g, 0.25 mM) and NaOH (0.03 g, 0.75 mM) were dissolved in 7 mL distilled water with continuous stirring, and the mixture was homogenized at room temperature for 30 minute. The final reaction mixture was sealed in a 23 mL polytetrafluoroethylene-lined stainless-steel autoclave and heated at 180°C for 96 hrs. The initial pH value of the reaction mixture was 7 and final pH value after the reaction was 6. The final product containing large quantities of hexagonal-shaped colourless crystals, was filtered, washed with water under vacuum, and dried at ambient conditions. The yield of the product was ~ 75% based on Cd.

4.2.3. Instrumentations. Powder X-ray diffraction (XRD) pattern was recorded on well ground sample in the 2θ range 5-50º using Bruker D8 Advance X-ray diffractometer with Cu Kα radiation (λ = 1.5418 Å) operating at 40 kV and 40 mA. The FTIR Spectrum (400-4000 cm^{-1}) of the compound **4.1** was noted using Nicolet Magna IR 750 series-II. Thermogravimetric analysis (TGA) of the compound **4.1** was carried out under nitrogen atmosphere (flow rate = 20 ml min^{-1}) using PerkinElmer Diamond instrument (STA 6000) in the temperature range of 30–800 °C (heating rate= 20°Cmin^{-1}). UV-Vis spectrum of compound **4.1** was checked using Shimadzu UV-1900i UV-VIS spectrophotometer.

4.2.4. Photoluminescence measurement. The excitation and emission spectra of compound **4.1** and details of luminescence titration in the presence of different analytes were recorded at room temperature in aqueous media (at 300 nm excitation wavelength) using Horiba FluoroMax4-spectrofluorometer.

4.2.5 Single-Crystal Structure determination of compound 4.1. Suitable single crystals of **4.1** was carefully selected under a polarizing microscope and glued carefully to a thin-glass fiber. The single-crystal data were collected using a Bruker D8 Quest machine. The X-ray generator was operated at 50 kV and 1 mA using Mo Kα (λ = 0.71073Å) radiation. Data were collected with a ω scan width of 0.5°. A total of 408 frames were collected in three different settings of φ (0, 90, 180°) by keeping the sample-to-detector distance fixed at 6.03 cm and the detector position (2θ) fixed at −25°. The final data sets were reduced by an APEX3 program, while a SAINTPLUS [4.72] program was utilized for the integration of diffraction profiles. The absorption correction (multi-scan) was carried out by a SADABS program.[4.73] We initially solved the structure by SIR 92 [4.74], and the full matrix least-square method (SHELXL-2016)[4.75] was used further, which is present in the WinGx suit of programs (Version 1.63.04a).[4.76, 4.77] We successfully located all of the non-hydrogen atoms from Fourier maps and refined them with anisotropic displacement parameters at the final cycles. Finally, we fixed all of the hydrogen atoms at the calculated positions and included them in the refinement process using a riding model associated with isotropic thermal parameters. Details of the structure solution and final refinement are given in Table 4.1.

Table 4.1: Crystal Data and Structure Refinement Parameters of [Cd(BTCH)(L)] (BTCH = mono protonated trimesate and L = 2,4,5-tri-4-pyridyl-1H-imidazole), **4.1**.

Empirical formula	C_{27} H_{17} Cd N_5 O_6
Formula weight	619.85
Crystal system	Monoclinic
Space group	*C*2/*c*
a(Å)	23.466(3)
b(Å)	10.1274(11)
c(Å)	21.189(2)
α(deg)	90
β (deg)	107.972(3)
γ (deg)	90
Volume($Å^3$)	4789.9(9)
Z	8
Calculated density, ρ_{calc}(mg /m^3)	1.719
Absorption coefficient, μ (mm^{-1})	0.968
Temperature	100(2) K
Wavelength(Mo Kα) (Å)	0.71073
θ range (deg)	1.825 to 27.156
Final R indices [I>2sigma(I)]	R_1 = 0.0280, wR_2 = 0.0624
R indices (all data)	R_1 = 0.0363, wR_2 = 0.0695

$R_1 = \Sigma \, ||F_0|-|F_c|| \, / \, \Sigma \, |F_0|$; $wR_2 = \{\Sigma[w(F_0^2 - F_c^2)^2] \, / \, \Sigma[w(F_0^2)^2]\}^{1/2}$. $w = 1/[\sigma^2(F_0)^2 + (aP)^2 + bP]$, $P = [max.(F_0^2,0) + 2(F_c)^2]/3$, where a = 0.0204 and b = 14.6331 for **4.1**.

4.2.6 Optical Studies. The luminescence spectrum of compound **4.1** was recorded at room temperature in an aqueous medium using a Horiba FluoroMax4-spectrofluorometer. The dispersion of compound **4.1** was prepared by using 2.7 mg of compound **4.1** in 2.7 mL distilled water, and performing ultrasonic agitation for 3 minutes. We have checked the excitation wavelength maxima by UV-Vis spectroscopy after adding 100 µL of compound **4.1** with 2 mL of distilled water taken in a quartz cuvette, then performed photoluminescence studies. We have prepared 5 mM, 10 mL aqueous solution of various metal ions such as, Fe^{3+}, Cr^{3+}, Al^{3+}, Cd^{2+}, Cu^{2+}, Mg^{2+}, Ca^{2+},

Co^{2+}, Ni^{2+}, K^{+}, Fe^{2+}, Mn^{2+}, Pb^{2+}, Zn^{2+} and Na^{+}. We have also prepared 5 mM, 5 mL acetonitrile solution of various nitro and non-nitro analytes such as TNP, DNP, 1,2-DNB, NT, B, 1,3-DNB, PhOH, 1,4-DNB, T, DNT, THB. Each photoluminescence titration was carried out using 50 µL of the above stock solution of **4.1** in 2 mL distilled water taken in a quartz cuvette at 300 nm excitation wavelength.

4.3. RESULTS AND DISCUSSION

4.3.1. Structure of compound 4.1. Compound **4.1** crystallized in a monoclinic crystal system with *C*2/*c* space group. The asymmetric unit of compound **4.1** consists of one Cd^{2+} ion, one monoprotonated benzene tricarboxylate (BTCH) and one 2,4,5-tri-4-pyridyl-1H-imidazole (L) ligand. The Cd^{2+} ion is six coordinated with two nitrogen atoms and four oxygen atoms and has a highly distorted octahedral geometry (see Fig. 4.1) through two nitrogen atoms from pyridine rings of L ligand and four oxygen atoms from carboxylate groups of BTCH ligand (see Fig. 4.2).

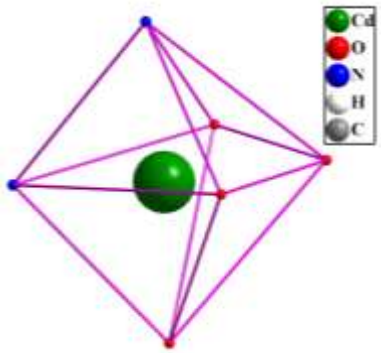

Fig. 4.1 Figure shows the coordination around Cd^{2+} ions in [Cd(BTCH)(L)], **4.1**.

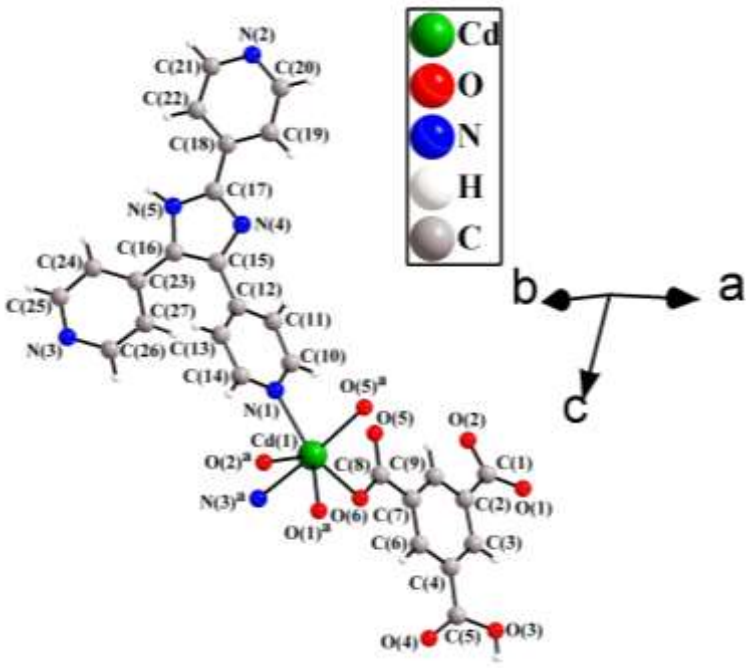

Fig. 4.2 Asymmetric unit along with symmetry generated atoms around Cd^{2+} ions in [Cd(BTCH)(L)], **4.1**. Symmetry code for symmetry generated atoms: O(2)^a x, 1+y,z; O(5)^a 1-x, 1-y, 1-z; N(3)^a ½-x, 1-y, 1-z.

The coordination modes of BTCH and L ligands are shown in figure 4.3. Out of the two carboxylate groups of BTCH, one is bidentate with one Cd^{2+} ion and other one is bidentate with two different Cd^{2+} ions. Two pyridine rings of ligand L connected with Cd^{2+} ions through the nitrogen atoms and the nitrogen atom of third pyridine remains free. The Cd-O bonds have an average distance of 2.34 Å, and Cu-N bonds have an average distance of 2.35 Å. The O/N-Cd-O/N bond angles are in the range of 54.60(6) to 175.51(7)°. The selected bond distances and bond angles are listed in Table 4.2 and Table 4.3 respectively.

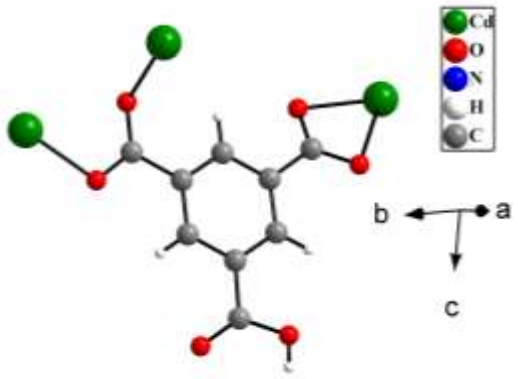

(a)

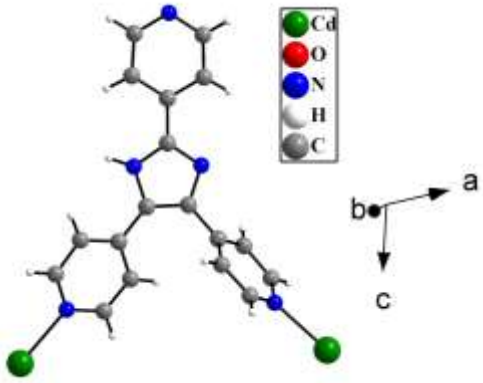

(b)

Fig. 4.3 Figure shows coordination modes of BTCH (a) and L ligand in [Cd(BTCH)(L)], **4.1**.

Table 4.2: Selected Bond Distances (Å) observed in [Cd(BTCH)(L)].

Bond	Distance (Å)
Cd(1)-O(6)	2.2009(19)
Cd(1)-N(1)	2.322(2)
Cd(1)-O(2)#1	2.342(2)
Cd(1)-O(5)#2	2.3811(19)
Cd(1)-N(3)#3	2.382(2)
Cd(1)-O(1)#1	2.4409(18)

Symmetry transformations used to generate equivalent atoms:

For **4.1**: #1 x,y+1,z #2 -x+1,-y+1,-z+1 #3 -x+1/2,-y+3/2,-z+1

Table 4.3: Selected Bond Angles (deg) observed in [Cd(BTCH)(L)].

Angle	Amplitude (º)
O(6)-Cd(1)-N(1)	132.68(8)
O(6)-Cd(1)-O(2)#1	136.98(7)
N(1)-Cd(1)-O(2)#1	88.63(7)
O(6)-Cd(1)-O(5)#2	98.20(7)
N(1)-Cd(1)-O(5)#2	85.50(7)
O(2)#1-Cd(1)-O(5)#2	96.26(7)
O(6)-Cd(1)-N(3)#3	83.59(8)
N(1)-Cd(1)-N(3)#3	90.26(8)
O(2)#1-Cd(1)-N(3)#3	85.10(8)
O(5)#2-Cd(1)-N(3)#3	175.51(7)
O(6)-Cd(1)-O(1)#1	84.65(7)
N(1)-Cd(1)-O(1)#1	142.61(7)
O(2)#1-Cd(1)-O(1)#1	54.60(6)
O(5)#2-Cd(1)-O(1)#1	91.53(7)
N(3)#3-Cd(1)-O(1)#1	92.74(8)

Symmetry transformations used to generate equivalent atoms:

For **4.1**: #1 x,y+1,z #2 -x+1,-y+1,-z+1 #3 -x+1/2,-y+3/2,-z+1

The Cd^{2+} ions are connected through one carboxylate group of BTCH ligand to form dimeric unit $[Cd_2(COO)_2]$. The dimers are connected by the other carboxylate groups of BTCH ligands to form one dimensional structure (Fig. 4.4a). The one-dimensional structures are further connected by L ligands to form two dimensional structures (Fig. 4.4b). Here each dimeric unit connected with four other dimeric units using double connectors (two sides using BTCH and two sides using L ligands) to from a two-dimensional network with Schläfli symbol of $4^4.6^2$ (Fig. 4.5).

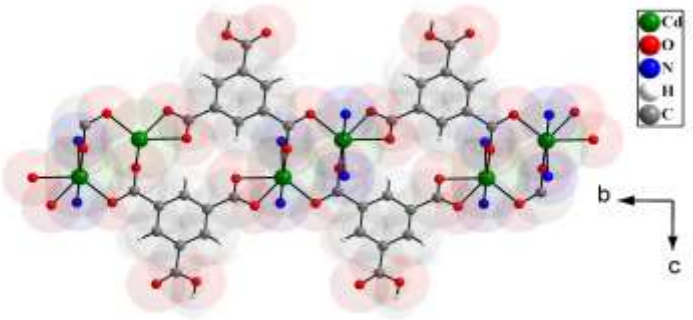

(a)

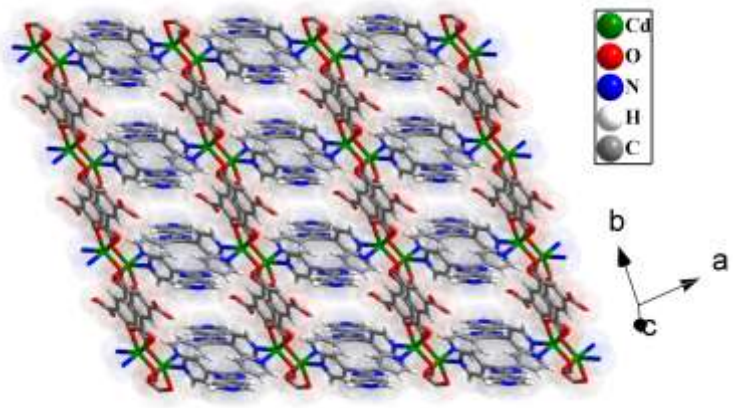

(b)

Fig. 4.4 (a) Figure shows the carboxylate connected one dimensional structure formed by the connectivity between Cd^{2+} ions and BTCH ligands in [Cd(BTCH)(L)], **4.1**. (b) The two dimensional structure formed by the connectivity between one dimensional structure and 2,4,5-tri-4-pyridyl-1H-imidazole) (L) ligands.

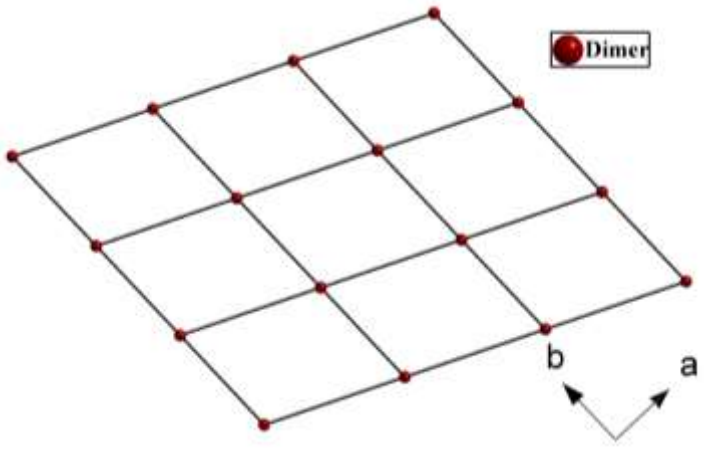

Fig. 4.5 Dimers connected network topology.

The presence of one free carboxylic acid groups of each BTCH ligand and one non-bonded pyridine ring of each L ligand makes the two-dimensional layer structure stabilized through the hydrogen bond interactions (Fig. 4.6). Here N(5) of imidazole moiety of ligand L of one layer acts as hydrogen bond donor and O(1) of carboxylate oxygen of another layer acts as hydrogen bond accepter. This N-H···O hydrogen bond interactions connect consecutive layers in both ways (donor and acceptor). On the other hand, O(3) of free carboxylic acid group of BTCH of one layer acts as hydrogen bond donor and N(2) of nitrogen atom of free pyridine ring of L ligand of alternate layer act as hydrogen bond acceptor. This O-H···N hydrogen bond interactions connect alternate layers also in both ways (donor and acceptor). Fig. 4.6 portraits hydrogen bond interactions among three layers by showing N-H···O hydrogen bonds between layer 1 and 2 and between layer 2 and 3 whereas O-H···N hydrogen bonds between layer 1 and 3. The details about the hydrogen bonds are summarized in Table 4.4.

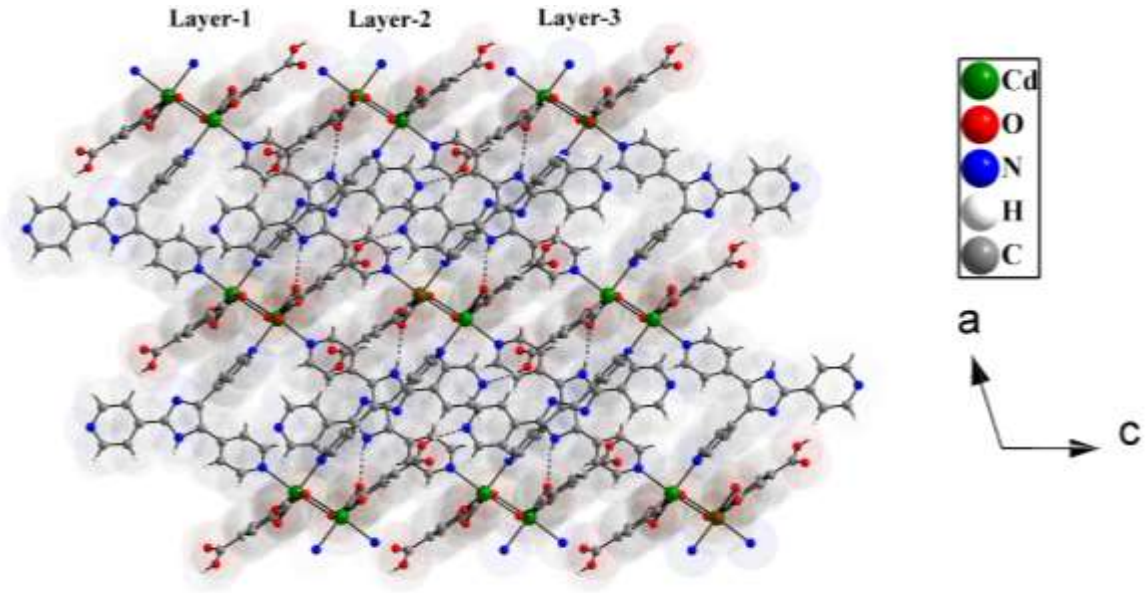

Fig. 4.6 Figure shows hydrogen bond interaction (dashed bond) among three layers to form three-dimensional supra-molecular structure in [Cd(BTCH)(L)], **4.1**.

Table 4.4: Summary of hydrogen-bond interaction observed in [Cd(BTCH)(L)], **4.1**.

D – H···A[a]	D – H (Å)	H···A (Å)	D···A (Å)	D – H···A (°)
O(3) – H(3A)···N(2)$^{\#1}$	0.82	1.93	2.7292(3)	164
N(5) – H(5)···O(1)$^{\#2}$	0.86	1.96	2.7709(4)	157

[a] #1 = -1/2+x,1/2+y,-1+z; #2 = 1/2+x,1/2-y,1/2+z

4.3.2 Characterizations of compound 4.1. Powder X-ray diffraction (XRD) pattern was recorded on well ground compound **4.1** in the 2θ range of 5−50° (see Fig. 4.7). The merged PXRD patterns indicated that the experimental PXRD pattern of the new product is in excellent harmonic with the simulated XRD pattern generated from single crystal X-ray diffraction data. The FTIR spectrum of the compound **4.1** was recorded in the spectral range 4000-500 cm^{-1} (see Fig. 4.8). The FTIR spectrum indicates that the compound **4.1** have no water molecules. The peak at around 1711 cm^{-1} due to the presence of C=O bonds. The peak at around 1610 cm^{-1} indicates the presence of C=C bonds. IR peak at around 1360 cm^{-1} due to the presence of C-H bending. The peak at around 1217 cm^{-1} indicates the presence of C-C bonds and at 724 cm^{-1} due to the presence of $–CH_2$ stretching. Thermogravimetric analysis (TGA) of the compound **4.1** have been carried out in a nitrogen atmosphere from 30°C to 800°C with a heating rate

of 20°C min^{-1} (see Fig. 4.9). The compound **1** showed no weight loss upto 300ºC confirming the absence of any solvent molecule as determined by single-crystal X-ray diffraction. The total observed weight loss of around 75.15% (calculated 79.30%) upto around 600º C is probably due to the decomposition of the compound to CdO.

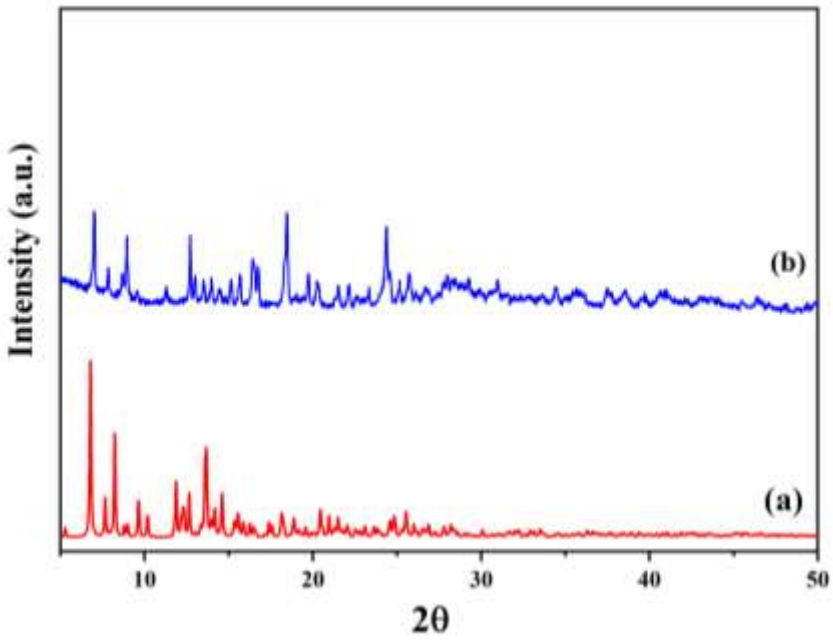

Fig. 4.7 Powder XRD (CuKα) patterns of [Cd(BTCH)(L)], **4.1**: (a) simulated from single crystal X-ray data, (b) experimental.

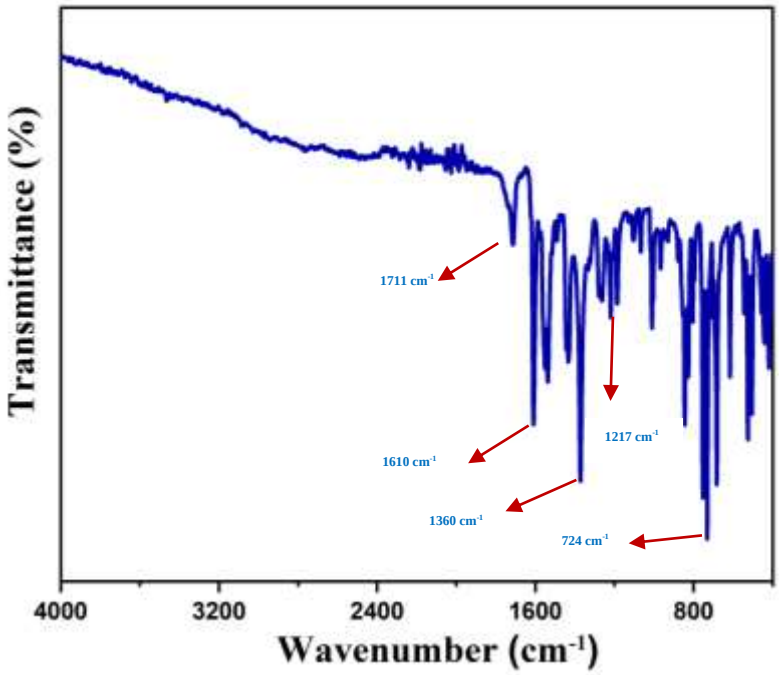

Fig. 4.8 IR spectrum of [Cd(BTCH)(L)], **4.1**.

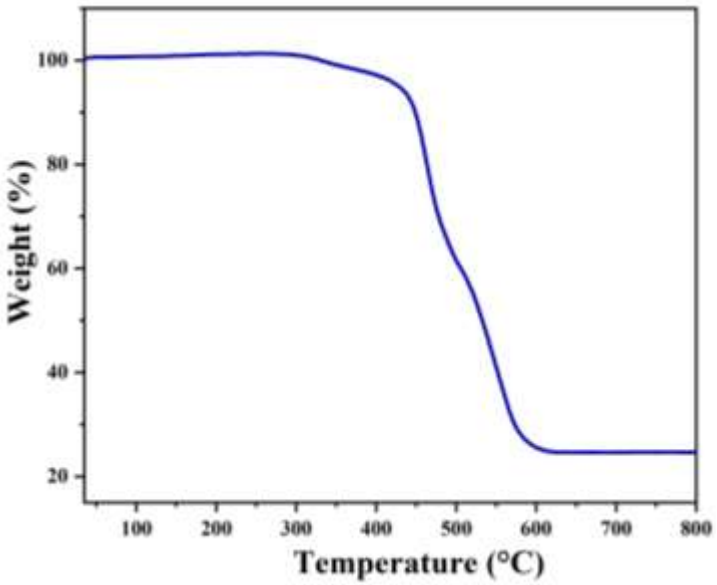

Fig. 4.9 Thermogravimetric analysis (TGA) of [Cd(BTCH)(L)], **4.1**, in nitrogen atmosphere.

4.3.3 Photoluminescence Properties

4.3.3.1 Metal ions detections. The compound **4.1** showed luminescence behavior in aqueous medium at room temperature. Compound **4.1** exhibited emission maximum at 400 nm after immersing 50 µL aqueous solution of **4.1** in 2 mL distilled water taken in a quartz cuvette at 300 nm excitation wavelength. The absorption spectrum of compound **4.1** is shown in fig. 4.10. The emission at 400 nm are due to intra-ligand π* → π and π* → n transition of the aromatic ligands. The excitation spectrum (λ_{em} = 400 nm) of compound **1** is shown in figure 4.11. The merged excitation and emission spectra of compound **4.1** and emission spectrum of the ligand L is shown in figure 4.12. The luminescence stability of compound **4.1** was investigated by measuring the luminescence intensity of same aqueous dispersion of compound **4.1** for five different days (five cycles). The observed intensity for the five cases remains almost constant (see fig. 4.13). The slight variation in intensity values is very common for dispersion state. To explain the sensitivity of **4.1** towards a trace amount of metal ions, luminescence-based titration was carried out with the gradual addition of various metal ions to 2 mL distilled water and 50 µL water dispersion of **4.1** containing quartz cuvette. These studies showed decrease of intensity as well as shifting of emission maximum from 400 nm to 440 nm with continuous addition of Fe^{3+} ion and in the presence of Al^{3+}, Cr^{3+} ions luminescence intensity decreases without shifting of emission peaks (Fig. 6.14, Fig. 6.15, and Fig. 6.16).

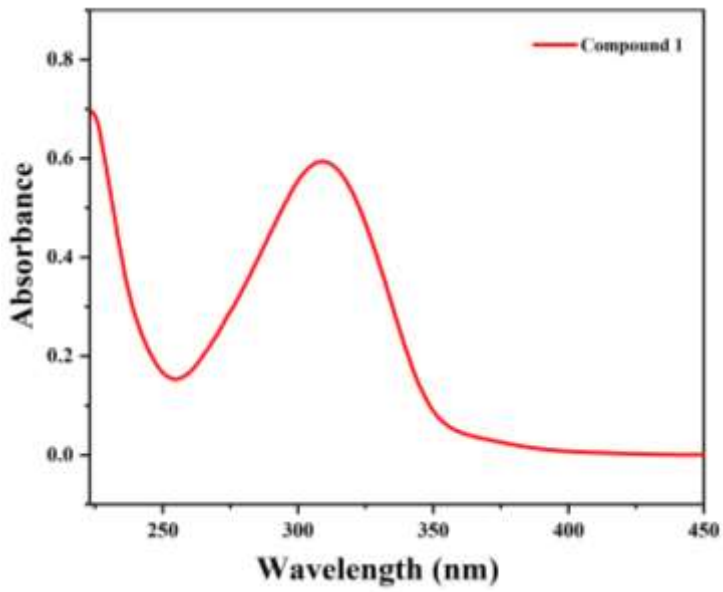

Fig. 4.10 Absorption spectrum of [Cd(BTCH)(L)], **4.1**.

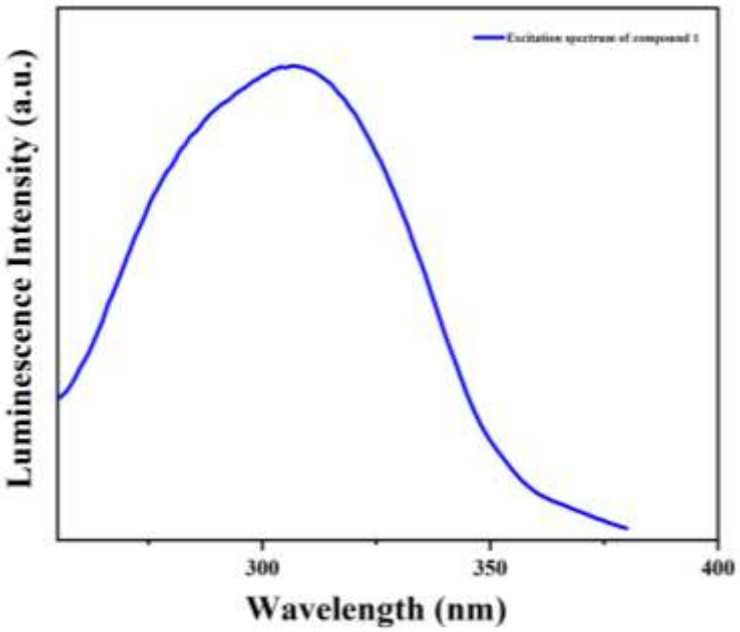

Fig. 4.11 Excitation spectrum of [Cd(BTCH)(L)], **4.1**, in aqueous medium (λ_{em} = 400 nm).

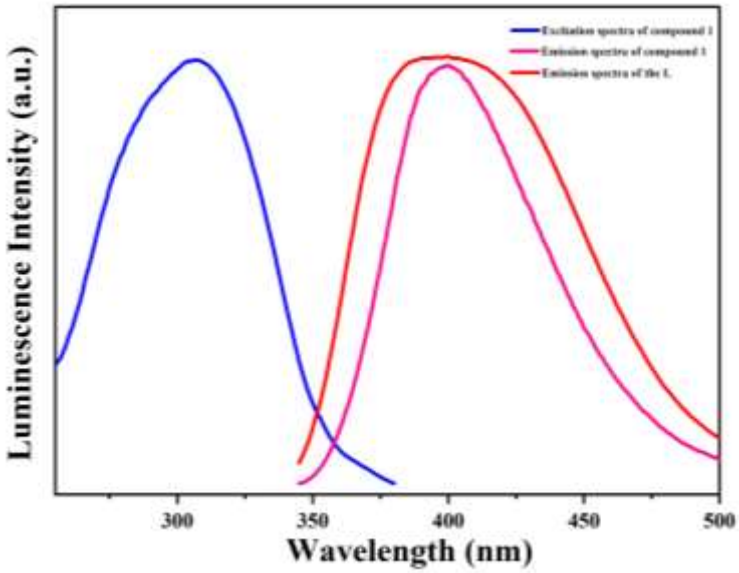

Fig. 4.12 The merged excitation and emission spectra of compound **4.1** and emission spectrum of the ligand L in aqueous medium.

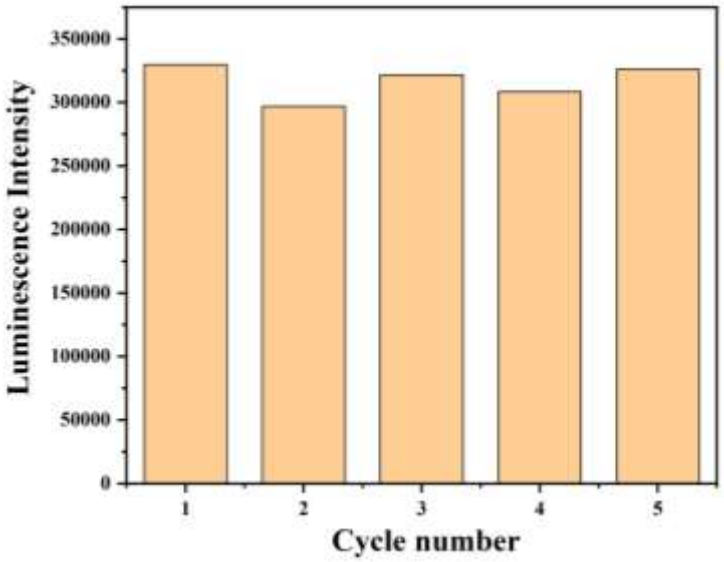

Fig. 4.13 Luminescence intensity of same aqueous dispersion of compound **4.1** for five different days (Cycles).

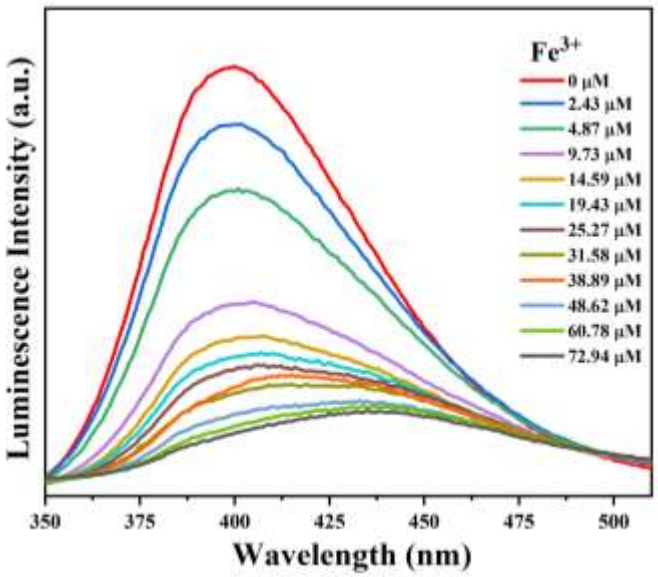

Fig. 4.14 Emission spectra of compound **4.1** dispersed in water upon incremental addition of water solution of Fe^{3+} ions (λ_{ex} = 300 nm). Final concentration of Fe^{3+} in the medium is indicated in the legend.

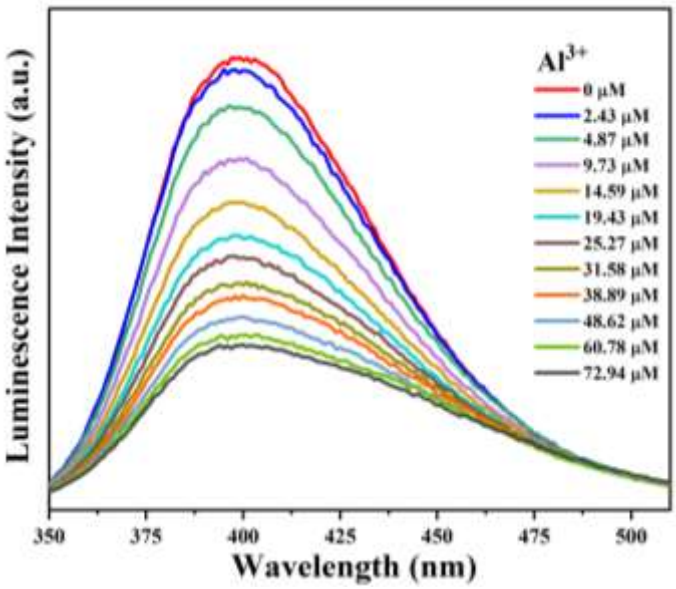

Fig. 4.15 Emission spectra of compound **4.1** dispersed in water upon incremental addition of water solution of Al^{3+} ions (λ_{ex} = 300 nm). Final concentration of Al^{3+} in the medium is indicated in the legend.

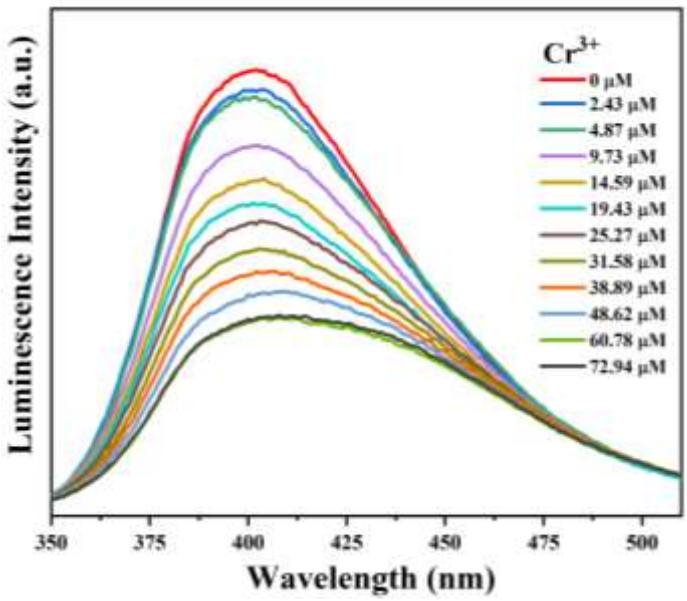

Fig. 4.16 Emission spectra of compound **4.1** dispersed in water upon incremental addition of water solution of Cr^{3+} ions (λ_{ex} = 300 nm). Final concentration of Cr^{3+} in the medium is indicated in the legend.

Similar luminescence based titrations have been carried out with other metal ions such as Cd^{2+}, Zn^{2+}, Ni^{2+}, K^{+}, Cu^{2+}, Ca^{2+}, Mn^{2+}, Na^{+}, Co^{2+}, Fe^{2+}, Pb^{2+}, and Mg^{2+} ions (see Fig. 4.17- Fig. 4.22). In these cases, negligible luminescence quenching or moderate to low turn on effect has been observed. The changes of luminescence intensity based on the emission at 400 nm in the case of all metal ions after the addition of metal ions upto 72.94 μM are shown in fig. 4.23 as bar diagram with respect of $[I_0\text{-}I/I_0]$ versus analytes (I = luminescence intensity after the addition of metal ions at 72.94 μM, I_0 = luminescence intensity before the addition of metal ions). These results indicate that compound **4.1** has significantly different luminescence behavior towards different metal ions. The incremental addition of Fe^{3+} shows almost 85.55% of luminescence quenching effect, which is comparatively higher than that of Al^{3+} (63.14%) and Cr^{3+} (54.48%).

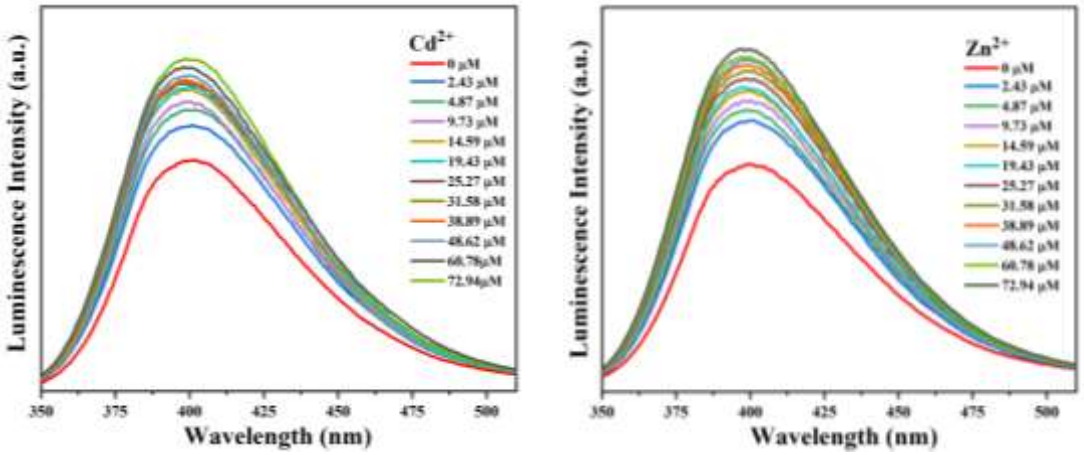

Fig. 4.17 (a) Emission spectra of compound **4.1** dispersed in water upon incremental addition of water solution of Cd^{2+} ions (λ_{ex} = 300 nm). Final concentration of Cd^{2+} in the medium is indicated in the legend. (b) Emission spectra of compound **4.1** dispersed in water upon incremental addition of water solution of Zn^{2+} ions (λ_{ex} = 300 nm). Final concentration of Zn^{2+} in the medium is indicated in the legend.

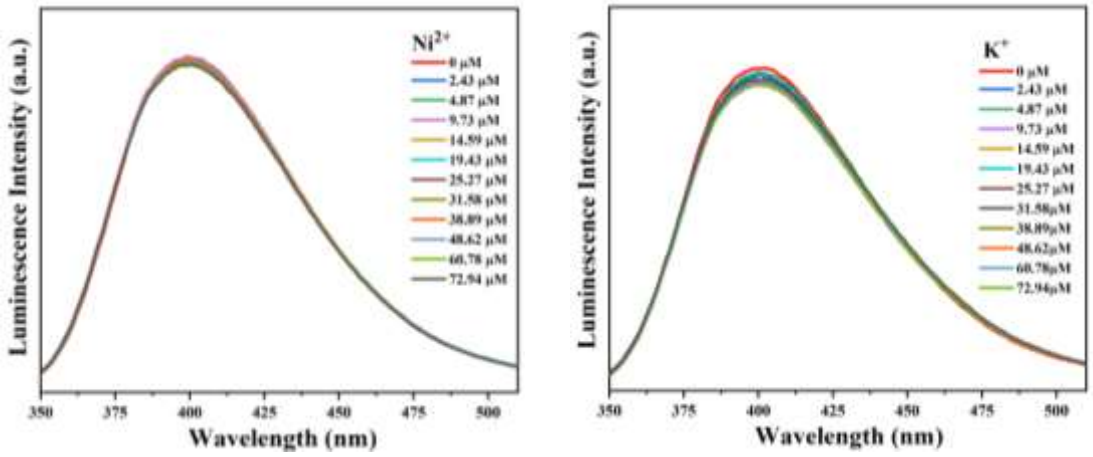

Fig. 4.18 (a) Emission spectra of compound **4.1** dispersed in water upon incremental addition of water solution of Ni^{2+} ions (λ_{ex} = 300 nm). Final concentration of Ni^{2+} in the medium is indicated in the legend. (b) Emission spectra of compound **4.1** dispersed in water upon incremental addition of water solution of K^{+} ions (λ_{ex} = 300 nm). Final concentration of K^{+} in the medium is indicated in the legend.

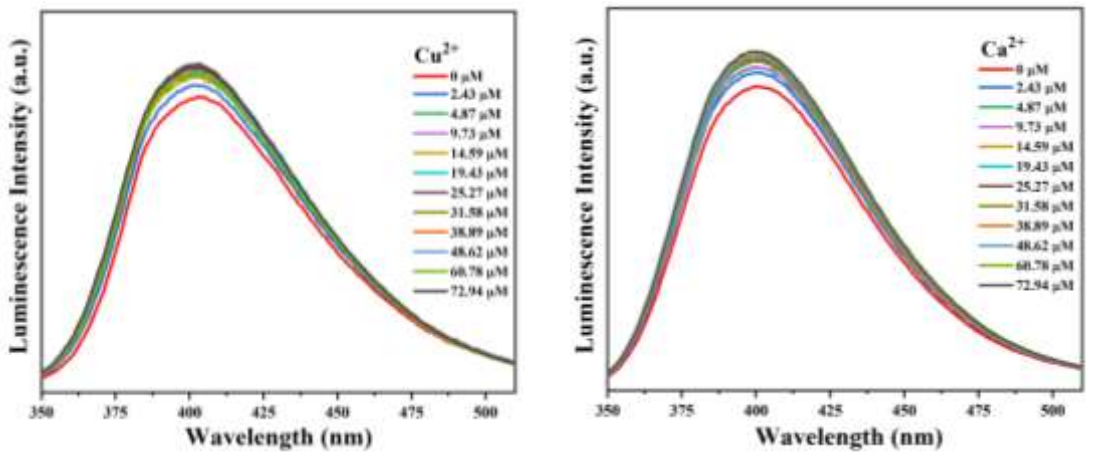

Fig. 4.19 (a) Emission spectra of compound **4.1** dispersed in water upon incremental addition of water solution of Cu^{2+} ions (λ_{ex} = 300 nm). Final concentration of Cu^{2+} in the medium is indicated in the legend. (b) Emission spectra of compound **4.1** dispersed in water upon incremental addition of water solution of Ca^{2+} ions (λ_{ex} = 300 nm). Final concentration of Ca^{2+} in the medium is indicated in the legend.

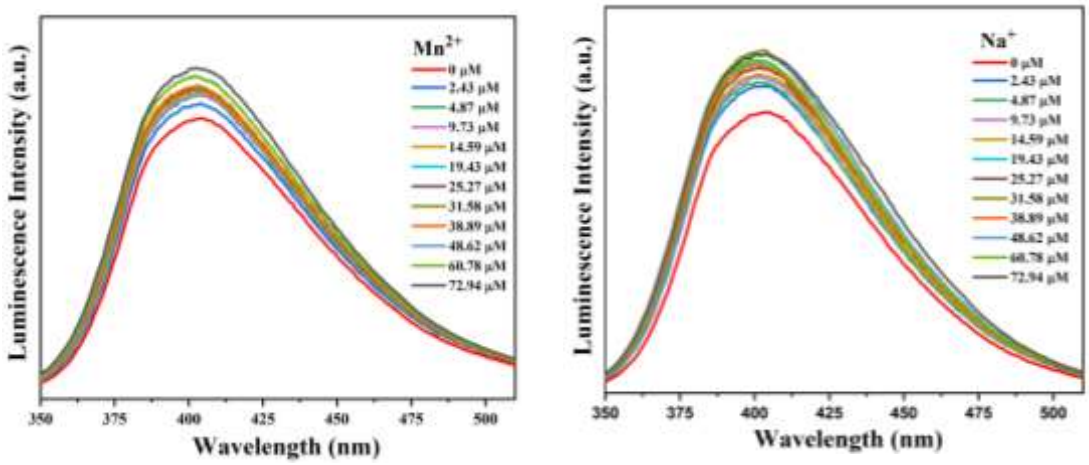

Fig. 4.20 (a) Emission spectra of compound **4.1** dispersed in water upon incremental addition of water solution of Mn^{2+} ions (λ_{ex} = 300 nm). Final concentration of Mn^{2+} in the medium is indicated in the legend. (b) Emission spectra of compound **4.1** dispersed in water upon incremental addition of water solution of Na^{+} ions (λ_{ex} = 300 nm). Final concentration of Na^{+} in the medium is indicated in the legend.

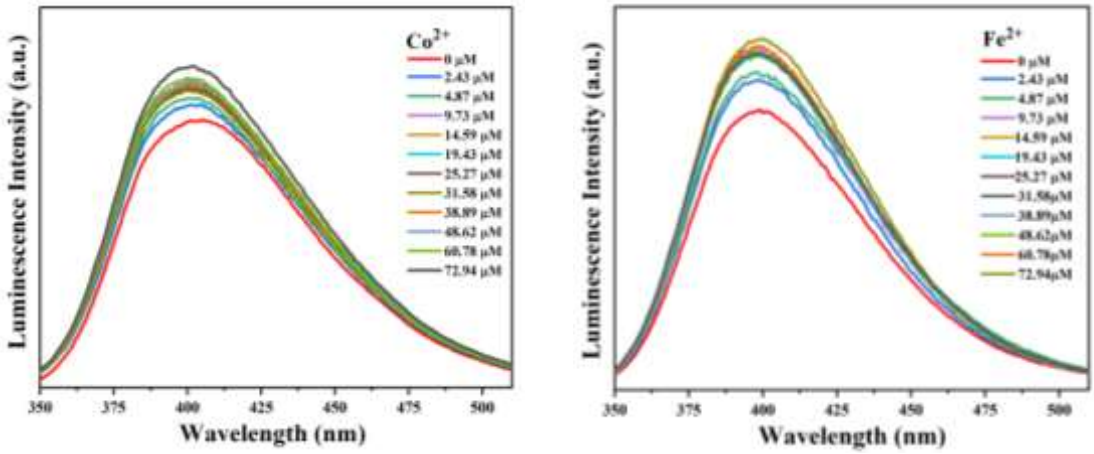

Fig. 4.21 (a) Emission spectra of compound **4.1** dispersed in water upon incremental addition of water solution of Co^{2+} ions (λ_{ex} = 300 nm). Final concentration of Co^{2+} in the medium is indicated in the legend. (b) Emission spectra of compound **4.1** dispersed in water upon incremental addition of water solution of Fe^{2+} ions (λ_{ex} = 300 nm). Final concentration of Fe^{2+} in the medium is indicated in the legend.

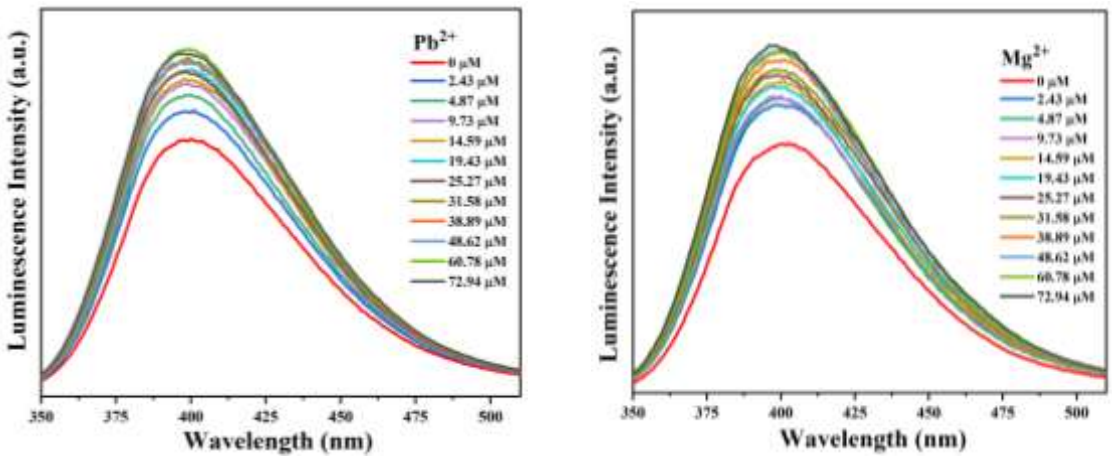

Fig. 4.22 (a) Emission spectra of compound **4.1** dispersed in water upon incremental addition of water solution of Pb^{2+} ions (λ_{ex} = 300 nm). Final concentration of Pb^{2+} in the medium is indicated in the legend. (b) Emission spectra of compound **4.1** dispersed in water upon incremental addition of water solution of Mg^{2+} ions (λ_{ex} = 300 nm). Final concentration of Mg^{2+} in the medium is indicated in the legend.

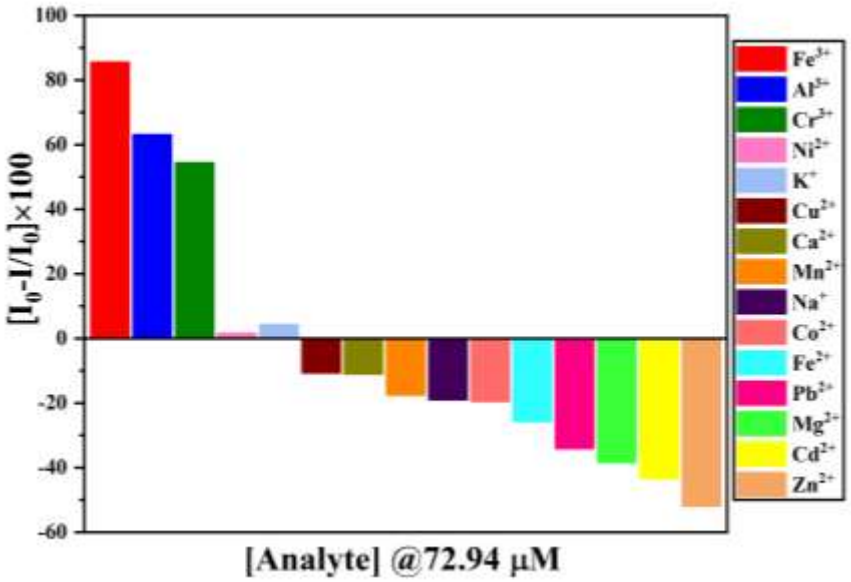

Fig. 4.23 Changes of luminescence intensity with respect of emission of **4.1** (at 400 nm) with 72.94 μM of different metal ions.

The limit of detections for the luminescence quenching responses in the presence of Fe^{3+}, Al^{3+}, and Cr^{3+} ions have been calculated (up to 25.27 μM) and the values are 0.568 μM(31.71 ppb), 1.721 μM(46.43 ppb) and 0.840 μM (43.67 ppb) for Fe^{3+}, Al^{3+}, and Cr^{3+} ions, respectively (see Fig. 4.24-4.26). The observed detection limits are lower than the higher limit of U.S. Environmental Protection Agency (according to EPA the maximum Contaminant Levels of iron, aluminium and chromium are 300 ppb, 200 ppb, 100 ppb respectively).[4.78]

We have also checked the selectivity of the compound **4.1** towards the detection of Fe^{3+}, Al^{3+}, and Cr^{3+} in three separate experiments by observing the luminescence quenching effect of Fe^{3+}, Al^{3+} and Cr^{3+} metal ions in the presence of Cd^{2+}, Cu^{2+}, Mg^{2+}, Ca^{2+}, Co^{2+}, K^{+}, Mn^{2+}, Pb^{2+}, Zn^{2+}, Na^{+}, Ni^{2+} and Fe^{2} ions. The photoluminescence spectrum of compound **4.1** in aqueous medium was recorded using specifically designed experimental protocol and to these experimental strategies, 2.43 μM of each metal ion prepared in aqueous solution was added in **4.1** with sequentially followed by the stepwise addition of 5mM aqueous solution of Fe^{3+} ion solution continuously upto 60.85 μM and monitoring the corresponding emissions spectrums (see Fig. 4.27).

Similar selectivity experiments were performed towards Al^{3+} and Cr^{3+} metal ions and the corresponding emissions spectrums are shown in, Fig. 4.28 and Fig. 4.29. Initially addition of various ions showed very small effect on luminescence intensity. However, the addition of aqueous solution of Fe^{3+}, Al^{3+} and Cr^{3+} ions gave significant luminescence quenching effect, and the quenching efficiency of Fe^{3+}, Al^{3+} and Cr^{3+} remaining unaffected. The sensitivity of the metal ions were also explained by using Stern-Volmer plots. The equation of Stern-Volmer (SV) is $(I_0/I) = K_{sv}[A]+1$, where I and I_0 are the luminescence intensities of the probe, after and before addition of the analytes, [A] is the molar concentration and Ksv is the luminescence quenching/enhancement constant. As shown in fig. 4.30, the linear increase in $[I_0/I]$ for the three metal ions (Fe^{3+}, Cr^{3+}, Al^{3+}) up to 72.94 μM have been observed. These increasing trends of linear variation of SV plot indicate static quenching. For the other metal ions, either very small increasing or decreasing trends of linear variation have been observed due to small quenching/turn-on effect. We have also fitted the experimental data in the S-V equation and K_{SV} values of the analytes are 8.15×10^4 M^{-1}, 2.44×10^4 M^{-1}, 1.82×10^4 M^{-1}, 0.02×10^4 M^{-1}, 0.03×10^4 M^{-1}, -0.05×10^4 M^{-1}, -0.09×10^4 M^{-1}, -0.15×10^4 M^{-1}, -0.15×10^4 M^{-1}, -0.14×10^4 M^{-1}, -0.13×10^4 M^{-1}, -0.24×10^4 M^{-1}, -0.27×10^4 M^{-1} , -0.26×10^4 M^{-1} and -0.31×10^4 M^{-1} for Fe^{3+}, Al^{3+}, Cr^{3+}, Ni^{2+}, K^{+}, Cu^{2+}, Ca^{2+}, Mn^{2+}, Na^{+}, Co^{2+}, Fe^{2+}, Pb^{2+}, Mg^{2+}, Cd^{2+} and Zn^{2+} metal ions, respectively. The higher

K_{SV} values showed extraordinary sensitivity of compound **4.1** towards Fe^{3+}, and moderate sensitivity upon addition of Al^{3+}, Cr^{3+} metal ions.

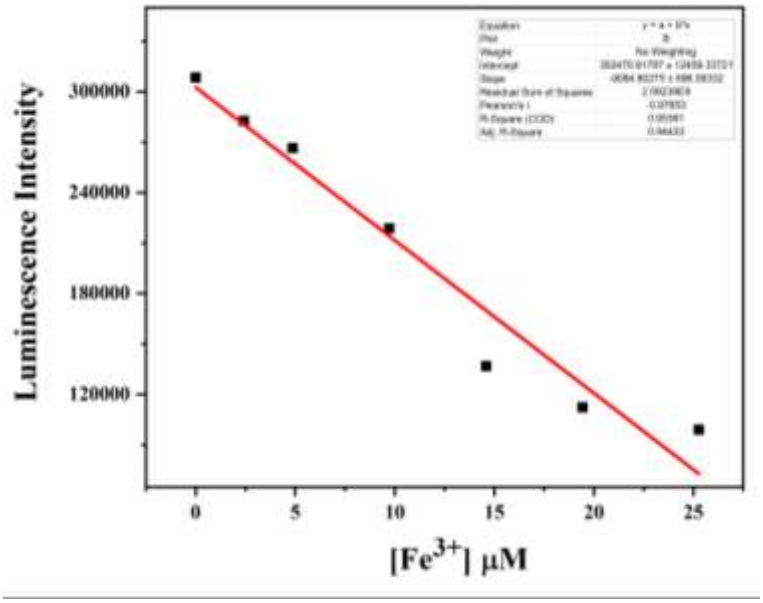

Fig. 4.24 The plot of the changes of luminescence intensity of compound **4.1** (λ_{em} = 400 nm) vs concentration of Fe^{3+} solution (up to 25.27 µM) indicating the detection limit, which calculated using the equation, LOD = 3σ/m, where σ = standard deviation of blank determination and m = slope of the linear curve.

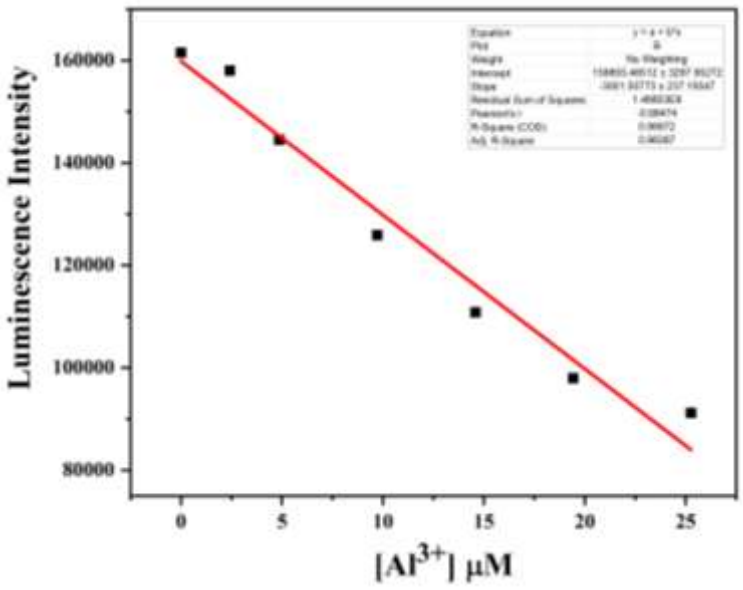

Fig. 4.25 The plot of the changes of luminescence intensity of compound **4.1** (λ_{em} = 400 nm) vs concentration of Al^{3+} solution (up to 25.27 µM) indicating the detection limit, which calculated using the equation, LOD = 3σ/m, where σ = standard deviation of blank determination and m = slope of the linear curve.

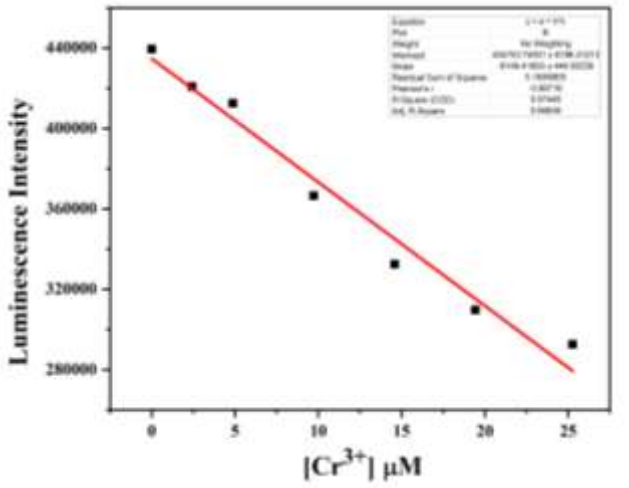

Fig. 4.26 The plot of the changes of luminescence intensity of compound **4.1** (λ_{em} = 400 nm) vs concentration of Cr^{3+} solution (up to 25.27 µM) indicating the detection limit, which calculated using the equation, LOD = 3σ/m, where σ = standard deviation of blank determination and m = slope of the linear curve.

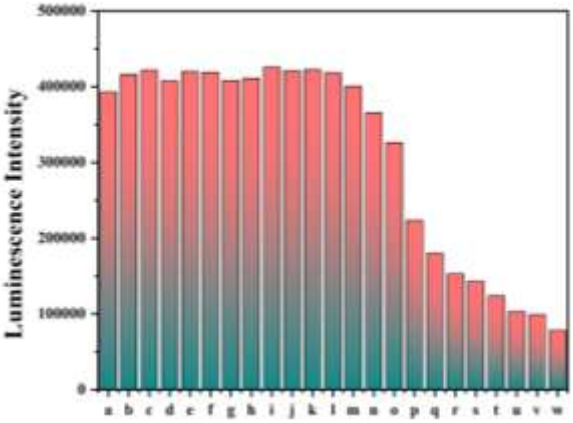

Fig. 4.27 Bar diagram presenting the luminescence intensity (observed at 400 nm) after the consecutive addition of the analytes. The composition and concentration of the system were as follows: (a) **4.1** in aqueous dispersion, (b) a + 2.43 μM Cd^{2+}, (c) b + 2.43 μM Cu^{2+}, (d) c + 2.43 μM Mg^{2+}, (e) d + 2.43 μM Ca^{2+}, (f) e + 2.43 μM Co^{2+}, (g) f + 2.43 μM K^{+}, (h) g + 2.43 μM Mn^{2+}, (i) h + 2.43 μM Pb^{2+}, (j) i + 2.43 μM Zn^{2+}, (k) j + 2.43 μM Na^{+}, (l) K + 2.43 μM Ni^{2+}, (m) l + 2.43 μM Fe^{2+}, (n) m + 2.43 μM Fe^{3+}, (o) n + 2.43 μM Fe^{3+}, (p) o + 4.87 μM Fe^{3+}, (q) p + 4.87 μM Fe^{3+}, (r) q + 4.87 μM Fe^{3+}, (s) r + 4.87 μM Fe^{3+}, (t) s + 7.31 μM Fe^{3+}, (u) t + 7.31 μM Fe^{3+}, (v) u + 9.73 μM Fe^{3+}, (w) v + 12.16 μM Fe^{3+}.

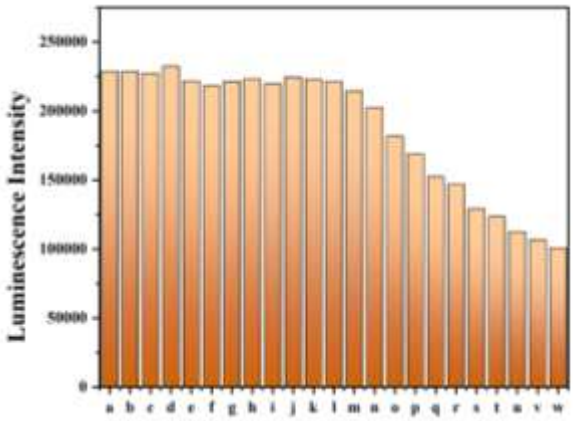

Fig. 4.28 Bar diagram presenting the luminescence intensity (observed at 400 nm) after the consecutive addition of the analytes. The composition and concentration of the system were as follows: (a) **4.1** in aqueous dispersion, (b) a + 2.43 μM Cd^{2+}, (c) b + 2.43 μM Cu^{2+}, (d) c + 2.43 μM Mg^{2+}, (e) d + 2.43 μM Ca^{2+}, (f) e + 2.43 μM Co^{2+}, (g) f + 2.43 μM K^{+}, (h) g + 2.43 μM Mn^{2+}, (i) h + 2.43 μM Pb^{2+}, (j) i + 2.43 μM Zn^{2+}, (k) j + 2.43 μM Na^{+}, (l) K + 2.43 μM Ni^{2+}, (m) l + 2.43 μM Fe^{2+}, (n) m + 2.43 μM Al^{3+}, (o) n + 2.43 μM Al^{3+}, (p) o + 4.87 μM Al^{3+}, (q) p + 4.87 μM Al^{3+}, (r) q + 4.87 μM Al^{3+}, (s) r + 4.87 μM Al^{3+}, (t) s + 7.31 μM Al^{3+}, (u) t + 7.31 μM Al^{3+}, (v) u + 9.73 μM Al^{3+}, (w) v + 12.16 μM Al^{3+}.

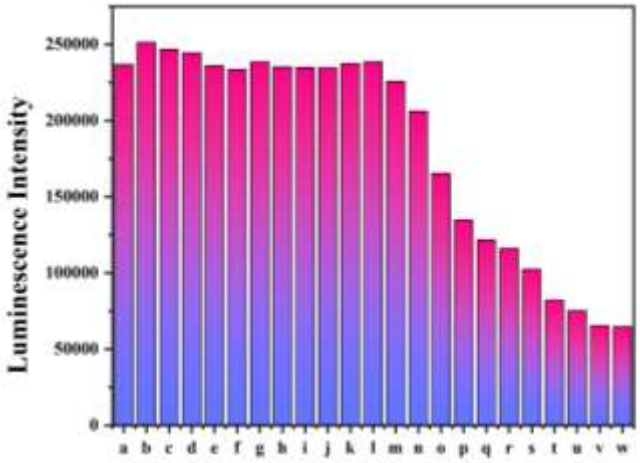

Fig. 4.29 Bar diagram presenting the luminescence intensity (observed at 400 nm) after the consecutive addition of the analytes. The composition and concentration of the system were as follows: (a) **4.1** in aqueous dispersion, (b) a + 2.43 μM Cd^{2+}, (c) b + 2.43 μM Cu^{2+}, (d) c + 2.43 μM Mg^{2+}, (e) d + 2.43 μM Ca^{2+}, (f) e + 2.43 μM Co^{2+}, (g) f + 2.43 μM K^{+}, (h) g + 2.43 μM Mn^{2+}, (i) h + 2.43 μM Pb^{2+}, (j) i + 2.43 μM Zn^{2+}, (k) j + 2.43 μM Na^{+}, (l) K + 2.43 μM Ni^{2+}, (m) l + 2.43 μM Fe^{2+}, (n) m + 2.43 μM Cr^{3+}, (o) n + 2.43 μM Cr^{3+}, (p) o + 4.87 μM Cr^{3+}, (q) p + 4.87 μM Cr^{3+}, (r) q + 4.87 μM Cr^{3+}, (s) r + 4.87 μM Cr^{3+}, (t) s + 7.31 μM Cr^{3+}, (u) t + 7.31 μM Cr^{3+}, (v) u + 9.73 μM Cr^{3+}, (w) v + 12.16 μM Cr^{3+}.

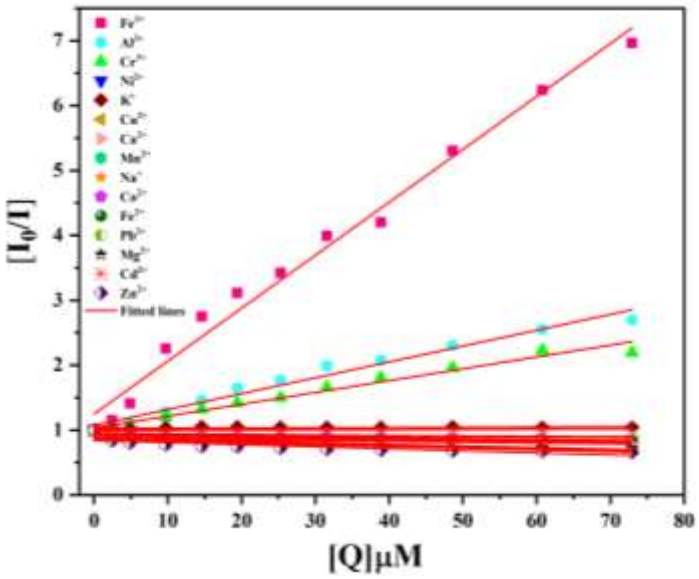

Fig. 4.30 Plot of I_0/I of compound **4.1** (at 400 nm) vs concentration of analytes in the higher concentration range of analytes (upto 72.94 μM). I_0 and I are the luminescence intensity in absence and presence of the analyte, respectively.

The time-correlated single photon counting (TCSPC) of the compound **4.1** with the incremental addition of Fe^{3+}, Cr^{3+}, Al^{3+} ions were also checked (see Fig. 31- Fig. 33 and Table 4.5). In the case of Fe^{3+} the luminescence life time have been slightly increased with the addition Fe^{3+} ions. A comparative study with others previously reported materials and compound **4.1** for sensing of the Fe^{3+}, Al^{3+} and Cr^{3+} ions are shown in Tables 4.6–4.8, respectively [4.78-4.98].

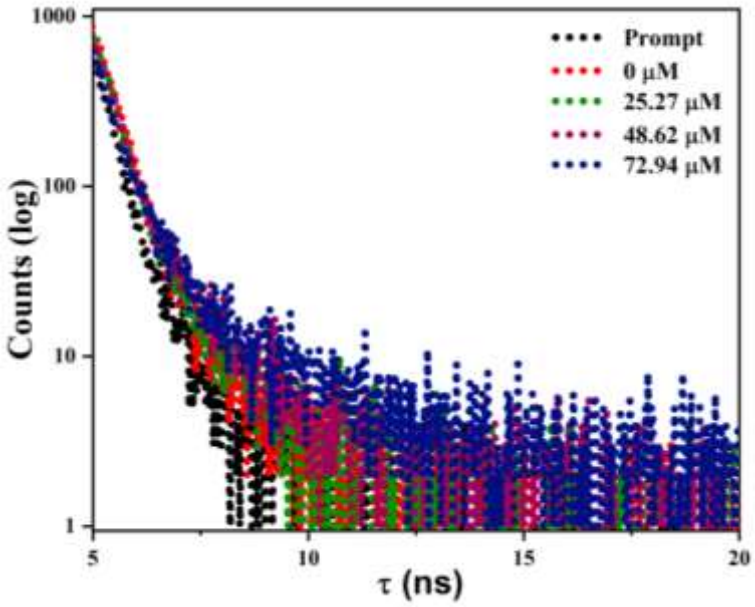

Fig. 4.31 Luminescence lifetime decay profile of compound **4.1** before and after the addition of the Fe^{3+} ions. The final concentration of Fe^{3+} ions in the medium is indicated in the legend. The instrument response function (prompt) is also shown. Here, λ_{ex} = 300 nm and λ_{em} = 400 nm were set during the experiment.

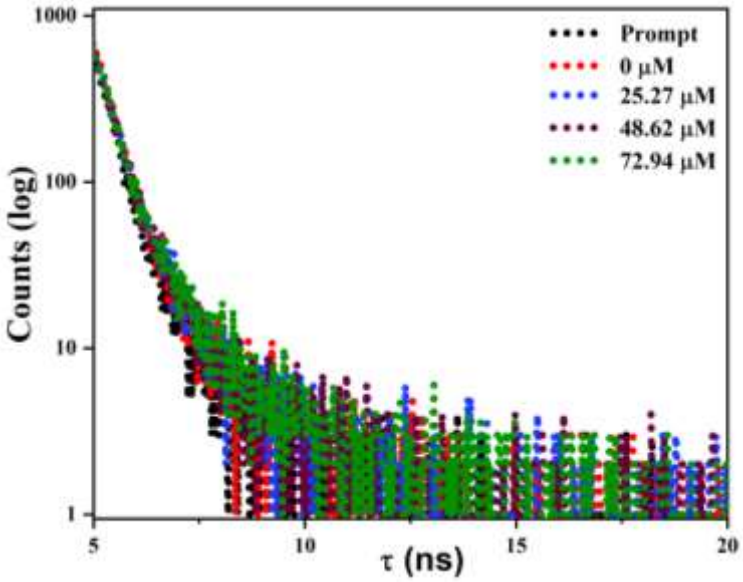

Fig. 4.32 Luminescence lifetime decay profile of compound **4.1** before and after the addition of the Al^{3+} ions. The final concentration of Al^{3+} ions in the medium is indicated in the legend. The instrument response function (prompt) is also shown. Here, λ_{ex} = 300 nm and λ_{em} = 400 nm were set during the experiment.

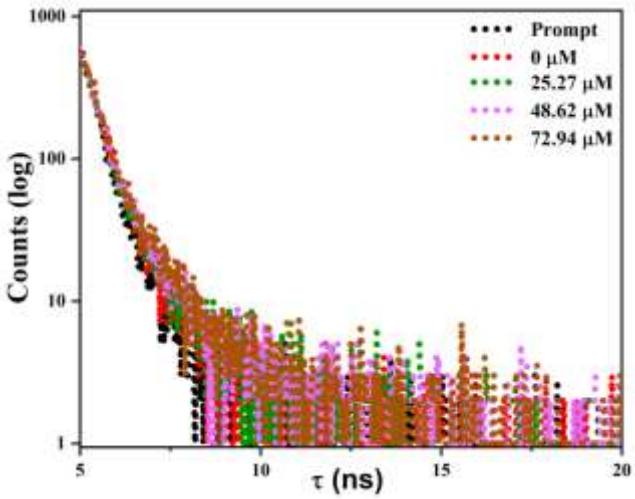

Fig. 4.33 Luminescence lifetime decay profile of compound **4.1** before and after the addition of the Cr^{3+} ions. The final concentration of Cr^{3+} ions in the medium is indicated in the legend. The instrument response function (prompt) is also shown. Here, λ_{ex} = 300 nm and λ_{em} = 400 nm were set during the experiment.

Table 4.5: Details of Time-Resolved Experiments of Compound **4.1** before and after the Addition of Fe^{3+}, Al^{3+}, and Cr^{3+}.

Analytes	Concentration (μM)	Lifetime (ns)
Fe^{3+}	0	0.593
	25.27	0.632
	48.62	0.886
	72.94	1.150
Al^{3+}	0	0.560
	25.27	0.570
	48.62	0.583
	72.94	0.621
Cr^{3+}	0	0.556
	25.27	0.574
	48.62	0.580
	72.94	0.614

Table 4.6: A summary of the sensing behaviours of Fe^{3+} ions using various reported CPs.

Materials	Solvent	Mechanism	Limit Of Detection(μM)	Ref.
Compound **1**	Quenching	Quenching	0.568	
Tb^{3+}@Cd-MOF	Aqueous	Quenching	0.89	[79]
Cd-MOF	Aqueous	Quenching	28	[80]
$[Cd(ttc)(H_2O)]\cdot H_2O\}_n$ (ttc = 1-imidazole-1-yl-2,4,6-benzene-tricarboxylic acid)	Aqueous	Quenching	0.053	[81]
$[Zn(L^1)_{0.5}(L^2)_{0.5}(H_2O)]\cdot DMF$ L^1 = 2,3,5,6-tetra(4-carboxyphenyl)pyrazine L^2 = 1,2-di(4-pyridyl)ethylene	Aqueous	Quenching	3.4	[82]
$[Tb(Hmcd)(H_2O)(DMF)_2]_n$ H_4mcd=9,9'-methylenebis(9H-carbazole-3,6-dicarboxylic acid.	Aqueous	Quenching	5	[83]
MIL-53(Al)	Aqueous	Quenching	150	[84]
$[\{Zn_2(2,6\text{-}NDC)_2(L)\}\cdot xG]_n$ L = 2,5-bis(3-pyridyl)-3,4-diaza-2,4-hexadiene 2,6-H_2NDC = 2,6-naphthalenedicarboxylic acid	Aqueous	Turn-On	0.93	[85]

Table 4.7: A summary of the sensing behaviour of Al^{3+} ions using various reported CPs.

Materials	Solvent	Mechanism	Limit Of Detection (μM)	Ref.
Compound **1**	Aqueous	Quenching	1.721	
$\{[Co_3(TTHA)(bibp)_2(H_2O)]\}_n$ H_6TTHA = 1,3,5-triazine-2,4,6-triamine hexaacetic acid bibp = 4,4′-bis(imidazolyl)biphenyl	Aqueous	Turn-On	0.35	[86]
$[Co(OBA)(DATZ)_{0.5}(H_2O)]$ OBA = 4,4′-oxybis(benzoic acid) DATZ = 3,5-diamino-1,2,4-triazole	Aqueous	Turn-On	0.43	[87]
$[Cd_2(L1)(BDC)_2 \cdot 1.5i\text{-PrOH}]_n$ L1 = 9,10-bis(di(pyridine-4-yl)methylene)-9,10-dihydroanthracene	Aqueous	Quenching	11.8	[88]
$\{[Co_3(BIBT)_3(BTC)_2(H_2O)_2] \cdot solvents\}_n$ BIBT = 4,7-bi(1H-imidazol-1-yl)benzo [2,1,3]thiadiazol H_3BTC=1,3,5-benzenetricarboxylicacid)	DMA	Turn-On	0.10	[89]
$\{[Cd(BBZB)(2,6\text{-}NDC)] \cdot CH_3OH\}_n$ BBZB = 4,7-bis(1*H*-benzimidazole-1-yl)-2,1,3-benzothiadiazole 2,6-NDC = 2,6-naphthalenedicarboxylate	DMF	Turn-On	0.61	[90]
Tb-MOF	Aqueous	Quenching	6.1	[91]
JXUST-18	Ethanol	Turn-On	0.184	[92]

Table 4.8: A summary of the sensing behaviour of Cr^{3+} ions using various reported CPs.

Materials	Solvent	Mechanism	Limit Of Detection(LOD (μM)	Ref.
Compound **1**	Aqueous	quenching	0.840	
$\{[Co_3(TTHA)(bibp)_2(H_2O)]\}_n$ H_6TTHA = 1,3,5-triazine-2,4,6-triamine hexaacetic acid bibp = 4,4′-bis(imidazolyl)biphenyl	Aqueous	Quenching	0.56	[86]
$\{Cu_2(DPQ)_2(OBPBI)\}_n$ H_2DPQ = 4, 4′-(quinoxaline-2, 3-diyl)dibenzoic acid OBPBI = 1, 1′-[oxybis(4, 1-phenylene)]bis(1*H*-imidazole)	Aqueous	Turn-On	0.026	[93]
$[Zn_2(TCBPDC)_{0.5}(H_2O)_2]_n \cdot 2.5H_2O \cdot 5DMF$ $H_8TCBPDC$ = 4′,4‴,4⁗,4⁗′-(ethene-1,1,2,2-tetrayl)tetrakis(([1,1′-biphenyl]-3,5-dicarboxylic acid)	EtOH-H_2O	Quenching	1.39	[94]
Co–EDDA	Aqueous	Turn-On	0.54	[95]
$Zn_3(bpdc)_2(pdc)(DMF) \cdot 6DMF$ bpdc = 4,4′-biphenyldicarboxylic acid pdc = pyridine-3,5-dicarboxylate	DMF	Quenching	25.1	[96]
$[Eu_2(ppda)_2(npdc)(H_2O)] \cdot H_2O$	Aqueous	Quenching	16.6	[97]
$[Cd(H_2dhbdc)(NI\text{-}mbpy\text{-}34)_2]_n$ H_4dhbdc = 2,5-dihydroxyterephthalic acid NI-mbpy-34 = *N*-(pyridin-3-ylmethyl)-4-(pyridin-4-yl)-1,8-naphthalimide	Aqueous	Turn-On	0.34	[98]

4.3.3.2 Nitro-explosive detections. To examine the sensitivity of **4.1** towards a trace amount of nitro-explosives, the luminescence based titrations were performed with the incremental addition of nitro and non-nitro analytes solution (in acetonitrile) to the aqueous dispersion of compound **4.1**. Compound **4.1** showed significant decrease of luminescence intensity as well as shifting of emission maximum from 400 nm to 455 nm in case of TNP. The

change in luminescence intensity of compound **4.1** with the incremental addition of TNP (up to 72.94 μM) is shown in fig. 4.34.

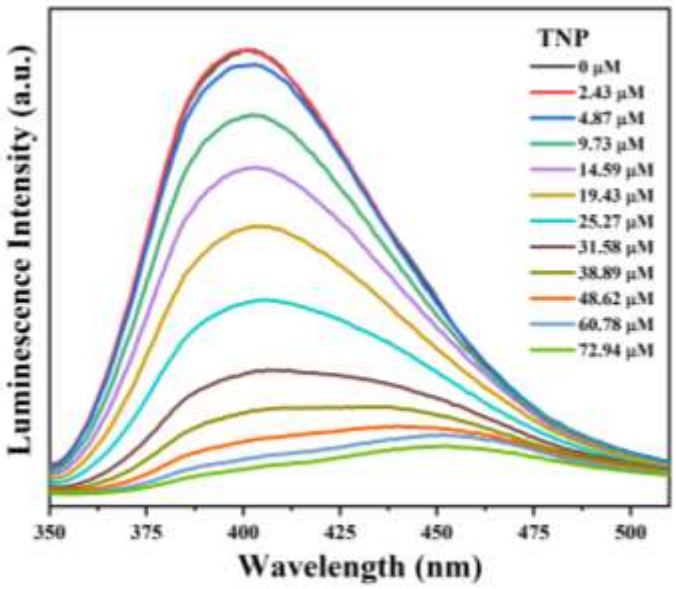

Fig. 4.34 The emission spectra of compound **4.1** dispersed in water upon incremental addition of acetonitrile solution of TNP (λ_{ex} = 300 nm). Final concentration of TNP in the medium is indicated in the legend.

In the presence of DNP, the luminescence intensity gradually decreased with out shifting of emission peaks (see Fig. 4.35). Similar luminescence-based experiments were also carried out with other nitro and non-nitro analytes such as 1,2-DNB, NT, B, 1,3-DNB, PhOH, 1,4-DNB, THB, DNT, T (see, Fig. 4.36- Fig. 4.40). The changes of luminescence intensity based on the emission at 400 nm in the case of nitro and non-nitro analytes upto 72.94 μM are shown in Fig. 4.41, as bar diagram with respect of $[(I_0\text{-}I)/I_0]$ versus analytes (I = luminescence intensity after the addition of metal ions at 72.94 μM, I_0 = luminescence intensity before the addition of metal ions). These results indicate that compound **4.1** has differential luminescence response towards these analytes. The incremental addition of TNP shows almost 94.11% of luminescence quenching effect, which is comparatively higher than that of DNP (56.19%). The incremental addition of nitro and non-nitro analytes (upto 72.94 μM) in the aqueous dispersion of compound **4.1** showed a low to moderate increase in luminescence intensity for 1,2-DNB (3.51%), NT(7.20%) , B (20.55%), 1,3-DNB (24.80%), PhOH (26.61%) , 1,4-DNB (26.90%), THB (31.20%), DNT (31.85%), T (46.99%), respectively.

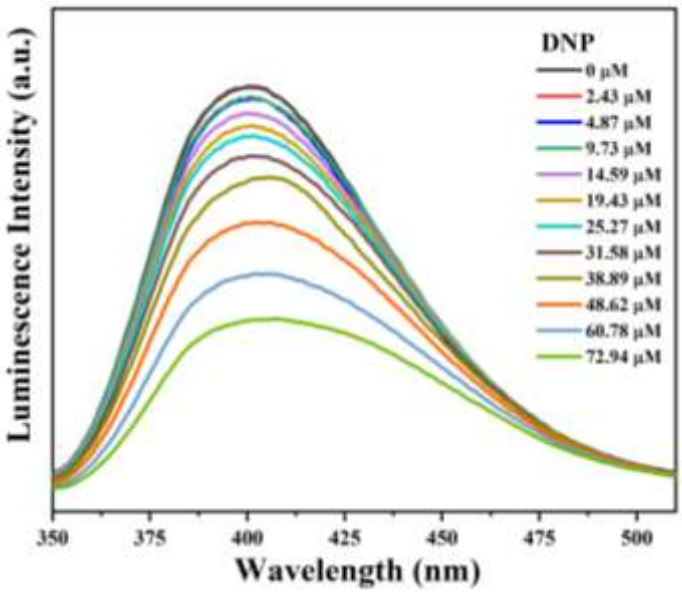

Fig. 4.35 The emission spectra of compound **4.1** dispersed in water upon incremental addition of acetonitrile solution of DNP (λ_{ex} = 300 nm). Final concentration of DNP in the medium is indicated in the legend.

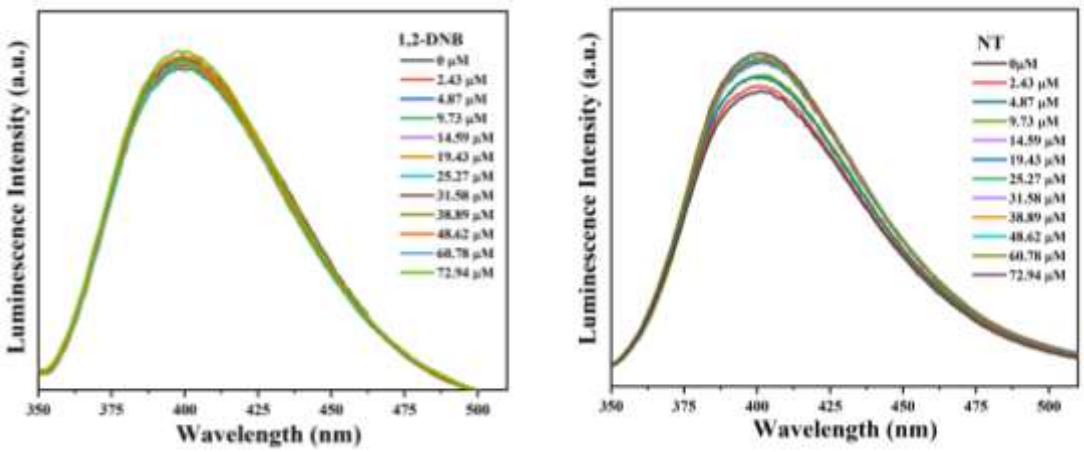

Fig. 4.36 (a) The emission spectra of compound **4.1** dispersed in water upon incremental addition of acetonitrile solution of 1,2-DNB (λ_{ex} = 300 nm). Final concentration of 1,2-DNB in the medium is indicated in the legend. (b) The emission spectra of compound **4.1** dispersed in water upon incremental addition of acetonitrile solution of NT (λ_{ex} = 300 nm). Final concentration of NT in the medium is indicated in the legend.

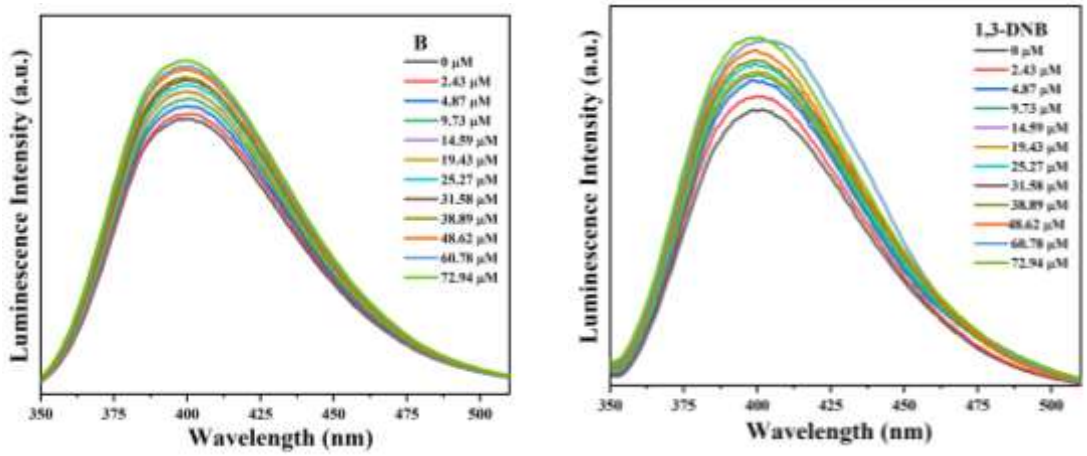

Fig. 6.37 (a) The emission spectra of compound **4.1** dispersed in water upon incremental addition of acetonitrile solution of benzene (λ_{ex} = 300 nm). Final concentration of benzene in the medium is indicated in the legend. (b) The emission spectra of compound **4.1** dispersed in water upon incremental addition of acetonitrile solution of 1,3-DNB (λ_{ex} = 300 nm). Final concentration of 1,3-DNB in the medium is indicated in the legend.

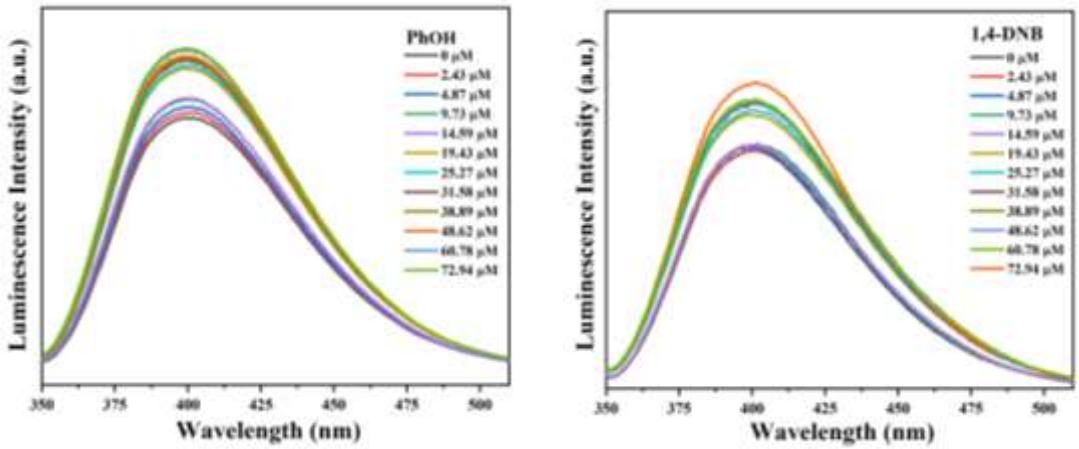

Fig. 4.38 (a) The emission spectra of compound **4.1** dispersed in water upon incremental addition of acetonitrile solution of phenol (λ_{ex} = 300 nm). Final concentration of phenol in the medium is indicated in the legend. (b) The emission spectra of compound **4.1** dispersed in water upon incremental addition of acetonitrile solution of 1,4-DNB (λ_{ex} = 300 nm). Final concentration of 1,4-DNB in the medium is indicated in the legend.

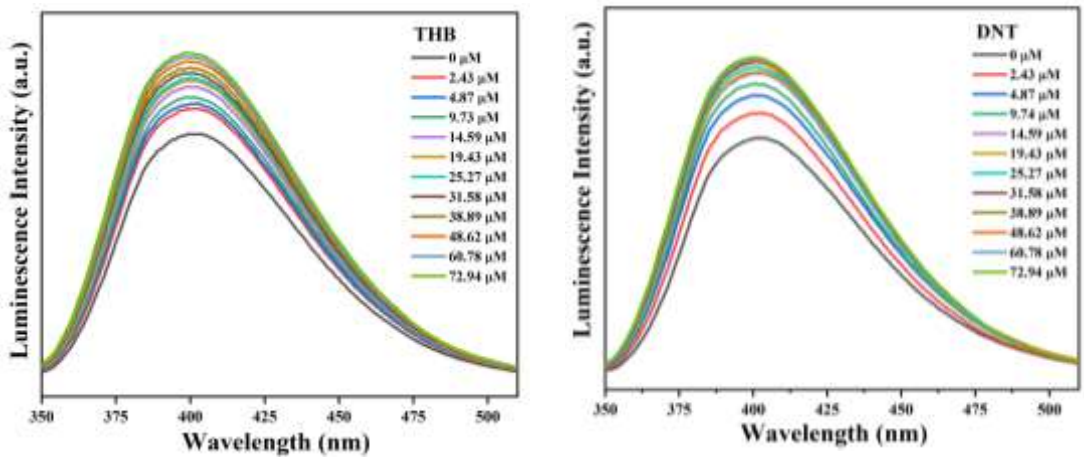

Fig. 3.39 (a) The emission spectra of compound **4.1** dispersed in water upon incremental addition of acetonitrile solution of THB (λ_{ex} = 300 nm). Final concentration of THB in the medium is indicated in the legend. (b) The emission spectra of compound **4.1** dispersed in water upon incremental addition of acetonitrile solution of DNT (λ_{ex} = 300 nm). Final concentration of DNT in the medium is indicated in the legend.

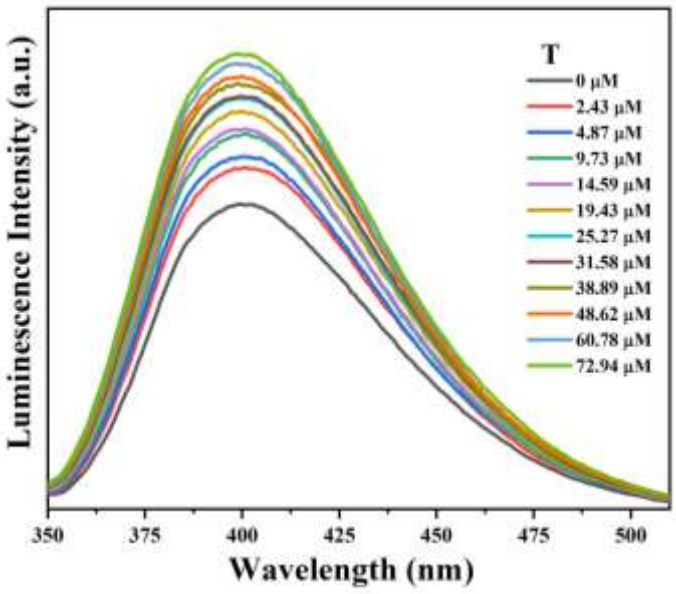

Fig. 4.40 The emission spectra of compound **4.1** dispersed in water upon incremental addition of acetonitrile solution of Toluene (λ_{ex} = 300 nm). Final concentration of Toluene in the medium is indicated in the legend.

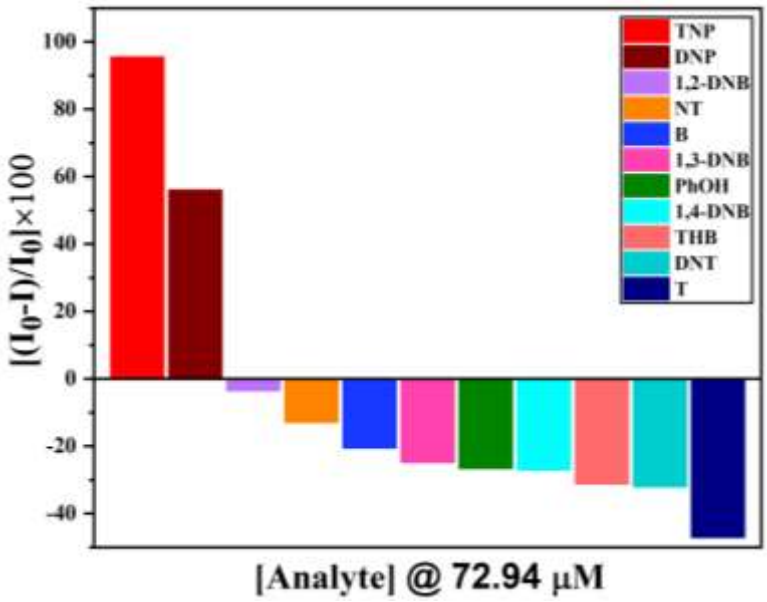

Fig. 4.41 Changes of luminescence intensity with respect of emission of **4.1** (at 400 nm) with 72.94 μM of different analytes.

The limit of detections for the luminescence quenching responses in the presence of TNP has been calculated (up to 48.62 μM) and the value is 69 ppb (see Fig. 4.42). The selectivity for the detection of TNP in the presence of 1,3,5-trihydroxybenzene (THB) was confirmed by a specially designed experimental protocol. The luminescence spectrum of the compound **1** dispersed in the water was recorded and then 9.73 μM solution of THB was added sequentially in two equal portion (4.87 μM in each portion) followed by 9.73 μM TNP solution in similar way and the corresponding emission were measured. The addition of THB showed turn-on effect, however, the subsequent addition of TNP gave significant luminescence quenching effect (see Fig. 4.43). The sensitivity of the analytes is explained by using Stern-Volmer plots. The equation of Stern-Volmer (SV) is $(I_0/I) = Ksv[A]+1$, where I and I_0 are the luminescence intensities of the probe, after and before addition of the analytes, [A] is the molar concentration and Ksv is the luminescence quenching/enhancement constant, respectively. As shown in, Fig. 4.44 the linear increase/decrease in $[I_0/I]$ of nitro and non-nitro analytes at the low concentration region have been observed (up to 14.59 μM). With increasing concentration, the SV plot started to bend upwards for TNP due to the combine effect of static and dynamic quenching (see Fig. 4.45). We have fitted the experimental data in the S-V equation in the lower concentration region (upto 14.59 μM) and the obtained K_{SV} values are 2.594×10^4 M^{-1}, 0.446×10^4 M^{-1}, -

0.0212×10^4 M^{-1}, -0.204×10^4 M^{-1}, -0.611×10^4 M^{-1}, -0.767×10^4 M^{-1}, -0.481×10^4 M^{-1}, -0.152×10^4 M^{-1}, -0.874×10^4 M^{-1}, -1.285×10^4 M^{-1}, -1.153×10^4 M^{-1} for TNP, DNP, 1,2-DNB, NT, B, 1,3-DNB, PhOH, 1,4-DNB, THB, DNT, T, respectively. These values show that **4.1** exhibits a significant extent of luminescence quenching in the presence of TNP. The static quenching can be certified to the ground state interaction between the compound **4.1** and TNP. A summary of sensing behavior of TNP using various other related materials is provided in Table 4.9.

Table 4.9: A summary of the sensing behavior of TNP ions using various reported CPs.

Materials	Solvent	Mechanism	Limit Of Detection (LOD)(μM)	Ref
Compound **4.1**	Aqueous	Quenching	0.302	
$[Mn_2(phen)_2(nia)_2]_\infty$ phen = 1,10-phenanthroline nia = 5-nitroisopthalic acid	Aqueous	Quenching	0.09	[99]
Cd-MOF	CH_3OH	Quenching	26.3	[80]
$[Eu_2(ppda)_2(npdc)(H_2O)]\cdot H_2O$	Aqueous	Quenching	2.97	[97]
Ni-OBA-Bpy-18	Aqueous	Quenching	0.15	[100]
$\{[NH_2(CH_3)_2]_2[Cd(\mu_4$-TDBAT$)]\cdot 3H_2O\cdot DMF\}_n$ TDBAT = 5,5′-((thiophene-2,5 dicarbonyl)bis(azanediyl))diisophthalate)	Ethanol	Quenching	12.8	[101]
$\{[Eu_6L_6(\mu_3\text{-}OH)_8(H_2O)_3]_8\cdot H_2O\}_n$ L = (10-[(2-amino-4-carboxyl-phenyl)ethynyl]anthracene-9-carboxylic acid)	DMF	Quenching	1.93	[102]
$\{[Cd_2(5$-nip$)_2(pdiq)_2(H_2O)_2(CH_3OH)]\cdot H_2O\}_n$ H_2nip = 5-nitroisophthalic acid pdiq = 6-(pyridin-4-yl)-5,6-dihydrobenzo[4,5]imidazo[1,2-*c*]quinazoline]	CH_3CN	Quenching	0.275	[103]

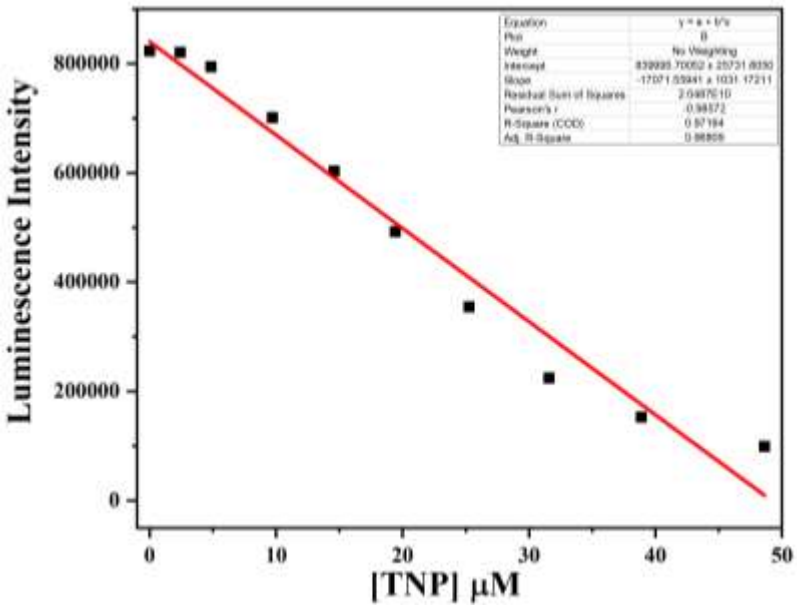

Fig. 4.42 The plot of the changes of luminescence intensity of compound **4.1** (λ_{em} = 400 nm) vs concentration of TNP solution (up to 48.62 µM) indicating the detection limit, which calculated using the equation, LOD = 3σ/m, where σ = standard deviation of blank determination and m = slope of the linear curve.

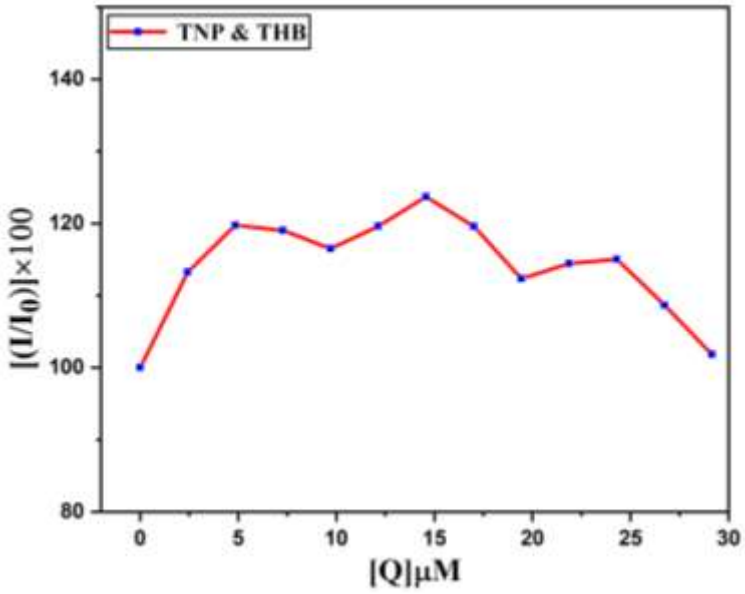

Fig. 4.43 Changes in percentage of luminescence intensity of **4.1** (at 400 nm) upon the addition of acetonitrile solution of THB followed by TNP.

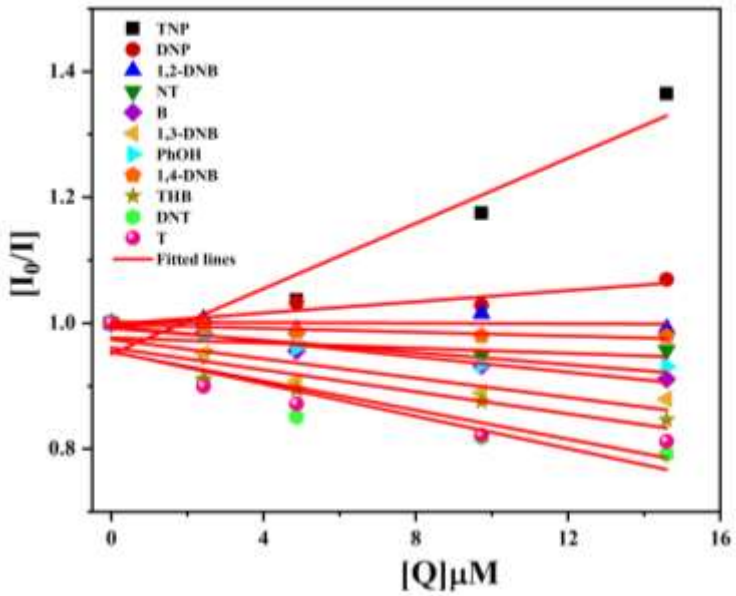

Fig. 4.44 Plot of I_0/I of compound **4.1** (at 400 nm) *vs.* concentration of analytes in the lower concentration range of analytes (upto 14.59 μM). I_0 and I are the luminescence intensity in absence and presence of the analyte, respectively.

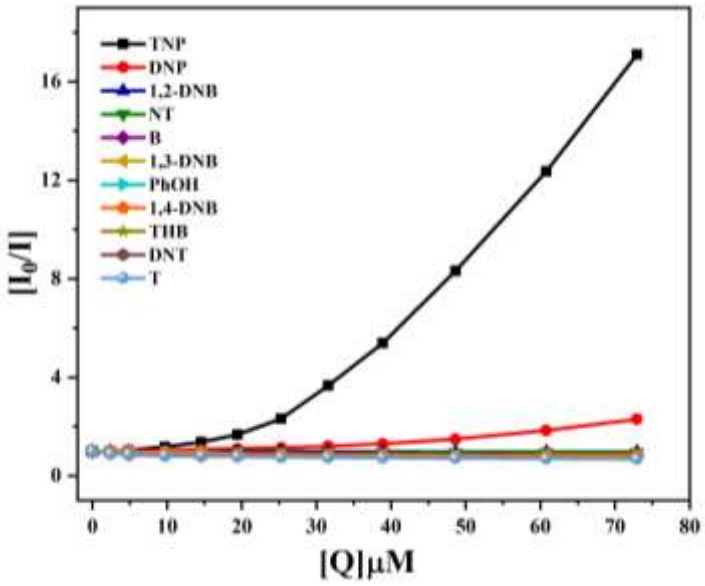

Fig. 4.45 Plot of the luminescence intensity ratio (I_0/I) based on the emission of **4.1** (observed at 400 nm) after the accumulation of 72.94 μM of different analytes. The colour symbols show the data points for **4.1** in the presence of indicated analytes.

4.3.3.3 Sensing Mechanism. Due to the presence of non-bonded pyridine ring of each L ligand as well as the free carboxylate oxygen atoms of the BTCH ligand in the structure of compound **4.1**, there is a possibility to form molecular level interaction between compound **4.1** and the metal ions. Among these Fe^{3+}, Cr^{3+} and Al^{3+} are hard in character and have the ease of molecular level interaction [4.82,4.88] with the compound **4.1** through hard–hard acid–base interaction. In addition to these Cr^{3+} and Fe^{3+} ions have unoccupied d-orbitals, which allow for the ligand-to-metal charge-transfer (LMCT) as an extra efficient non-radiative decay mechanism [4.3, 4.104]. Besides that, Fe^{3+} ions have absorption bands at around 300 nm shown in figure 4.46. So, for Fe^{3+} ions, the inner filter effect plays an important role in overall decrease in luminescence intensity when Fe^{3+} ions were added to compound **4.1.**

Among nitro and non-nitro analytes only TNP and DNP exhibited luminescence quenching. But rest of the tested analytes showed an increase in luminescence intensity when these analytes were added to the compound **4.1**. The increase in luminescence intensity is due to the increase of rigidity of the compound **4.1** *via* π-π interaction between non-bonded pyridine ring of compound **4.1** and aromatic ring of the explosives. From figure 4.47 one can also observe the second absorption band TNP and DNP is well overlapped with the emission spectra of the compound **4.1**. So, in the case of TNP and DNP, energy transfer [4.80,4.97] from the excited state of the ligands of compound **4.1** to the analytes (TNP and DNP) is the reason behind the luminescence quenching effect. A Schematic diagram of mechanism of luminescence quenching based on energy transfer processes are shown in Figure 4.48. FTIR spectra of the recovered samples after the sensing experiment in four cases (Fe^{3+}, Al^{3+}, Cr^{3+} and TNP) show no significant changes of IR spectra from the original compound (see Fig. 4.49)

.

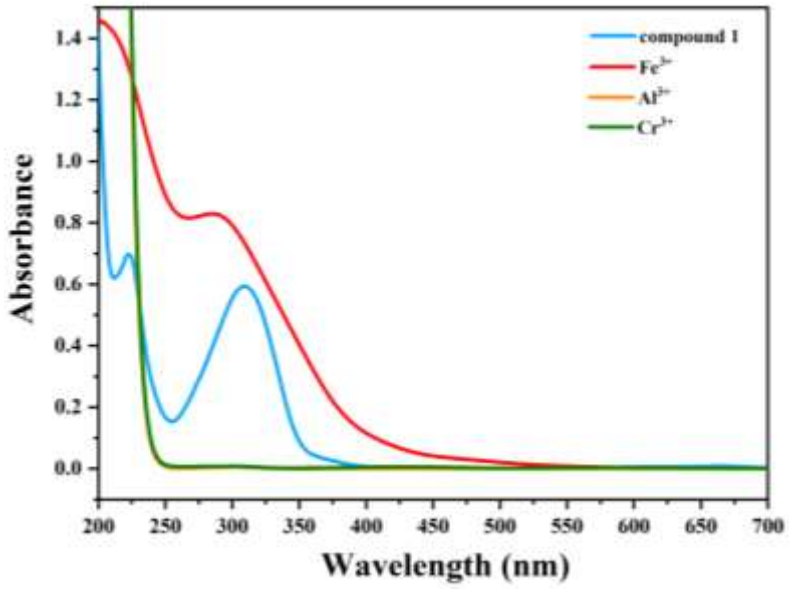

Fig. 4.46 Blue line represents the absorption spectra of [Cd(BTCH)(L)], **4.1** in aqueous medium and rest of the graphs represent the absorption spectra of Fe^{3+}, $Al^{3+,}$ Cr^{3+} ions in aqueous medium (243.12 µM).

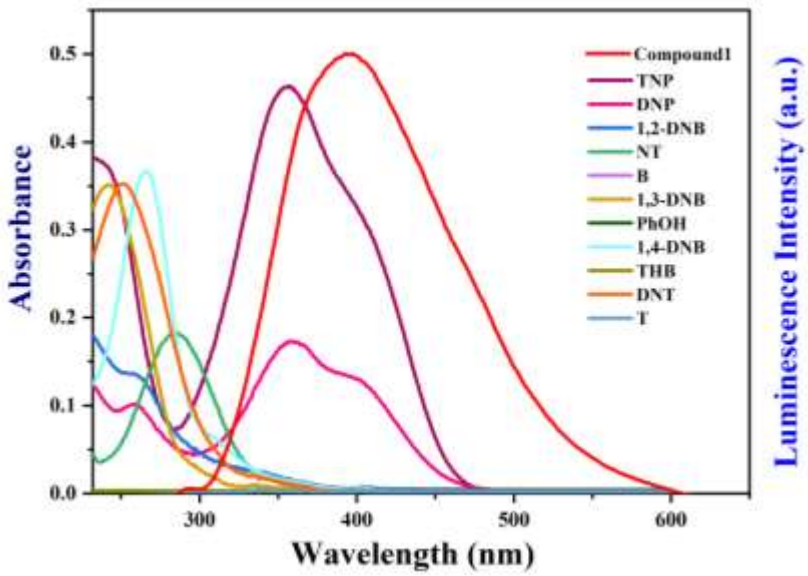

Fig. 4.47 Absorption spectra of different analytes (121.56 µM) and luminescence spectra of **4.1**.

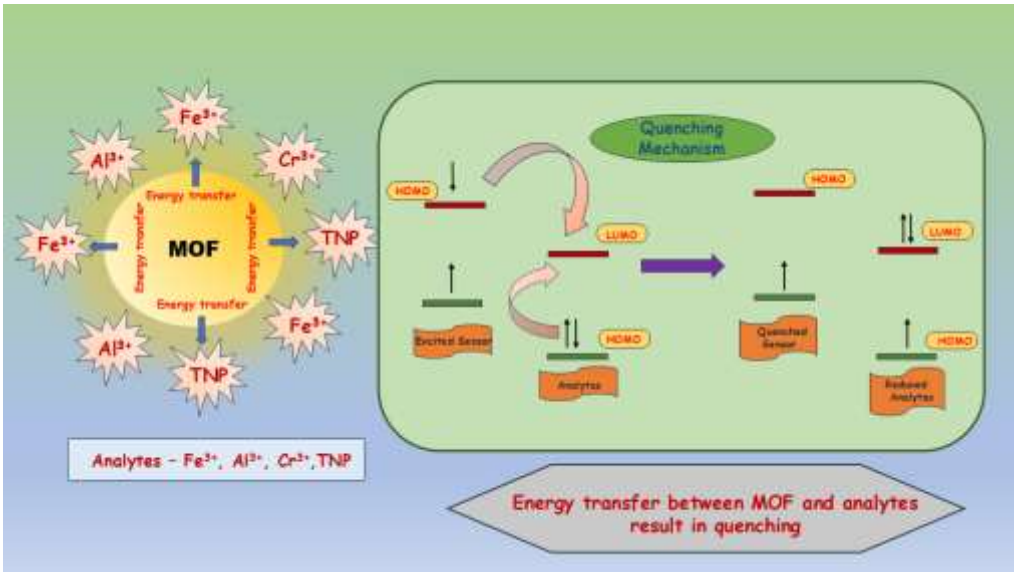

Fig. 4.48 Schematic diagram of mechanism of luminescence quenching

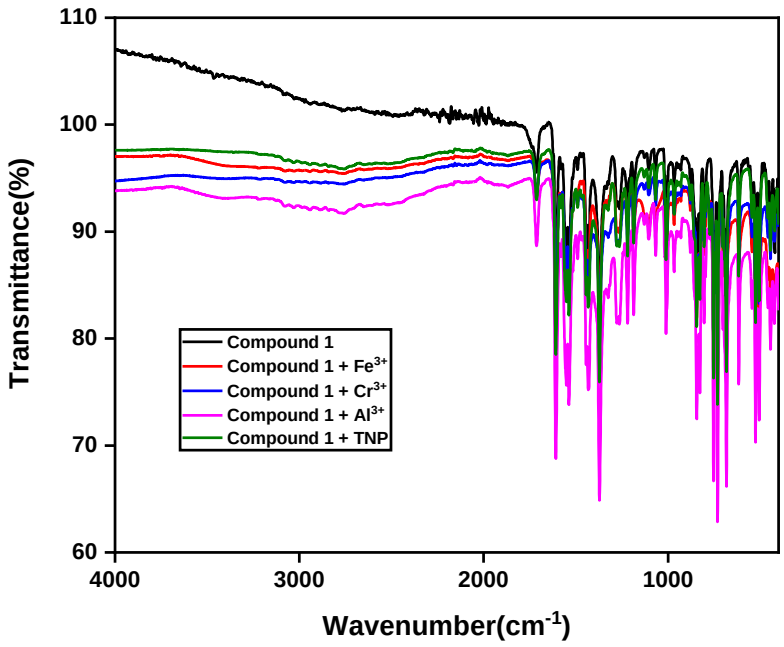

Fig. 4.49 Merged FTIR spectra of compound **4.1** and recovered samples of compound **4.1** after sensing experiment in four cases (Fe^{3+}, Al^{3+}, Cr^{3+} and TNP).

4.4 CONCLUSION

In summary, a new two-dimensional Cd-based coordination polymer was successfully prepared by using trimesic acid and 2,4,5-tri-4-pyridyl-1H-imidazole monohydrate as organic ligands under hydrothermal conditions. The synthesized compound has been characterized by single-crystal X-ray diffraction techniques, powder X-ray diffraction, Fourier Transform Infrared (FTIR) and thermogravimetric analysis (TGA). The compound 4**.1** exhibited photoluminescence-based sensing behaviors towards Fe^{3+}, Al^{3+} and Cr^{3+} ions in aqueous medium based on luminescence quenching effect. The limit of detection for Fe^{3+}, Al^{3+} and Cr^{3+} ions are 54, 71 and 59 ppb, respectively. The compound 4**.1** also exhibited photoluminescence-based sensing behavior towards TNP with detection limit is 69 ppb in term of luminescence quenching effect. These results indicate that the synthesized compound **4.1** could be multifunctional with respect to metal ions and nitro explosive sensing.

4.5 REFERENCES

(4.1) H.-C. Zhou, J. R. Long and O. M. Yaghi, Chem. Rev., 2012, **112**, 673–674.

(4.2) Y.-T. Yan, J. Liu, G.-P. Yang, F. Zhang, Y.-K. Fan, W.-Y. Zhang and Y.-Y. Wang, CrystEngComm., 2018, **20**, 477-486.

(4.3) P. Daga, P. Manna, P. Majee, D. K. Singha, S. Hui, A. K. Ghosh, P. Mahata and S. K. Mondal, Dalton Trans., 2021, **50**, 7388-7399.

(4.4) Z. Yin, Y.-L. Zhou, M.-H. Zeng and M. Kurmoo, Dalton Trans., 2015, **44**, 5258–5275.

(4.5) W. P. Lustig, S. Mukherjee, N. D. Rudd, A. V. Desai, J. Li and S. K. Ghosh, Chem. Soc. Rev., 2017, **46**, 3242–3285.

(4.6) H. Wang, W. P. Lustig and J. Li, Chem. Soc. Rev., 2018, **47**, 4729–4756.

(4.7) P. Manna, A. Hasija, D. Chopra and P. Mahata, New J. Chem., 2023, **47**, 19846.

(4.8) H.-Y. Li, Y.-L. Wei, X.-Y. Dong, S.-Q. Zang and T. C. W. Mak, Chem. Mater., 2015, **27,** 1327–1331.

(4.9) S. Pramanik, C. Zheng, X. Zhang, T. J. Emge and J. Li, J. Am. Chem. Soc., 2011,**133,** 4153–4155.

(4.10) F.-Y. Yi, D. Chen, M.-K. Wu, L. Han and H.-L. Jiang, ChemPlusChem., 2016, **81**, 675–690.

(4.11) Y. Zhang, S. Yuan, G. Day, X. Wang, X. Yang and H.-C. Zhou, Coord. Chem. Rev., 2018, **354**, 28–45.

(4.12) P. Daga, S. Sarkar, P. Majee, D. K. Singha, S. Hui, P. Mahata and S. K. Mondal, Mater. Adv., 2021, **2**, 985–995.

(4.13) R. Gao and D. Yan, Chem. Commun., 2017, **53,** 5408–5411.

(4.14) J. Liu, L. Chen, H. Cui, J. Zhang, L. Zhang and C.-Y. Su, Chem. Soc. Rev., 2014, **43**, 6011–6061.

(4.15) X.-Y. Dong, R. Wang, J.-Z. Wang, S.-Q. Zang and T. C. W. Mak, J. Mater. Chem. A., 2015, **3**, 641–647.

(4.16) P. Mahata, S. Natarajan, P. Panissod and M. Drillon, J. Am. Chem. Soc., 2009, **131**, 10140–10150.

(4.17) A. Dhakshinamoorthy, A. M. Asiri and H. Garcia, Adv. Mater., 2019, **31**, 1900617.

(4.18) Z.-G. Liang, G.-M. Li, X.-Y. Ren, J.-H. Li, J. Pan and S.-D. Han, Inorg. Chem., 2023, **62,** 8663–8669.

(4.19) M. Z. Wu, J. Y. Shi, P. Y. Chen, L. Tian and J. Chen, Inorg. Chem., 2019,**58**, 3130–3136.

(4.20) R. Debnath, R. Bhowmick, P. Ghosh, S. Biswas and S. Koner, New J. Chem., 2022, **46**, 8523.

(4.21) B. Manna, A. V. Desai and S. K. Ghosh, Dalton Trans., 2016, **45**, 4060–4072.

(4.22) N. Stock and S. Biswas, Chem. Rev., 2012, **112,** 933–969.

(4.23) D.-M. Chen, X.-Z. Ma, X.-J. Zhang, N. Xu and P. Cheng, Inorg. Chem., 2015, **54**, 2976–2982.

(4.24) Y.-T. Yan, J. Liu, G.-P. Yang, F. Zhang, Y.-K. Fan, W.-Y. Zhang and Y.-Y. Wang, CrystEngComm., 2018, **20**, 477-486.

(4.25) Z. Zhan, X. Liang, X. Zhang, Y. Jia and M. Hu, Dalton Trans., 2019, **48**, 1786–1794.

(4.26) L. Liu, J. Hao, Y. Shi, J. Qiu and C. Hao, RSC Adv., 2015, **5,** 3045–3053.

(4.27) K. Jayaramulu, R. P. Narayanan, S. J. George and T. K. Maji, Inorg. Chem., 2012, **51**, 10089–10091.

(4.28) P. Kovacic, R. Somanathana, J. Appl. Toxicol., 2014,**34**, 810−824.

(4.29) X. Sun, Y. Wang, Y Lei, Chem. Soc. Rev., 2015, **44**, 8019−8061.

(4.30) Pragya, V. Saini, K. Rangan, B. Khungar, New J. Chem., 2022, **46**, 16907−16913.

(4.31) Y. Zan, Y. Kang, B. Wang, S. Cui, Z. Shen, J. Shu, X. Kong, L. Chen, X. Yan, Y. Li, Dyes Pigm., 2022, **202**, 110296.

(4.32) P. G. Thorne and T. F. Jenkins, Field Anal. Chem. Technol., 1997, **1**, 165–170.

(4.33) K. M. Wollin and H. H. Dieter, Arch. Environ. Contam. Toxicol., 2005, **49**, 18–26.

(4.34) S. S. Nagarkar, A. V. Desai , P. Samanta and S. K. Ghosh, Dalton Trans., 2015, **44,** 15175–15180.

(4.35) C. P. Doherty, S. E. Cox, A. J. Fulford, S. Austin, D. C. Hilmers, S. A. Abrams, A. M. Prentice, PLoS One., 2008, **3,** e2133.

(4.36) X.-M. Tian, S.-L. Yao, C.-Q. Qiu, T.-F. Zheng, Y.-Q. Chen, H. Huang, J.-L. Chen, S.-J. Liu and H.-R. Wen, Inorg. Chem., 2020, **59,** 2803–2810.

(4.37) M. Zheng, H. Tan, Z. Xie, L. Zhang, X. Jing and Z. Sun, ACS Appl. Mater. Interfaces., 2013, **5,** 1078–1083.

(4.38) W.-Q. Tong, W.-N. Liu, J.-G. Cheng, P.-F. Zhang, G.-P. Li, L. Hou and Y.-Y. Wang, Dalton Trans., 2018, **47**, 9466–9473.

(4.39) S. K. Sahoo, D. Sharma, R. K. Bera, G. Crisponi and J. F. Callan, Chem. Soc. Rev., 2012, **41**, 7195–7227.

(4.40) K. P. Carter, A. M. Young and A. E. Palmer, Chem. Rev., 2014, **114**, 4564–4601.

(4.41) H. Zhang, R. Fan, W. Chen, J. Fan, Y. Dong, Y. Song, X. Du, P. Wang and Y. Yang, Cryst. Growth Des., 2016, **16**, 5429–5440.

(4.42) X.-P. Zhang, L. Fu, O. A. Blatova and G.-H. Cui, J. Solid State Chem., 2023, **324**, 124124.

(4.43) S. Chen, Z. Shi, L. Qin, H. Jia and H. Zheng, Cryst. Growth Des., 2017, **17**, 67–72.

(4.44) N. C. Andrews and N. Engl, J. Med., 1999, **341**, 1986–1995.

(4.45) A. B. Bon, A. M. Costero, S. Gill, M. Parra, J. Soto, R. M. Manez and F. Sancenon, Chem. Commun., 2012, **48,** 3000–3002.

(4.46) P. D. Pigatto, A. Ronchi and G. Guzzi, Int. J. Hematol., 2016, **103**, 724.

(4.47) M.-H. Yu, T.-L. Hu and X.-H. Bu, Inorg. Chem. Front., 2017, **4**, 256–260.

(4.48) G. Dong, K. Duan, Q. Zhang and Z. Liu, Inorg. Chim. Acta., 2019, **487,** 322–330.

(4.49) Y. Liu, C. Liu, X. Zhang, L. Liu, C. Ge, X. Zhuang, N. Zhang, Q. Yang, Y.-Q. Huang and Z. Zhang, J. Solid State Chem., 2019, **272**, 1–8.

(4.50) Y.-P. Li, X.-H. Zhu, S.-N. Li, Y.-C. Jiang, M.-C. Hu and Q.-G. Zhai, ACS Appl. Mater. Interfaces., 2019, **11**, 11338–11348.

(4.51) W.-X. Li, J.-H. Gu, H.-X. Li, M. Dai, D. J. Young, H.-Y. Li and J.-P. Lang, Inorg. Chem., 2018, **57**, 13453–13460.

(4.52) X. Zheng, Y. Zhao, P. Jia, Q. Wang, Y. Liu, T. Bu, M. Zhang, F. Bai and L. Wang, Inorg. Chem., 2020, **59**, 18205–18213.

(4.53) V. Rai, P. Vajpayee, S. N. Singh and S. L. Mehroto, Plant Sci., 2004, **167**, 1159–1169.

(4.54) Y.-S. Wang, Z.-Y. Pan, J.-M. Lang, J. M. Xu and Y.-G. Zheng, J. Hazard. Mater., 2007, **147,** 319–324.

(4.55) T.-Y. Gu, M. Dai, D. J. Young, Z.-G. Ren and J.-P. Lang, Inorg. Chem., 2017, **56**, 4668–4678.

(4.56) R. Lv, J. Wang, Y. Zhang, H. Li, L. Yang, S. Liao, W. Gu and X. Liu, J. Mater. Chem. A., 2016, **4**, 15494–15500.

(4.57) Y. Yu, Y. Wang, H. Yan, J. Lu, H. Liu, Y. Li, S. Wang, D. Li, J. Dou, L. Yang and Z. Zhou, Inorg. Chem., 2020, **59**, 3828–3837.

(4.58) D. A. Brown, W. K. Glass, M. R. Jan and R. M. W. Mulders, Environ. Technol. Lett., 1986, **7**, 283–288.

(4.59) M. Bellouard, M. Gasser, S. Lenglet, F. Gilardi, N. Bararpour, M. Augsburger, A. Thomas and J.-C. Alvarez, Chem. Res. Toxicol., 2022, **35,** 807–816.

(4.60) C. Fu, X. Sun, G. Zhang, P. Shi and P. Cui, Inorg. Chem., 2021, **60**, 1116–1123.

(4.61) A. Kathiravan, A. Gowri, T. Khamrang, M. D. Kumar, N. Dhenadhayalan, K.-C. Lin, M. Velusamy, M. Jaccob, Anal. Chem., 2019, **91,** 13244−13250.

(4.62) A. S. Tanwar, N. Meher, L. R. Adil, P. K. Iyer, Analyst., 2020, **145**, 4753−4767.

(4.63) Y. Fan, T. Tao, H. Wang, Z. Liu, W. Huang, H. Cao, Dyes Pigm., 2021,**191**, 109355.

(4.64) X. Zhou, L. Liu, D. Wu, Y. Niu, S. Zheng, J. Lu, Y. Feng, and X.-S. Tai, ACS Omega., 2024, **9**, 11339−11346.

(4.65) Q.-H. Tan, Y.-Q. Wang, X.-Y. Guo, H.-T. Liu and Z.-L. Liu, RSC Adv., 2016, **6**, 61725–61731.

(4.66) S. A. Diamantis, A. Margariti, A. D. Pournara, G. S. Papaefstathiou, M. J. Manos and T. Lazarides, Inorg. Chem. Front., 2018, **5**, 1493–1511.

(4.67) J. Posta, H. Berndt, S.-K. Luo and G. Schaldach, Anal. Chem., 1993, **65**, 2590–2595.

(4.68) T. Wu, C. Liu, K. J. Tan, P. P. Hu and C. Z. Huang, Anal. Bioanal. Chem., 2010, **397**, 1273–1279.

(4.69) S. Liu, F. Lu and J.-J. Zhu, Chem. Commun., 2011, **47**, 2661–2663.

(4.70) S.-H. Park, N. Kwon, J.-H. Lee, J. Yoon and I. Shin, Chem. Soc. Rev., 2020, **49**, 143–179.

(4.71) Q. Huang, Acta Cryst., E65 2009, o2329.

(4.72) Bruker Apex3 v2017.3-0, Saint V8.38A, SAINT V8.38A; Bruker AXS Inc.: Madison, WI, 2018.

(4.73) L. Krause, R. Herbst-Irmer, G. M. Sheldrick, D. Stalke, J. Appl. Crystallogr., 2015,**48**, 3− 10.

(4.74) A. Altomare, G. Cascarano, C. Giacovazzo, A. Guagliardi, Completion and Refinement of Crystal Structures with SIR92. J. Appl. Crystallogr., 1993, **26,** 343−350.

(4.75) G. M. Sheldrick, Crystal Structure Refinement with SHELXL. Acta Crystallogr., Sect. C: Struct. Chem., 2015, **71,** 3−8.

(4.76) L. J. Farrugia, WinGX suite for Small-Molecule Single-Crystal Crystallography. J. Appl. Crystallogr., 1999, **32**, 837−838.

(4.77) A. L. Spek, Single-Crystal Structure Validation with the Program PLATON. J. Appl. Crystallogr., 2003, **36**, 7−13.

(4.78) A. M. Dietrich and G. A. Burlingame, Environ. Sci. Technol., 2015, **49,** 708−720.

(4.79) L. Liu, D. Chen, A. -N. Dou, Q. -Q. Xu, F. -Y. L, A. -X. Zhu and R. -R. Zhu, ChemPlusChem., 2024, **89**, e202400192.

(4.80) X. Zhou, L. Liu, D. Wu, Y. Niu, S. Zheng, J. Lu, Y. Feng and X. -S. Tai, ACS Omega., 2024, **9**, 11339−11346.

(4.81) W. Liu, H. -L. Cui, J. Zhou, Z. -T. Su, Y. -Z. Zhang, X, -L. Chen and E. -L. Yue, ACS Omega., 2023, **8**, 24635−24643.

(4.82) J. -M. Liu, Y. -B. Ren, H. -Y. Xu, L. -J. Li, Y. -J Mu, J. -L Du, Inorganica Chimica Acta., 2021, **527**, 120583.

(4.83) X. Li, J. Tang, H. Liu, K. Gao, X. Meng, J. Wu and H. Hou, Chem. Asian J., 2019, **14**, 3721 – 3727.

(4.84) C. -X. Yang, H, -B. Ren and X. -P. Yan, Anal. Chem., 2013, **85**, 7441−7446.

(4.85) D. Mukherjee, A. Pal, S. C. Pal, A. Saha and M. C. Das, Inorg. Chem., 2022, **61**, 16952−16962.

(4.86) R. Luo, C. Xu, H. -J. Yu, Y. Yin, Y. Fan, D. -M. Zhang and F. Shao, Cryst. Growth Des., 2024, **24**, 2064−2074.

(4.87) D. K. Singha, P. Mahata, Inorg. Chem., 2015, **54**, 6373−6379.

(4.88) J. Zhang, Y. Yue, Z. Lin, X. Tao, D. Yin, Chi Zhang doi.org/10.1021/acs.inorgchem.4c04040.

(4.89) X. -M Tian, S. -L Yao, C.-Q Qiu, T.-F Zheng, Y.-Q Chen, H. Huang, J-L Chen, S.-J Liu and H. -R. Wen, Inorg. Chem., 2020, **59,** 2803−2810.

(4.90) B. -L. Chai, S. -L Yao, X. Xie, H. Xu, T.-F. Zheng, J. -Y. Li, J. -L Chen, S. -J Liu and H. -R. Wen Cryst. Growth Des., 2022, **22**, 277−284.

(4.91) X. Jing, J. Liu, M. Guo, G. Chen, G. Ren, J. Li, H. Qin, Z. Yao, Y. Wan, W. Song, H. Zeng, F. Yang, D. Zhao and K. Hu New J. Chem., 2023, **47**, 13619.

(4.92) D. -G. Cai, C. -Q. Qiu, Z. -H. Zhu, T. -F. Zheng**,** W.-J. Wei**,** J.-L. Chen, S.-J. Liu**,** H. -R. Wen Inorg. Chem., 2022, **61**, 14770−14777.

(4.93) S. Shen, Y. Zhang, L. Liang, X. -Y. Zhang, K. Huang, and D.-B. Qin, Cryst. Growth Des., 2024 , **24**, 7580−7587.

(4.94) Q. Guo, T. Ma, L. Zhou, J.-X Ma, J. Yanga and Q. Yang New J. Chem., 2020, **44**, 7293.

(4.95) C. Lin, M. Wang, J. Tang, Z. Zhu, P. Wu, A. Hu, L. Zhang and J. Wang, Inorg. Chem., 2021, **60**, 16803−16809.

(4.96) X. Meng, M. -J. Wei, H. -N Wang, H.-Y Zang and Z. -Y. Zhou, Dalton Trans., 2018, **47**, 1383.

(4.97) Z. Zhan, X. Liang, X. Zhang, Y. Jia and M. Hu, Dalton Trans., 2019, **48**, 1786.

(4.98) M. -J. Tsai, K. -S. Liao, L.-J. Hsu, J.-Y. Wu, Journal of Solid State Chemistry., 2021, **304** 122564.

(4.99) U. Mondal, K. Raksha, P. Mondal, D. P. Banerjee ,2024, **19**, e202400374.

(4.100) S. Chongdar, U. Mondal, T. Chakraborty, P. Banerjee and A. Bhaumik ACS Appl. Mater. Interfaces., 2023, **15,** 14575−14586.

(4.101) M. Şevik, S. M. Sezdi, E. Kavak, T. A. Arici and M. Arici Cryst. Growth Des., 2023, **23** 5163−5172.

(4.102) Y. Zhao, C. -A. Wang, J. -K Li, Q. -L Li, Q. Guo, J. Ru, C. -L Ma and Y. -F Han RSC Adv., 2022, **12**, 26945-26952.

(4.103) G. Bairy, A. Dey, B. Dutta, P. P. Ray, C. Sinha Cryst. Growth Des., 2022, **22**, 3138−3147.

(4.104) P. Daga, P. Majee, D. K. Singha, P. Manna, S. Hui, A. K. Ghosh, P. Mahata and S. K. Mondal, New J. Chem., 2020, **44**, 4376-4385.

Chapter 5

pH Independent Selective formation of VO_2^+ motif incorporating a Family of Hydrazone Ligands: Synthesis, Structure and Luminescence based Sensing Studies towards Selective Metal Ions

ABSTRACT

Two new dioxidovanadium compounds with the general formula $[V^{V}O_2(L)]$ (L = hydrazone ligand) were synthesized in three different methods (acidic, neutral and basic medium) using either $V^{IV}OSO_4.\ 5H_2O$ or $[V^{IV}O(acac)_2]$ or $NH_4V^{V}O_3$ as the starting material and hydrazone ligands. In both cases, the five coordinated V^{5+} ion adopted distorted square pyramidal geometry through the coordination of two oxido ligands and one hydrazone ligand. In compound **5.1**, the presence of free hydroxyl groups stabilized the molecular species through intra-molecular O–H…N type hydrogen bond interactions. In compound **5.2**, the free amino groups involve in both the intra-molecular N–H…N type and inter-molecular N – H…O type hydrogen bond interactions. The compound **5.1** showed highly selective luminescence turn on behaviour along with 33 nm blue shift in presence of Al^{3+} ions in aqueous medium. The experimental limit of detection (LOD) was found to be 66 nM. Whereas the compound **5.2** showed luminescence quenching behaviour in the presence of Fe^{3+}, Al^{3+} and Cr^{3+} ions. The LODs were observed to be 312, 408 and 280 nM for Fe^{3+}, Al^{3+} and Cr^{3+} ions, respectively. The luminescence response mechanism of both the compounds in presence of metal ions has been correlated with the molecular level interactions.

5.1 INTRODUCTION

Vanadium, the third element of the first-row d-block elements is distinctive having ability to exist in eight oxidation states ranging from -III to +V, two of which, namely, +IV and +V are stable in aerobic medium. In spite of being a trace element, vanadium has significant biochemical significance.[5.1, 5.2] The chemistry of vanadium complexes has attracted a special attention due to their catalytic properties and a number of biological activities, namely, insulin simulated work, heart and blood vessels related properties, and diet controller activities, bacteria killing effects, prevetion of viral infections (including anti-HIV), or cytotoxic agents[5.1]. Moreover, vanadium based compounds are potentially active for many tropical diseases leveled as epidemic, *e.g*., leishmania parasites infection, amoebic dysentery, American trypanosomiasis and dengue caused infected mosquitoes.[5.2]

Between the two stable oxidation states, namely +IV and +V, from the chemical point of view, the +V state has attracted special attention due to presence of three different motifs namely, VO^{3+}, $V_2O_3^{4+}$ and VO_2^{+} in this oxidation state. It has been established very recently,[5.3] that the formation, stabilization and their interconversion of these three motifs are both pH as well as solvent dependent in the presence of a suitable multidentate ligand.

Moreover, vanadium compounds are used as optical sensor.[5.4] Optical sensory materials, based on variations in luminescence or absorption spectra are mostly useful because of their simplicity of usage, great sensitivity, opportunity of including them in online recognition pathways for use over a varied range of metal ion concentrations, and for real time monitor time and space checking of these metal ions.[5.5, 5.6] The presence of non-biodegradable inorganic toxic chemicals *e.g*., CrO_4^{2-} /$Cr_2O_7^{2-}$ and SeO_3^{2-} /SeO_4^{2-} in water[5.7, 5.8] and also different organic contaminants including various drugs[5.9, 5.10], which are harmful to our physiological system are of great concerns. All of these are dangerous to the human health and also troubling the whole ecosystem. Therefore, the effective techniques are required to treat these pollutants and avoid their hazardous effect.[5.11] The popular techonologies are gravimetric quartz crystal microbalance (QCM), surface acoustic wave (SAW) instrument and microelectromechanical (MEMS) device such as microcantilevers. But these detection procedures are laborious, time-consuming, therefore, the quick, reliable, easiest techniques are required. Recently, different types of materials with porous structures have been discovered, these are containing individual pores or cages that can trap specific molecules or ions.[5.12] Basically, the porous and crystalline MOFs are formed through the connectivites betrween organic and inorganic components. The organic component which are acting as a connecting ligand, such as various acid and amine moieties and the inorganic component

may be the ions of first row transition metals (Ti, V, Cr, Mn, Fe, Co, Cu and Zn), lanthanides, actinides (U and Th), p-block elements (In and Ga) or based on their clusters.[5.13-5.16] Moreover, vanadium based metal organic frameworks have wide applications namely, lithium-ion batteries, sensory materials to detect NO_x emissions, colorimetric L-Arginine sensing, conversion of solar energy via water splitting, elimination of some dyes and harmful drug from water.[5.17-5.22]

On the investigation of oxidovanadium(IV/V) compounds with hydrazone ligands as part of research,[5.23-5.31] we have utilized two tridentate monobasic hydrazone ligands ($HL^{5.1-5.2}$) (Scheme 1) which are derived from the reaction of 2-acetylpyridine with 2-hydroxybenzoylhydrazide ($HL^{5.1}$) and 2-aminobenzoylhydrazide ($HL^{5.2}$) (general abbreviation, HL). It is interesting to note that under aerial condition, these two ligands are unique for the formation and stabilization of VO_2^+ motif (compound **1**–**2**) (Scheme 2) leaving the other two namely, VO^{3+} and $V_2O_3^{4+}$ irrespective of the oxidation state of the starting material [*i.e.*, in +IV state; *e.g.*, $VOSO_4$ or $VO(acac)_2$ (where $acac^-$ representing the deprotonated form of acetylacetone, Hacac) or in +V state; *e.g.*, NH_4VO_3], the reaction medium (*i.e.*, either aqueous or non-aqueous) and the pH (*i.e.*, either acidic or neutral or basic) of the reaction medium which are depicted below (eqn. 1-3).

$$2V^{IV}OSO_4 + 2HL + {}^1/_2O_2 + H_2O + 2CH_3COONa \rightarrow 2[V^VO_2(L)] + 2CH_3COOH + 2NaHSO_4 \quad (1)$$

$$2V^{IV}O(acac)_2 + 2HL + {}^1/_2O_2 + H_2O \rightarrow 2[V^VO_2(L)] + 4Hacac \quad (2)$$

$$NH_4V^VO_3 + HL \rightarrow [V^VO_2(L)] + NH_4OH \quad (3)$$

It is also important to note that the attempts for the formation of mixed-ligand oxidovanadium(IV) complexes incorporating common hererocylic ligands such as 2, 2´-bipyridine (bipy) or 1, 10-phenanthroline (phen) in addition to these hydrazone ligands as well as the mixed-ligand oxidovanadium(V) complexes incorporating 8-hydroxyquinoline (Hhq) became unsuccessful.

Another interesting point is that these two ligands are not fluorescent active, but the dioxidovanadium complexes are active. Moreover, the reported dioxidovanadium(V) complexes act as good sensors for selective metal ion in aqueous solution which is hitherto unknown.

To the best of our understanding, we are reporting for the first time the dioxidovanadium(V) complexes containing these hydrazone ligands which were prepared in acidic medium (eqn. 1) and also in neutral medium

(eqn. 2) in addition to basic medium (eqn. 3). Moreover, the sensing behaviour of these complexes to different metal ions in aqueous solution is also reported for the first time.

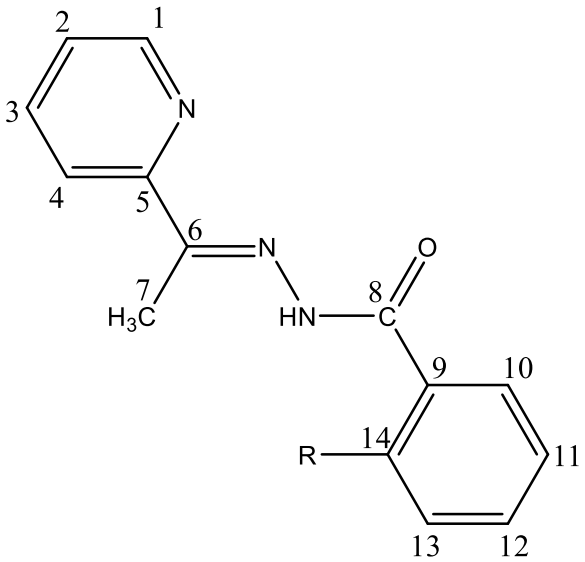

R	HL
OH	HL^1
NH_2	HL^2

(Scheme 1)

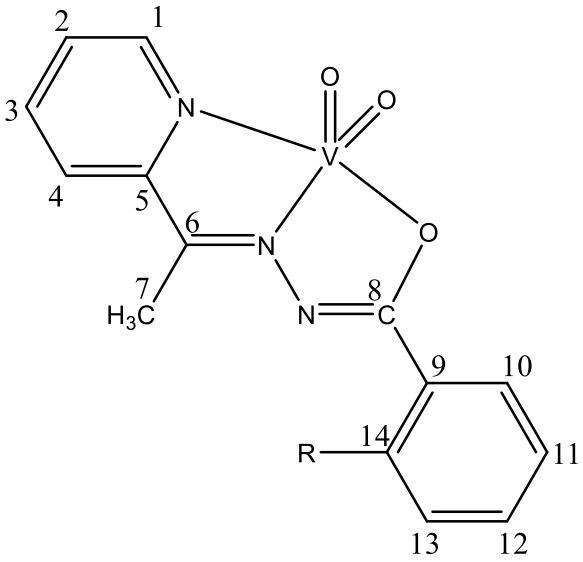

R	Compound
OH	**1**
NH_2	**2**

(Scheme 2)

Here, **1** means **5.1** and **2** means **5.2**

5.2 EXPERIMENTAL

5.2.1 Synthesis of the ligands $HL^{5.1\text{-}5.2}$. The two hydrazone ligands ($HL^{5.1–5.2}$) were synthesized by the same general method.

5.2.2 Synthesis of the ligands $HL^{5.1}$. 2-acetylpyridine (10 mmol) and 2-hydroxybenzoylhydrazide (10 mmol) were dissolved in methanol (50 ml). This solution was then heated under reflux for 3 h and the reaction mixture was then kept in the refrigerator. After 5 days, the precipitate formed was separated by filtration followed by washing with methanol and dried over silica gel (fused). Yield: 2.37 g (92.8%). M.P., 231 ºC. Anal. calcd (%) for $C_{14}H_{13}N_3O_2$: C, 65.87; H, 5.13; N, 16.46. Found: C, 65.89; H, 5.11; N, 16.44. ESI-MS (positive) in CH_3OH: m/z: calc.: 256.1087; found: 256.0824 $[M + H]^+$ (Fig. 5.1). FT-IR bands (KBr pellet, cm^{-1}): 3282, 3045, 1640,1547, 955 (Fig. 5.2). ^1H NMR (300 MHz, DMSO-d_6) δ 11.47 (s, 1H, O-H), 8.62 (d, J = 4.4, 1H, H-1), 8.14 (d, J = 8.0, 1H, H-5), 8.02 (d, J

= 7.5, 1H, H-4), 7.88 (t, *J* = 7.5, 1H, H-3), 7.50 – 7.40 (m, 2H, H-2, H-7), 7.06 – 7.00 (m, 2H, H-6, H-8) (Fig. 5.3). UV-visible (DMSO) (λ_{max}, nm (ε, M^{-1} cm^{-1}): 367 (8,320); 308 (20,260) (Fig. 5.4).

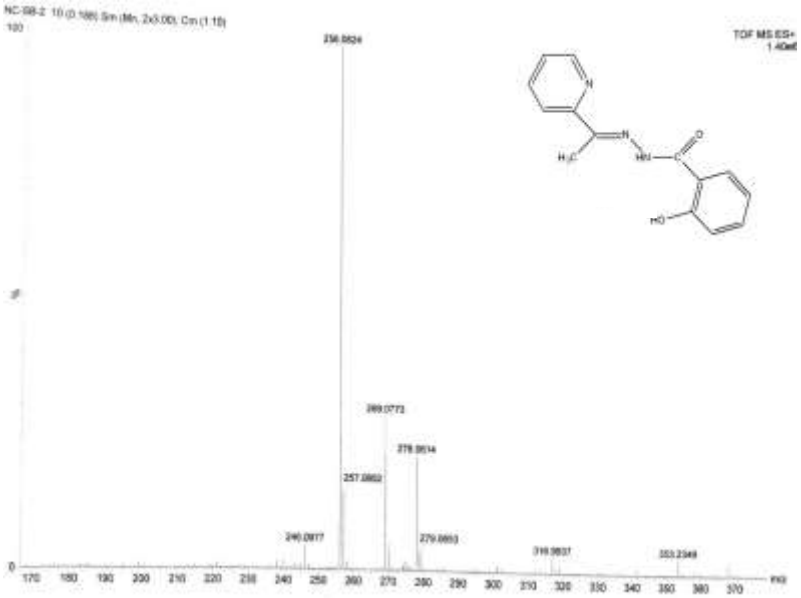

Fig. 5.1 ESI-MS (positive) in CH_3OH of $HL^{5.1}$.

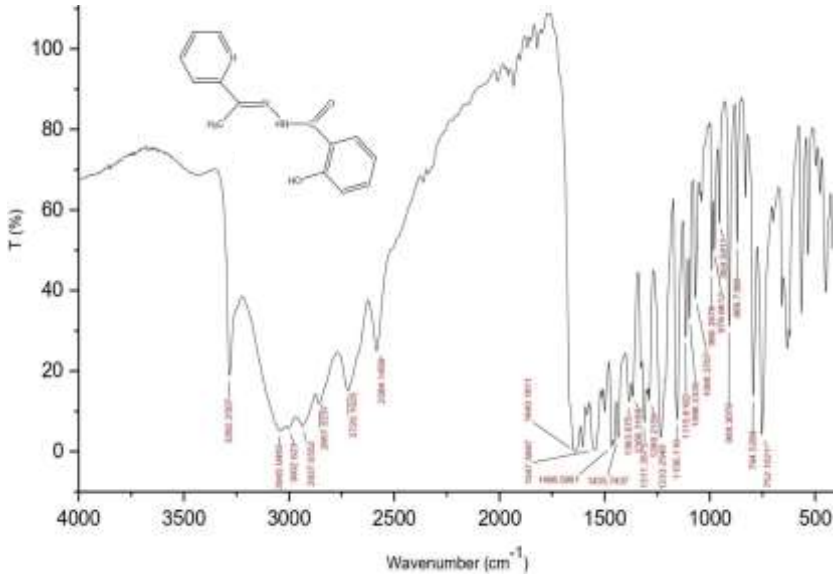

Fig.5.2 FT-IR bands (KBr pellet) of $HL^{5.1}$.

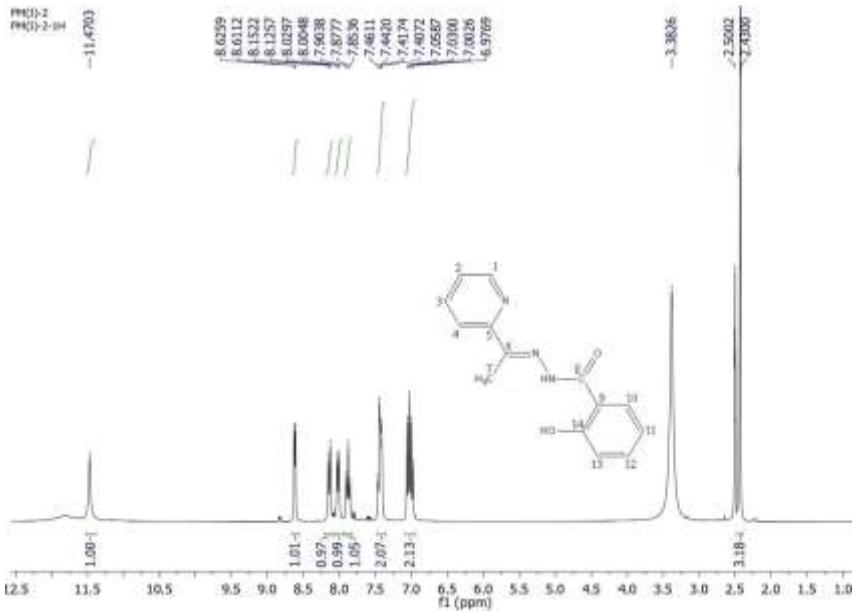

Fig. 5.3 ^{1}H NMR (300 MHz, DMSO-d_6) of $HL^{5.1}$.

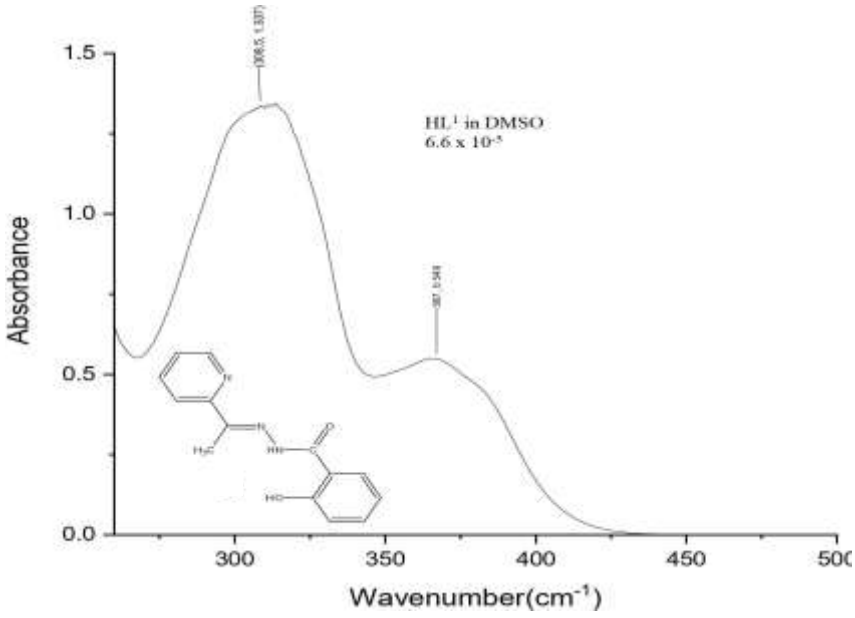

Fig. 5.4 UV-visible (in DMSO) of $HL^{5.1}$.

5.2.3 Synthesis of the ligands $HL^{5.2}$. $HL^{5.2}$ was also prepared following the same procedure used for $HL^{5.1}$. Yield: 2.29 g (90.1%). M.P., 194° C. Anal. calcd (%) for $C_{14}H_{14}N_4O$: C, 66.13; H, 5.55; N, 22.03. Found: C, 66.15; H, 5.57; N, 22.01. ESI-MS (positive) in CH_3OH: m/z: calc.: 255.1247; found: 255.0979 $[M + H]^+$ (Fig.

5.5). FT-IR bands (KBr pellet, cm^{-1}): 2979, 1646, 1583, 1012 (Fig. 5.6). ^1H NMR [This compound exists in two isomeric forms A and B in 3:1 ratio (scheme 3)] (300 MHz, DMSO-d_6); for A; δ 15.52 (brs, 1H, N-H) (A), 10.62 (brs, 1H, N-H) (B), 8.60 (d, J = 4.1, 1H, H-1) (A), 8.83 (d, J = 4.8, 1H, H-1) (B), 8.14 – 8.06 (m, 2H, H-3) (A+B), 7.88 – 7.79 (m, 2H, H-10) (A+B), 7.59 – 7.56 (m, 2H, H-12) (A+B), 7.49 (dd, J = 8.0, 1.2, 1H, H-4) (A), 7.45 – 7.37 (d, J = 7.89, 1.2, 1H, H-4) (B), 7.26 – 7.19 (m, 2H, H-11) (A+B), 6.79 (brd, J = 4.5, 1H, H-13) (A), 6.78 (brd, J = 4.4, 1H, H-13) (B), 6.68 – 6.59 (m, 2H, H-2) (A+B), 6.22 (brs, 2H, H(NH_2)) (A+B), 2.44 (s, 3H, H-7) (A), 2.43 (s, 3H, H-7) (B) (Fig. 5.7). UV-visible (DMSO) (λ_{max}, nm (ε, M^{-1} cm^{-1}): 357 (18,440); 298 (18,330) (Fig. 5.8).

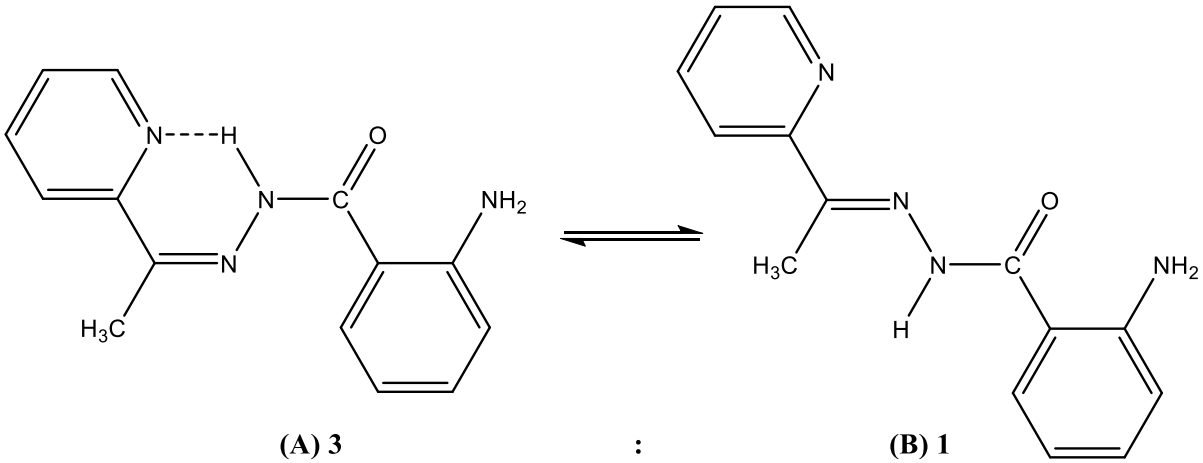

(A) 3 : (B) 1

(Scheme 3)

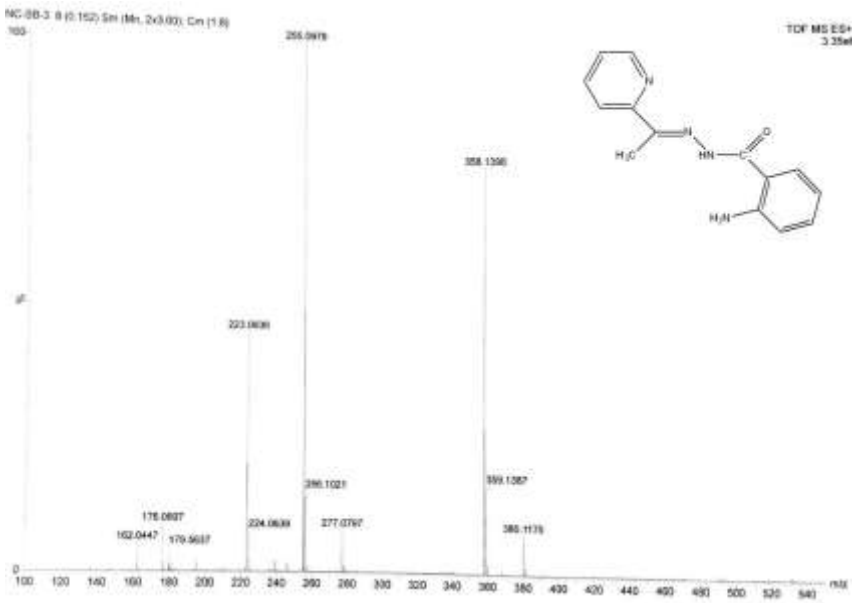

Fig. 5.5 ESI-MS (positive) in CH_3OH of HL[5.2].

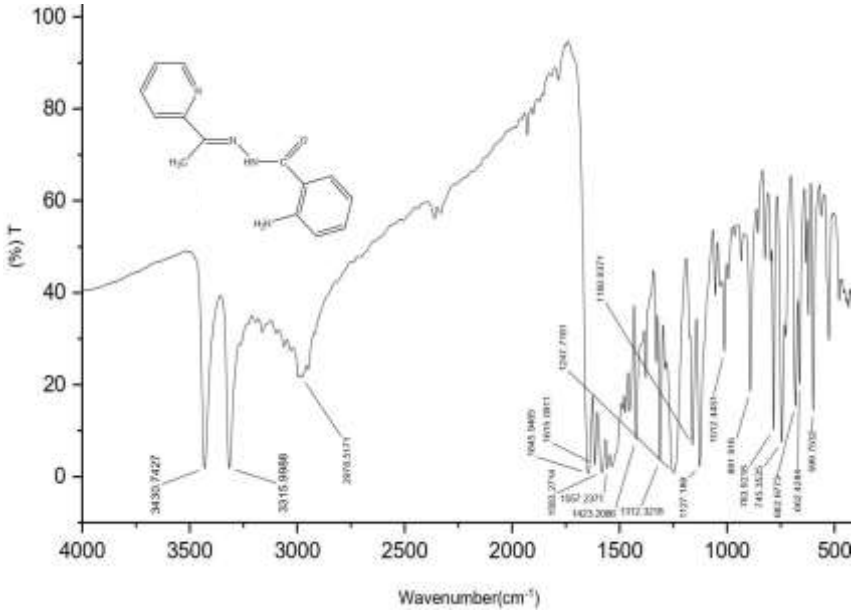

Fig.5.6 FT-IR bands (KBr pellet) of HL[5.2].

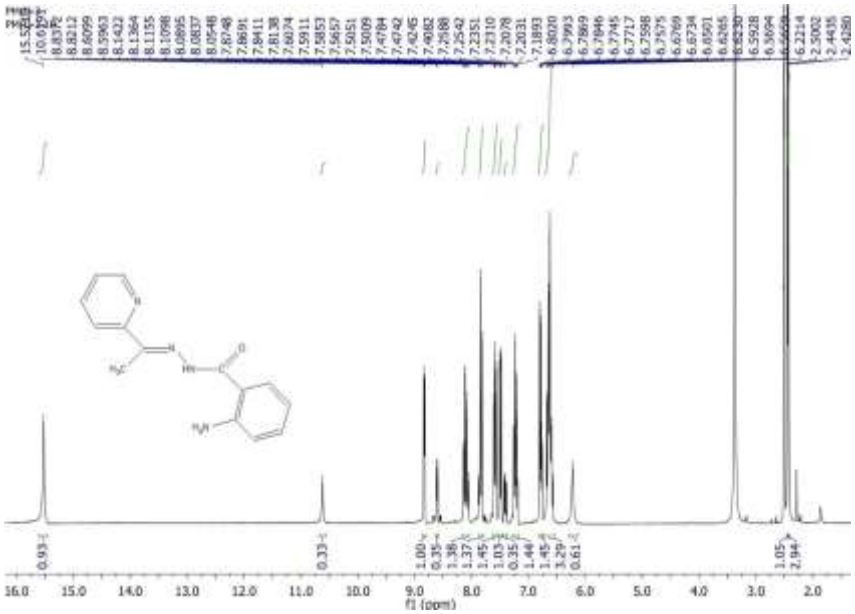

Fig. 5.7 ^{1}H NMR (300 MHz, DMSO-d_6) of $HL^{5.2}$.

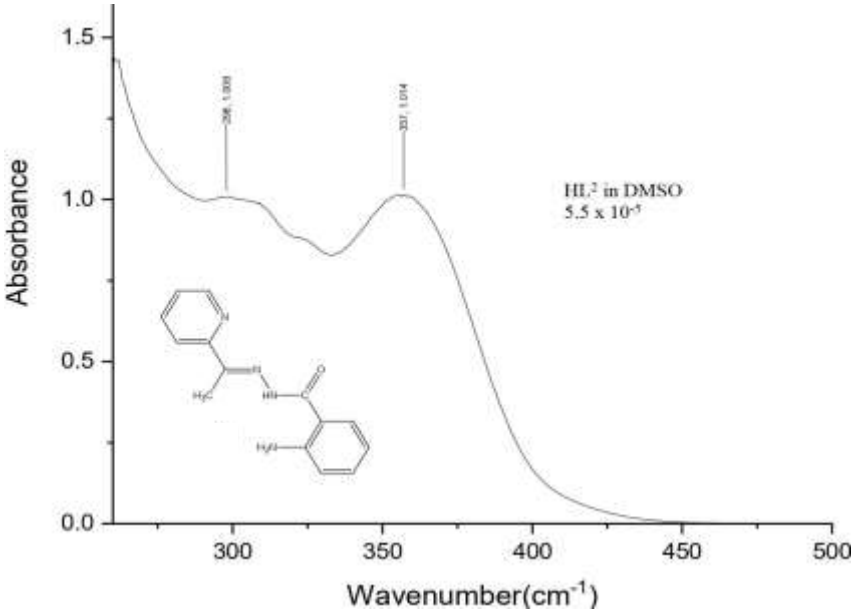

Fig. 5.8 UV-visible (in DMSO) of $HL^{5.2}$.

5.2.4 Synthesis of the complexes $[VO_2(L^{5.1\text{-}5.2})]$ (5.1–5.2). Both the two dioxidovanadium complexes $[V^{V}O_2(L)]$ (**5.1–5.2)** were synthesized by different simple general method using either $V^{IV}OSO_4$. $5H_2O$ or $[V^{IV}O(acac)_2]$ or $NH_4V^{V}O_3$ as the starting material.

5.2.5 Method 1. To a warm aqueous-methanolic solution (30 cm^3, 1:4 V/V) of $HL^{5.1}$ (0.255 g, 1 mmol) and CH_3COONa. $3H_2O$ (0.136 g, 1 mmol) was added aqueous solution (10 cm^3) of $VOSO_4$ $5H_2O$ (0.253 g, 1 mmol). The reaction mixture was stirred for 5 h at 60° C. Strongly fluorescent bright yellow crystalline compound thus obtained was filtered, washed with water, aqueous-methanol and then dried over silica gel (fused). Yield: 0.315 gm, (93.5%). Anal. calcd (%) for $C_{14}H_{12}N_3O_4V$: C, 49.87; H, 3.59; N, 12.46. Found: C, 49.89; H, 3.60; N, 12.44. ESI-MS (positive) in CH_3OH: m/z: calc.: 338.0347; found: 338.0102 $[M + H]^+$ (Fig. 5.9). FT-IR bands (KBr pellet, cm^{-1}): 3226, 1513, 1251, 1066, 949, 940 (Fig. 5.10). ^1H NMR (300 MHz, DMSO-d_6) δ 11.52 (s, 1H, O-H), 8.83 (d, J = 4.5, 1H, H-1), 8.40 (t, J = 7.4, 1H, H-3), 8.29 (d, J = 7.8, 1H, H-5), 7.84 – 7.77 (m, 2H, H-4, H-7), 7.51 (t, J = 7.6, 1H, H-2), 7.04 – 6.96 (m, 2H, H-6, H-8), 2.72 (s, 3H, H-CH_3) (Fig. 5.11). UV-visible (DMSO) (λ_{max}, nm (ε/dm^3, M^{-1} cm^{-1}): 385 (21,580); 277 (14,760) (Fig. 5.12).

The shiny yellow fluorescent compound **5.2** was also prepared following the same procedure adopted for compound **5.1** replacing HL^1 by HL^2. Yield: 0.314 g, (93.5%). Anal. calcd (%) for $C_{14}H_{13}N_4O_3V$: C, 50.01; H, 3.90; N, 16.66. Found: C, 50.02; H, 3.91; N, 16.65. ESI-MS (positive) in CH_3OH: m/z: calc.: 337.0507; found: 337.0291 $[M + H]^+$ (Fig. 5.13). FT-IR bands (KBr pellet, cm^{-1}): 3083, 1509, 1262, 1063, 947, 930 (Fig. 5.14). ^1H NMR (300 MHz, DMSO-d_6) δ 8.83 (d, J = 5.1, 1H, H-1), 8.37 (t, J = 7.8, 1H, H-3), 8.22 (d, J = 8.0, 1H, H-4), 7.77 – 7.72 (m, 2H, H-5, H-7), 7.23 (t, J = 7.6, 1H, H-2), 6.57 (t, J = 7.5, 1H, H-6), 6.82 (d, J = 8.3, 1H, H-8), 6.93 (s, 2H, H-NH_2), 2.72 (s, 3H, H-CH_3) (Fig. 5.15). UV-visible (DMSO) (λ_{max}, nm (ε/dm^3, M^{-1} cm^{-1}): 441 (11,990); 289 (10,440) (Fig. 5.16).

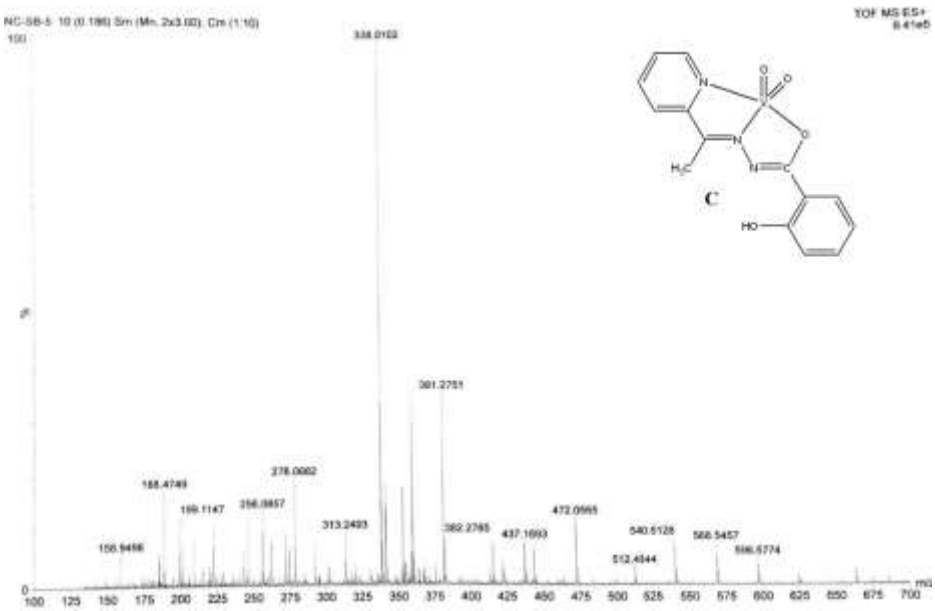

Fig.5.9 ESI-MS (positive) in CH_3OH of Compound **5.1**.

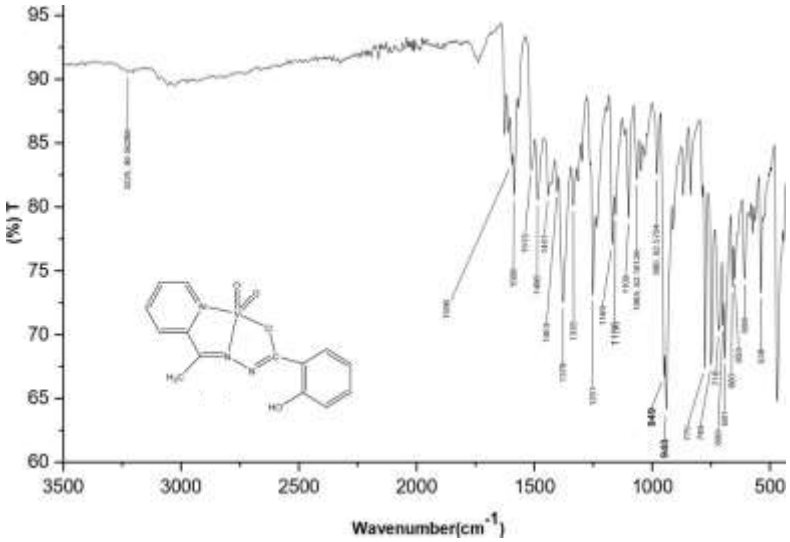

Fig.5.10 FT-IR bands (KBr pellet) of Compound **5.1**.

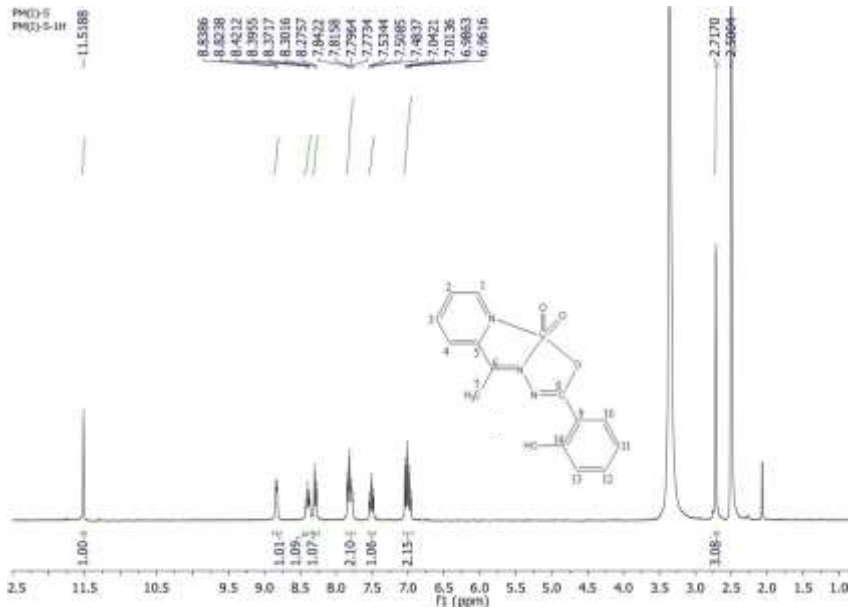

Fig.5.11 ^{1}H NMR (300 MHz, DMSO-d_6) of Compound **5.1**.

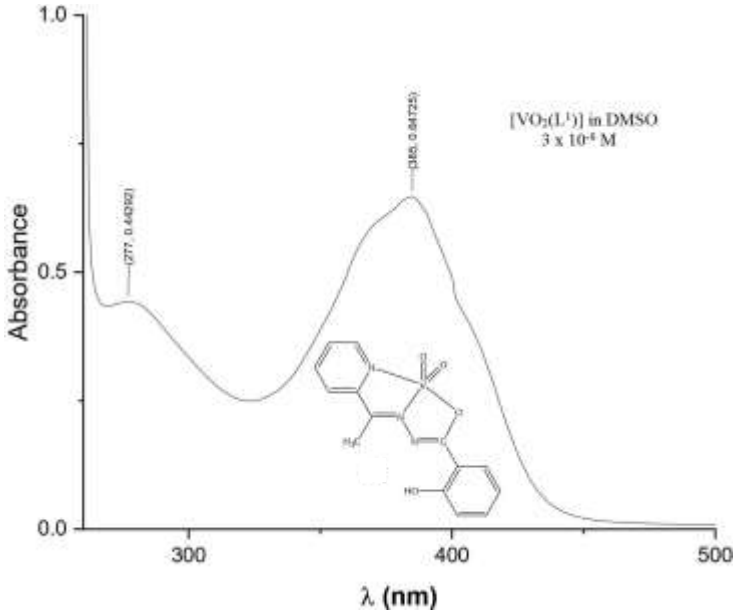

Fig.5.12 UV-visible (in DMSO) of Compound **5.1**.

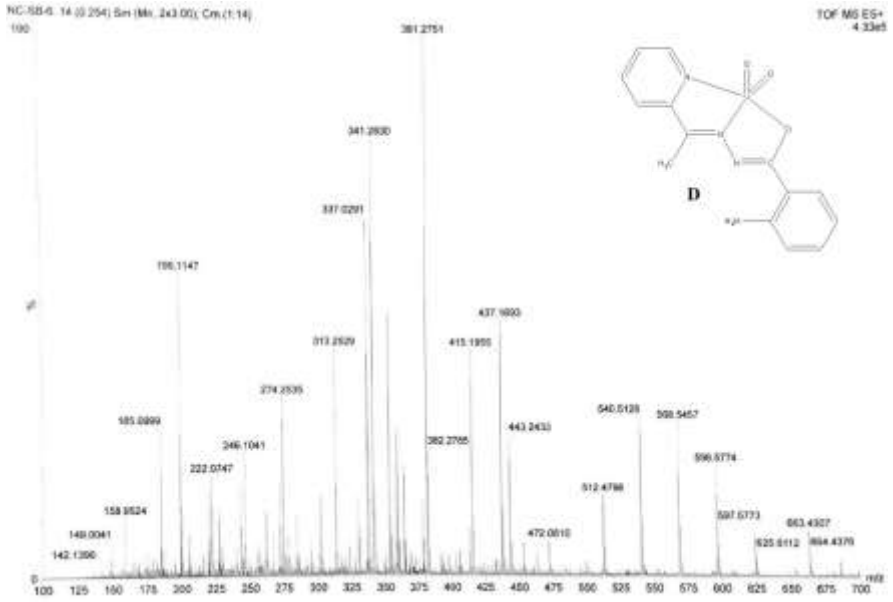

Fig.5.13 ESI-MS (positive) in CH_3OH of Compound **5.2**.

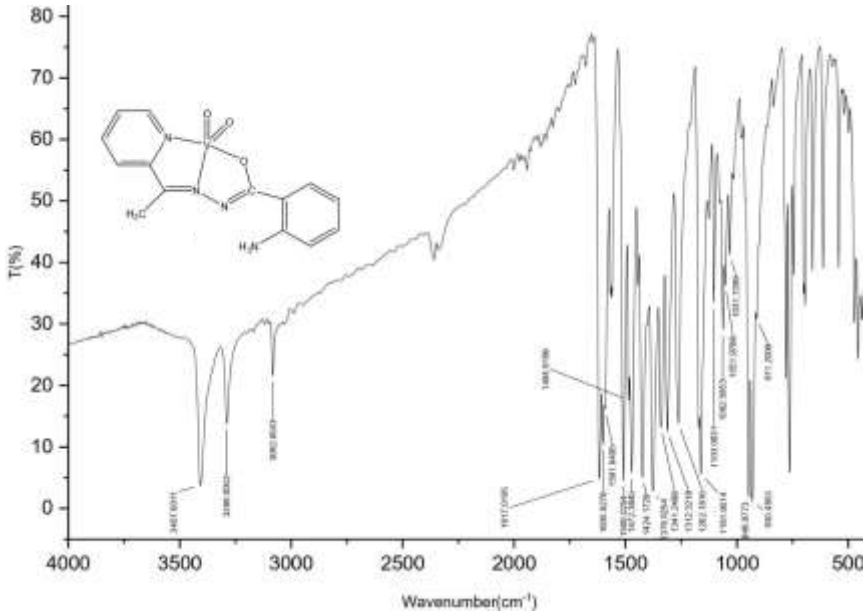

Fig.5.14 FT-IR bands (KBr pellet) of Compound **5.2**.

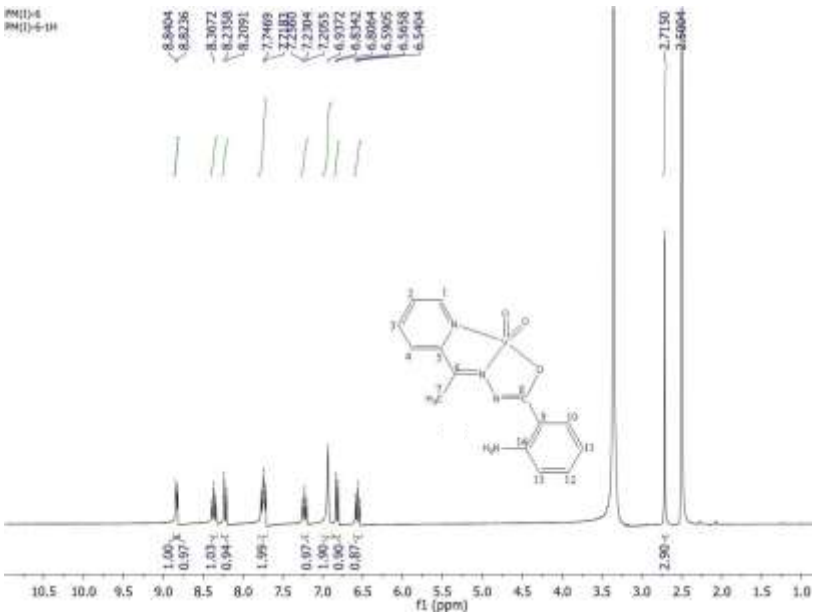

Fig.5.15 ^{1}H NMR (300 MHz, DMSO-d_6) of Compound **5.2**.

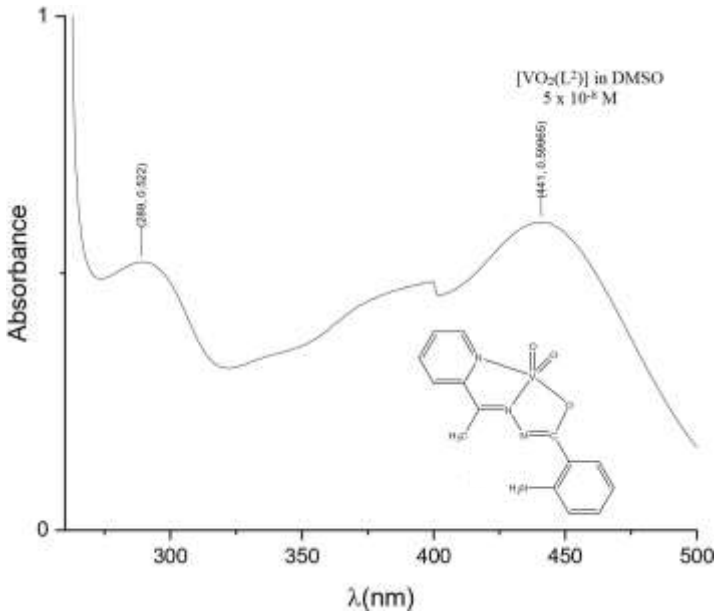

Fig.5.16 UV-visible (in DMSO) of Compound **5.2**.

5.2.6 Method 2. A total of 0.255 g of $HL^{5.1}$ (1.0 mmol) was dissolved in 30 cm^3 of methanol. To this solution was added methanolic solution of $[VO(acac)_2]$ (0.265 gm, 1 mmol). The mixture was then heated under reflux

for 3 h. A highly fluorescent yellow solution was obtained which was kept for slow evaporation at room temperature. A bright yellow strongly fluorescent crystals of compound **5.1** suitable for X-ray diffraction analysis were obtained after 6 days, were filtered, washed with methanol and dried over silica gel. Yield: 93%.

The reddish yellow compound **5.2** was also synthesized by following the same method adopted for compound **5.1** using $HL^{5.2}$ in place of HL^{1} in 92%.

These complexes were also synthesized by using non-hydroxylic solvents *viz*., chloroform and acetonitrile in comparable yield.

5.2.7 Method 3. To a warm methanolic solution (30 cm^3) of $HL^{5.1}$ (0.255 gm, 1 mmol) was added aqueous solution (20 cm^3) of NH_4VO_3 (0.117 gm, 1 mmol). The reaction mixture was stirred for 4 h at 60° C. Strongly fluorescent bright yellow crystalline compound **5.1** thus obtained was filtered, washed with water followed by aqueous-methanol and then dried over silica gel (fused). Yield: 94%.

The bright yellow fluorescent compound **5.2** was also synthesized by following the same method adopted for compound **5.1** using $HL^{5.2}$ in place of $HL^{5.1}$ in 95% yield.

5.2.8 Crystallographic data collection and refinement. Suitable single crystals of compound **5.1** and **5.2** were carefully selected under a polarising microscope and glued carefully to a thin glass fiber. The single crystal data were collected using Bruker D8 Quest machine. The X-ray generator was operated at 50 kV and 1 mA using Mo Kα (λ=0.71073Å) radiation. Data were collected with ω scan width of 0.5°. A total of 408 frames were collected in three different setting of φ (0, 90, 180°) keeping sample-to-detector distance fixed at 6.03 cm and the detector position (2θ) fixed at -25°. The final data sets were reduced by an APEX3 program, while a SAINTPLUS[5.32] program was utilized for the integration of diffraction profiles. The absorption correction (multi-scan) was carried out by a SADABS program.[5.33] We initially solved the structure by SIR 92,[5.34] and the full matrix least-square method (SHELXL-2016[5.35]) was used further, which is present in the WinGx suit of programs (Version 1.63.04a).[5.36, 5.37] We successfully located all the non-hydrogen atoms from Fourier maps and refined them with anisotropic displacement parameters at the final cycles. Finally, we fixed all the hydrogen atoms at calculated positions and included them in the refinement process using riding model associated with isotropic thermal parameters. Table 5.1 provide the summary of crystallographic data. Table 5.1: Summary crystallographic data of compound **5.1** and compound **5.2**.

Table 5.1: Crystal Data and Structure Refinement Parameters of compound **5.1** and **5.2**.

Parameters	Compound **5.1**	Compound **5.2**
Empirical formula	$C_{14}H_{12}N_3O_4V$	$C_{14}H_{13}N_4O_3V$
Formula weight	337.21	336.22
Crystal system	Monoclinic	Monoclinic
Space group	*C*2/*c*	$P2_1/n$
a(Å)	16.9063(13)	8.1922(6)
b(Å)	11.5085(8)	13.5959(9)
c(Å)	16.0545(12)	12.5135(10)
α(deg)	90	90
β (deg)	118.492(2)	100.518(2)
γ (deg)	90	90
Volume($Å^3$)	2745.3(4)	1370.34(17)
Z	8	4
Calculated density, ρ_{calc}(mg m^{-3})	1.632	1.630
Absorption coefficient, μ (mm^{-1})	0.745	0.743
Temperature	273(2) K	273(2) K
Wavelength(Mo Kα) (Å)	0.71073	0.71073
θ range (deg)	2.238 to 27.110	2.997 to 27.078
Final R indices [I>2sigma(I)]	R1 = 0.0374, wR2 = 0.1144	R1 = 0.0335, wR2 = 0.1021
R indices (all data)	R1 = 0.0467, wR2 = 0.1279	R1 = 0.0425, wR2 = 0.1212

$R_1=\Sigma||F_0|-|F_c||/\Sigma|F_0|$; $wR_2=\{\Sigma[w(F_0^2-F_c^2)^2]/\Sigma[w(F_0^2)^2]\}^{1/2}$,$w=1/[\sigma^2(F_0)^2+(aP)^2+bP]$;

$P=[\max.(F_0,0)^2+2(F_c)^2]/3$ where a = 0.0713, b = 1.8804 for compound **5.1;** a = 0.0678, b = 0.4741 for compound **5.2**.

5.2.9 Materials. Chemicals used for synthesis, acetylacetone (Loba chemical company, India), vanadyl sulphate pentahydrate (Loba chemical company, India), 2-hydroxybenzoylhydrazide (TCI, Japan), 2-aminobenzoylhydrazide (TCI, Japan) and chemicals used for the detection experiments, $CdCl_2.H_2O$ (Merck, 98%), $ZnSO_4.7H_2O$ (Merck, 99%), $Al(NO_3)_3.9H_2O$ (Merck, 98%), anhydrous $FeCl_3$ (Merck, 98%), $Cr(NO_3)_3.9H_2O$ (Sigma-Aldrich, 99%), $FeSO_4.4H_2O$ (Merck, 99%), $CuCl_2.2H_2O$ (Merck, 98.5%), $HgCl_2$

(Merck, 99.5%), $Pb(NO_3)_2$ (Merck, 99%), NaCl (Merck, 99%), KCl (Merck, 98.5%), $MnCl_2.4H_2O$ (Merck, 99%), $CoCl_2.6H_2O$ (Merck, 98%), $NiCl_2.6H_2O$ (Sigma-Aldrich, 98%) and $MgSO_4.7H_2O$ (Merck, 98%), were used as received without further purification. The water used was double distilled. [$V^{IV}O(acac)_2$] was prepared using the reported method.[5.38]

5.2.10 Optical Measurements. Photoluminescence properties of all the compounds were investigated at room temperature in water using a using Hitachi F-7100 luminescence spectrofluorometer. UV-Vis spectra of the solutions were measured using Shimadzu UV 3101PC spectrophotometer. The 5 mM metal salt solutions were prepared in water for absorption measurements. The stock solution of compound **5.1** was prepared by introducing 2.5 mg of compound **5.1** into 1 mL of acetonitrile (Sigma Aldrich). Then 25 µL of the above stock solution is taken into 2 mL of water in a quartz cuvette for final photoluminescence measurements. The stock solution of compound **5.2** was prepared by introducing 1.5 mg of compound **5.2** into 1 mL of acetonitrile. The photoluminescence measurements were performed using 50 µL of the above stock solution into 2 mL of water in a quartz cuvette. For time-correlated single photon counting (TCSPC) measurements, we utilized a HORIBA Jobin-Yvon instrument at room temperature.

5.3 RESULTS AND DISCUSSION

5.3.1 Synthesis of compound 5.1-5.2. Both the compounds were synthesized by using different tetravalent precursor *e.g.*, $V^{IV}OSO_4$ and $V^{IV}O(acac)_2$ as well as pentavalent precursor $NH_4V^{V}O_3$ in different hydroxylic solvents *e.g.*, CH_3OH, H_2O as well as non-hydroxylic solvents *e.g.*, chloroform, acetone and acetonitrile in excellent yield as described in eqns. 1–3. It is to be noted that the pH of the reaction medium varies from acidic (eqn. 1) to basic (eqn. 3) *via* neutral (eqn. 2) depending upon the nature of starting material.

5.3.2 Structural descrption of compound 5.1. Compound **5.1** comprises one V^{5+} ion along with two oxido ligands and one $L^{5.1}$ ligand in its asymmetric unit (Fig. 5.17). The nature of the coordination sphere is five connected VO_3N_2 type. The V^{5+} ion is surrounded by two oxido ligands, one pyridine nitrogen atom, one nitrogen atom of the imine moity and one oxygen atom of hydroxyl group of ligand $L^{5.1}$. The five coordinated V^{5+} ion has a distorted square pyramidal geometry. The important bond distances and angles are tabulated in Table 5.2 and Table 5.3.

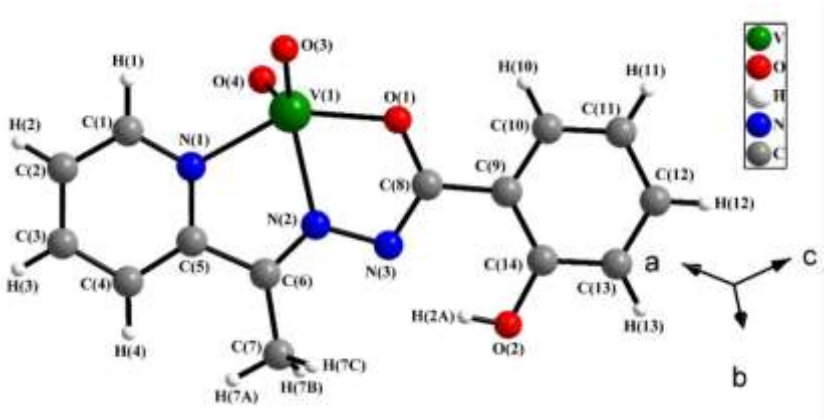

Fig. 5.17 Figure shows the asymmetric unit of compound **5.1**.

The presence of free hydroxyl group of ligand $L^{5.1}$ in compound **5.1** stabilized the molecular complex through intra-molecular hydrogen bond interactions. Where the N(3) atom of ligand $L^{5.1}$ acts as hydrogen bond acceptor (A) with H…A distance of 1.9 Å and O(2) atom acts as hydrogen bond donor (D) with D…A distance of 2.614 Å and D –H …A angle of 146°. The two molecular units are organized as dimeric unit through the π…π interactions between two benzene rings (Fig. 5.18). The centroid–centroid distance of 3.7 Å and parallel-displaced structure (between two benzene rings) have been observed for favouring the π…π interactions. The dimeric units are stacked further in *ac* plane to form one-dimensional arrangement (Fig. 5.19).

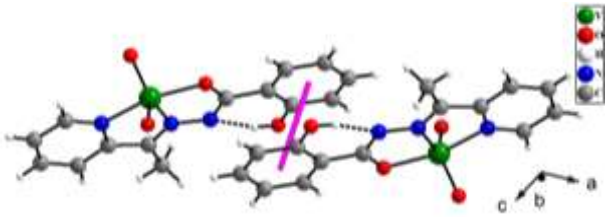

Fig. 5.18 Figure shows the structure of dimeric unit formed through the π…π interactions in compound **5.1**. The pink lines indicate the centroid-centroid distance (3.7 Å).

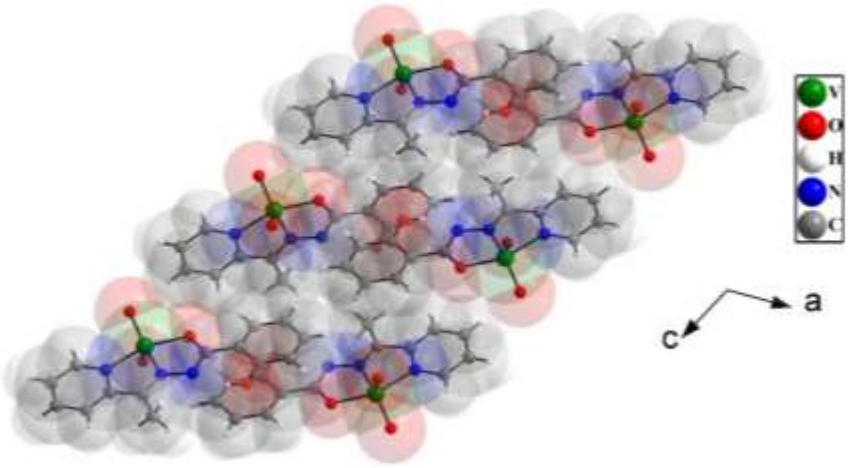

Fig. 5.19 The stacking arrangement of the dimeric units in *ac* plane.

The packing of the one-dimensional structures in the perpendicular direction of the *ab* plane stabilized the overall three-dimensional arrangement (Fig. 5.20).

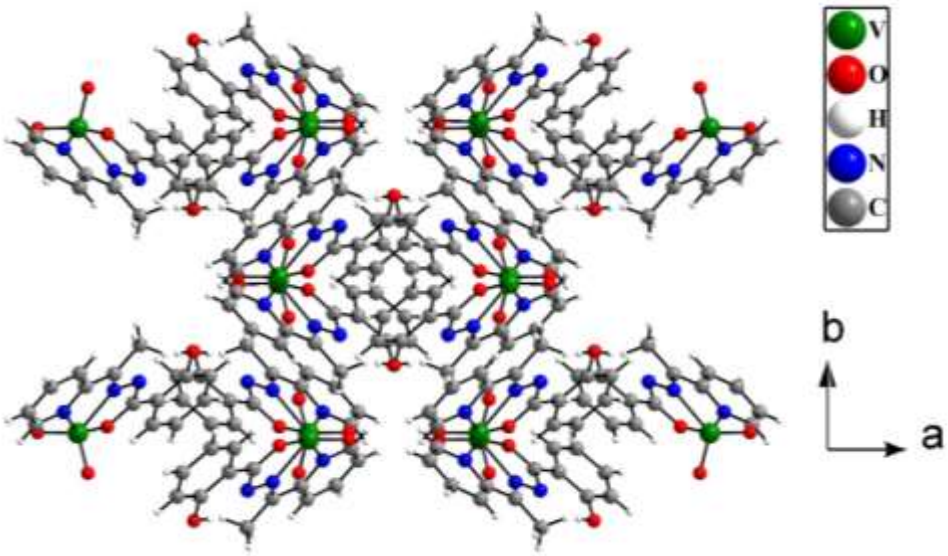

Fig. 5.20 Figure shows the three dimensional packing arrangement of the one dimensional structures of compound **5.1.**

5.3.3 Structure of compound 5.2. Similar to compound **5.1**, the compound **5.2** comprises one V^{5+} ion, two oxo ligands and one $L^{5.2}$ ligand in the asymmetric unit (Fig. 5.21). The coordination geometry around V^{5+} ion and the binding modes of ligand $L^{5.2}$ is similar with respect to $L^{5.1}$ observed in compound **5.1.** The important bond distances and angles are tabulated in Table 5.2 and Table 5.3.

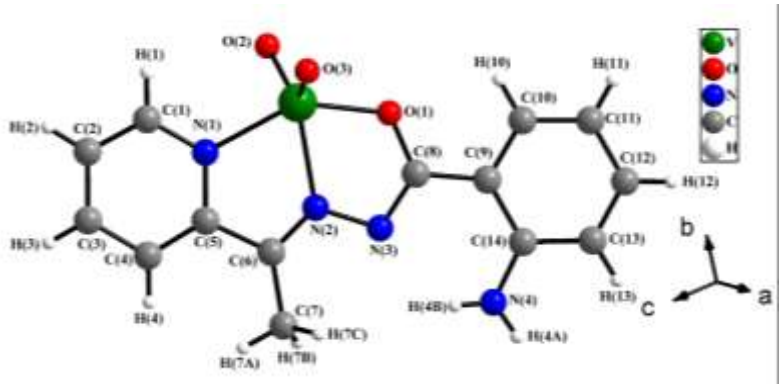

Fig. 5.21 Figure shows the asymmetric unit of compound **5.2**.

Table 5.2: Selected bond distances (Å) observed in compound **5.1** and **5.2.**

Bond	Magnitude (Å)	Bond	Magnitude (Å)
Compound **5.1**			
V(1)-O(1)	1.9646(16)	V(1)-N(1)	2.1143(18)
V(1)-O(3)	1.6154(19)	V(1)-N(2)	2.1165(17)
V(1)-O(4)	1.6064(19)		
Compound **5.2**			
V(1)-O(1)	1.9540(15)	V(1)-N(1)	2.1060(17)
V(1)-O(2)	1.6177(16)	V(1)-N(2)	2.1116(17)
V(1)-O(3)	1.6228(16)		

Table 5.3: Selected bond angles observed in compound **5.1** and **5.2.**

Angle	Magnitude (°)	Angle	Magnitude (°)
Compound **5.1**			
O(4)-V(1)-O(3)	110.60(11)	O(1)-V(1)-N(1)	146.15(7)
O(4)-V(1)-O(1)	104.31(9)	O(4)-V(1)-N(2)	118.80(9)
O(3)-V(1)-O(1)	101.03(9)	O(3)-V(1)-N(2)	130.18(9)
O(4)-V(1)-N(1)	96.18(9)	O(1)-V(1)-N(2)	73.56(7)
O(3)-V(1)-N(1)	96.45(9)	N(1)-V(1)-N(2)	73.00(7)
Compound **5.2**			
O(2)-V(1)-O(3)	109.75(9)	O(1)-V(1)-N(1)	144.77(7)

O(2)-V(1)-O(1)	101.97(8)	O(2)-V(1)-N(2)	134.50(8)
O(3)-V(1)-O(1)	104.09(8)	O(3)-V(1)-N(2)	115.30(8)
O(2)-V(1)-N(1)	95.32(7)	O(1)-V(1)-N(2)	73.45(6)
O(3)-V(1)-N(1)	98.45(7)	N(1)-V(1)-N(2)	72.54(6)

The presences of free amino group in ligand $L^{5.2}$ of compound **5.2** stabilized the molecular complex through the intra- and inter- molecular hydrogen bond interactions. For intra-molecular hydrogen bond interactions, the N(3) atom of ligand $L^{5.2}$ acts as hydrogen bond acceptor (A) with H…A distance of 2.14 Å [H(4B)…N(3)] and N(4) atom acts as hydrogen bond donor (D) with D…A distance of 2.71 Å and D –H …A angle of 128°. On the other hand for inter-molecular hydrogen bond interactions, the O(3) atom of oxo ligand acts as hydrogen bond acceptor (A) with H…A distance of 2.24 Å [H(4A)…O(3)] and N(4) atom acts as hydrogen bond donor (D) with D…A distance of 3.08 Å and D –H …A angle of 157°.

The two molecular units are arranged as dimeric unit through the π…π interactions between benzene rings and pyridine rings (Fig. 5.22). The centroid – centroid distance of 3.55 Å and parallel-displaced structure (between benzene and pyridine) favour the π…π interactions. Each of the dimeric unit connected with two other dimeric units through the inter-molecular N – H …O hydrogen bond interactions to form one dimensional supramolecular structure (Fig. 5.23).

The packing of the one-dimensional structures in the perpendicular direction of the *bc* plane stabilized the overall three-dimensional arrangement (Fig. 5.24).

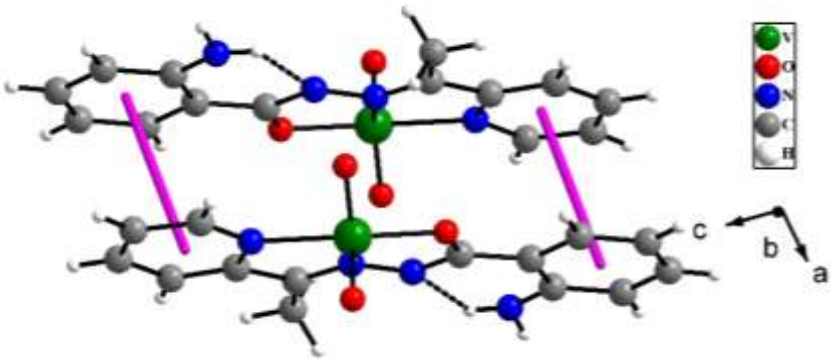

Fig. 5.22 Figure shows the structure of dimeric unit formed through the π…π interactions in compound **5.2**. The pink lines indicate the centroid-centroid distance (3.55 Å).

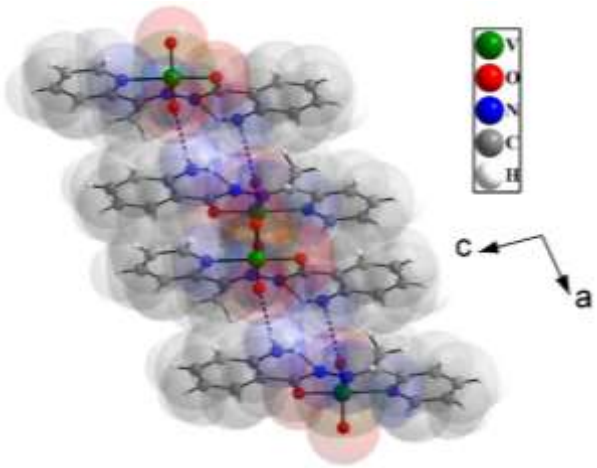

Fig. 5.23 The one-dimensional structure formed through the hydrogen bond interactions.

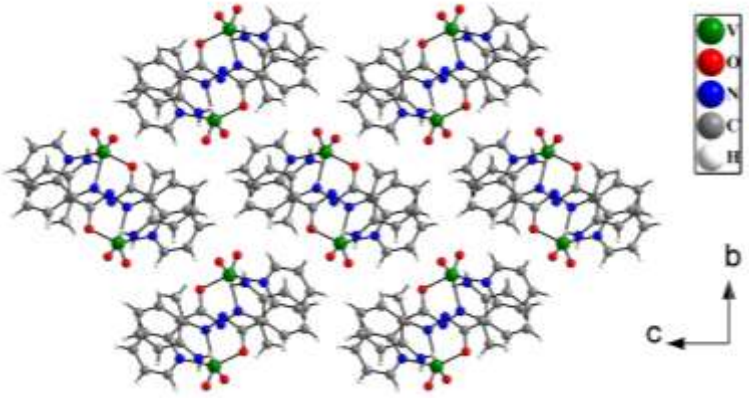

Fig. 5.24 Figure shows the three-dimensional packing arrangement of the one dimensional structures of compound **5.2**.

5.3.4 Structural comparison. Both the two compounds crystallized in monoclinic crystal systems. Between the two structures, compound **5.1** has *C*2/*c* space group whereas compound **5.2** has $P2_1/n$ space group. Both compounds have distorted square pyramidal geometries around V^{5+} ions with the same ligating atoms. Compound **5.1** formed dimeric unit through the π…π interactions of the two benzene rings whereas compound **5.2** formed dimeric unit through the π…π interactions between benzene and pyridine rings of two different molecular species. In compound **5.1**, the presence of free hydroxyl group stabilized the molecular species through intra-molecular O–H…N type hydrogen bond interaction. In compound **5.2**, the free amino group involve in both the intra-molecular N–H…N type hydrogen bond interaction and inter-molecular N – H…O type hydrogen bond interactions. The packing arrangements of the one-dimensionally stacked structures in the three dimensions are different for both structures (see Fig. 5.20 and 5.24).

5.3.5 IR spectroscopic studies. Disappearance of two ligand band 1640/1646 cm^{-1} due to υ(C=O) and 3045/2979 cm^{-1} due to υ(N-H) stretches and the appearance of a new band in the 1251/1262 cm^{-1} due to υ(C-$O_{enolate}$) indicates the transformation of keto form to enol form and subsequent metal coordination through deprotonation in compound **5.1**/compound **5.2** (see Fig.5.10 and 5.14). The υ(C=N) stretches appeared in the 1513/1509 cm^{-1} region. The characteristic υ(N-N) stretches appeared in the 1066/1063 cm^{-1} region. Both compounds exhibited two sharp bands in the 949/947 cm^{-1} and 940/930 cm^{-1} region which is attributed to antisymmetric and symmetric stretching respectively of *cis*-VO_2^+ motifs.

5.3.6 Thermogravimetric analysis of compound 5.1 and 5.2. Thermogravimetric analysis (TGA) of the compounds have been carried out in nitrogen atmosphere from 30 °C to 800 °C with a heating rate of 20 °C min^{-1}. The experimental final weight loss of compound **5.1** is 73.92% and this value matches well with the calculated weight loss value (73.04%) originated due to the decomposition of the compound **5.1** to V_2O_5 (see Fig. 5.25). Similarly, for compound **5.2**, the experimental weight loss is 71.63% which is also in great agreement with calculated weight loss value (72.96%) (see Fig. 5.26).

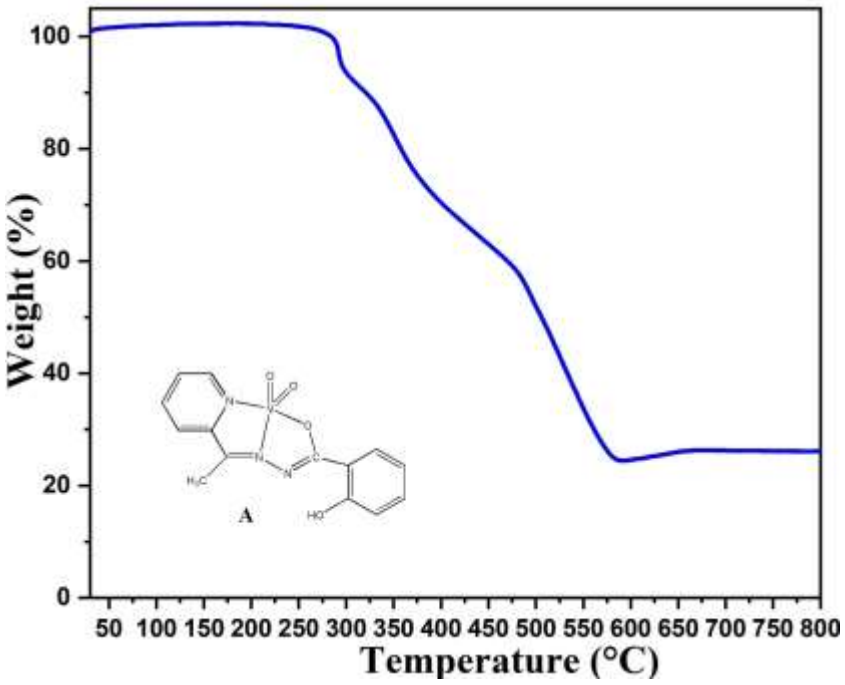

Fig. 5.25 Thermogravimetric analysis (TGA) of Compound **5.1**.

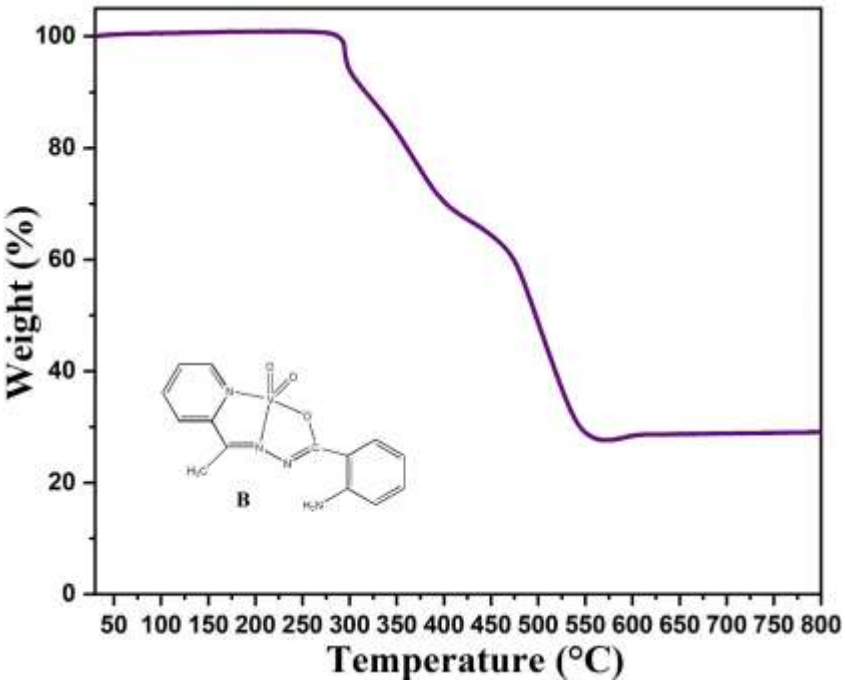

Fig. 5.26 Thermogravimetric analysis (TGA) of Compound **5.2**.

5.3.7 UV-Vis spectroscopy of compound 5.1 and 5.2. Both the compounds exhibited intense LMCT transitions of the type N(pyridine)→V^{5+} in the visible region with a main band positioned at 385/441 nm. The intra-ligand

based π-π* transitions were observed at around 277/289 nm region (see Fig.5.12 and 5.16). All the absorption studies were carried out in DMSO medium.

5.3.8 Study of photoluminescence property. Investigation on the photoluminescence behaviours of the compounds were carried out using water dispersion of the solid samples. The aqueous dispersion of compound **5.1** and compound **5.2** exhibited emission centred at 408 and 395 nm, respectively, using 300 nm light as source of excitation. The metal ions bonded aromatic ligands were accountable for the emission behaviours. The luminescence intensity of the compound **5.1** found to be very high compared to compound **5.2**. The very strong luminescence property of compound **5.1** is possibly due to restricted rotation of the C(8)-C(9) bond in presence of H-bonding involving –OH group (see Fig. 5.18 and 5.19). The presence of $–NH_2$ group in the compound **5.2** partially restricted the rotation around the C(8)-C(9) bond resulting in moderate luminescence intensity (see Fig. 5.22 and 5.23).

To investigate the performance of compound **5.1** in detecting the presence of very small amount of metal ions, titrations were carried out through the monitoring of the luminescence intensity along with the systematic accumulation of analytes (metal ions) to the water dispersion of compound **5.1**. A dramatic alteration in the emission spectra was observed in presence of Al^{3+} ion. A 33 nm blue shift in the emission peak position from 408 nm to 375 nm occurred in addition to an increase in luminescence intensity (see Fig. 5.27). The compound **5.1** also responded to the Fe^{3+} ions by showing a huge decrease in luminescence intensity. The alteration in emission intensity with the increasing concentration of Fe^{3+} (upto 62.50 μM) is shown in Fig. 5.28. The emission of the compound was quenched about 91% of the starting emission intensity upon the addition of the Fe^{3+}.

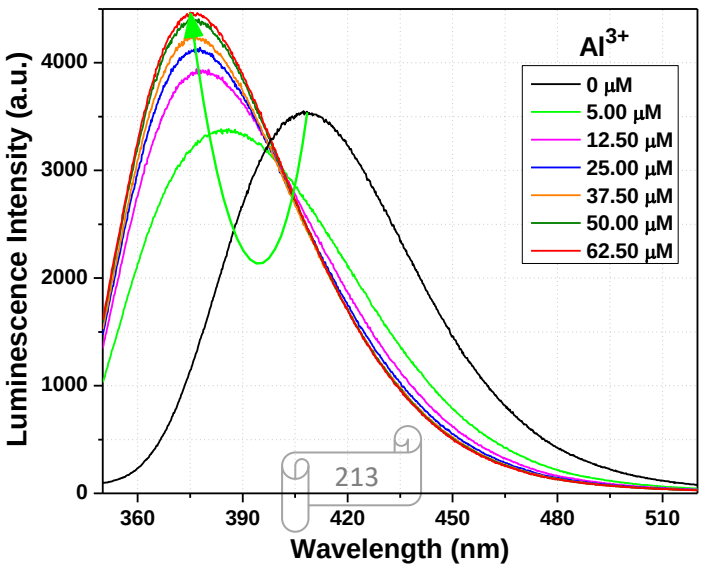

Fig. 5.27 Luminescence spectra of compound **5.1** dispersed in water upon incremental addition of water solution of Al^{3+} ions (λ_{ex} = 300 nm). Final concentration of Al^{3+} ions in the medium is indicated in the legend.

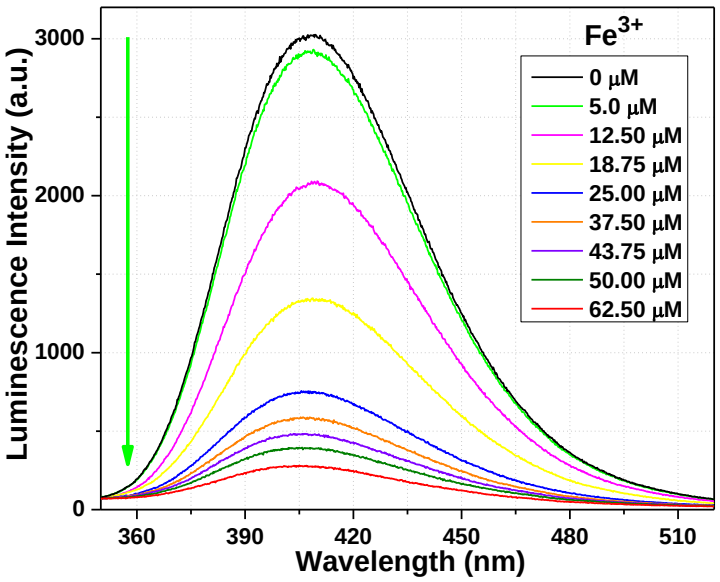

Fig. 5.28 Luminescence spectra of compound **5.1** dispersed in water upon incremental addition of water solution of Fe^{3+} ions (λ_{ex} = 300 nm). Final concentration of Fe^{3+} ions in the medium is indicated in the legend.

Following the same approach, titrations of compound **5.1** were also performed further using other cations such as Na^+, K^+, Mg^{2+}, Mn^{2+}, Pb^{2+}, Cr^{3+}, Hg^{2+}, Cu^{2+}, Ni^{2+}, Co^{2+}, Fe^{2+}, Zn^{2+} and Cd^{2+} ions in aqueous medium through the changes of luminescence intensity (see Fig. 5.29-5.41). For these metal ions either the luminescence intensity remained unchanged or increased to a small magnitude. The variations of emission intensity based on the peak at 408 nm in the case of other cations upto the accumulation of 62.50 μM metal ions is presented in Fig. 5.42. The

calculation of the detection limit (LOD) for Al^{3+} was carried out by applying the equation [5.39, 5.40], LOD = 3σ/m, where σ represents standard deviation of emission intensity and m represents slope of the linear plot in smaller concentration range (see Fig. 5.43). Using the above equation, the calculated LOD was 66 nM (1.6 ppb in water).

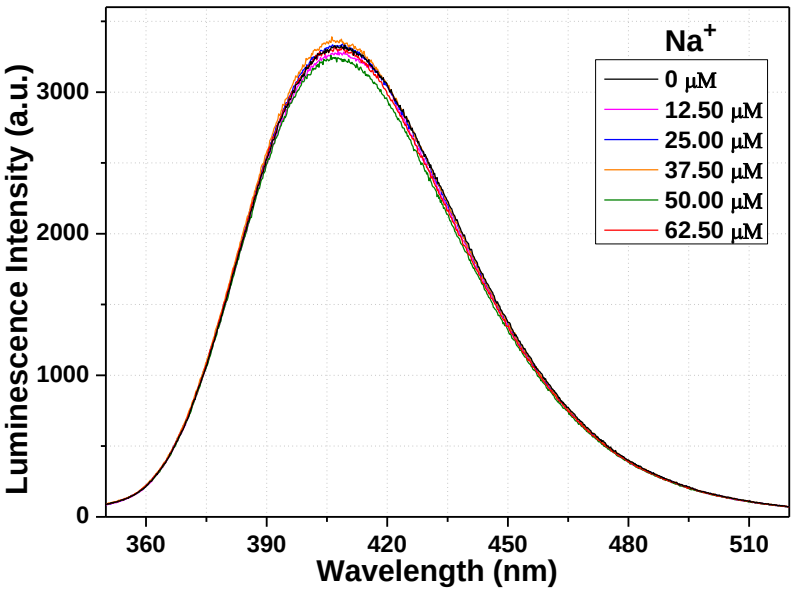

Fig. 5.29 Luminescence spectra of compound **5.1** dispersed in water upon incremental addition of water solution of Na^+ ions (λ_{ex} = 300 nm). Final concentration of Na^+ ions in the medium is indicated in the legend.

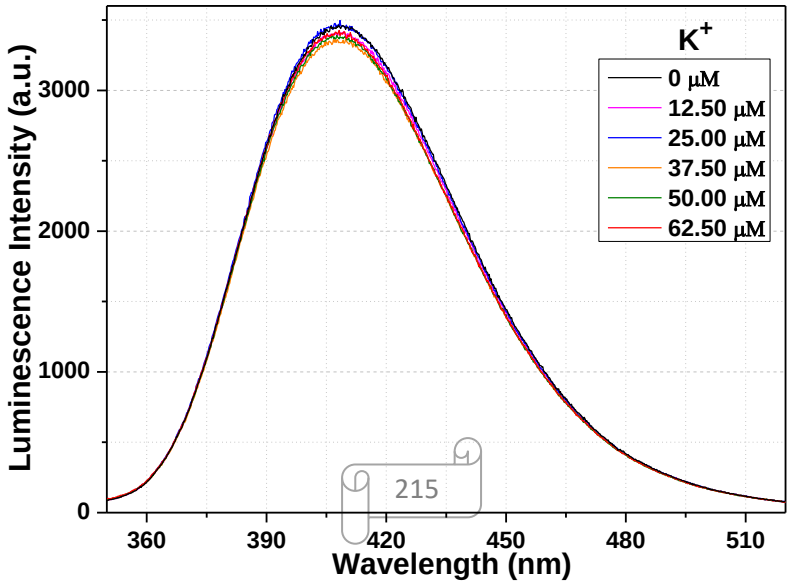

Fig. 5.30 Luminescence spectra of compound **5.1** dispersed in water upon incremental addition of water solution of K^+ ions (λ_{ex} = 300 nm). Final concentration of K^+ ions in the medium is indicated in the legend.

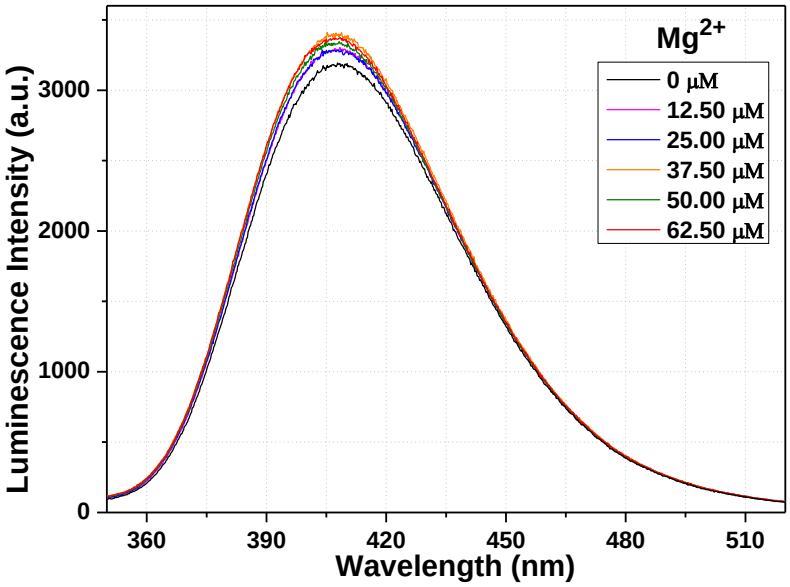

Fig. 5.31 Luminescence spectra of compound **5.1** dispersed in water upon incremental addition of water solution of Mg^{2+} ions (λ_{ex} = 300 nm). Final concentration of Mg^{2+} ions in the medium is indicated in the legend.

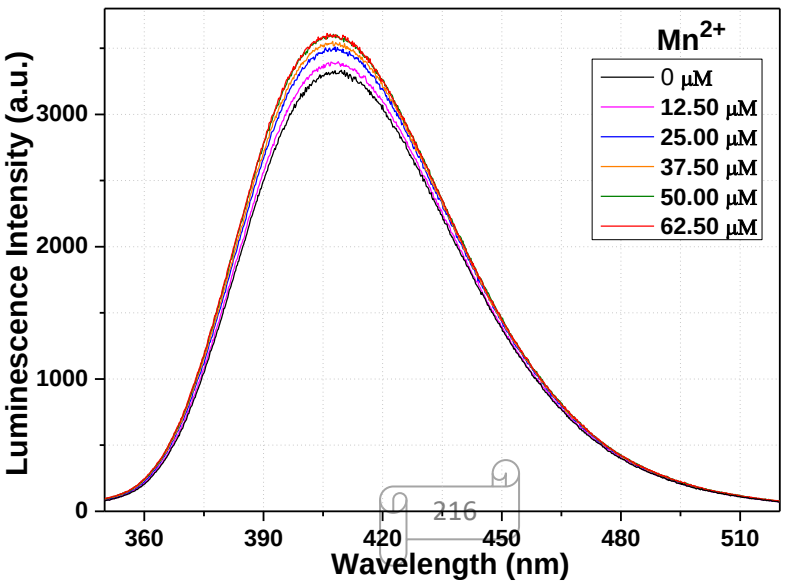

Fig. 5.32 Luminescence spectra of compound **5.1** dispersed in water upon incremental addition of water solution of Mn^{2+} ions (λ_{ex} = 300 nm). Final concentration of Mn^{2+} ions in the medium is indicated in the legend.

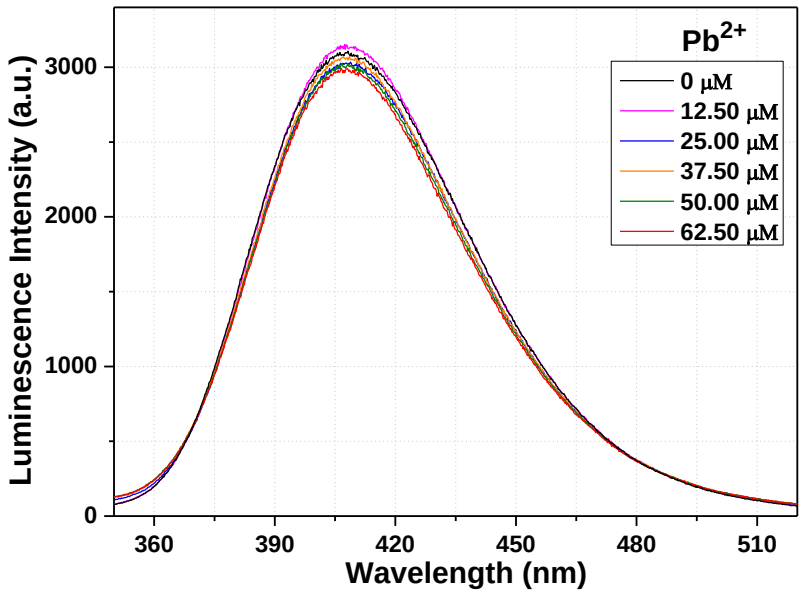

Fig. 5.33 Luminescence spectra of compound **5.1** dispersed in water upon incremental addition of water solution of Pb^{2+} ions (λ_{ex} = 300 nm). Final concentration of Pb^{2+} ions in the medium is indicated in the legend.

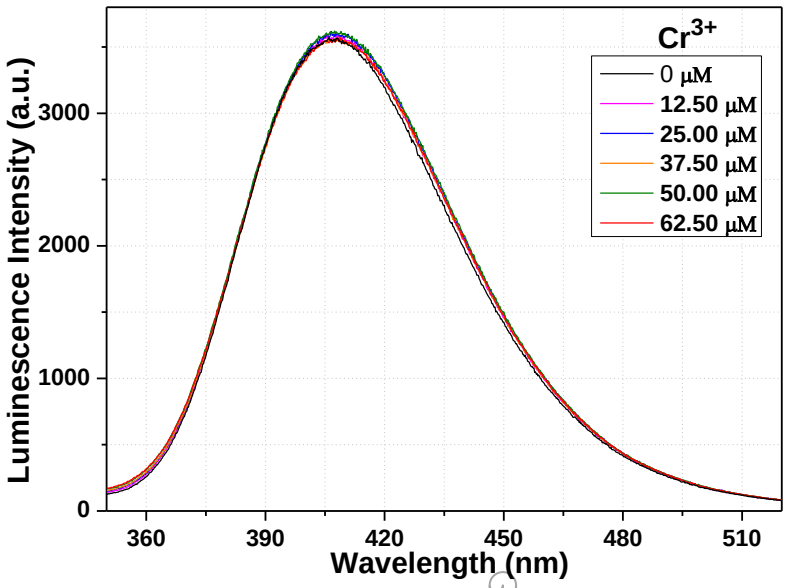

Fig. 5.34 Luminescence spectra of compound **5.1** dispersed in water upon incremental addition of water solution of Cr^{3+} ions (λ_{ex} = 300 nm). Final concentration of Cr^{3+} ions in the medium is indicated in the legend.

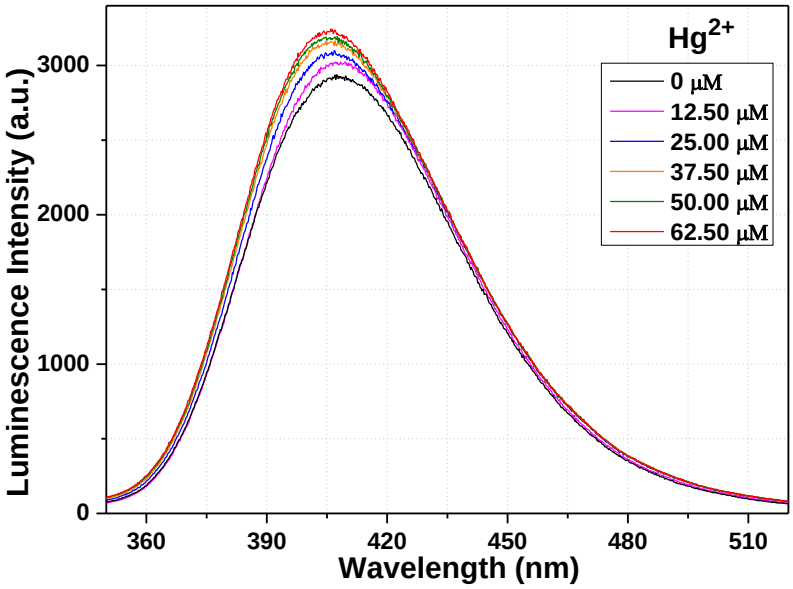

Fig. 5.35 Luminescence spectra of compound **5.1** dispersed in water upon incremental addition of water solution of Hg^{2+} ions (λ_{ex} = 300 nm). Final concentration of Hg^{2+} ions in the medium is indicated in the legend.

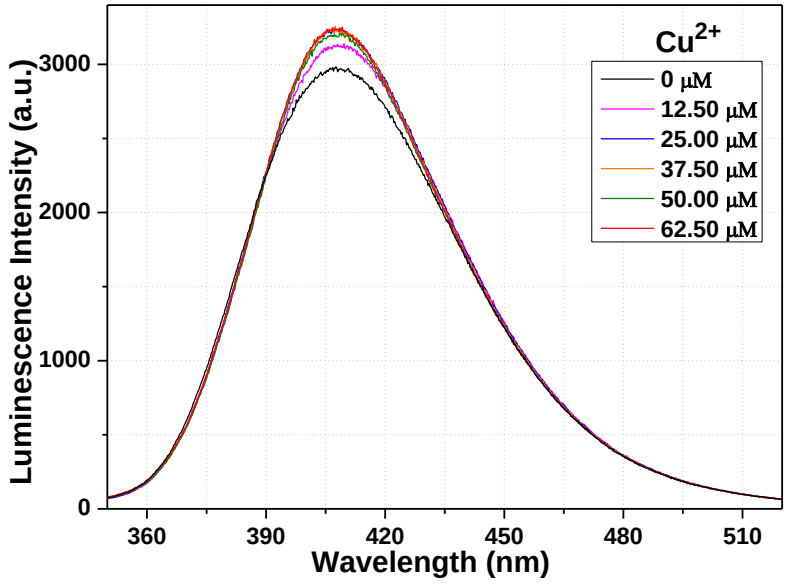

Fig. 5.36 Luminescence spectra of compound **5.1** dispersed in water upon incremental addition of water solution of Cu^{2+} ions (λ_{ex} = 300 nm). Final concentration of Cu^{2+} ions in the medium is indicated in the legend.

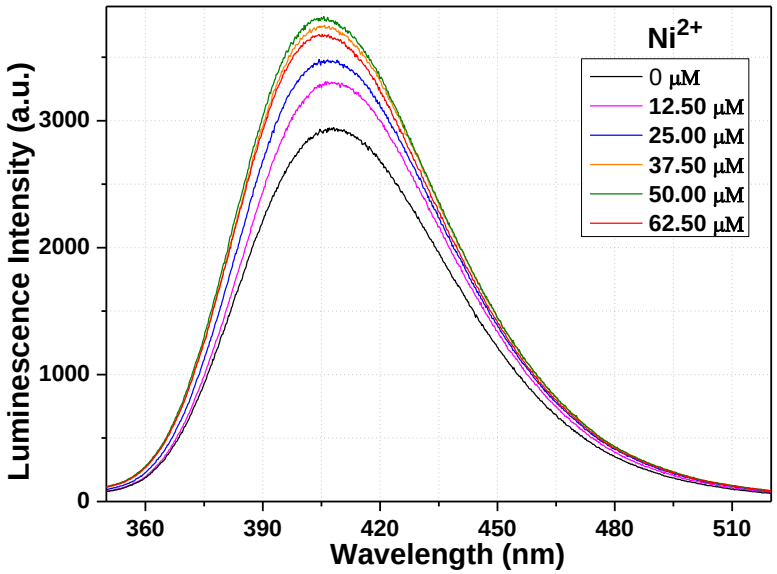

Fig. 5.37 Luminescence spectra of compound **5.1** dispersed in water upon incremental addition of water solution of Ni^{2+} ions (λ_{ex} = 300 nm). Final concentration of Ni^{2+} ions in the medium is indicated in the legend.

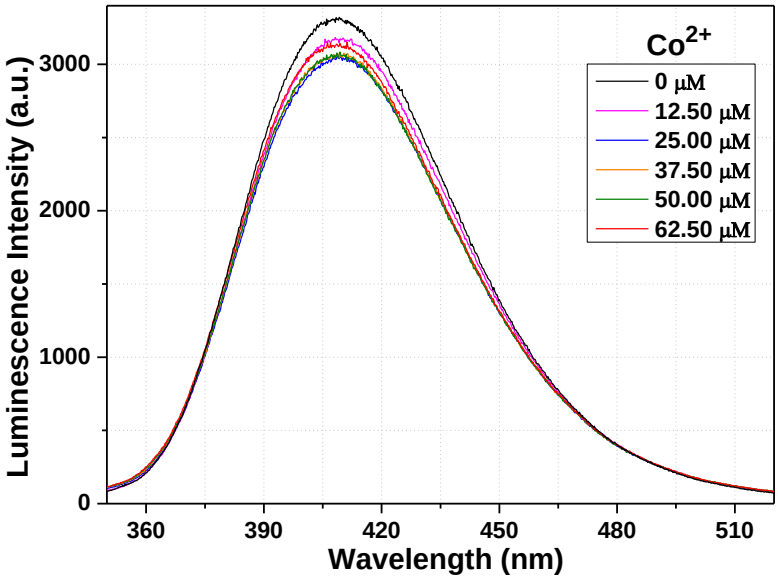

Fig. 5.38 Luminescence spectra of compound **5.1** dispersed in water upon incremental addition of water solution of Co^{2+} ions (λ_{ex} = 300 nm). Final concentration of Co^{2+} ions in the medium is indicated in the legend.

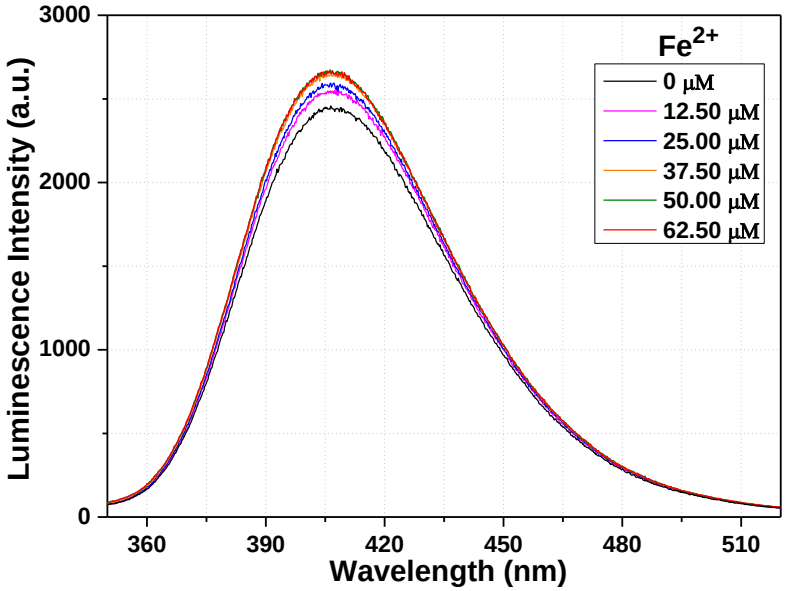

Fig. 5.39 Luminescence spectra of compound **5.1** dispersed in water upon incremental addition of water solution of Fe^{2+} ions (λ_{ex} = 300 nm). Final concentration of Fe^{2+} ions in the medium is indicated in the legend.

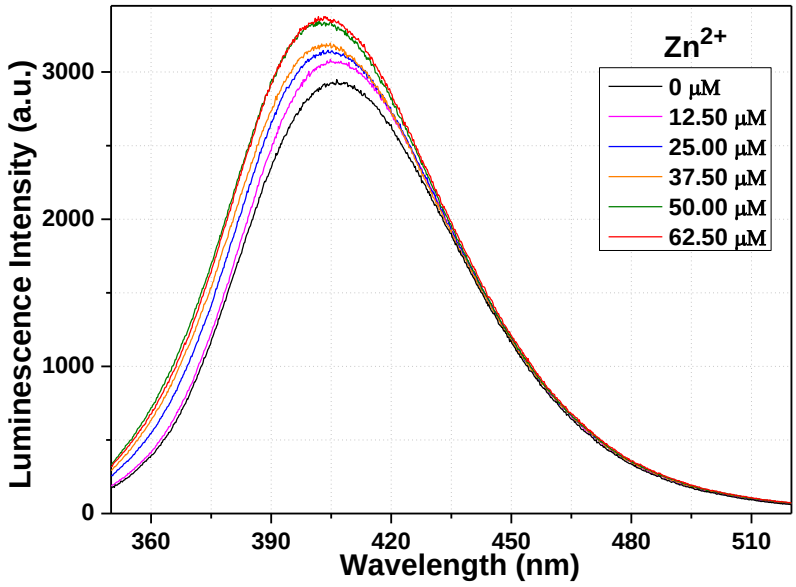

Fig. 5.40 Luminescence spectra of compound **5.1** dispersed in water upon incremental addition of water solution of Zn^{2+} ions (λ_{ex} = 300 nm). Final concentration of Zn^{2+} ions in the medium is indicated in the legend.

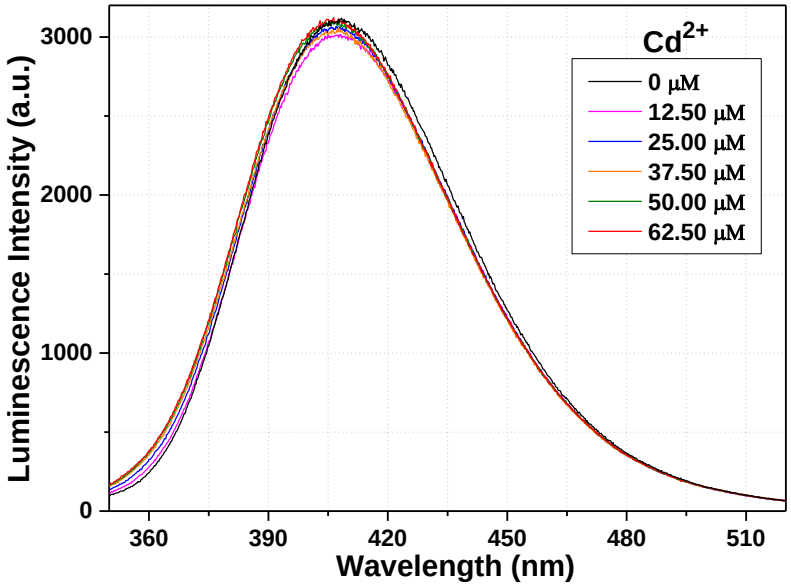

Fig. 5.41 Luminescence spectra of compound **5.1** dispersed in water upon incremental addition of water solution of Cd^{2+} ions (λ_{ex} = 300 nm). Final concentration of Cd^{2+} ions in the medium is indicated in the legend.

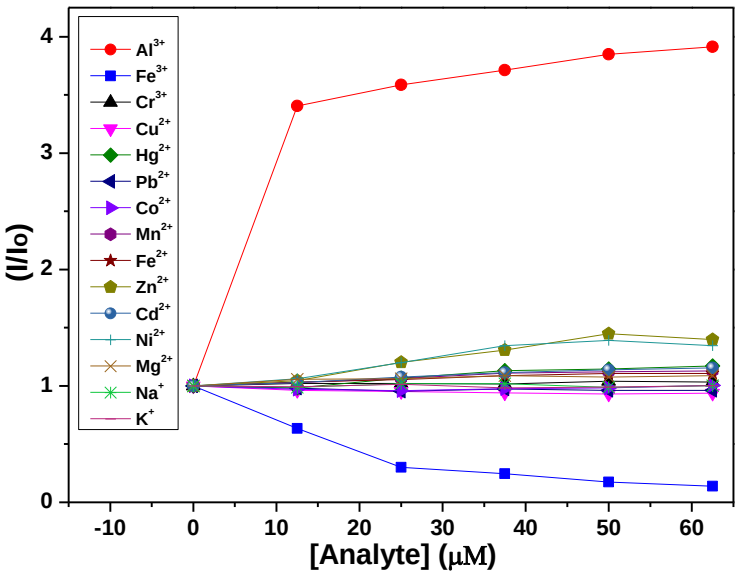

Fig. 5.42 Depiction of fractional of luminescence intensity plot of compound **5.1** (at 375 nm) *vs* concentration of analytes. Intensity of emission in absence and presence of analytes represented as I_0 and I, respectively.

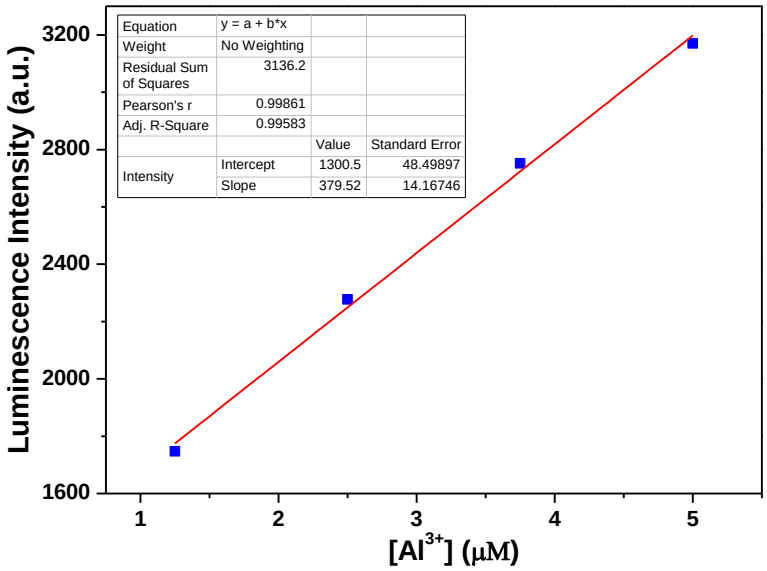

Fig. 5.43 Plot of luminescence intensity *vs* concentration of Al^{3+}.

The outcome of pH variation on the luminesnce intensity of compound **5.1** has also been investigated. Compound **5.1** is stable within the pH value of 4 to 9 (see Fig. 5.44 – 5.46). At pH < 4 and pH > 9, due to the breakdown of the complex, luminescence intensity decreases. In the pH range of 4 to 9, the nature and intensity of emission is almost similar. So, the interaction of Al^{3+} with compound **5.1** is responsible for luminescence turn-on behaviour.

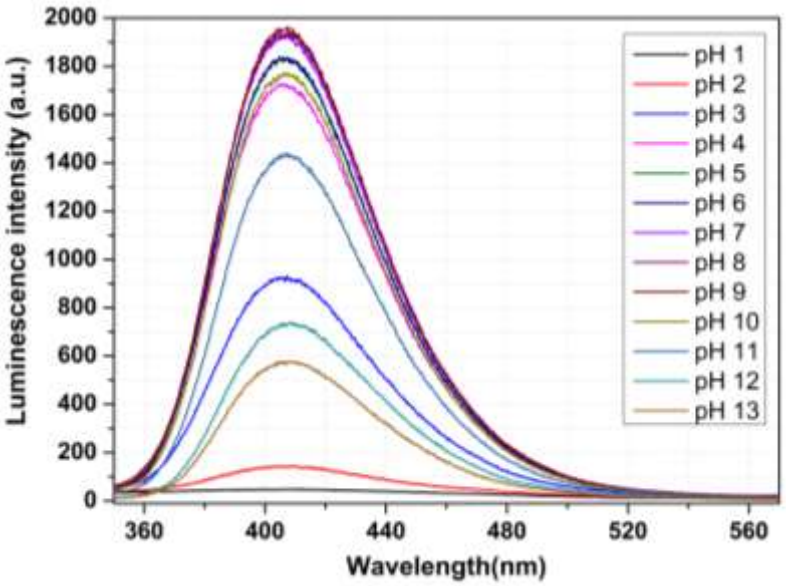

Fig. 5.44 Luminescence spectra of compound **5.1** in aqueous solution at different pH. The pH of the solution is indicated in the legend.

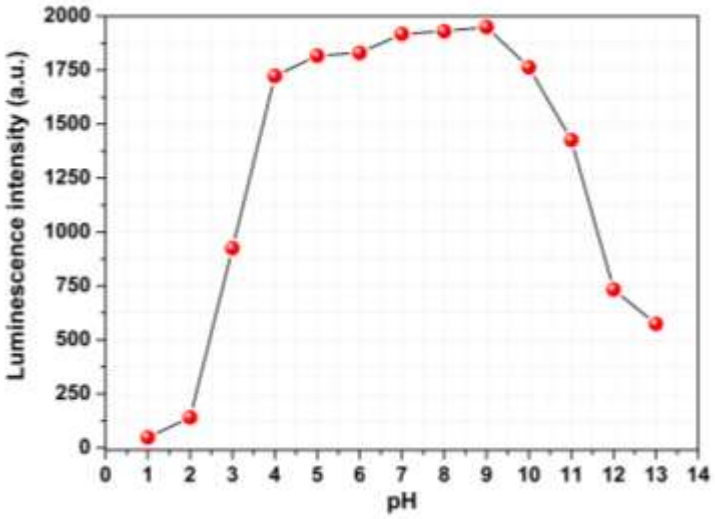

Fig. 5.45 Changes in luminescence intensity of compound **5.1** at different pH.

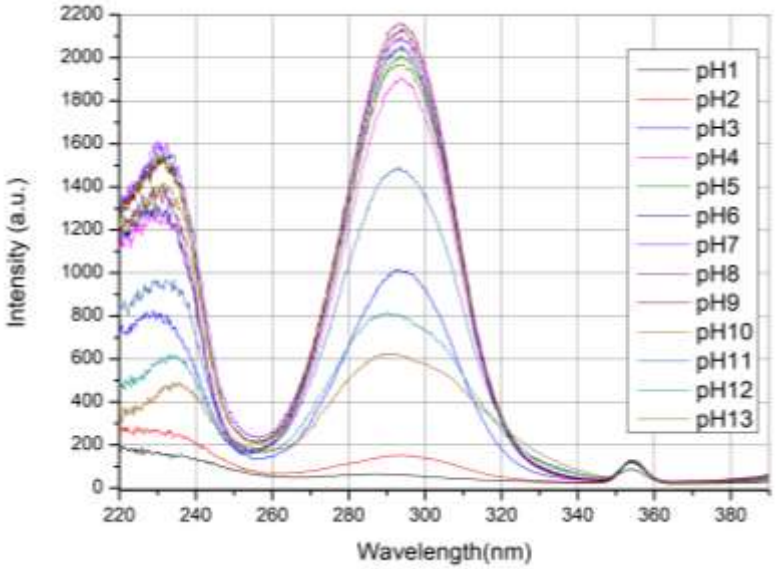

Fig. 5.46 Excitation spectra of compound **5.1** at different pH.

We have also investigated the effect on the emission intensity in the presence of nitro explosives of compound **5.1**. Upon the addition of TNP, DNP, NP, NT, DNT, NB compound **5.1** showed luminescence quenching efficiencies of 99%, 95%, 75%, 98%, 89%, and 68%, respectively (see Fig 5.47-5.52). The quenching efficiency follows the order: TNP ≈ NT > DNP > DNT > NP > NB (see Fig 5.53).

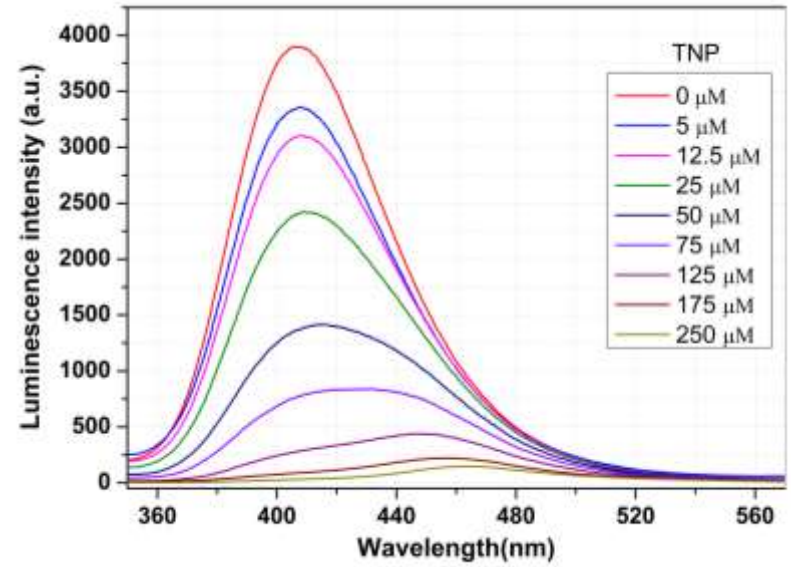

Fig. 5.47 Luminescence spectra of compound **5.1** dispersed in water upon incremental addition of TNP solution (λ_{ex} = 300 nm). The final concentration of the TNP in the medium is indicated in the legend.

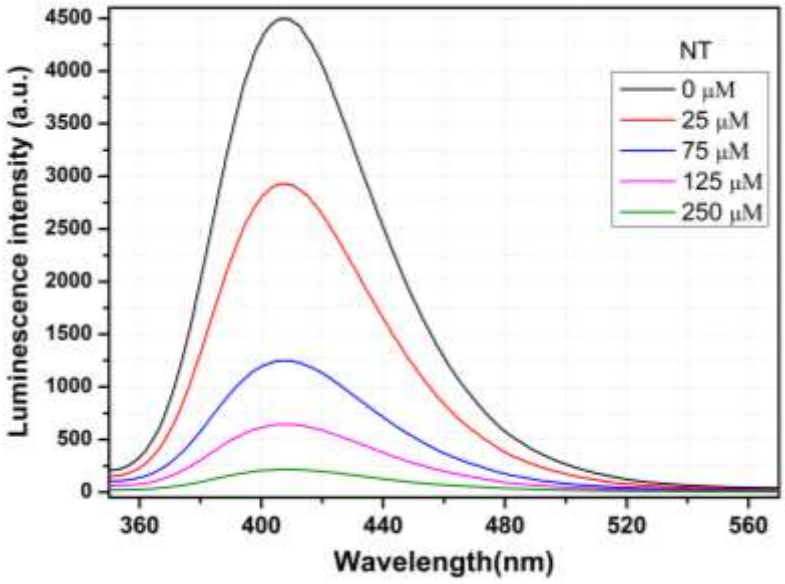

Fig. 5.48 Luminescence spectra of compound **5.1** dispersed in water upon incremental addition of NT solution (λ_{ex} = 300 nm). The final concentration of the NT in the medium is indicated in the legend.

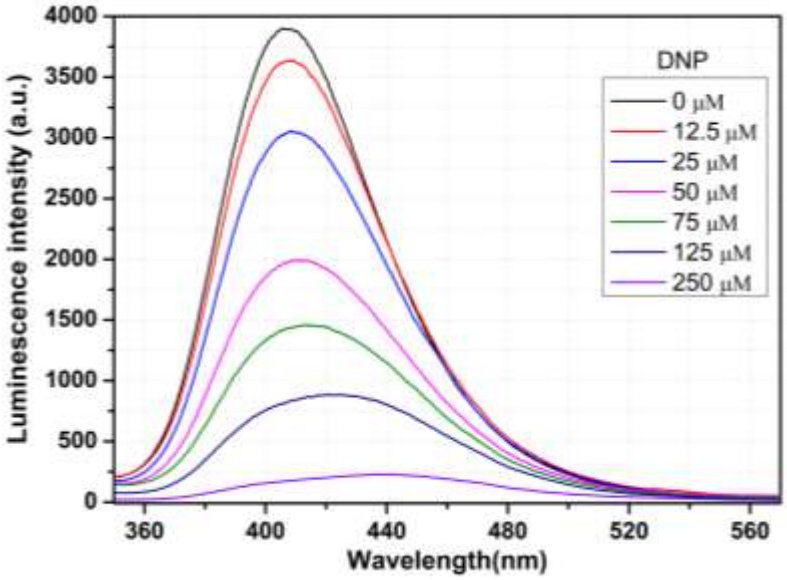

Fig. 5.49 Luminescence spectra of compound **5.1** dispersed in water upon incremental addition of DNP solution (λ_{ex} = 300 nm). The final concentration of the DNP in the medium is indicated in the legend.

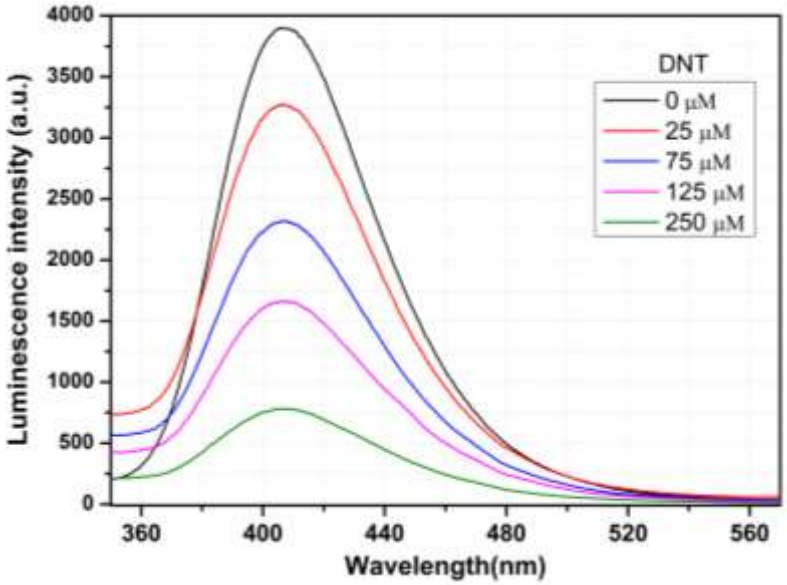

Fig. 5.50 Luminescence spectra of compound **5.1** dispersed in water upon incremental addition of DNT solution (λ_{ex} = 300 nm). The final concentration of the DNT in the medium is indicated in the legend.

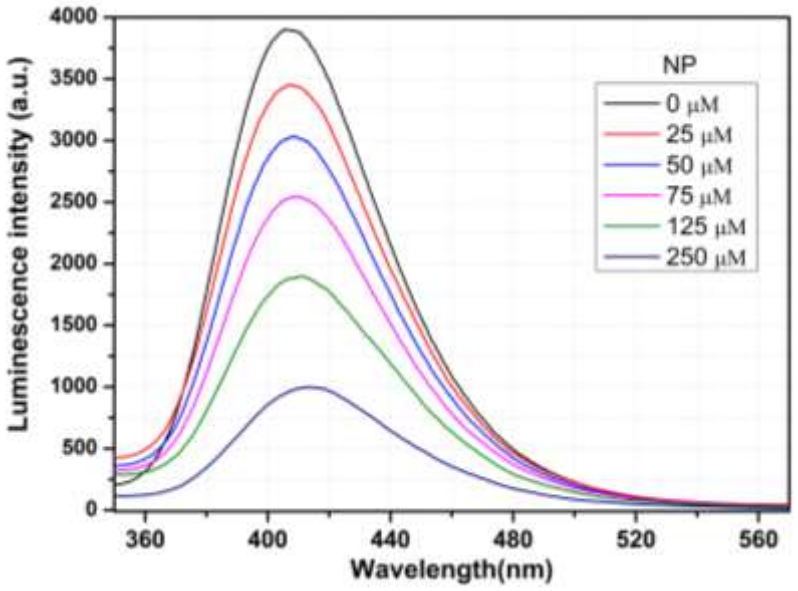

Fig. 5.51 Luminescence spectra of compound **5.1** dispersed in water upon incremental addition of NP solution (λ_{ex} = 300 nm). The final concentration of the NP in the medium is indicated in the legend.

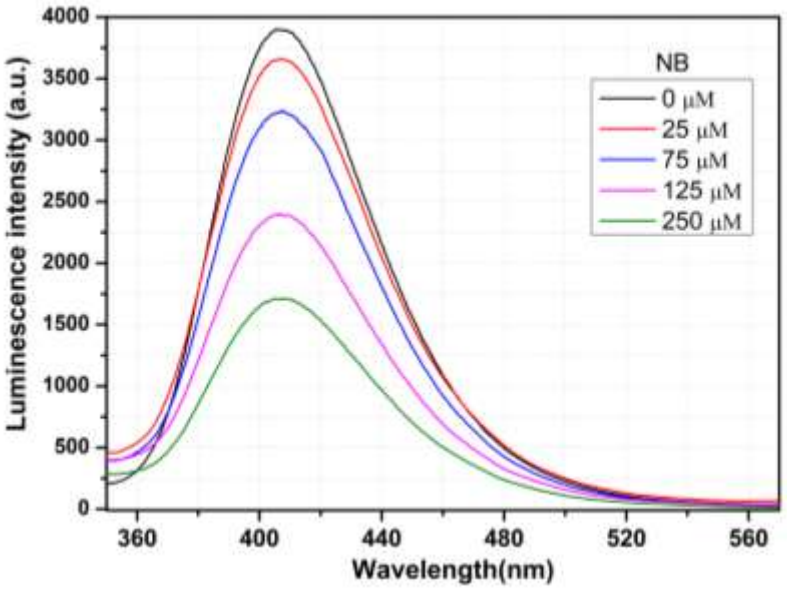

Fig. 5.52 Luminescence spectra of compound **5.1** dispersed in water upon incremental addition of NB solution (λ_{ex} = 300 nm). The final concentration of the NB in the medium is indicated in the legend.

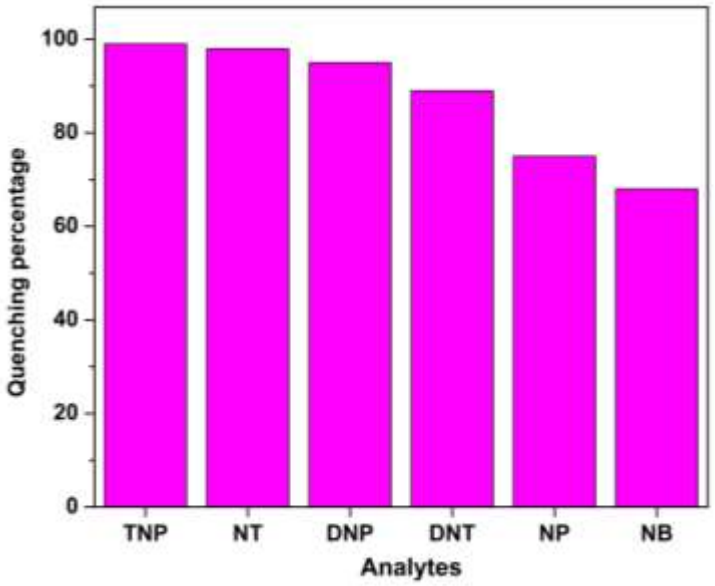

Fig. 5.53 Bar diagram represents luminescence quenching ability of compound **5.1** in water.

In the presence of parathion, azinphos-methyl, and endosulfan pesticide, compound **5.1** showed luminescence quenching of 84%, 81%, and 40%, respectively (see Fig. 5.54-5.56). In contrast, compound **5.1** displayed negligible luminescence quenching when exposed to other pesticides like malathion, dichlorvos, and diazinon (see Fig. 5.57-5.59).

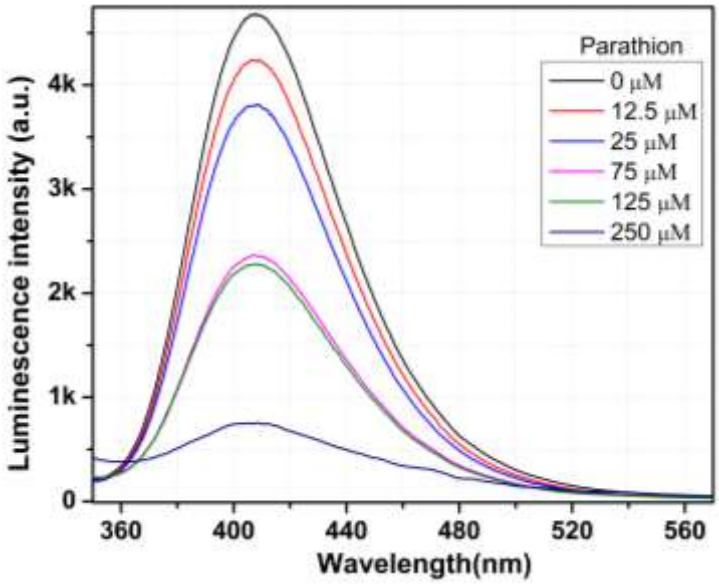

Fig. 5.54 Luminescence spectra of compound **5.1** dispersed in water upon incremental addition of parathion solution (λ_{ex} = 300 nm). The final concentration of the parathion in the medium is indicated in the legend.

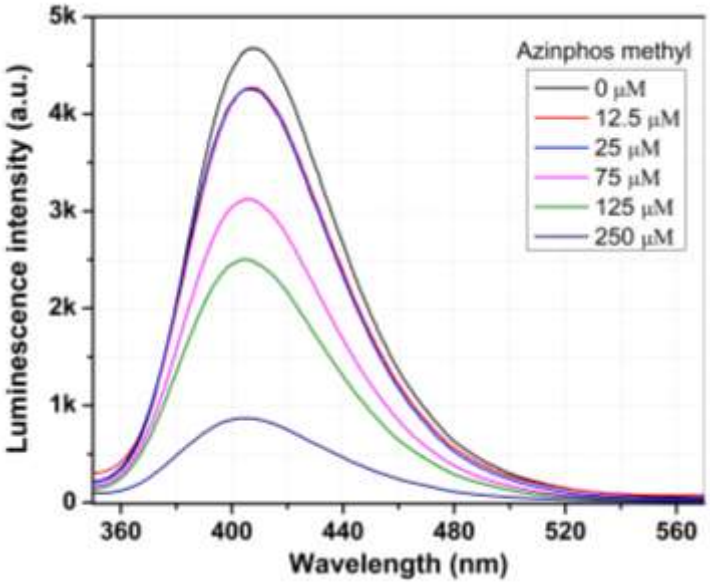

Fig. 5.55 Luminescence spectra of compound **5.1** dispersed in water upon incremental addition of azinphos-methyl solution (λ_{ex} = 300 nm). The final concentration of the azinphos-methyl in the medium is indicated in the legend.

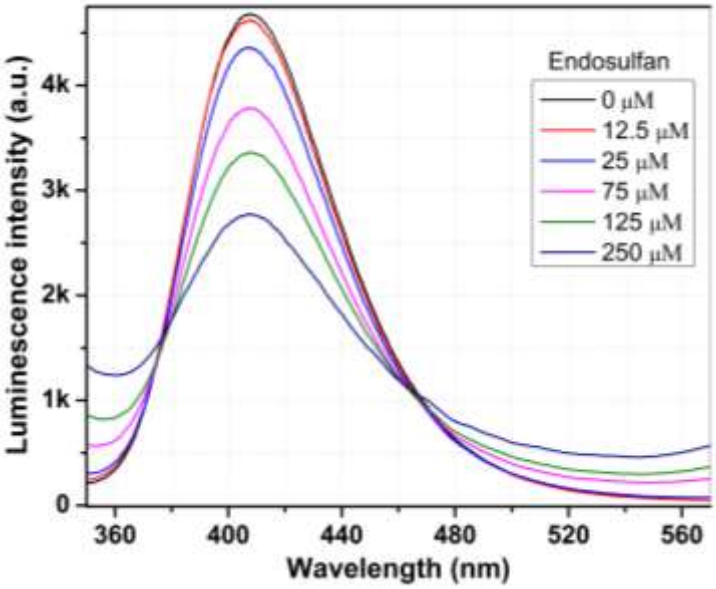

Fig. 5.56 Luminescence spectra of compound **5.1** dispersed in water upon incremental addition of endosulfan solution (λ_{ex} = 300 nm). The final concentration of the endosulfan in the medium is indicated in the legend.

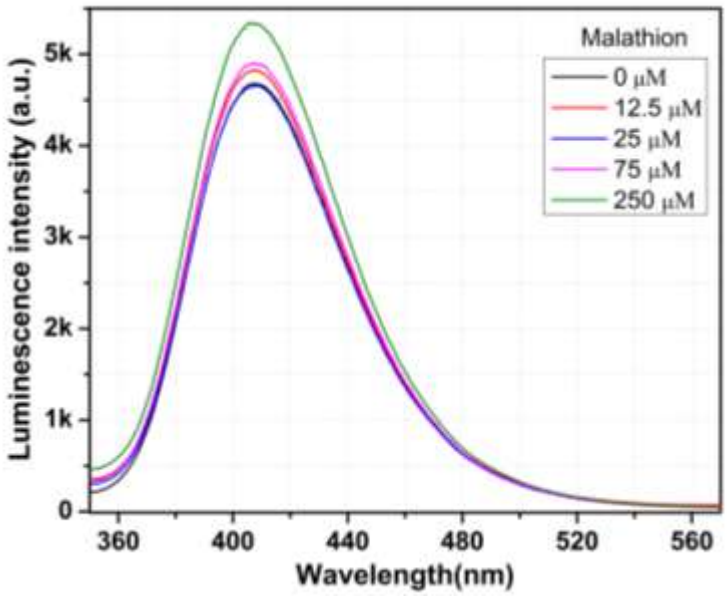

Fig. 5.57 Luminescence spectra of compound **5.1** dispersed in water upon incremental addition of malathion solution (λ_{ex} = 300 nm). The final concentration of the malathion in the medium is indicated in the legend.

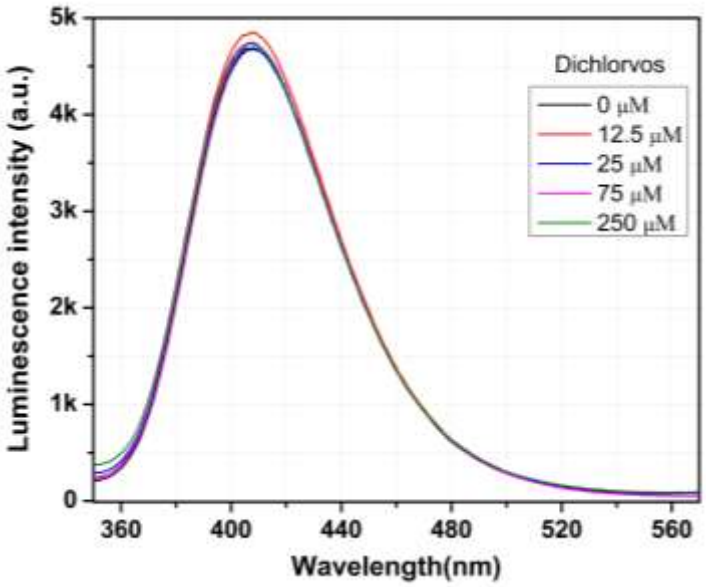

Fig. 5.58 Luminescence spectra of compound **5.1** dispersed in water upon incremental addition of dichlorvos solution (λ_{ex} = 300 nm). The final concentration of the dichlorvos in the medium is indicated in the legend.

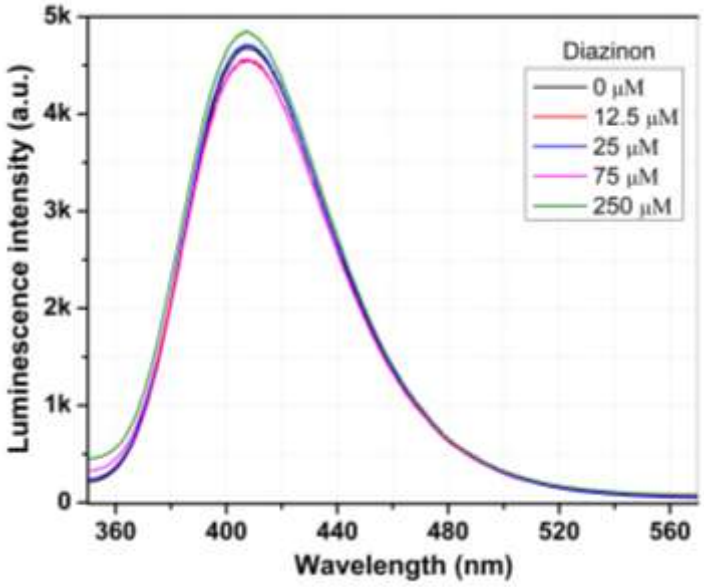

Fig. 5.59 Luminescence spectra of compound **5.1** dispersed in water upon incremental addition of diazinon solution (λ_{ex} = 300 nm). The final concentration of the diazinon in the medium is indicated in the legend.

To investigate the performance of compound **5.2** in detecting a very small amount of metal ions, emission intensity alternation based titrations were carried out through the regular mixing of analytes (metal ions) to the water dispersion of the compound. The variation in emission intensity along with the cumulative accumulation of Al^{3+} (upto 62.50 μM) in the compound is presented in Fig. 5.60. The emission of compound **5.2** was quenched about 43% of the starting intensity upon the accumulation of the Al^{3+}.

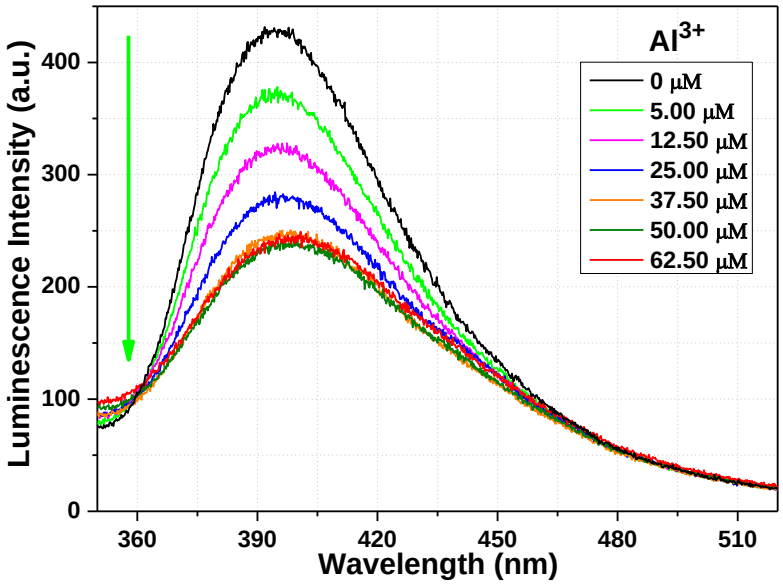

Fig. 5.60 Luminescence spectra of water dispersion of compound **5.2** upon gradual accumulation of aqueous solution of Al^{3+} ions (λ_{ex} = 300 nm). Ultimate Al^{3+} ions concentration of the system is presented in the legend.

Analogous luminescence intensity alternation based titrations of compound **5.2** were also executed with other cations such as Fe^{3+}, Na^{+}, K^{+}, Mg^{2+}, Mn^{2+}, Pb^{2+}, Cr^{3+}, Hg^{2+}, Cu^{2+}, Ni^{2+}, Co^{2+}, Fe^{2+}, Zn^{2+} and Cd^{2+} ions (see Fig. 5.61-5.74). In case of Fe^{3+} and Cr^{3+}, significant amount (68% and 58%) of quenching was observed. Hg^{2+} and Cu^{2+} also showed quenching behaviour. But, in presence of other metal ions either the luminescence intensity remained unchanged or decreased to a small magnitude. The variations of emission intensity centred at 395 nm in the presence of all the cations upto the accumulation of 62.50 μM cations is shown in Fig. 5.75.

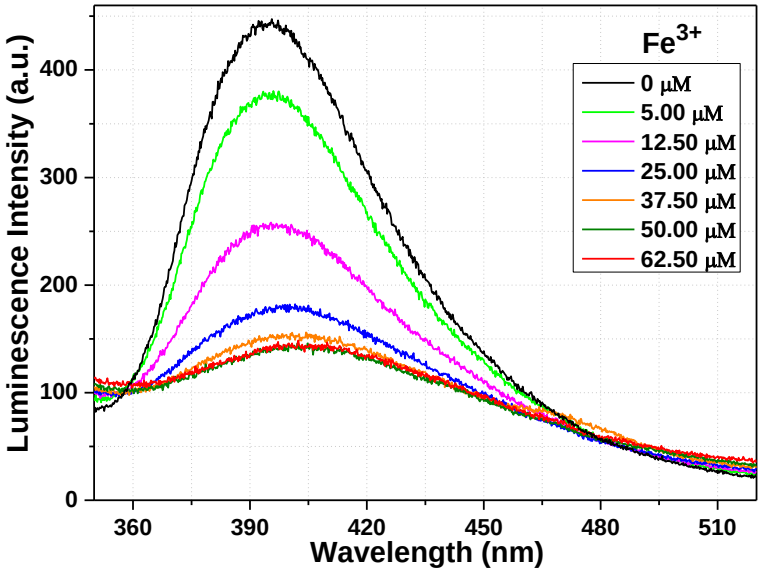

Fig. 5.61 Luminescence spectra of compound **5.2** dispersed in water upon incremental addition of water solution of Fe^{3+} ions (λ_{ex} = 300 nm). Final concentration of Fe^{3+} ions in the medium is indicated in the legend.

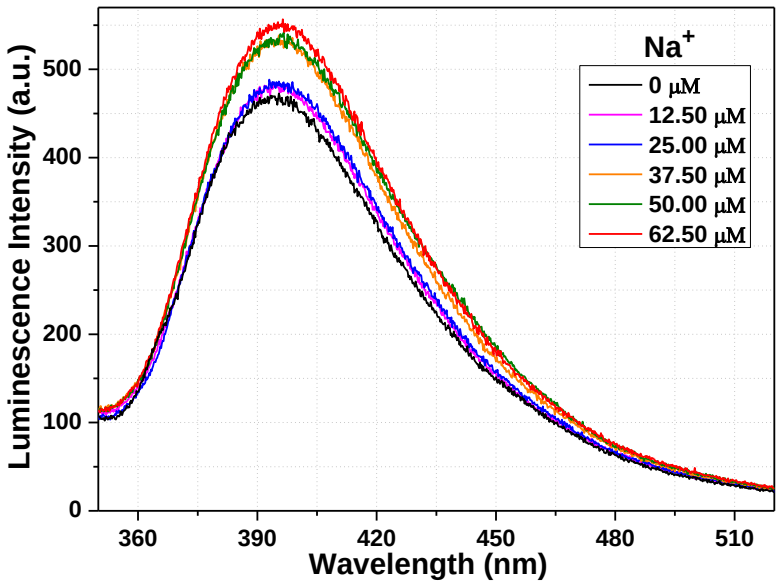

Fig. 5.62 Luminescence spectra of compound **5.2** dispersed in water upon incremental addition of water solution of Na^+ ions (λ_{ex} = 300 nm). Final concentration of Na^+ ions in the medium is indicated in the legend.

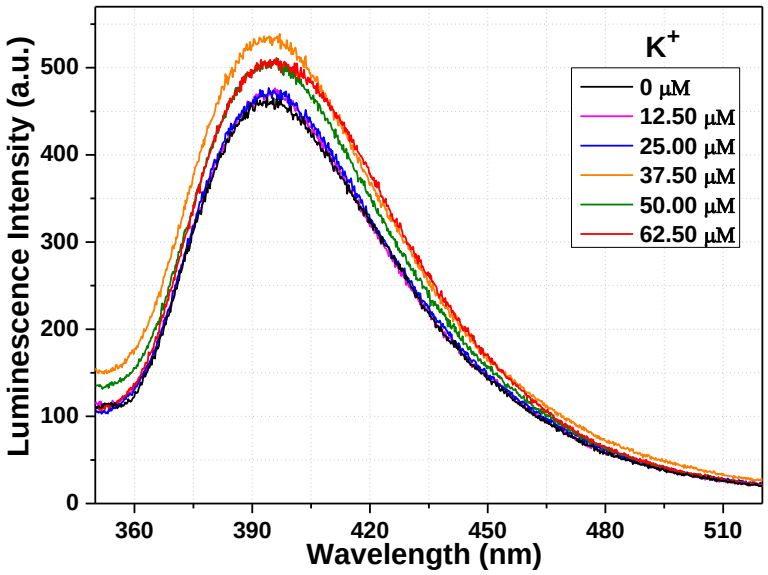

Fig. 5.63 Luminescence spectra of compound **5.2** dispersed in water upon incremental addition of water solution of K^+ ions (λ_{ex} = 300 nm). Final concentration of K^+ ions in the medium is indicated in the legend.

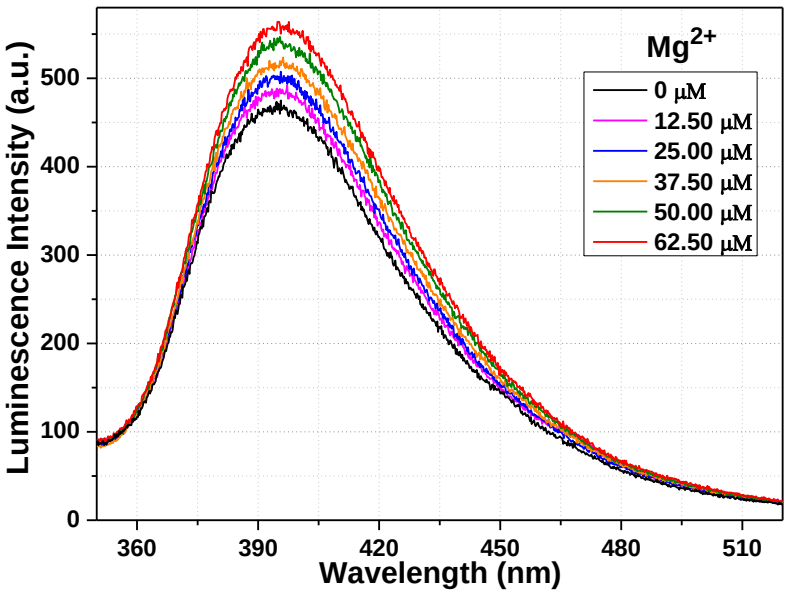

Fig. 5.64 Luminescence spectra of compound **5.2** dispersed in water upon incremental addition of water solution of Mg^{2+} ions (λ_{ex} = 300 nm). Final concentration of Mg^{2+} ions in the medium is indicated in the legend.

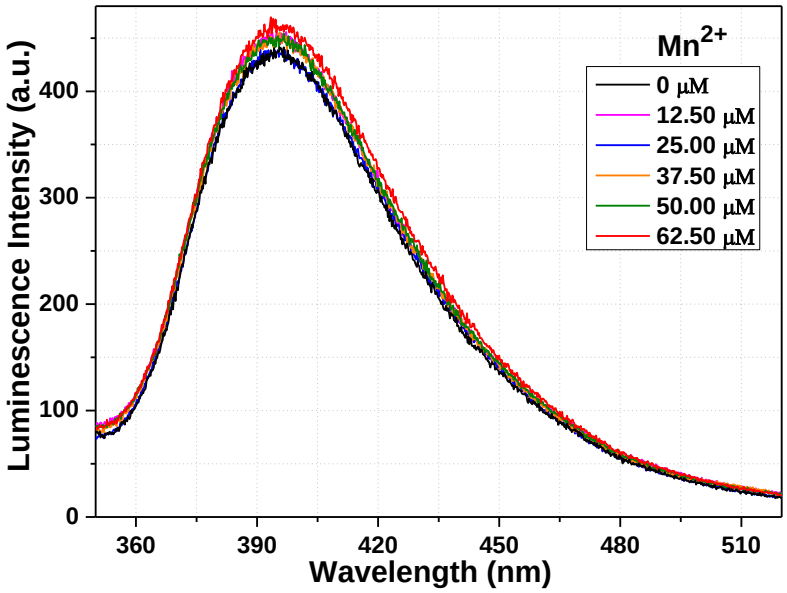

Fig. 5.65 Luminescence spectra of compound **5.2** dispersed in water upon incremental addition of water solution of Mn^{2+} ions (λ_{ex} = 300 nm). Final concentration of Mn^{2+} ions in the medium is indicated in the legend.

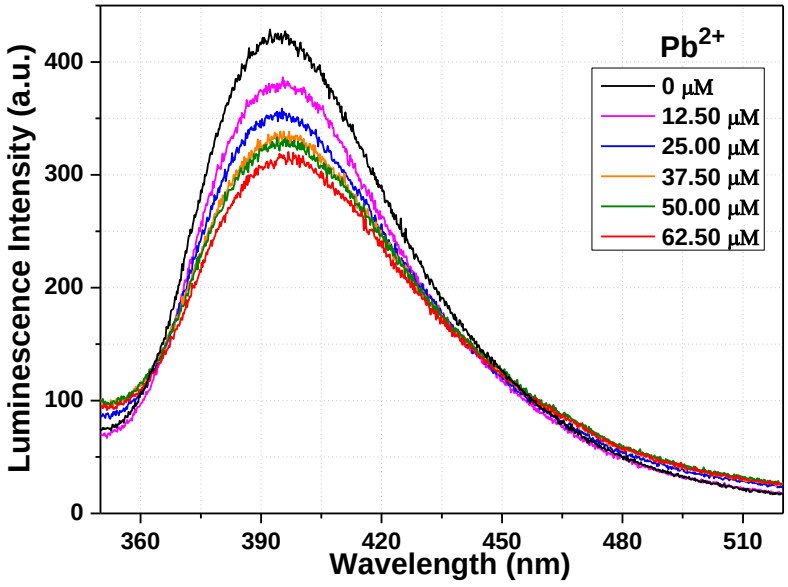

Fig. 5.66 Luminescence spectra of compound **5.2** dispersed in water upon incremental addition of water solution of Pb^{2+} ions (λ_{ex} = 300 nm). Final concentration of Pb^{2+} ions in the medium is indicated in the legend.

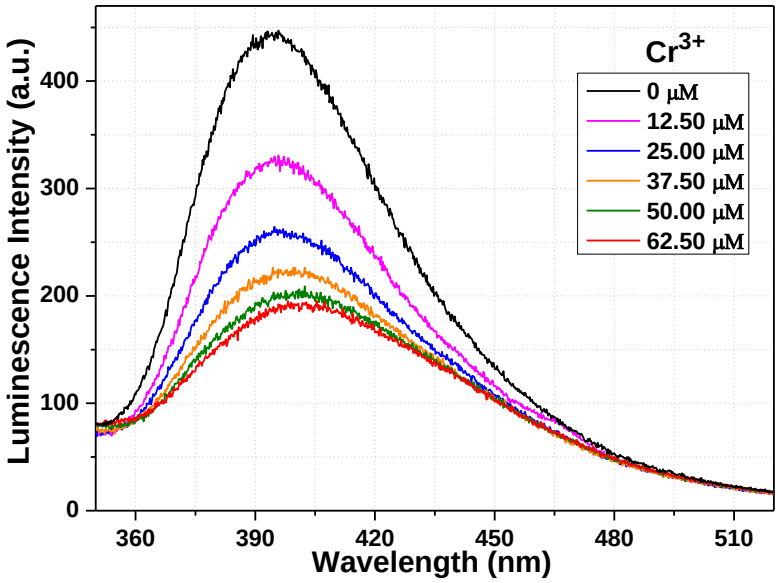

Fig. 5.67 Luminescence spectra of compound **5.2** dispersed in water upon incremental addition of water solution of Cr^{3+} ions (λ_{ex} = 300 nm). Final concentration of Cr^{3+} ions in the medium is indicated in the legend.

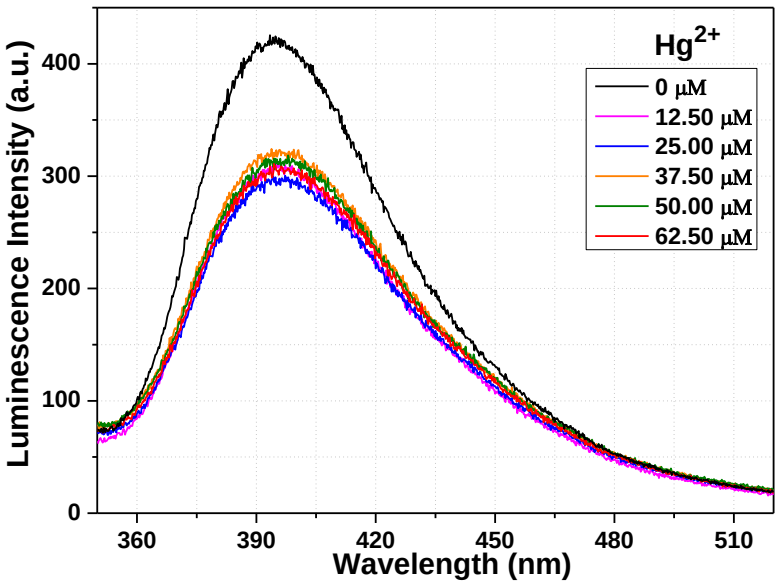

Fig. 5.68 Luminescence spectra of compound **5.2** dispersed in water upon incremental addition of water solution of Hg^{2+} ions (λ_{ex} = 300 nm). Final concentration of Hg^{2+} ions in the medium is indicated in the legend.

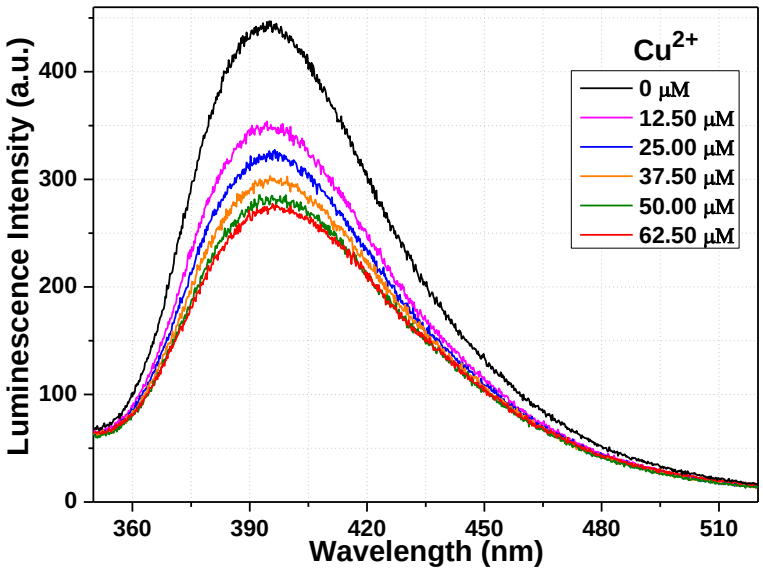

Fig. 5.69 Luminescence spectra of compound **5.2** dispersed in water upon incremental addition of water solution of Cu^{2+} ions (λ_{ex} = 300 nm). Final concentration of Cu^{2+} ions in the medium is indicated in the legend.

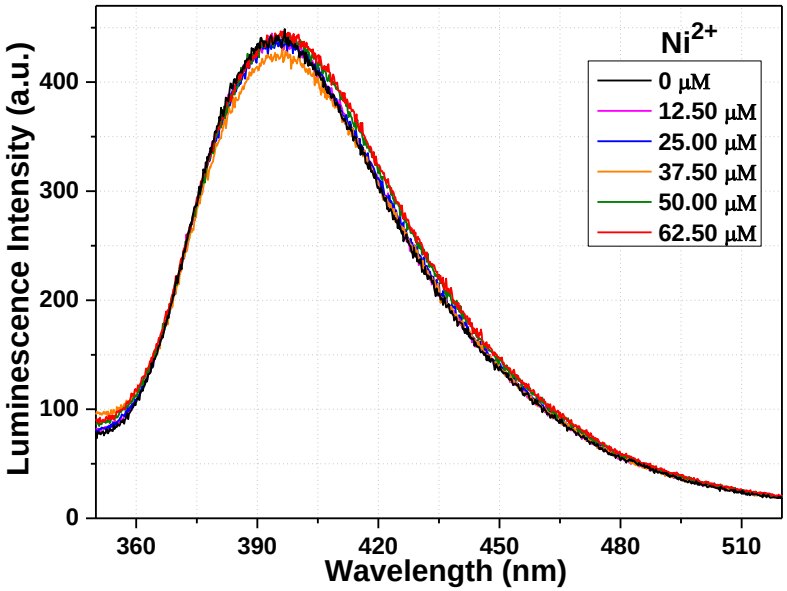

Fig. 5.70 Luminescence spectra of compound **5.2** dispersed in water upon incremental addition of water solution of Ni^{2+} ions (λ_{ex} = 300 nm). Final concentration of Ni^{2+} ions in the medium is indicated in the legend.

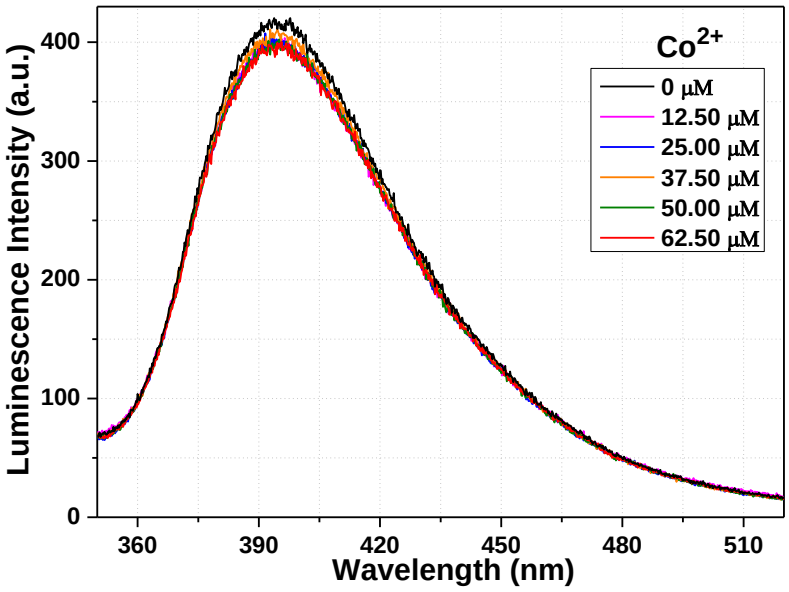

Fig. 5.71 Lu minescence spectra of compound **5.2** dispersed in water upon incremental addition of water solution of Co^{2+} ions (λ_{ex} = 300 nm). Final concentration of Co^{2+} ions in the medium is indicated in the legend.

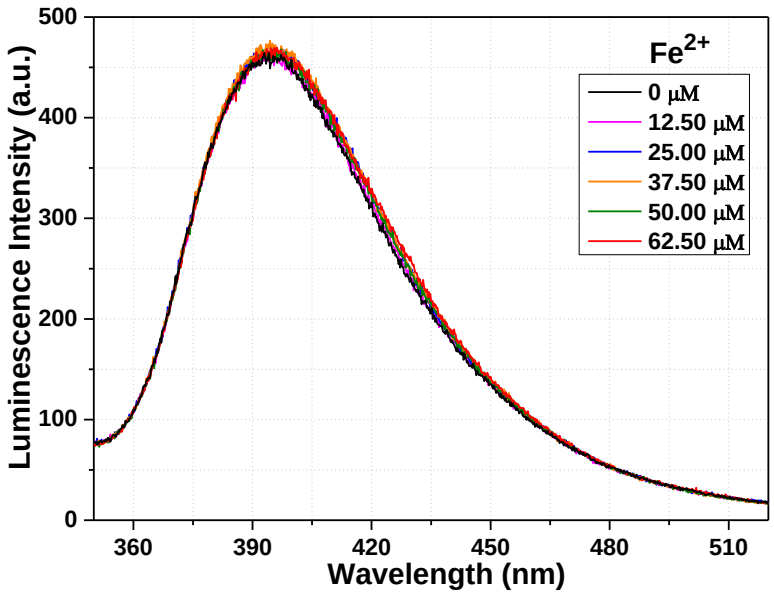

Fig. 5.72 Luminescence spectra of compound **5.2** dispersed in water upon incremental addition of water solution of Fe^{2+} ions (λ_{ex} = 300 nm). Final concentration of Fe^{2+} ions in the medium is indicated in the legend.

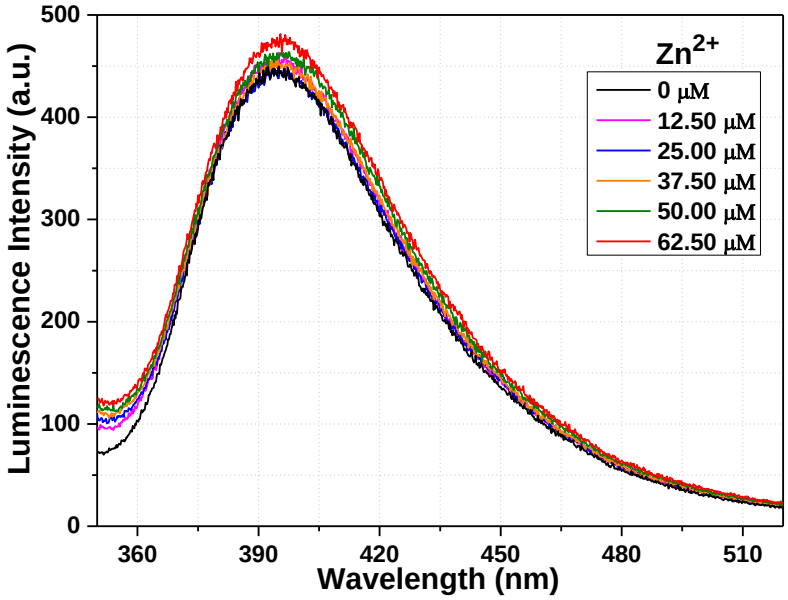

Fig. 5.73 Luminescence spectra of compound **5.2** dispersed in water upon incremental addition of water solution of Zn^{2+} ions (λ_{ex} = 300 nm). Final concentration of Zn^{2+} ions in the medium is indicated in the legend.

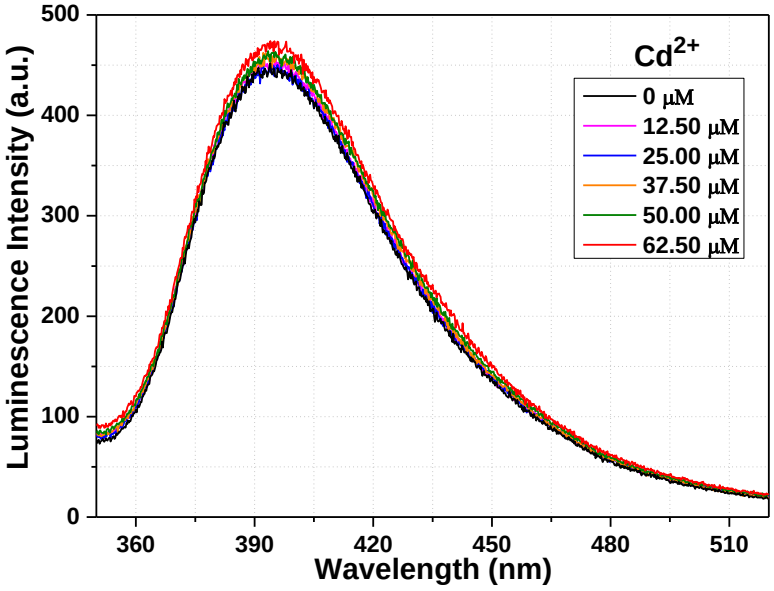

Fig. 5.74 Luminescence spectra of compound **5.2** dispersed in water upon incremental addition of water solution of Cd^{2+} ions (λ_{ex} = 300 nm). Final concentration of Cd^{2+} ions in the medium is indicated in the legend.

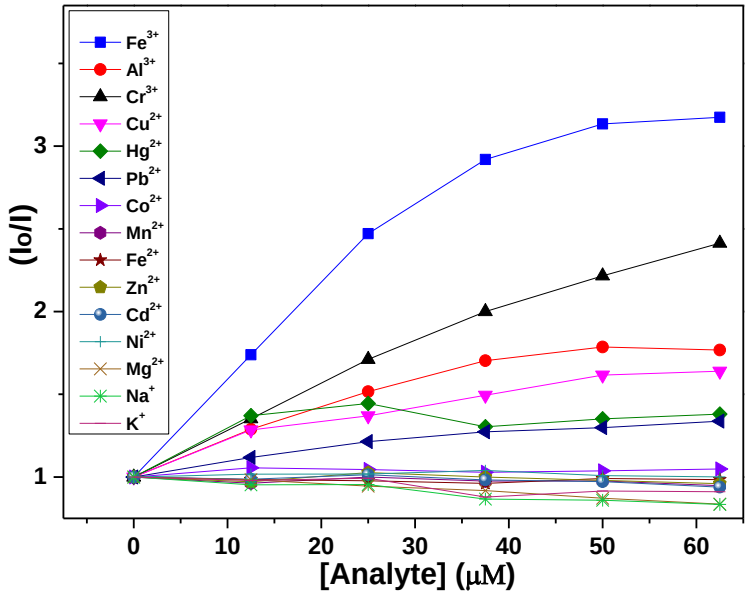

Fig. 5.75 Depiction of fractional of luminescence intensity plot of compound **5.2** (at 395 nm) *vs* concentration of analytes. Emission intensity in absence and presence of analytes represented as I_0 and I, respectively.

The non-linear variation of (I_o/I) with the concentration of the analytes in case of Fe^{3+}, Al^{3+} and Cr^{3+} (see Fig. 5.75) indicated that the compound **5.2** is very much selective luminescence based detector for Fe^{3+}, Al^{3+} and Cr^{3+} ions. The LODs were found to be 312, 408 and 280 nM for Fe^{3+}, Al^{3+} and Cr^{3+} ions respectively (see Fig. 5.76-5.78). The obtained K_{SV} value is 3.31 $\times 10^4$, 2.36 $\times 10^4$ and 3.53 $\times 10^4$ M^{-1} for Fe^{3+}, Al^{3+} and Cr^{3+} ions respectively based on the experimental data fitting (upto 5 μM) applying S−V equation (see Fig. 5.79).

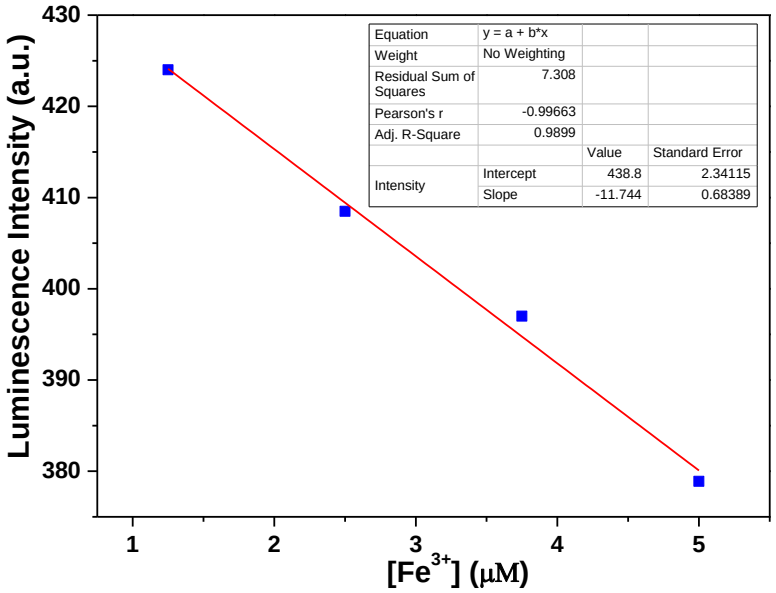

Fig. 5.76 Plot of luminescence intensity *vs* concentration of Fe^{3+}.

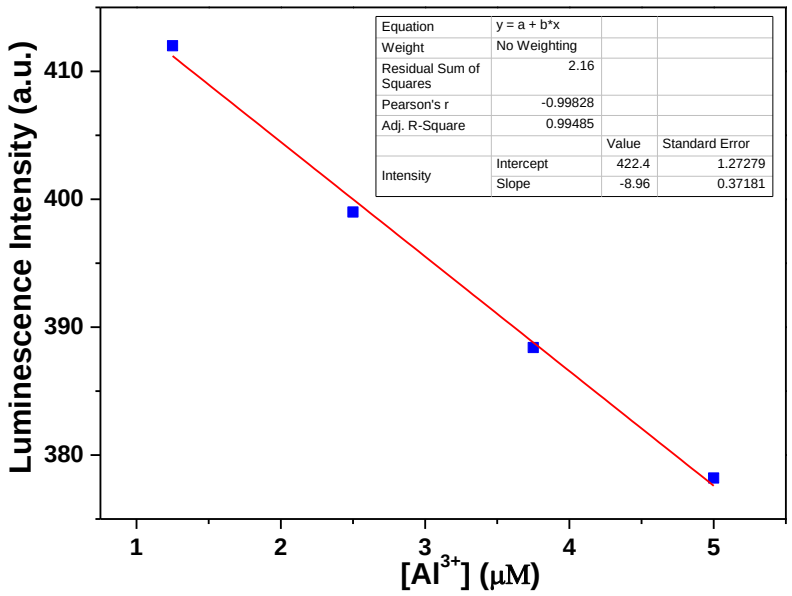

Fig. 5.77 Plot of luminescence intensity *vs* concentration of Al^{3+}.

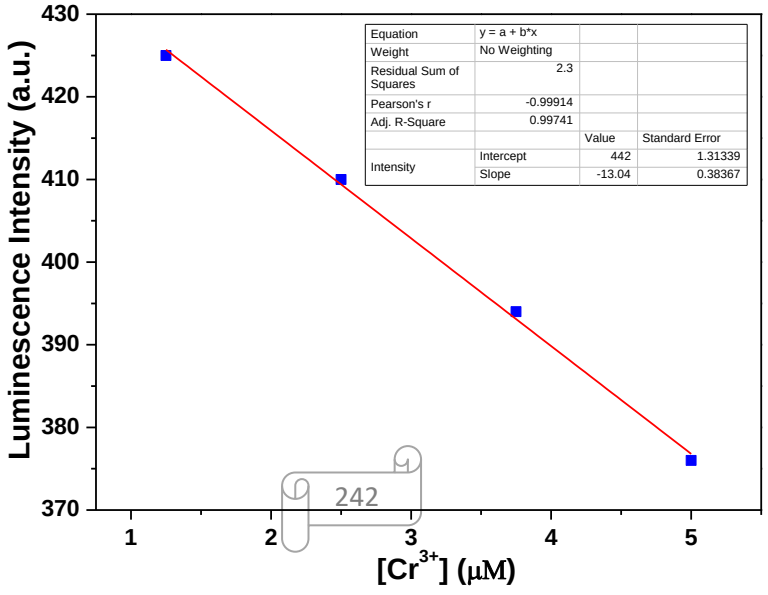

Fig. 5.78 Plot of luminescence intensity *vs* concentration of Cr^{3+}.

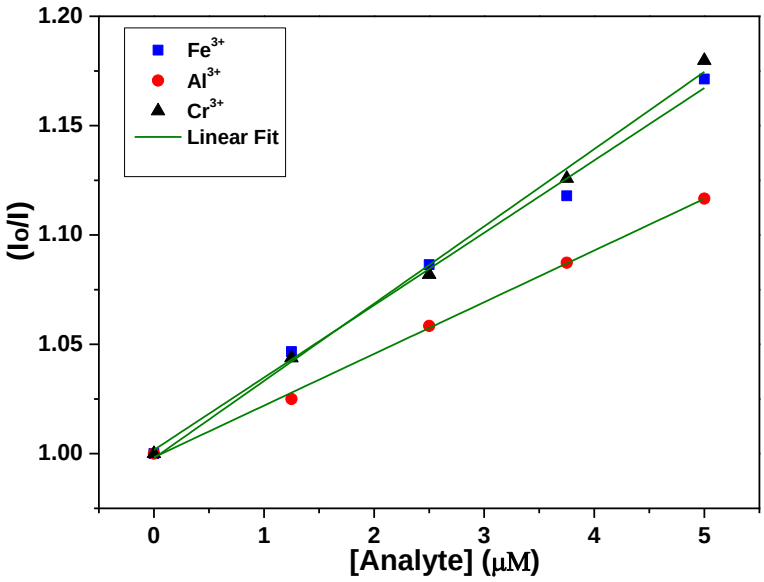

Fig. 5.79 Plot of I_0/I of compound **4.2** (at 395 nm) vs concentration of [Analyte] in lower concentration range of analyte. I_0 and I are luminescence intensity in absence and presence of analyte, respectively.

We have also conducted luminescence-based titration of compound **5.2** by adding various nitro explosives. Upon the addition of TNP, DNP, NP, NT, DNT, and NB, compound **5.2** exhibited luminescence quenching

efficiencies of 98%, 96%, 91%, 89%, 63%, and 59%, respectively (see Fig.5.80-5.85). The quenching efficiencies of the selected nitro compounds follow the order: TNP ≈ DNP > NP > NT > DNT > NB (see Fig. 5.86).

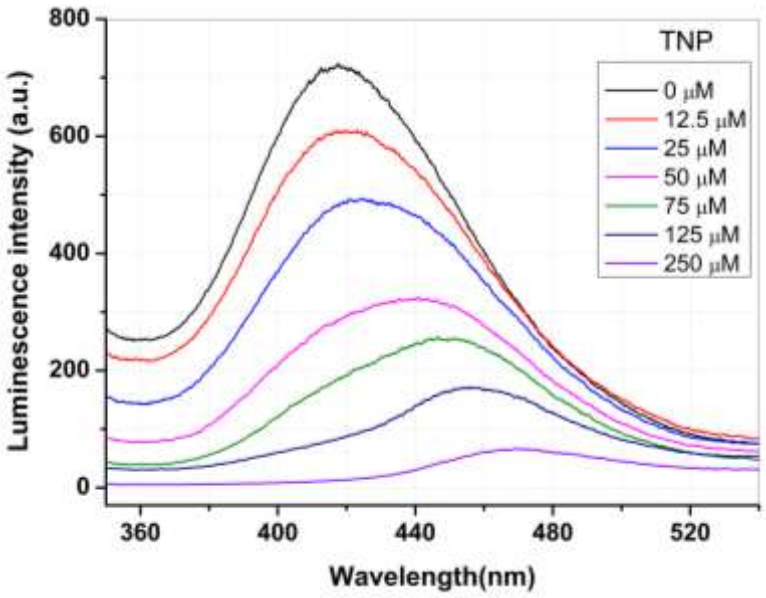

Fig. 5.80 Luminescence spectra of compound **5.2** dispersed in water upon incremental addition of TNP solution (λ_{ex} = 300 nm). The final concentration of the TNP in the medium is indicated in the legend.

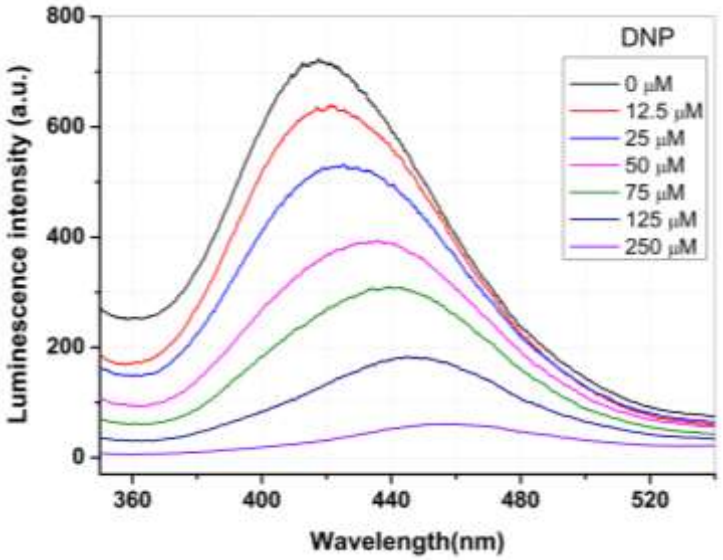

Fig. 5.81 Luminescence spectra of compound **5.2** dispersed in water upon incremental addition of DNP solution (λ_{ex} = 300 nm). The final concentration of the DNP in the medium is indicated in the legend.

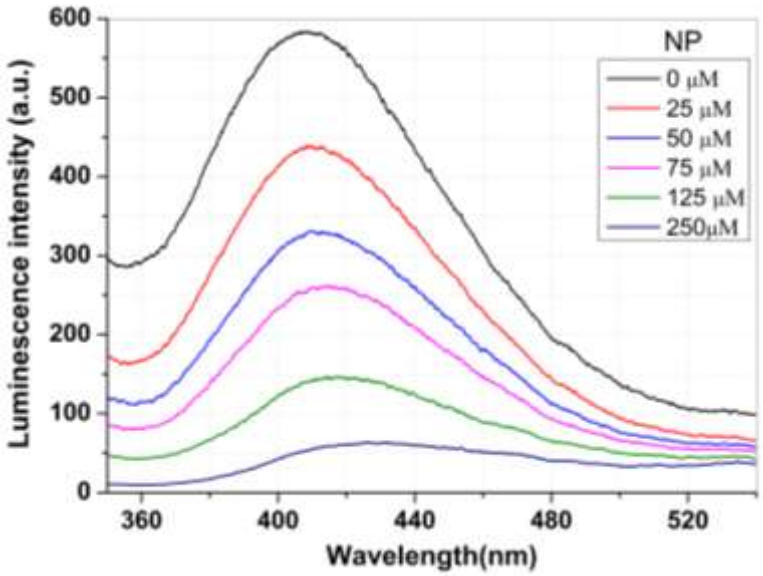

Fig. 5.82 Luminescence spectra of compound **5.2** dispersed in water upon incremental addition of NP solution (λ_{ex} = 300 nm). The final concentration of the NP in the medium is indicated in the legend.

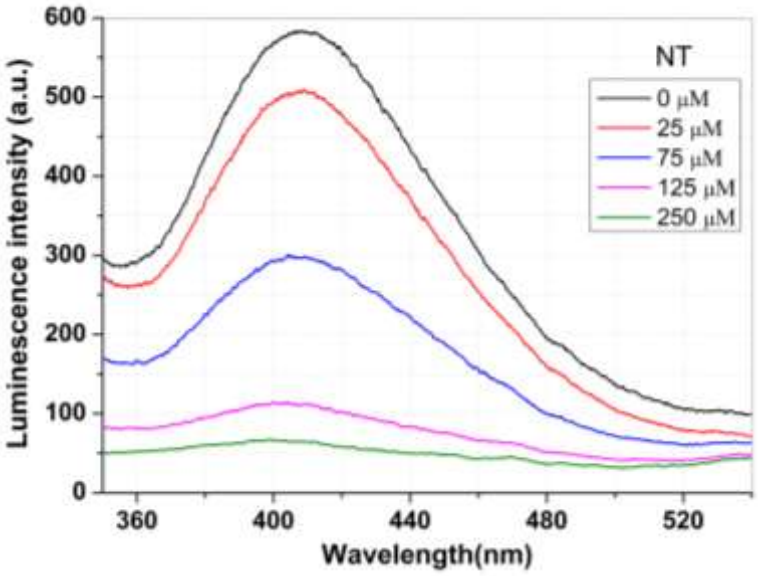

Fig. 5.83 Luminescence spectra of compound **5.2** dispersed in water upon incremental addition of NT solution (λ_{ex} = 300 nm). The final concentration of the NT in the medium is indicated in the legend.

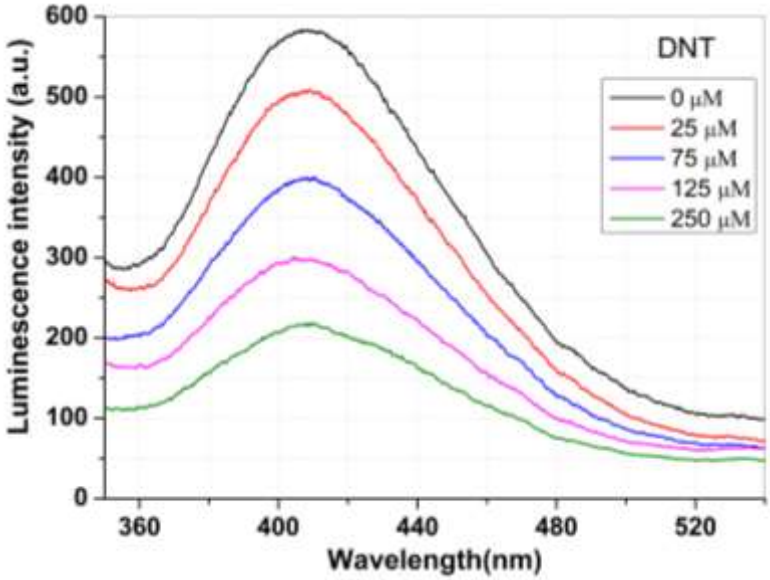

Fig. 5.84 Luminescence spectra of compound **5.2** dispersed in water upon incremental addition of DNT solution (λ_{ex} = 300 nm). The final concentration of the DNT in the medium is indicated in the legend.

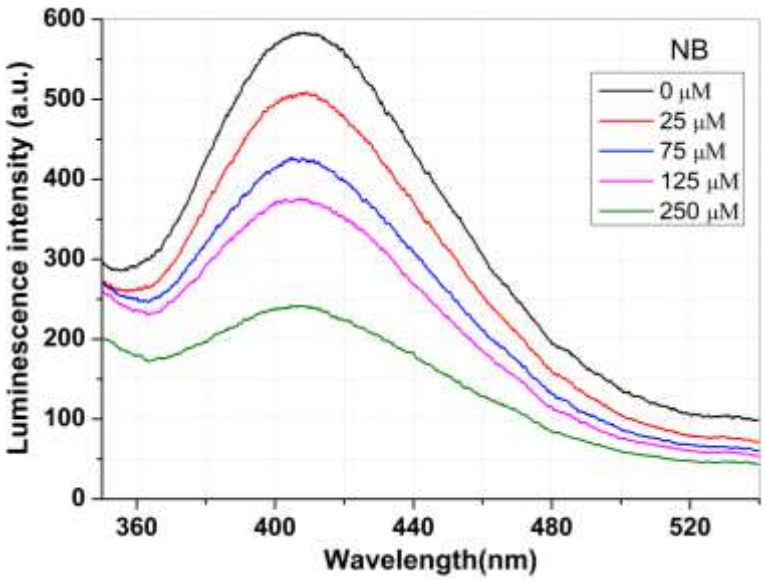

Fig. 5.85 Luminescence spectra of compound **5.2** dispersed in water upon incremental addition of NB solution (λ_{ex} = 300 nm). The final concentration of the NB in the medium is indicated in the legend.

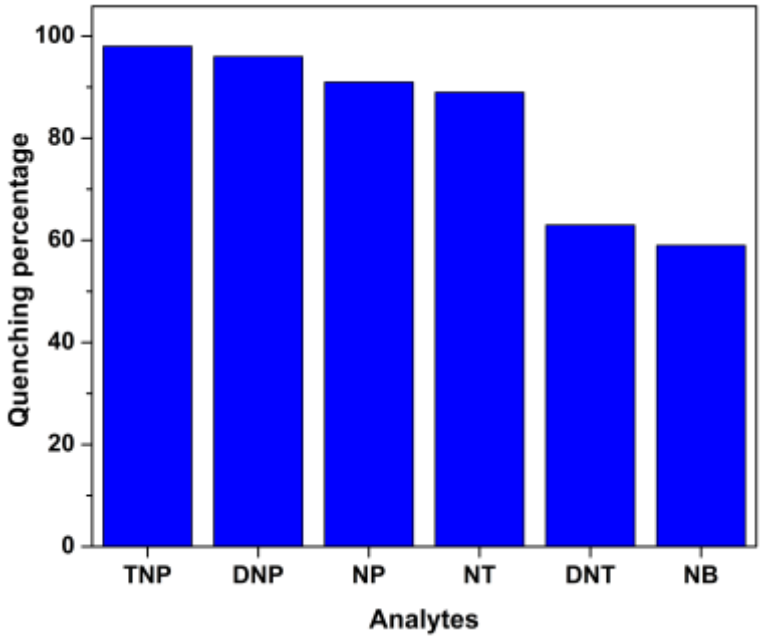

Fig. 5.86 Bar diagram represents luminescence quenching ability of compound **5.2** in water.

Interestingly, when azinphos-methyl pesticide was added to compound **5.2**, it exhibited luminescence turn-on behavior, while parathion induced luminescence quenching. Other pesticides are not capable to show considerable luminescence response (see Fig. 5.87-5.92).

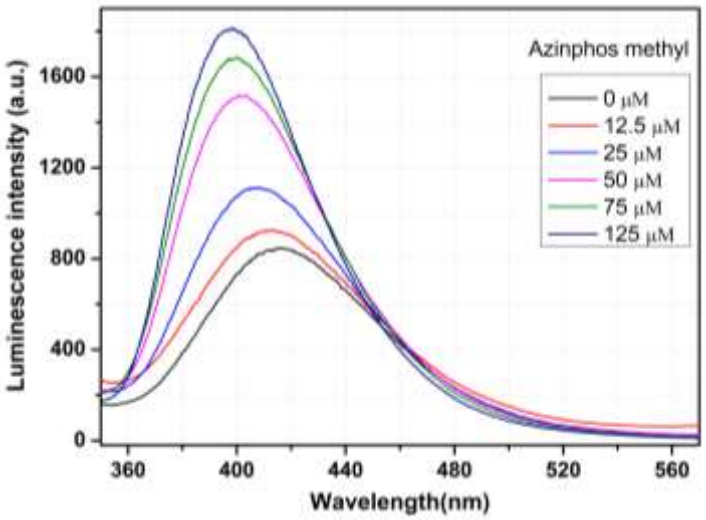

Fig. 5.87 Luminescence spectra of compound **5.2** dispersed in water upon incremental addition of azinphos-methyl solution (λ_{ex} = 300 nm). The final concentration of the azinphos-methyl in the medium is indicated in the legend.

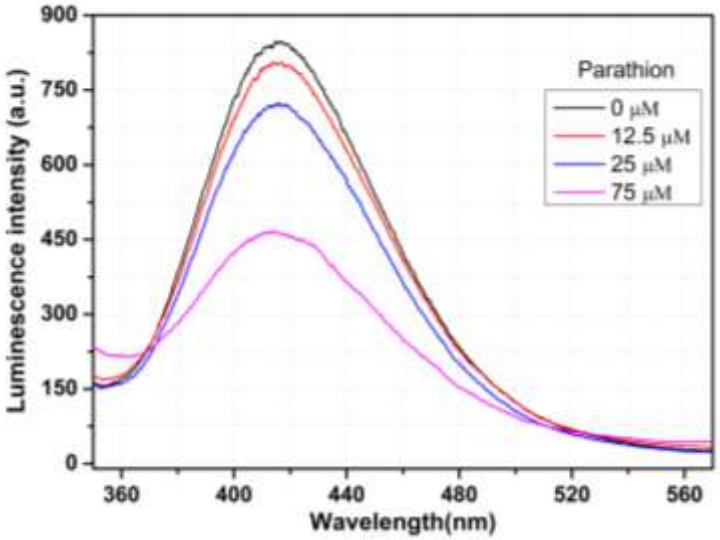

Fig. 5.88 Luminescence spectra of compound **5.2** dispersed in water upon incremental addition of parathion solution (λ_{ex} = 300 nm). The final concentration of the parathion in the medium is indicated in the legend.

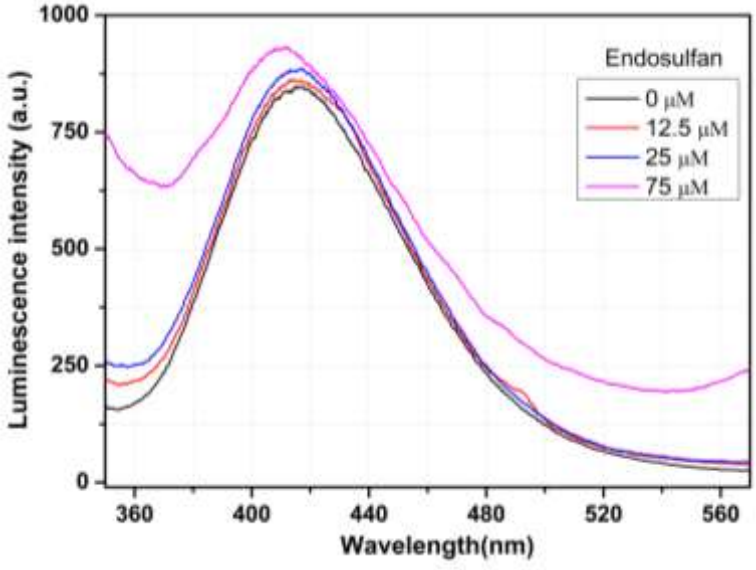

Fig. 5.89 Luminescence spectra of compound **5.2** dispersed in water upon incremental addition of endosulfan solution (λ_{ex} = 300 nm). The final concentration of the endosulfan in the medium is indicated in the legend.

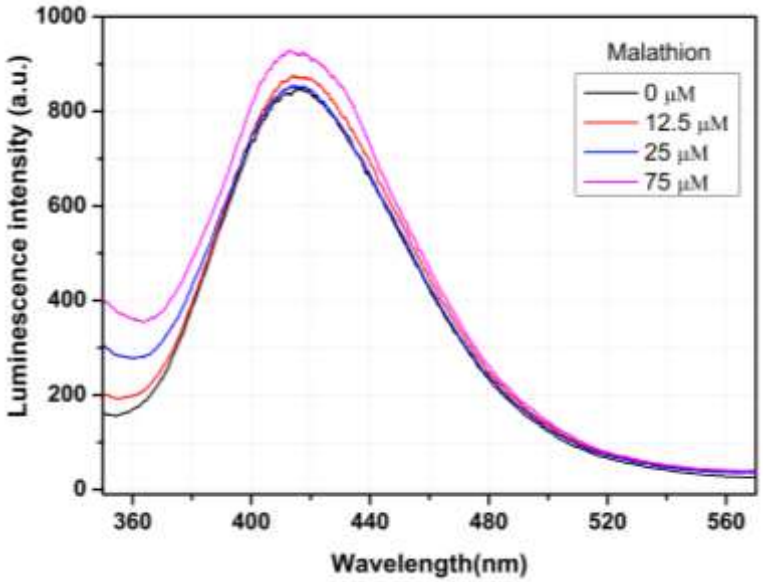

Fig. 5.90 Luminescence spectra of compound **5.2** dispersed in water upon incremental addition of malathion solution (λ_{ex} = 300 nm). The final concentration of the malathion in the medium is indicated in the legend.

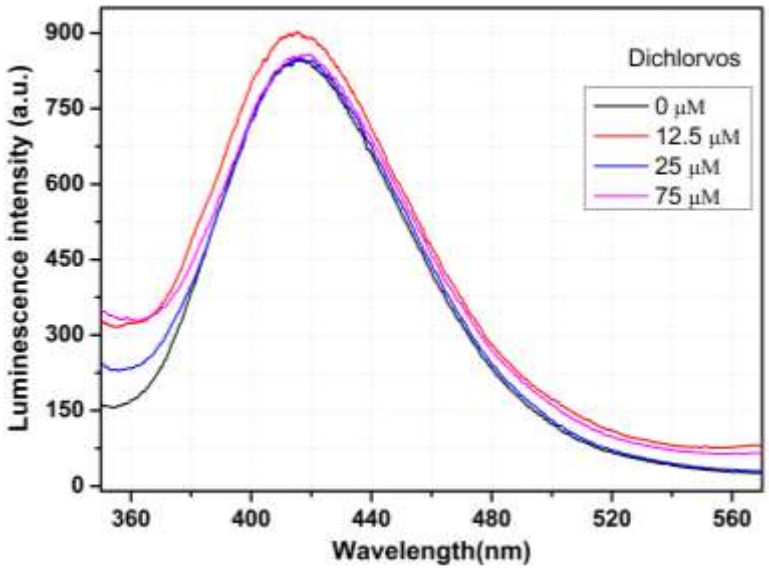

Fig. 5.91 Luminescence spectra of compound **5.2** dispersed in water upon incremental addition of dichlorvos solution (λ_{ex} = 300 nm). The final concentration of the dichlorvos in the medium is indicated in the legend.

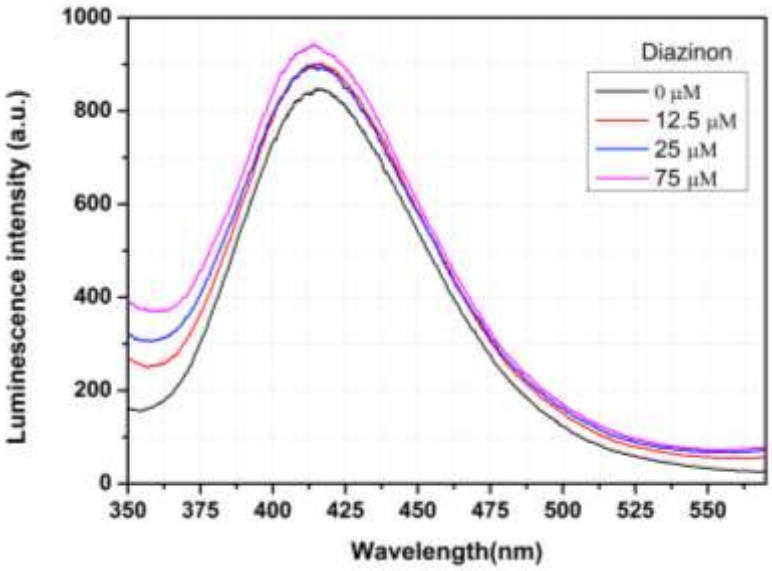

Fig. 5.92 Luminescence spectra of compound **5.2** dispersed in water upon incremental addition of diazinon solution (λ_{ex} = 300 nm). The final concentration of the diazinon in the medium is indicated in the legend.

The change in luminescence intensity of a metal organic compound (MOC) due to the interaction with added metal ions depend on the possibility of the inter molecular connections between compounds and metal ions. The analyte metal ions find a suitable binding site in the MOC and form a bond with the ligands. Consequently, the rigidity of the structure of the MOC increases further. Increase in structural rigidity results in the enhancement of luminesce intensity (turn-on). However, in several cases despite the increase in structural rigidity luminescence quenching is observed. This is due to the favourable LMCT and/or MLCT transitions from exposed donor sites (Lewis base) of compounds to the metal ions (Lewis acid) or vice versa. The LMCT or MLCT provides an additional path to the non-radiative decay of excited state energy which causes the quenching of luminescence intensity.

We have taken absorption spectra of compound **5.1** with the addition of Al^{3+}. Upon the accumulation of Al^{3+}, an isosbestic point was observed at ~305 nm which validates that complexation phenomenon between the compound **5.1** and the cations (Fig. 5.93). Al^{3+} ions due to high charge to radius ratio, it can bind the oxygen [O(2)] orginated from phenolic–OH group of the phenyl ring of compound **5.1** through metal-ligand interactions with higher covalent character. Due to this covalent nature results in the 33 nm blue shift in the luminescence peak position. This interaction along with a possible weak interaction with nitrogen [N(3)] of the compound also contributes to the increase in the rigidity of the compound resulting in the increase in luminescence intensity (see scheme 4). On the other hand, the luminescence quenching of the compound in case of Fe^{3+} ions was due to the interactions of the phonolic–OH [O(2)] with higher ionic character and nitrogen atom [N(3)] with the Fe^{3+}

ions (see scheme 4). In this case, the predominant LMCT process due to availability of vacant d- orbital on Fe^{3+} ion is responsible for the observed luminescence quenching.

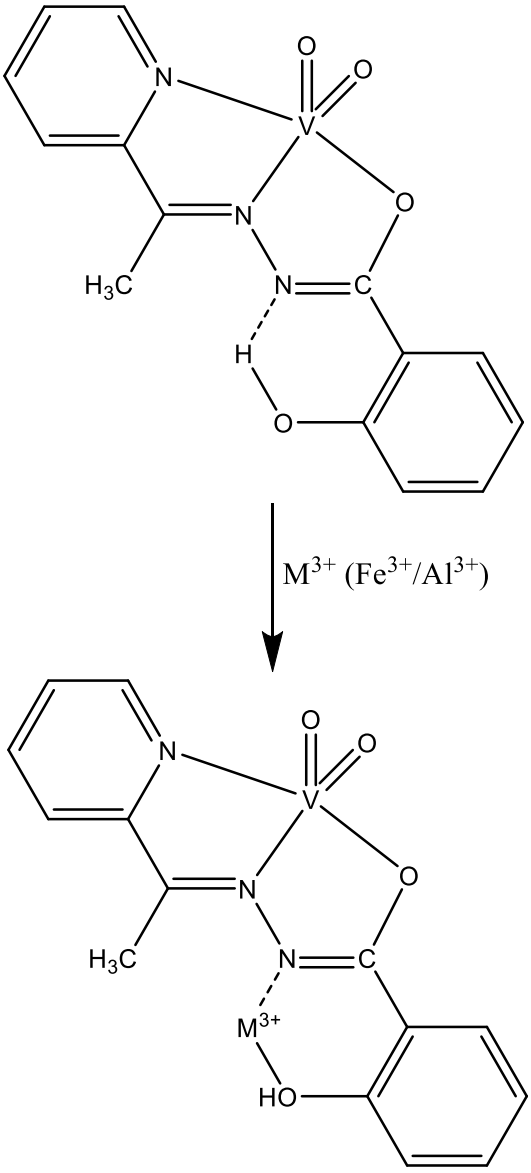

Scheme 4. Mode of interaction between the compound **5.1** and Al^{3+}/Fe^{3+}.

For compound **5.2**, the disruption of stronger intra-molecular hydrogen bonds and subsequent weaker interaction with the analyte metal ions (Fe^{3+}, Al^{3+}, Cr^{3+} and Cu^{2+}) causes relaxation of molecular rigidity (see Scheme 5). The moderate luminescence quenching (upto 62.50 µM) in this case seems to be due to the decreased molecular rigidity and LMCT transitions.

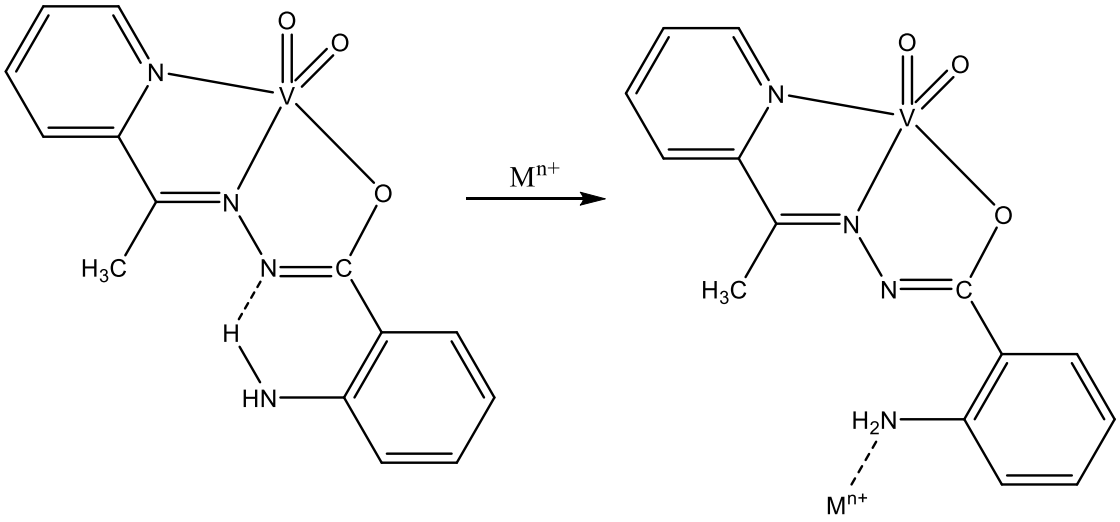

Scheme 5. Mode of interaction between the compound **5.2** and metal ions (M^{3+}).

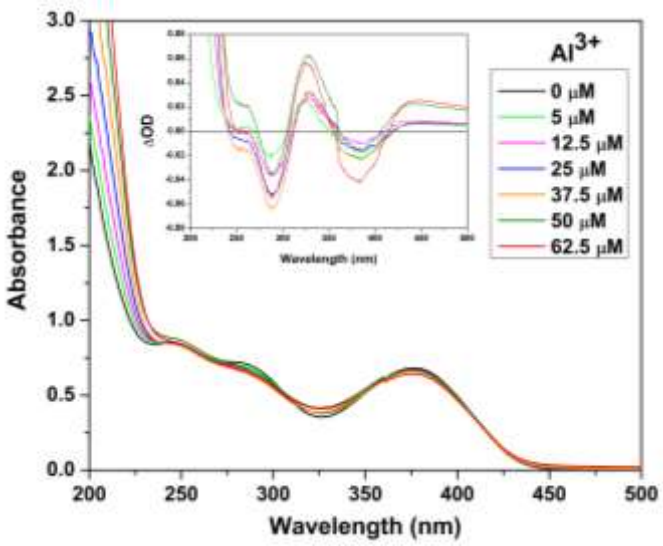

Fig. 5.93 Absorption spectra of compound **5.1** with the addition of Al^{3+}.

5.3.9 Luminescence Lifetime measurements. The time dependent luminescence intensity decay profile of the two compounds and after the addition of Al^{3+} and Fe^{3+} ions were measured using TCSPC technique. The decay curves fitting were performed using a bi-exponential function and the outcomes are shown in table 5.4. It is clearly visible that the decay profile of the compound **5.1** at emission wavelength 375 nm gets altered to a good extent in presence Al^{3+} ions (Fig. 5.94). The average life time values were found to be increased from 0.69 ns to 0.92 ns (62.5 μM). The increased life time value support the luminescence turn-on effect through the reduction of non-radiative pathways by increasing the structural rigidity. On the other hand, at the emission wavelength 408 nm the decay part of the profile showed a single exponential decay of 4.5 ns. In presence of Fe^{3+} ions, the

lifetime decreased gradually; at higher concentrations of Fe^{3+} the decay showed an additional fast component of 0.1 ns (Fig. 5.95, Table 5.4). The average lifetime was observed to be reduced from 4.5 ns to 1.0 ns (62.5 μM). This largely decreased value of lifetime supports the increased non-radiative pathways via LMCT from the organic ligands to Fe^{3+} ions. For compound **5.2** at emission wavelength 395 nm, in presences of Al^{3+} and Fe^{3+} ions, the life time value decreased from 4.8 ns to 3.12 ns (62.5 μM) and 1.2 ns (47 μM) respectively (Fig. 5.96 and Fig. 5.97, and Table 5.4). The reduction of structural rigidity through the disruption of intra-ligand hydrogen bonds, favoured the non-radiative decay pathways. This probably, is the main factor for the lower value of lifetime in presence of the metal ions (Al^{3+} and Fe^{3+}). Interestingly, change of lifetime value is more in the case of Fe^{3+} ions than the Al^{3+} ions. This clearly supports the LMCT as additional non-radiative decay pathways for Fe^{3+} ions.

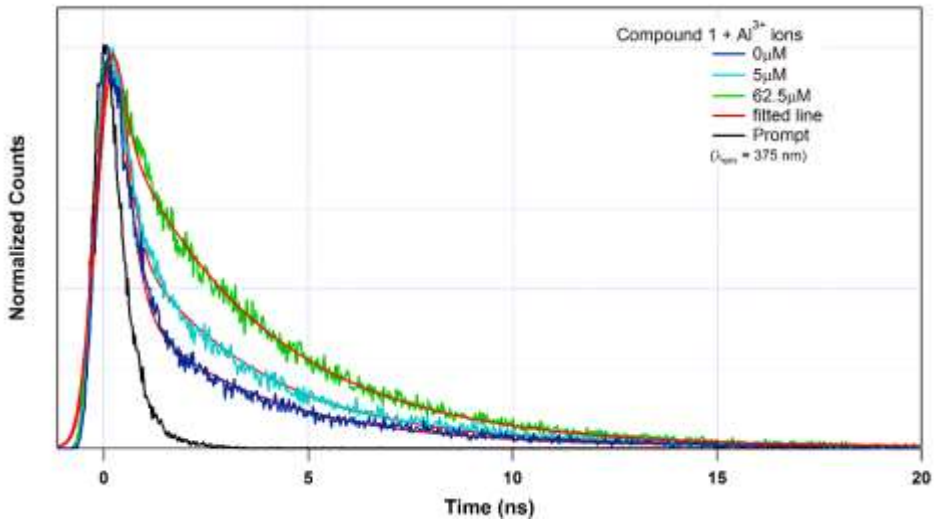

Fig. 5.94 Luminescence intensity decay profile of compound **5.1** before and after the addition of Al^{3+} ions. The final concentrations of Al^{3+} ions in the medium are indicated in the legend. The instrument response function (prompt) is also shown. Here, λ_{ex} = 300 nm and λ_{em}= 375 nm were set during the experiment.

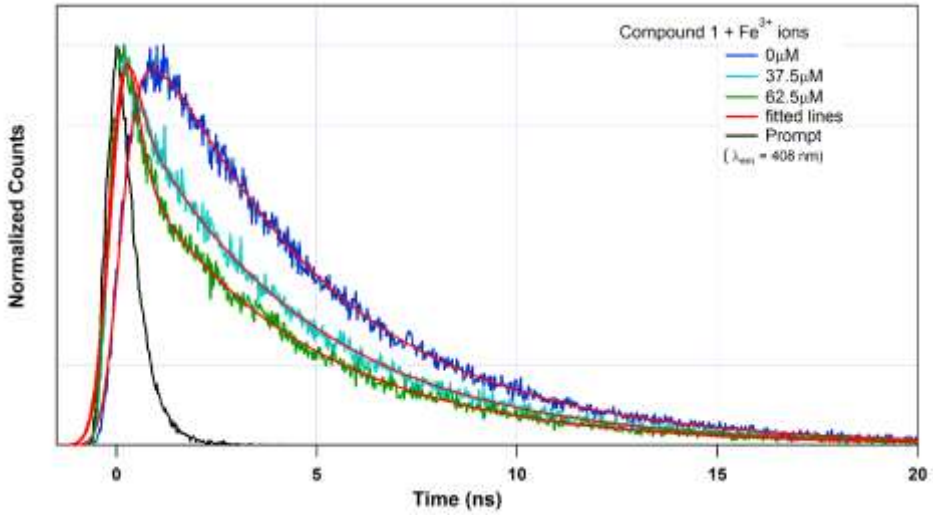

Fig. 5.95 Luminescence intensity decay profile of compound **5.1** before and after the addition of Fe^{3+} ions. The final concentrations of Fe^{3+} ions in the medium are indicated in the legend. The instrument response function (prompt) is also shown. Here, λ_{ex} = 300 nm and λ_{em}= 408 nm were set during the experiment.

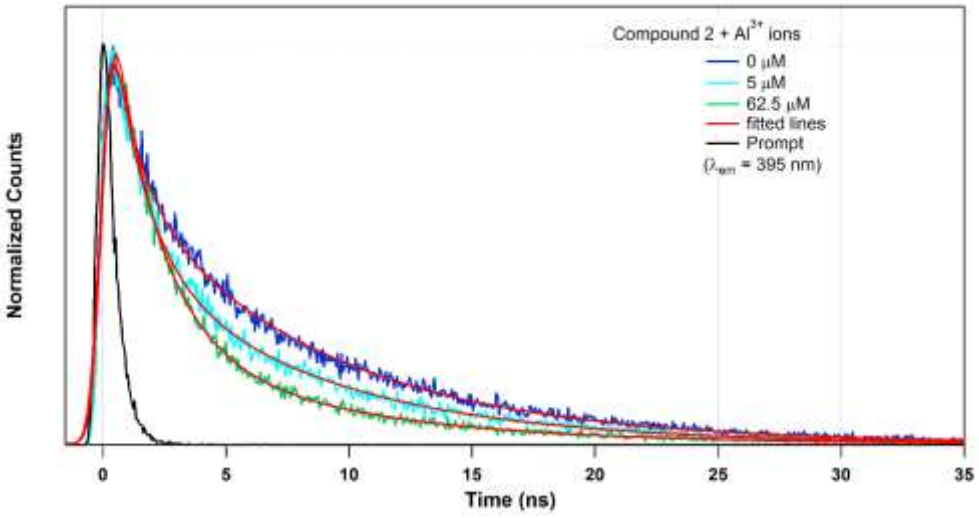

Fig. 5.96 Luminescence intensity decay profile of compound **5.2** before and after the addition of Al^{3+} ions. The final concentrations of Al^{3+} ions in the medium are indicated in the legend. The instrument response function (prompt) is also shown. Here, λ_{ex} = 300 nm and λ_{em}= 395 nm were set during the experiment.

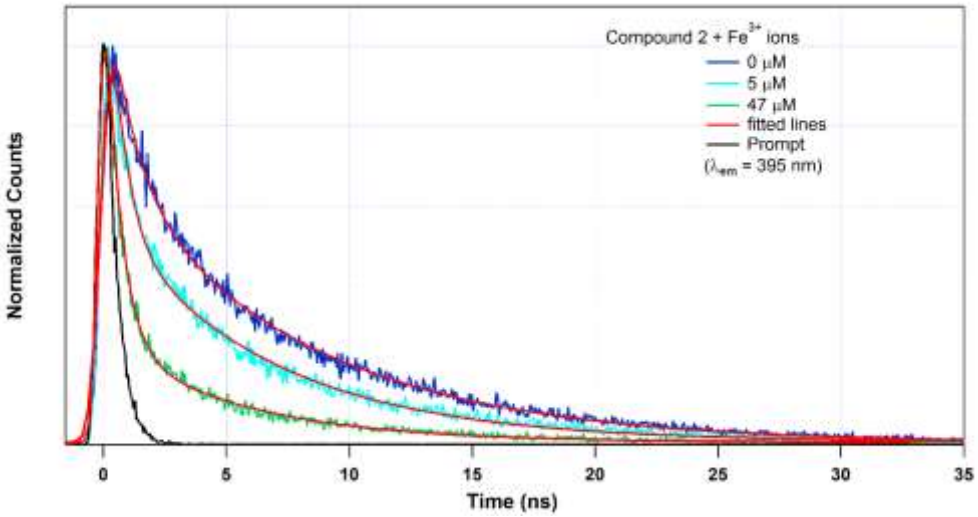

Fig. 5.97 Luminescence intensity decay profile of compound **5.2** before and after the addition of Fe^{3+} ions. The final concentrations of Fe^{3+} ions in the medium are indicated in the legend. The instrument response function (prompt) is also shown. Here, λ_{ex} = 300 nm and λ_{em}= 395 nm were set during the experiment.

Table 5.4: Luminescence life time of compound **5.1** and **5.2** in presence of metal ions (λ_{ex} = 300 nm).

Concentration of metal ions (μM)	**a_1**	**t_1**	**a_2**	**t_2**	**<t> (ns)**
Compound **5.1** in absence and presence of Al^{3+} ions ((λ_{em} = 375 nm)					
0	0.86	0.25	0.14	3.3	0.67
5	0.82	0.20	0.18	3.2	0.74
12.5	0.79	0.15	0.21	3.4	0.83
37.5	0.79	0.10	0.21	3.5	0.82
62.5	0.79	0.10	0.21	3.6	0.92
Compound **5.1** in absence and presence of Fe^{3+} ions ((λ_{em} = 408 nm)					
0			1.00	4.5	4.50
12.50			1.00	4.4	4.40
31.25			1.00	4.4	4.40
50.00	0.78	0.10	0.22	4.3	1.00
62.50	0.78	0.15	0.22	4.2	1.00
Compound **5.2** in absence and presence of Al^{3+} ions ((λ_{em} = 395 nm)					
0	0.45	1.10	0.55	8.0	4.80
5.00	0.60	1.40	0.40	7.6	3.88
12.50	0.68	1.45	0.32	7.6	3.41
25.00	0.71	1.45	0.29	7.3	3.14
62.50	0.76	1.80	0.24	7.3	3.12
Compound **5.2** in absence and presence of Fe^{3+} ions ((λ_{em} = 395 nm)					
0	0.45	1.10	0.55	8.0	4.80
5.00	0.64	0.60	0.36	6.6	2.76
12.50	0.68	0.70	0.32	6.3	2.49
47.16	0.84	0.60	0.16	5.6	1.40

5.4 CONCLUSION

Two new dioxidovanadium metal-organic compounds were synthesized in three different methods using either $V^{IV}OSO_4$. $5H_2O$ or $[V^{IV}O(acac)_2]$ or $NH_4V^{V}O_3$ as the starting material and hydrazone ligands. Molecular level structure determination studies were performed using single crystal X-ray diffraction experiments. In both the cases, the five coordinated V^{5+} ion adopted distorted square pyramidal geometry through the coordination of two oxido ligands and one hydrazone ligand. Structural studies established the stabilization of the structures through hydrogen bond and π electrons based interactions. The photoluminescence properties of the compounds were utilized for the discriminatory detection of metal ions. The compound **5.1** showed extremely discriminating luminescence turn on behaviour along with the 33 nm blue shift in presence of Al^{3+} ions in aqueous medium and the observed detection limit (LOD) was observed to be 66 nM. Whereas the compound **5.2** showed luminescence quenching behaviour in presence of three tri-valent cations - Fe^{3+}, Al^{3+} and Cr^{3+}. The LODs were found to be 312 nM (Fe^{3+}), 408 nM (Al^{3+}) and 280 nM (Cr^{3+}). With the help of the luminescence lifetime measurements along with the other experimental observations we have been able to propose a suitable mechanism for the dramatic response of these two compounds towards Al^{3+} and Fe^{3+}. It was found that for both the compounds the added metal ions interacted in the molecular level and that results in either increase or decrease in structural rigidity in different cases. Consequently, the extent of non-radiative decay of the excited state population gets affected which is manifested as luminescence turn-on in case of compound **5.1** with Al^{3+} and quenching in other cases.

5.5 REFERENCES

(5.1) D. C. Crans, J. J. Smee, L. Yanng, *Chem. Rev*., 2004, **104**, 849-902.

(5.2) D. Rehder, *Future Med. Chem*., 2012, **4**, 1823-1837.

(5.3) D. Patra, A. Pal, S. Nath, R. Kundu, M. G. B. Drew, T. Ghosh, *J. Inorg. Biochem.*, 2022, **234**, 1 – 15.

(5.4) L. M. Ramos, L. L. G. Justino, S. M. Fonseca, H. D. Burrows, *NJC*., 2015, **39**, 1488 – 1496.

(5.5) M. A. Palacios, Z. Wang, V. A. Montes, G. V. Zyryanov, P. Anzenbacher Jr, *J. Am. Chem. Soc.*, 2008, **130**, 10307-10314.

(5.6) M. A. Palacios, Z. Wang, V. A. Montes, G. V. Zyryanov, B. J. Hausch, K. Jursikova, P. Anzenbacher Jr, *Chem. Commun.*, 2007, 3708-3710.

(5.7) J. S. Marciano, R. R. Ferreira, A. Souza, R. F. S. Barbosa, A. J. Junior, D. S. Rosa, *Int. J. Biol. Macromol*., 2021, **181**, 112–124.

(5.8) J. Borrull, A. Colom, J. Fabregas, F. Borrull, E. Pocurull, *Chemosphere.*, 2021, **276**, 130023.

(5.9) T. Shahnaz, M. Madhar Fazil S, Padmanaban.V. C, S. Narayanasamy, *Int. J. Biol. Macromol*., 2020, **151**, 322–332.

(5.10) M. E. Mahmoud, G. M. Nabil, M. M. Zaki, M. M. Saleh, *Int. J. Biol. Macromol.*, 2019, **137**, 455–468.

(5.11) M. E. Mahmoud, M. F. Amira, M. M. H. M. Azab, A. M. Abdelfattah, *International Journal of Biological Macromolecules.*, 2021, **188**, 879–891.

(5.12) L. Sarkisov, *J. Phys. Chem. C.*, 2012, **116**, 3025−3033.

(5.13) K. Yu, Y.-R. Lee, J. Y. Seo, K.-Y. Baek, Y.-M. Chung, W.-S. Ahn, *Microporous Mesoporous Mater*., 2021, **316**, 110985.

(5.14) W. Xia, B. Zheng, T. Li, F. Lian, Y. Lin, R. Liu, *Carbohydr. Polym*., 2020, **250**, 116848.

(5.15) Y. Sun, H.-C. Zhou, *Sci. Technol. Adv. Mater*., 2015, **16**, 054202.

(5.16) P. Silva, S. M. Vilela, J. P. Tom´e, F. A. A. Paz, *Chem. Soc. Rev*., 2015, **44**, 6774–6803.

(5.17) Y. Ma, A. Huang, H. Zhou, S. Ji, S. Zhang, R. Li, H. Yao, X. Cao, P. Jin, *J. Mater. Chem.*, 2017, **5**, 6522–6531.

(5.18) K. Schneider, W. Maziarz, *Sensors.*, 2018, **18**, 4177.

(5.19) M. Talebi, K. Dashtian, R. Zare-Dorabei, H. Ghafuri, M. Mahdavi, F. Amourizi, *Analytica Chimica Acta*., 2023, **1247**, 340924.

(5.20) S. V. P. Vattikuti, N. D. Nam, J. Shim, *Ceram. Int.*, 2020, **46**, 18287–18296.

(5.21) S. V. P. Vattikuti, P. A. K. Reddy, P. C. NagaJyothi, J. Shim, C. Byon, *J. Alloys Compd*., 2018, **740**, 574–586.

(5.22) N. Sahraeian, F. Esmaeilzadeh, D. Mowla, *Ceram. Int.*, 2021, **47**, 923–934.

(5.23) T. Ghosh, B. Mondal, T. Ghosh, M. Sutradhar, G. Mukherjee, M. G. B. Drew, *Inorg. Chim. Acta*., 2007, **360**, 1753-1761.

(5.24) T. Ghosh, B. Mondal, R. A Patra, *Trans. Met Chem*., 2007, **32**, 468-474.

(5.25) B. Mondal, T. Ghosh, M. Sutradhar, G. Mukherjee M. G. B. Drew, T. Ghosh, *Polyhedron*., 2008, **27**, 2193-2201.

(5.26) B. Mondal, M. G. B. Drew, R. Banerjee, T. Ghosh, *Polyhedron*., 2008, **27**, 3197–3206.

(5.27) B. Mondal, M. G. B. Drew, T. Ghosh, *Inorg. Chim. Acta*., 2009, **362**, 3303-3308.

(5.28) B. Mondal, M. G. B. Drew, T. Ghosh, *Inorg. Chim. Acta*., 2010, **363**, 2296-2306.

(5.29) D. Patra, N. Biswas, B. Mondal, P. Mitra, M. G. B. Drew, T. Ghosh, *RSC Adv*., 2014, **4**, 22022-22034.

(5.30) N. Biswas, D. Patra, B. Mondal, M. G. B. Drew, T. Ghosh, *J. Coord. Chem*., 2016, **69**, 318-329.

(5.31) N. Biswas, D. Patra, B. Mondal, S. Bera, S. Acharyya, A. K. Biswas, T. K. Mukhopadhyay, A. Pal, M. G. B. Drew, T. Ghosh, *Dalton Trans*., 2017, **46**, 10963-10985.

(5.32) Bruker (2018). *Apex3 v2017.3-0*, *Saint V8.38A*, *SAINT V8.38A*; Bruker AXS Inc.: Madison, WI, 2018.

(5.33) L. Krause, R. Herbst-Irmer, G. M. Sheldrick, *J.Appl. Crystallogr.*, 2015, **48**, 3-10.

(5.34) A. Altomare, G. Cascarano, C. Giacovazzo, A. Guagliardi, *J. Appl. Crystallogr.*, 1993, **26**, 343-350.

(5.35) G. M. Sheldrick, Crystal Structure Refinement with SHELXL. *Acta Crystallogr., Sect. C: Struct. Chem.*, 2015, **71**, 3-8.

(5.36) L. J. Farrugia, *WinGX* suite for Small-Molecule Single-Crystal Crystallography. *J. Appl. Crystallogr.*, 1999, **32**, 837-838.

(5.37) A. L. Spek, Single-Crystal Structure Validation with the Program PLATON. *J. Appl. Crystallogr.*, 2003, ***36***, 7-13.

(5.38) R. A. Rowe, M. M. Jones, *Inorg. Synth.*, 1957, **5**, 113.

(5.39) D. K. Singha, P. Majee, S. Hui, S. K. Mondal, P. Mahata, *Dalton Trans.*, 2020, **49**, 829-840.

(5.40) P. Daga, P. Manna, P. Majee, D. K. Singha, S. Hui, A. K. Ghosh, P. Mahata, S. K. Mondal, *Dalton Trans*., 2021, **50**, 7388-7399.

List of Publications

1. **P. Manna**, A. K. Chandra, and P. Mahata, A Two-Dimensional Mixed Ligands based Coordination Polymer of Cadmium: Synthesis, Single Crystal Structure and Luminescence Quenching based Sensing Behaviours towards $Fe^{3+,}$ Cr^{3+}, Al^{3+} ions and TNP in Aqueous Phase, Inorganica Chimica Acta, 2025, (Articles in press)**.**
2. B. Mondal, **P. Manna**, D. K. Singha, P. Majee, S. Azam, S. Dutta, S. Halder, T. Ghosh, S. K. Mondal and P. Mahata, pH Independent Selective formation of VO_2^+ motif incorporating a Family of Hydrazone Ligands: Synthesis, Structure and Luminescence based Sensing Studies towards Selective Metal Ions, *Inorg. Chem*, 2024**, 63**, 46, 22203–22213.
3. **P. Manna**, A. Hasija, D. Chopra and P. Mahata, Selective dye sorption and metal ion sensing behaviours of a new Cd-based MOF, *New J. Chem.*, 2023,**47**, 19846-19855.
4. **P. Manna**, A. K. Chandra, V. D. Patel, D. Gupta and P. Mahata, Effect of Hydrogen Bonding on the Luminescence Lifetime and Device Resistance: A Case Study Based on Two New Related Cd-Based Coordination Polymers, *Crystal Growth & Design*, 2022, **22**, 7, 4559-4569.

- **These works are included in this thesis.**

1. P. Daga, **P. Manna**, P. Majee, D. K. Singha, S. Hui, A. K. Ghosh, P. Mahata and S. K. Mondal, Response of a Zn(II)-based metal–organic coordination polymer towards trivalent metal ions (Al^{3+}, Fe^{3+} and Cr^{3+}) probed by spectroscopic methods, *Dalton Trans*, 2021, **50**, 7388–7399.

2. P. Daga, P. Majee, D. K. Singha, **P. Manna**, S. Hui, A. K. Ghosh, P. Mahata and S. K.Mondal, Dramatic luminescence signal from a Co(II)-based metal–organic compound due to the construction of charge-transfer bands with Al^{3+} and Fe^{3+} ions in water: steady-state and time-resolved spectroscopic studies, *New J. Chem*, 2020, **44**, 4376—4385.

3. D. Ghosh, S. Dhibar, A. Dey, **P. Manna**, P. Mahata, Dr. B Dey, A Cu(II)-Inorganic Co−Crystal as a Versatile Catalyst Towards 'Click' Chemistry for Synthesis of 1,2,3-triazoles and β-hydroxy-1,2,3-triazoles, *ChemistrySelect*, **2020**, 5, 75– 82.

- **These works are not included in this thesis:**

List of scientific conference attended and poster presentation

- National Seminar on Chemical Sciences: Today and Tomorrow (CSTT-2019), Department of Chemistry, Jadavpur University, Kolkata-700032, India, 14th March, **2019**.

- National Seminar on Celebration of the International Year of the Periodic Table (CIYPT), Department of Chemistry Jadavpur University, Kolkata-700032, India, 13 & 14th August, **2019**.

- National Seminar on Emerging Trends in Chemical Sciences, Department of Chemistry, Jadavpur University, Kolkata-700032, India, 7th January, **2020**.

- National Seminar on RECENT TRENDS IN INORGANIC CHEMISTRY, Inorganic chemistry section, Department of Chemistry, Jadavpur University, Kolkata-700032, India, 6th March, **2020**.

- International Seminar on Recent Advances in Chemistry and Material Science (RACMS-2022), Indian Chemical Society in association with the Bangladesh Chemical Society, Bangladesh and Department of Chemistry, Jadavpur University, Kolkata, July 30-31 & August 02-03, **2022**.

- International Conference on “Modern Trends in Inorganic Chemistry, December 15-17, 2022.